Monitoring morphologic surface changes from aerial and satellite imagery, on Earth and Mars

Francois F. Ayoub

To cite this version:

Francois F. Ayoub. Monitoring morphologic surface changes from aerial and satellite imagery, on Earth and Mars. Applied geology. Universite Toulouse III Paul Sabatier, 2014. English. NNT : . tel-01101043

HAL Id: tel-01101043

https://theses.hal.science/tel-01101043

Submitted on 7 Jan 2015

THÈSE

En vue de l'obtention du

DOCTORAT DE L'UNIVERSITÉ DE TOULOUSE

Délivré par : *l'Université Toulouse 3 Paul Sabatier (UT3 Paul Sabatier)*

Présentée et soutenue le *1er juillet 2014* **par :**
François AYOUB

Suivi de changements morphologiques de surface à partir d'images aériennes et satellitaires, sur Terre et Mars

JURY

Jean-Philippe GASTELLU	Professeur d'Université	Président du jury
Alexis RIGO	Chargé de Recherche	Directeur de thèse
Jean-Philippe AVOUAC	Professeur d'Université	Directeur de thèse
Gilles PELTZER	Professeur d'Université	Rapporteur
Daniel RAUCOULES	Ingénieur de Recherche	Rapporteur
Patrick PINET	Directeur de Recherche	Examinateur

École doctorale et spécialité :
SDU2E : Sciences de la Terre et des Planètes Solides
Unité de Recherche :
Institut de Recherche en Astrophysique et Planétologie (UMR 5277)
Directeur(s) de Thèse :
Alexis RIGO et *Jean-Philippe AVOUAC*
Rapporteurs :
Gilles PELTZER et *Daniel RAUCOULES*

Remerciements

Il est d'usage en début de manuscrit de remercier les différentes personnes ayant accompagné, de près ou de loin, ces quelques années en thèse. Je ne dérogerai pas à la règle tant ceux-ci sont agréables à formuler, humanisent ces froids recueils scientifiques, et s'avèrent être la section la plus lue des thèses (?).

Tout d'abord je souhaite remercier le *Tectonics Observatory*, la *Moore Fundation*, le *Keck Institute for Space Studies* et la *Nasa* pour leur financement.

Je remercie les membres du jury pour leur temps, leur travaux d'évaluation, leur commentaires et leur discussions lors du rapport d'évaluation et de la soutenance.

J'en viens à remercier mes deux directeurs de thèse. Alexis Rigo, que je remercie doublement, d'une part pour m'avoir chaleureusement accueilli comme visiteur *"longue durée"* à l'ex-DTP il y a quelques années, et d'autre part pour avoir accepté être mon directeur de thèse malgré la distance Toulouse-Pasadena. Jean-Philippe Avouac, mon directeur de thèse certes, mais plus encore étant donné les quelques 10 années passées à travailler ensemble. Un immense merci pour m'avoir fait découvrir et apprécier la recherche scientifique et fait que ces années soient un vrai plaisir; cela par ton enthousiasme scientifique, la liberté et la confiance que tu m'as accordées, et ta constante disponibilité malgré un agenda surchargé.

Après tant d'années passées au sein du laboratoire il ne m'est pas possible de remercier nominativement tous les stagiaires, thésards, postdocs, visiteurs, assistants, techniciens, ingénieurs, enseignants, professeurs que j'ai eu la chance de rencontrer. Ralph Waldo Emerson disait: *"Tout homme que je rencontre m'est supérieur en quelque matière. C'est pourquoi je m'instruis auprès de lui."*. Tous, avez d'une façon ou d'une autre participé à ces travaux, par une simple question, un commentaire, une discussion, une collaboration, ou tout simplement en arrondissant les angles de la science par de nombreuses pauses café, déjeuner, sportives, et autres BBQ, campings, et randos. Je vous en remercie. Je mentionnerai tout de même Sébastien Leprince, mon voisin de bureau et *best buddy* en télédétection depuis les premiers jours, ainsi qu'Heather Steele notre assistante en or.

Je terminerai par le coeur de mon écosystème en adressant mes plus tendres remerciements à Emmanuelle, et en gardant une pensée pour Thibault, Mathilde et Pauline qui, un jour peut-être, lirons (amusés ?) un bout de cette thèse.

à mes chers parents, André et Danielle…

Contents

Introduction

Introduction to remote sensing

What is remote sensing? Wikipedia (2014) quotes "Remote sensing is the acquisition of information about an object or phenomenon without making physical contact with the object. In modern usage, the term generally refers to the use of aerial sensor technologies to detect and classify objects on Earth (both on the surface, and in the atmosphere and oceans) by means of propagated signals (e.g. electromagnetic radiation). It may be split into active remote sensing, when a signal is first emitted from aircraft or satellites, or passive (e.g. sunlight) when information is merely recorded". A trivial example of remotely sensed imagery is the Earth imagery that composes the background of Google Earth/Map and Bing maps.

Remote sensing started soon after the beginning of the space age in 1957, when the first man-made satellite, sputnik-1, was sent to orbit. Three years after, in 1960, the first remote sensing satellite, TIROS-1 a weather dedicated satellite, took pictures of the Earth (Fig. 1). However, it is usually acknowledged that remote sensing of the Earth started with the advent of the Landsat-1 launched in 1972. Every 16 days, Landsat-1 acquired images of the (almost) entire earth, at a spatial resolution of 80 m/pix, with 4 spectral bands ("colors"). The last satellite of that Landsat program (USGS, 2014c), Landsat-8, was launched mid-2013, and offer higher spatial (up to 15 m/pix) and spectral (11 bands) resolution. From that pioneering program, hundreds of Earth-observation satellites have been launched targeting a wide range of specifications and purposes. More than 500 satellites are currently "observing" the Earth.

The satellite instrument (the "camera") differs depending on the application at stake. Among the passive electo-optical sensors some instruments are designed for

FIGURE 1: First image of weather satellite TIROS-1 in 1960. Credit NASA.

higher ground resolution (0.5 m/pix Worldview satellite), while other are designed for higher spectral resolution (220 bands Hyperion). Active sensors instruments are also widely used. Radar and laser instruments for instance records specific phenomena or properties that would be out of reach using passive instrument. Light detection and ranging (LiDAR), a laser based instrument, is used in vegetation monitoring as it permits the recording of both the vegetation height and ground height below the canopy. Radar instrument can see through cloud and at night, and are used for topography mapping, and atmospheric properties sounding.

What are these hundreds of satellites used for? The applications are countless: Weather forecast, atmospheric pollution, ionospheric property; Ocean temperature, topography, salt concentration, tsunamis, ships surveillance; Monitoring of the cryosphere, urban sprawl, deforestation, desertification, agriculture, coastal erosion, volcanic activity; Mining, oil & gaz exploration; Disaster assessment and management, population monitoring. All of these applications, by no means an exhaustive list, adopted remotely sensed images as integral part of their activities.

Imagery alone is not enough though. Soon after the first acquisitions, it was realized that the raw imagery does not provide the information looked for. It is the information hidden behind the raw image, or series of images, that once extracted is of direct interest to the application considered. Examples of questions that you want the imagery to answer: What is the carbone dioxide concentration of the atmosphere? What is the topography of that area? How many new buildings are there? How healthy is the crop field? Is the coastline changing? By how much has the glacier retreated? Did it also thin while retreating? What is the roads network? What areas were affected by the landslide? Have these sand dunes moved? Did the earthquake deformed the ground? By how much? Answers to these questions are not easily and readily accessible from the images alone. Research groups have therefore developed methodologies and processes to detect, extract, measure, and quantify these informations.

Some applications require one image to obtain the information needed. For instance the monitoring of a crop field health can be done with one image through the so-called analysis Normalized Difference Vegetation Index (NDVI[1]) (Fig. 2). In tectonics, images are used to characterize active tectonic faults from their geomorphologic footprint on the landscape (Peltzer et al., 1989, Tapponnier and Molnar, 1977); this is a static approach that necessitates only one image. Some applications, however, require two or more images acquired at different dates to monitor the evolution of "something" through time. For instance, the comparison of the forest footprints between a pair of images will inform on the deforestation that occured between the acquisition dates (Fig. 3). In tectonics, a dynamic approach this time consists in measuring the ground deformation due to a fault rupture from a pair of images acquired at different dates (Massonnet et al., 1993, Raucoules et al., 2010, Van Puymbroeck et al., 2000).

In this thesis we will focus on a subset of the applications and instruments mentioned previously. Specifically, we will concentrate on the use of optical instrument to measure the displacement or deformation of a ground surface from a time-series of images. Details on that application range and methods are described in the next section. Remote sensing allows the measurement of large areas with a spatial density not achievable from in-situ measurements. These measurements are critical to better understand the underlying geomorphological processes, whether for scientific knowledge, predictions, or hazard assessment.

---

[1] NDVI is based on a ratio between spectral bands.

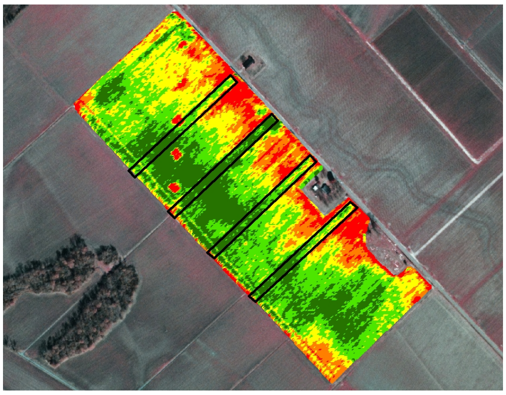

Figure 2: NDVI analysis from a multi-spectral satellite image. Credit LSU AgCenter.

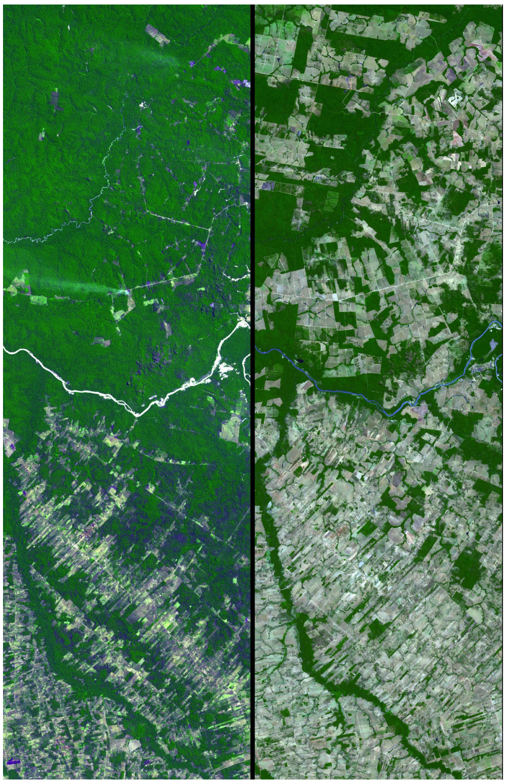

Figure 3: Deforestation evidence from multi-temporal satellite images. Credit JPL-NASA.

Monitoring surface displacement from remote sensing

Here, and from now on, "surface" means the surface of the Earth whether it is the bare ground, a glacier, a dune field,. . . and "displacement" means any deformation, migration, flux,. . . of the surface (or part of it). Specific example of measuring surface displacement include the measurement of the ground deformation induced by earthquake, the advance or retreat of a glacier, the migration of sand dunes, the expansion or deflation of a volcano mount, the sliding of a landslide. To measure surface displacement, at least two images are needed, acquired at different moment in time (days, months, years), and bracketing the event, whether sudden (e.g., earthquake), or continuous (glacier flux). Using image processing methods detailed below, the surface displacement can be measured from the two images by detecting and measuring the relative "shift" of the surface between them.

Measuring surface displacement from optical satellite imagery was first discussed by Crippen (1992) who accidently measured sand dunes migration while looking for earthquake ground deformation, and Scambos et al. (1992) who measured glacier flux from a pair of Landsat images. In recent years several studies used satellite imagery to measure co-seismic ground deformation (Binet and Bollinger, 2005, De Michele et al., 2008, Dominguez et al., 2003, Klinger et al., 2006, Michel and Avouac, 2002, Van Puymbroeck et al., 2000), glacier flux (Berthier et al., 2005, Scherler et al., 2008), landslide (Delacourt et al., 2004), and dune field (Necsoiu et al., 2009, Vermeesch and Drake, 2008). Leprince et al. (2007) proposed a methodological process flow to accurately extract surface displacement from a pair of satellite images. The method is summarized next, and the reader is encouraged to refer to this work for more details as this thesis is strongly based on it. The algorithms described in Leprince et al. (2007) have been implemented in a software, COSI-Corr (Co-registration of Optically Sensed Images and Correlation) (Tectonics-Observatory, 2014), and is distributed to the academic community since 2007.

There are three types of acquisition systems (ASPRS, 2004):

Frame system acquires the image in a single shot (the image is entirely acquired in one "click"). This system is not common on satellite.

Pushbroom system acquires the image line-by-line. The full image is constructed by the sequential acquisition of lines as the scene pass in front of the camera, such as a desktop scanner (one "click" per line).

Whiskbroom system acquires one pixel at a time. Like the pushbroom sensor, the whiskbroom acquires line by line, but acquires also every pixel of the line sequentially, using a fast rotating mirror.

Satellite imagers mostly use *pushbroom* systems[2]. Aerial imagery mostly use *frame* system[3], and will be the subject of the first part of this thesis. *Whiskbroom* systems are not common and will not be discussed further.

How to measure surface displacement from satellite imagery? From the raw images as acquired by the satellite to the final map of the surface displacement, a series of processing steps are needed. The process is summarized in the chart flow on Figure 4 , and works as follow:

---

[2] Except on recent or upcoming small satellites, e.g., Skybox and PlanetSat constellations.

[3] Leica cameras are exception.

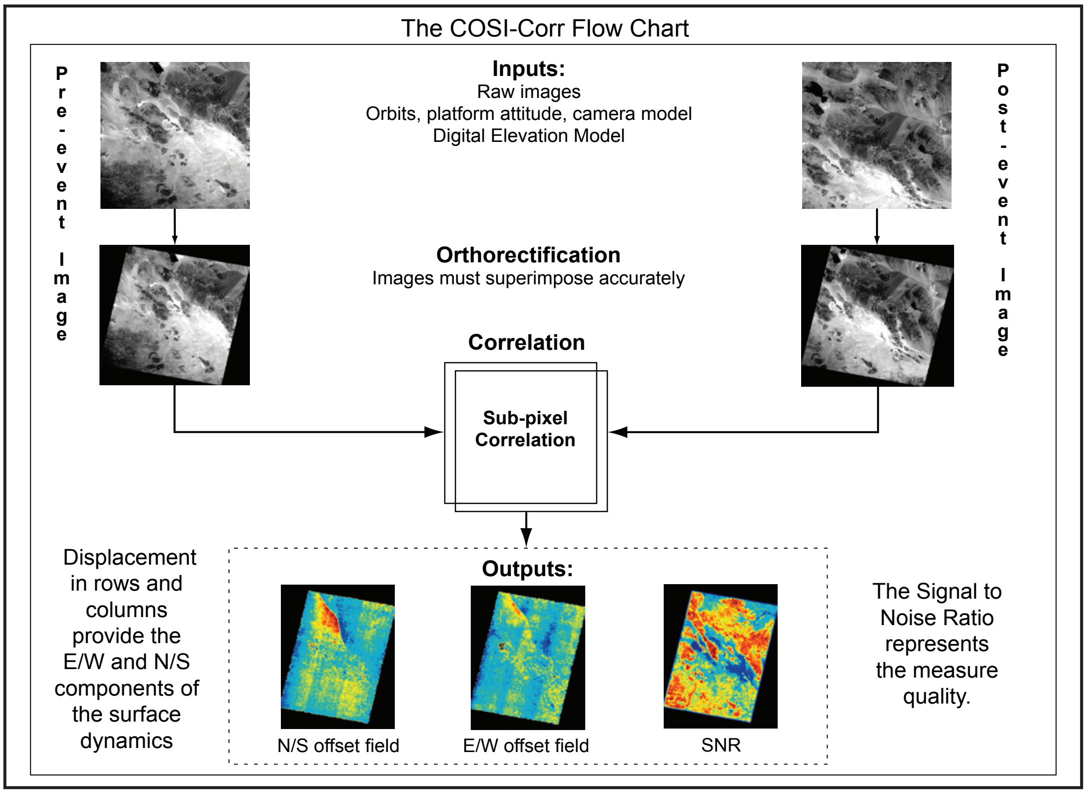

Figure 4: COSI-Corr flow chart of the imagery processing for accurate deformation measurement.

1. We start with the two raw images with their meta-data, and a Digital Elevation Model (DEM) which provides the scene topography. The meta-data of the image contains the geometric information of the camera during the acquisition: camera geometry and orientation, satellite position, speed, and jitter.

2. Using the images meta-data and DEM, a geometric acquisition model of each pixel is defined. That is, we establish the X, Y, Z coordinates in space of the ground imaged by each pixel of the images. Once the model is defined for both images, they are projected on a common cartographic projection (the so-called orthorectification) such that they are properly aligned to each other before comparison.

3. Once the images are in a common reference frame, they are compared through correlation: a sliding patch of size a few pixels (32×32 to 128×128 usually) step-and-correlate over the entire images: at each step, the patches of the two images are correlated; the correlation provides the displacement in pixel in the column and row directions of the features in the 2 patches, which can

be translated into a displacement in East/West and North/South. The final output is a East/West and North/South displacements maps, along with a map of the measurements confidence.

This process flow has been applied to various studies as mentioned earlier. How does this approach, which has be developed for, and used on, satellite imagery, adapt to aerial imagery, in particular archive film-based imagery? And how does it apply in a planetary context, to Mars specifically? This is the subject of this thesis and is described in the next section.

Thesis objectives

This work is divided into two main parts. The first part investigates the extension of the method described in Leprince et al. (2007) to aerial (frame) imagery, and presents a case study on a rifting event in Iceland. The second part of this thesis, illustrates the application of the method to Mars. In particular the method is applied to very high resolution imagery for the monitoring of sand mobility over a dune field. The measurements, first of their kind, brought new insight on Martian eolian processes.

Aerial imagery

As mentioned earlier, Landsat program is somehow the commonly acknowledged start of remote sensing. However, image acquisition of the earth started before that with aerial imagery[4]. Although the first aerial photo dates back from the early 20th century, federal, civil, and classified programs of aerial acquisitions started in mid-20th with objectives that were mostly topography extraction and land use mapping. Images were acquired on films, which were either reproduced, or printed on paper for use by photogrametrists. Similarly, defence departments launched spy satellites before the advent of Landsat. These classified surveillance programs started in the early 1960s (Keystone-USA; Kosmos-Russia), acquired images on large rolls of films, and returned the roll to Earth in a capsule (Fig. 6). During the last decade, some of these archives have been declassified and are now

---

[4] Images acquired from an airplane, as opposed to from a satellite

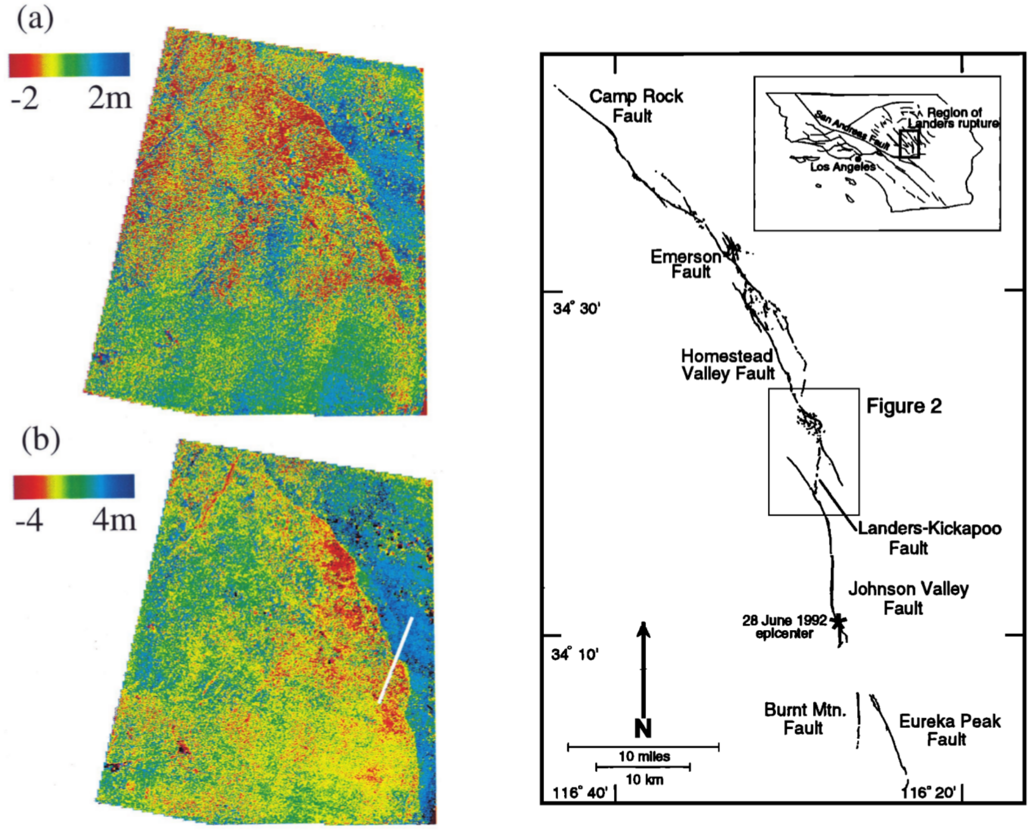

Landers ground deformation obtained from the correlation of 10 m/pix satellite imagery. From Van Puymbroeck et al. (2000). Coarse fault trace are recovered along with distributed deformations.

Landers ground rupture as mapped by field investigations. From Spotila and Sieh (1995). Fault trace is recovered in details, but no distributed deformation can be measured.

FIGURE 5: Comparison of surface displacement obtained between coarse satellite imagery and field mapping. Aerial imagery, with higher resolution, should recover the details of the rupture and distributed deformation.

accessible to the civil community. All these archives, whether aerial or declassified spy imagery, and despite varying resolution and quality, provide an opportunity to either study past events (Fig. 5), or to extend the monitoring of an area back in time.

Chapter 1 The first part of this study focuses on the implementation of aerial imagery into COSI-Corr porcess flow in the context of seismo-tectonic events monitorinf. Based on the early results obtained with aerial imagery for measuring coseismic ground deformation (Michel and Avouac, 2006), landslide (Delacourt et al., 2004), or volcano deformation (de Michele and Briole,

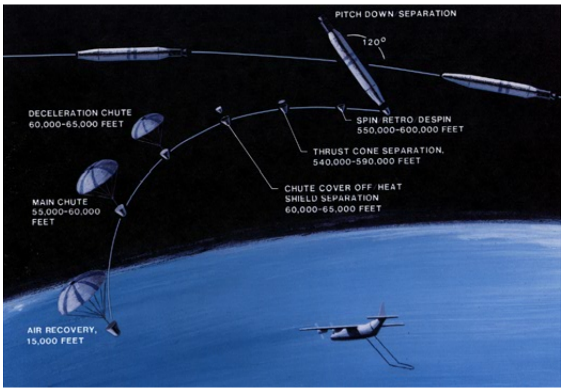

FIGURE 6: Spy imagery films return to Earth

2007), this chapter specifies a method based on Leprince et al. (2007) and photogrammetry procedures for the processing of aerial archive imagery (film based), and assess the potential and limitation of such images. In particular limitations such as scan artefacts, film distortions, distributed deformations, and unique topography issue are investigated through the application of the technique to the Landers and Hector Mine earthquakes. This chapter has been published under Ayoub et al. (2009)

Chapter 2 The second chapter presents a full study using archive aerial imagery. We investigate and quantify the Krafla, Iceland rift opening crisis that occurred in the mid-seventies using a mixture of modern satellite imagery, aerial imagery and declassified spy images. Temporal and spatial rift opening sequences could be estimated from the various acquisitions dates of the images. This chapter has been published under Hollingsworth et al. (2012)

Mars aeolian processes

Since Mariner-4 fly-by in 1965, Mars has been hosting a number of observation satellites. In 2004 and 2006, Mars Express and Mars Reconnaissance orbiter (MRO)(Fig. 7) respectively were sent to Mars orbit. Each carries about half a dozen instruments, among which some high resolution optical sensors. The *High Resolution Stereo Camera* (HRSC) on Mars Express acquires stereo imagery and color imagery of up to 2 m/pix resolution. The *High Resolution Science Experiment* (HiRISE) and the *Context Camera* (CTX) on MRO acquires images at a resolution of 0.25 and 6 m/pix respectively. Ironically, such high resolution, 0.25 m/pix, is not available on Earth due to federal restriction at 0.5 m/pix for civilian imagery[5].

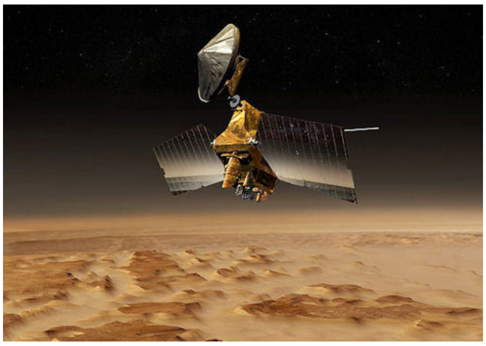

FIGURE 7: Mars Reconnaissance Orbiter. Credit NASAS & Univ. Arizona.

In the absence of liquid water, wind is the defacto main erosion agent on the planet today. Recurrent global dust storms and abundant bedforms suggest an active landscape subject to erosive winds. However, the low atmosphere density predicts the opposite and question about the "activeness" of these bedforms is raised. Thanks to the advent of HiRISE and its very high resolution, evidences of sand activity over dune fields were recently reported in Silvestro et al. (2010) and Hansen et al. (2011) who visually compared multi-temporal HiRISE images. However, Silvestro et al. (2010) could not determine if the sand ripple displacement observed was due to loose, by-passing sand over a fossilized bedforms, or part of a fully active dune process. We explored that question leveraging COSI-Corr sub-pixel capability and HiRISE imagery high resolution.

Chapter 3 Before moving to Mars and HiRISE imagery, this chapter is a short study presenting the main sources of errors found in the surface displacement maps when using pushbroom systems. We focus on the distortions due to the satellite non-perfect acquisition geometry. Distortions are characterized for several Earth satellites (SPOT, ASTER and Quickbird) and for HiRISE which will be used in the two next chapters. Specifically we document the main sources of distortions which are the unrecorded jitter of the satellite during acquisition, and the CCD arrays alignments residual. This chapter has been published under Ayoub et al. (2008)

Chapter 4 The first scientific objective of this work on Mars follows up the study of Silvestro et al. (2010), aimed at demonstrating unambiguously that Nili

---

[5] The restriction may be decreased to ~0.3 m/pix with the launch of WorldView-3 in 2014. Stay tuned...

Patera dune field is currently active. To measure aeolian bedform dynamics, the HiRISE geometry and Mars projection system were first implemented into COSI-Corr. A pair of HiRISE images acquired 3 months apart over the Nili Patera dune field was used to track the migration of the sand ripples laying on top of the dunes. We find that the entire dune field is covered with migrating ripples, confirming the active state of the dune field, as opposed to a fossilized state. An estimate of the sand flux is inferred, with a surprising amplitude comparable to some of the Antartica dune field. This chapter has been published under Bridges et al. (2012b)

Chapter 5 Encouraged by the results of the previous chapter, the HiRISE team acquired ∼10 additional images over Nili Patera, all together covering one Mars year. We characterize from the time-series analysis the seasonal sand flux variation throughout the year using the approach defined in the previous chapter. The sand flux seasonal variation is then used, jointly with sand flux prediction from atmospheric simulations, to estimate the sand mobility threshold, i.e., the shear stress threshold. This chapter is under review at Nature Communications at the time of this thesis writing.

Chapter 1

Co-registration and Correlation of Aerial Photographs for Ground Deformation Measurements

François Ayoub, Sébastien Leprince, Jean-Philippe Avouac

Division of Geological and Planetary Sciences, Caltech, California, U.S.A.

Foreword - This chapter describes the framework for aerial imagery processing. Although it is focused on analog imagery, i.e., acquired on film, the method described here can be easily adapted to digital aerial imagery. Since the publication of this work in 2009, additional methods and tools have been added to the framework, usually developed from the demand of a specific study as illustrated in Chapter 2. All the algorithms have been implemented in COSI-Corr software and distributed to the academic community. This work is referenced as Ayoub et al. (2009).

1.1 Introduction

In principle, ground displacements can be tracked through cross-correlation or feature tracking on multitemporal aerial photographs. This approach has been used with some success for a variety of applications, e.g., landslides (Delacourt et al., 2004), volcano (de Michele and Briole, 2007), and is of particular interest in seismotectonics. Large earthquakes generally produce ground ruptures which are an important source of information on earthquake mechanics in complement to geodetic and seismological measurements. Field measurements suffer from a number of limitations: fault ruptures have a complex geometry and the zone of anelastic co-seismic strain is sometimes distributed and difficult to detect in the field; fault slip can generally be measured only on a limited number of locations where clear offset piercing points are observable such as roads or terrace risers for example; the fault-perpendicular component is generally not measurable in the field. Optical satellite imagery can help overcome some of these limitations, the principle of the approach being that surface deformation can be measured by co-registration and correlation of images acquired before and after an earthquake (Van Puymbroeck et al., 2000). The technique has been implemented for operational use in a software for Co-Registration of Optically Sensed Images and Correlation (COSI-Corr) (Leprince et al., 2007), available from the Caltech Tectonics Observatory (http://www.tectonics.caltech.edu). The technique has proven effective in a number of studies of large, Mw>7, earthquakes (Avouac et al., 2006, Binet and Bollinger, 2005, Dominguez et al., 2003, Feigl et al., 2002, Klinger et al., 2005, Michel and Avouac, 2002). However, the resolution of satellite images, e.g., 2.5–10 m SPOT, 15 m ASTER, is sometimes insufficient to measure subtle fault displacement less than about 1 m (Leprince et al., 2007) and is therefore of limited use to analyze the details of co-seismic deformation or to investigate earthquakes with magnitude Mw less than 7. In addition, satellite images with appropriate geometric accuracy and ground resolution are not available for some past earthquakes which are known to have produced surface ruptures. The use of aerial photography with sub-metric ground resolution would extend the applicability of the technique to earthquakes too small to be measured from satellite images, or for which good quality satellite images would not be available. Michel and Avouac (2006) obtained encouraging results on the 1992 Landers earthquake using aerial photography from the United States Geological Survey (USGS). Motivated by this result, we have adapted to aerial images the procedure designed by (Leprince et al.,

2007) for the processing of satellite images. Hereafter, we describe this adaptation and assess the performance and limitations of the technique.

Retrieving accurate ground deformation of sub-resolution amplitude requires a number of processing steps. Prior to comparison, images must be finely co-registered. This is achieved by orthorectifying the images on a common projection while accounting for acquisition distortion, scaling difference, and topography. Special attention needs to be paid to the resampling to preserve the original image information. Ultimately, the correlation of the reconstructed images provides a map of the horizontal ground displacements.

We first detail the various steps in the processing: reconstruction mapping; resampling; co-registration optimization, and correlation. We next show an application to the 1992, Mw 7.3, Landers, California, earthquake. The technique is validated and sources of artifacts due to the scanning quality and to topographic distortions are identified and investigated. Finally, we present an application to the 1999, Mw 7.1, Hector Mine, California, earthquake to illustrate that, in the case of the co-seismic deformation measurements, some ambiguity between real ground displacement and mis-registration can arise, and we show how this ambiguity can be resolved.

1.2 Methodology

1.2.1 Technique Overview

The technique requires the digitization of the film based photographs with a high spatial and radiometric resolution scanner. Digital photography is not considered in this study as aerial photography archives are mainly film based. However, the technique described in this paper could be used with digital frame cameras as well.

Prior to comparison, images are co-registered through their orthorectification on a common reference system. Cumulative uncertainties on both the acquisition parameters and topography lead to mis-registrations between the orthorectified images to be compared. The co-registration is therefore improved by optimizing the acquisition parameters of the second image (the slave) with respect to the first orthorectified image (the master).

Orthorectified and precisely co-registered images are then correlated using a sliding window. At each step, horizontal offsets along the East/West and North/South directions are measured and stored.

1.2.2 Orthorectification & Resampling

We chose to orthorectify the images on the UTM grid for the following reasons: it provides a support independent from the acquisition system, allowing the pairing of images from different devices, e.g., satellite and aerial images; the relative displacements between orthorectified images are directly measured in length unit; the orthorectified images are cartographically correct, possibly a useful by-product.

The orthorectification transformation is defined using photogrammetry technique (Wolf, P and Dewitt, B, 2000); that is, definition of the camera's Interior Orientation (IO), and Exterior Orientation (EO) with the help of Ground Control Points (GCPs). The orthorectification transform, which associates ground coordinates (UTM in our case) to pixel coordinates, is applied to the UTM grid on which the images are projected. This defines the transformation matrices, containing the x and y coordinates of the pixels in the image to project.

The orthorectified images are constructed by resampling the raw images according to the transformation matrices. It is common practice to use the nearest neighbor, bilinear, or bicubic kernel for resampling. However, these kernels can corrupt the image information by introducing aliasing and may ultimately bias the correlation (Leprince et al., 2007). We therefore use the ideal sine cardinal (*sinc*) kernel, truncated to a length between 11 and 25 samples, and whose lobes are determined from the transformation matrices.

1.2.3 GCP Selection

GCPs are used to define an image's EO. A common method in selecting GCPs consists in measuring in-situ ground coordinates of features clearly identifiable on the image. This method is costly and might not be applicable depending on the area accessibility. The need for GCPs can be alleviated if on-board Kinematic GPS (KGPS) and Inertial Navigation Unit (INU) estimate directly the image's EO (Schwarz et al., 1993). The use of KGPS and INU have been common practice for the last couple of years. However, for more generality and to include older (pre-KGPS/INU) photographs, our approach assumes that the EO is not constrained from these techniques, and that no field measurements of GCPs are available.

GCPs are selected on the master image to obtain a proper orthorectified master with a minimum of topographic distortion. This requires georeferencing the image to the DEM as precisely as possible. Based on feature recognition, tie points are selected between the raw master and some external data such as a high resolution map, or an already georeferenced image (SPOT, aerial image, etc). The georeferencing of the external data (map,...) provides the horizontal coordinates, while the elevation is read from the DEM. If no external data are available, the shaded DEM can be used to define GCPs. In this case, the DEM provides both horizontal and vertical coordinates. Although this method works well with medium/high resolution satellites, it suffers from large inaccuracies with aerial images due to the usually large difference in resolution with the DEM. GCPs optimization explained in 1.2.4 allows some refinement generally yielding good results.

Once the master image is orthorectified, GCPs are selected on the slave image to achieve the best co-registration with the orthorectified master image. The slave's GCPs are defined by selecting tie points between the orthorectified master and the raw slave. The georeferenced master provides the horizontal ground coordinates while the DEM provides the elevation.

For our application of co-seismic ground deformation measurement, it might not be possible to define GCPs outside the deformation zone. Indeed, the footprint of aerial photographs is typically on the order of a few kilometers, while the deforming zone of earthquakes large enough to produce ground ruptures (with magnitudes $\mathrm{Mw} > 6.5$) is generally several tens of kilometers wide. As a consequence, selecting tie points between images bracketing the seismic event may introduce systematic error, since the ground coordinates of the slave tie points may have changed. In that case, information on ground deformation at the scale of the area covered by the GCPs is filtered out but the deformation at much smaller wavelengths such as the fault trace, the fault slip, and the near-field deformation, will still be retrieved. Satellite images with a larger footprint like SPOT ($60 \times 60\,\mathrm{km}$) generally contain areas far enough from the main deformation (i.e., away from the fault trace) where GCPs can be selected without introducing significant errors. If, for example, external data on ground deformation are available through, e.g., field survey, GPS measures, or SPOT correlation maps, it is then possible to correct for GCPs' ground coordinates that have undergone co-seismic displacement. Tie points are selected as previously explained, and ground coordinates retrieved from the orthorectified master are corrected according to these external data. Alternatively, the theoretical displacements at the GCPs locations can be estimated from an a priori earthquake source model (Hudnut et al., 1994).

1.2.4 Co-registration Optimization

Manual tie points selection leads to unavoidable mis-registrations between the orthorectified master and the orthorectified slave. However, these mis-registrations can be reduced afterwards by optimizing the slave GCPs as follows:

1. Start with the GCPs derived from the tie points selected between the orthorectified master and the slave image.
2. Estimate of the slave's EO based on the GCPs.
3. Orthorectification of the slave image and correlation with the orthorectified master image.
4. Correction of each GCP ground coordinate based on the ground offset found between the master and slave orthorectified images at each GCP location.
5. Return to (2) with the updated GCPs ground coordinates. Iterate until ground offset found between the master and slave images become negligible.

In practice, to reduce computation time, only patches centered around each GCP are orthorectified and correlated.

The optimized GCPs generally lead to a sub-pixel co-registration between the orthorectified images. This optimization suppresses the need for a meticulous and time consuming precise tie point selection; a manual, coarse selection is sufficient as the optimization adjusts GCP coordinates. Nevertheless, tie points must be selected in areas where correlation has a good chance of succeeding (good local texture), and where no obvious temporal change may bias the correlation (e.g., strong shadow, man made changes). Residual mis-registration comes from all the artifacts (e.g., DEM error, acquisition distortions) which were left unaccounted for.

GCP optimization can also be applied to the master if its GCPs were to be determined from an already orthorectified image. The shaded DEM can be used as the master image, but this method is more subject to decorrelations, and correlation is generally possible only in areas with rough, vegetation-free topography.

It should be noted that the procedure assumes the topography unchanged between acquisitions, so that the slave and master images can be orthorectified using the same DEM. This is only an approximation. Theoretically, one should instead use a pre- and post- earthquake DEM to orthorectify the pre- and post- earthquake images, respectively, to account for the change in topography. Unfortunately, access to a pre- and post-earthquake DEM is rare. Also, given the uncertainties of the DEM values and georeferencing, which are generally large compared to the aerial photography resolution, it is best to use a single DEM: the orthorectification errors due to the DEM errors might be presumed to affect similarly the orthorectification of the master and slave images. We will see later that this approximation is a source of systematic error that can be corrected.

1.2.5 Correlation

To measure precisely the relative offset between two images, several methods have been proposed in the literature. The one used in this study is based on phase correlation and described in detail in Leprince et al. (2007). The correlation method must be robust to noise and sub-pixel accurate, while using relatively small correlation windows (typically 32 × 32 pixels).

The correlation is a two steps process. The first step determines – at a multi-pixel scale – the shift between images from their correlation matrix. The second step refines the measurements at a sub-pixel scale by estimating the slope difference of the images' Fourier transform. To reduce windowing artifacts in the Fourier transforms, image patches are weighted with a Hanning window. Also, to improve further the correlation quality, a mask that filters out high frequencies is applied to the images' Fourier transforms.

Correlation is processed using a sliding window that scans the two images. Each correlation provides an offset in column and row directions, and a Signal to Noise Ratio (SNR, ranging from 0 to 1) which assess the measurement quality. In case of a UTM projection the measured offsets, in column and row, correspond directly

Study Case	Date	NAPP Code	Film Type	Scan Origin	Res. (μm)
Landers	07/25/1989	1790-161	CIR	USGS MD	14, 21 10
	10/03/1995	6825-253	B/W	USGS MD	7, 14, 21 10
	06/01/2002	12498-144	CIR	USGS	14, 21
Hector Mine	07/25/1989	1790-210	CIR	USGS	21
	06/01/2002	12488-50	CIR	USGS	21

TABLE 1.1: Data references. Scans were obtained from the USGS and from a microdensitometer (MD) originally designed for astronomy. CIR: Color Infra-Red.

to horizontal displacements along the East-West and North-South directions respectively.

1.3 Test Results

1.3.1 The 1992, Mw 7.3, Landers earthquake

In Michel and Avouac (2006), the Kickapoo step over of the 1992 Landers, California, earthquake was studied successfully using USGS National Aerial Photography Program (NAPP) photographs (USGS-NAPP, 1987). This program acquired images of the continental United States in a 5-7 year cycle. The aircraft altitude is around 20,000 feet (6100 m) and films are 9 × 9 inches, covering an area of slightly less than 10×10 km. The ground resolution is announced at 1 m while the film nominal resolution is about 10 μm corresponding to around 0.4 m on ground. Michel and Avouac (2002) used films scanned at 10 μm with a microdensitometer (MD) originally designed for astronomy with a theoretical positional accuracy of 0.6 μm and a root mean square error (rmse) of 0.2 μm. However, errors of up to 1 μm in repetitiveness were observed, leading to ground errors of up to 4 cm. In practice, access to a microdensitometer may be limited. To validate our methodology with more easily available data, we have studied the same case example using films scanned at 21 μm delivered by the USGS (Table 1.1).

Regarding the DEM, we used the freely available SRTM DEM, with a ground resolution of 1 arc-second (∼30 m). It has an absolute height accuracy of 16 m and a relative height accuracy of 10 m. The absolute horizontal accuracy is 20 m and the relative horizontal accuracy is 15 m. These accuracies are quoted at 90% level (JPL-NASA, 2000). The IO of the 1989 and 1995 images were established with the help of the camera calibration reports provided by the USGS. The 1995 image was co-registered first to the topography as the SRTM mission was carried out in 2000 (both post-earthquake). A shaded image of the DEM was generated (Fig. 1.1) with illumination parameters estimated from the 1995 image shadow pattern. Four GCPs were selected between the image and the shaded DEM. Horizontal and vertical coordinates were both obtained from the georeferenced DEM. Using patches of 256 × 256 pixels, GCPs were optimized according to the procedure outlined in 1.2.4. The average residual mis-registration was estimated to 2.4 m while the standard deviation residual was estimated to 18 m. This latter uncertainty is slightly higher than the 15 m relative horizontal accuracy of the SRTM DEM. More GCPs would have properly constrained the co-registration, but the limited topography in the image did not allow it. The 1995 EO was determined using the optimized GCPs. The image was then orthorectified on a 1 m resolution grid (UTM, North, Zone 11).

Five tie points, quite distant from each other, were taken on one side of the fault between the orthorectified 1995 image and the raw 1989 image (the fault was localized after a coarse pre-process with tie points selected at the four image corners). Horizontal coordinates were obtained from the 1995 orthorectified image, and elevation was read from the DEM to convert these tie points into GCPs. GCP optimization was carried out with 256 × 256 pixels patches. After three iterations the optimization converged. The average residual mis-registration was evaluated to 1 mm, and the standard deviation residual to 35 cm. The 1989 image was orthorectified with the help of the optimized GCPs on the same 1995 orthorectified image grid.

Images were then correlated using a 64×64 pixel window (64×64 m on the ground), with a 16 pixel sliding step. The results of the correlation process are presented in Figs. 1.2, 1.3, and 1.4. The fault ruptures appear clearly as discontinuities in the displacement maps. Horizontal fault slip is easily measured from profiles run perpendicular to the fault trace (Fig. 1.5). As also shown by Michel and Avouac (2006), the ruptures map and the measured fault slip are in excellent agreement

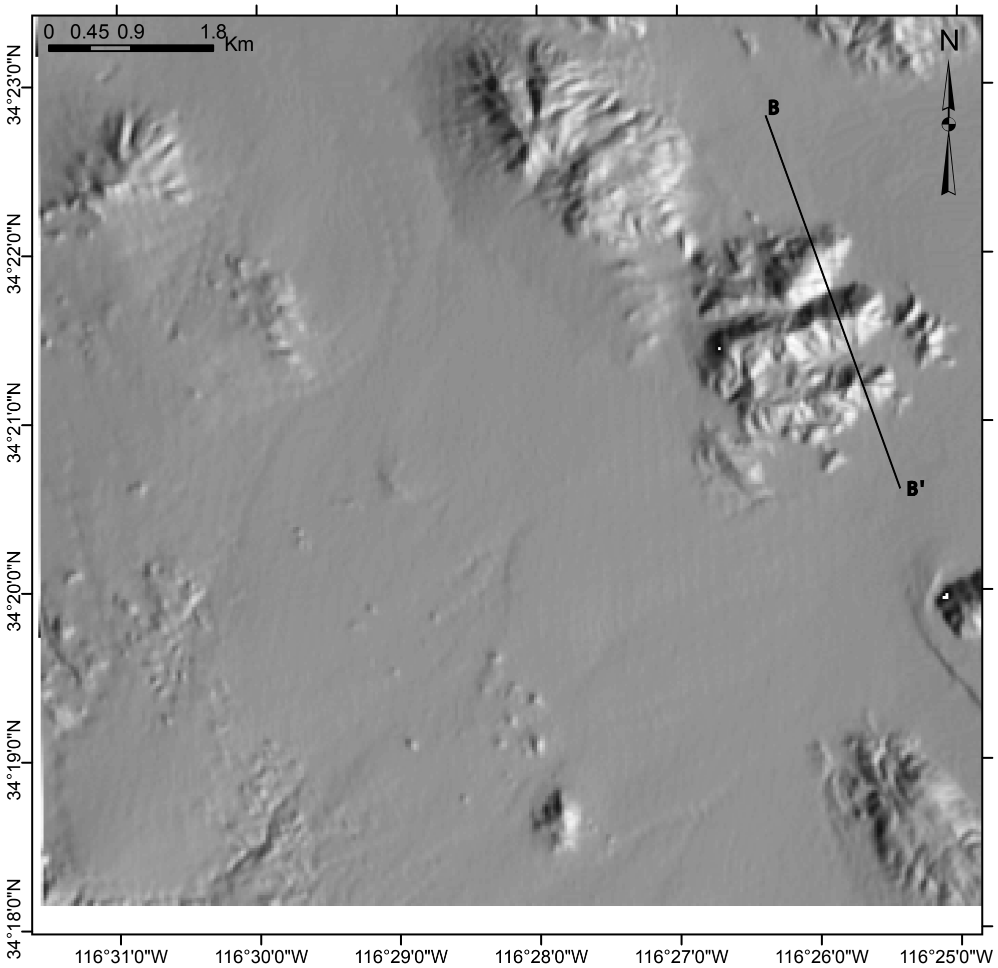

FIGURE 1.1: Shaded DEM of the study area. Profile BB' locates the profile on Fig. 1.3, and Fig. 1.9, and reported on Fig. 1.10.

with the field investigation of Sieh et al. (1993). To illustrate the potential of the technique we point to a secondary fault, mapped but not measured during field investigations, which is both detected and measured from the aerial photographs (Fig. 1.2). The horizontal slip is estimated to 20 cm (one-fifth of the images resolution) validating the sub-pixel change detection capability of the technique. In some areas, correlation is lost leading to very small SNR or outliers. Only 0.3% of the total number of measurements fall within this category. Inspection of the decorrelation areas show that they result from man made changes (new or modified buildings), or coincide with areas which are nearly translation invariant at the correlation window scale, e.g., radiometrically constant sandy areas, straight and isolated roads. It should be noted that the images were particularly suited to cross-correlation as NAPP follows strict acquisition specifications, e.g., no cloud cover, limited haze, and limited shading. A strong variation in sun illumination, for example, will cause shading and radiometric (depending on ground reflectance) differences in the images that can seriously compromise the correlation output.

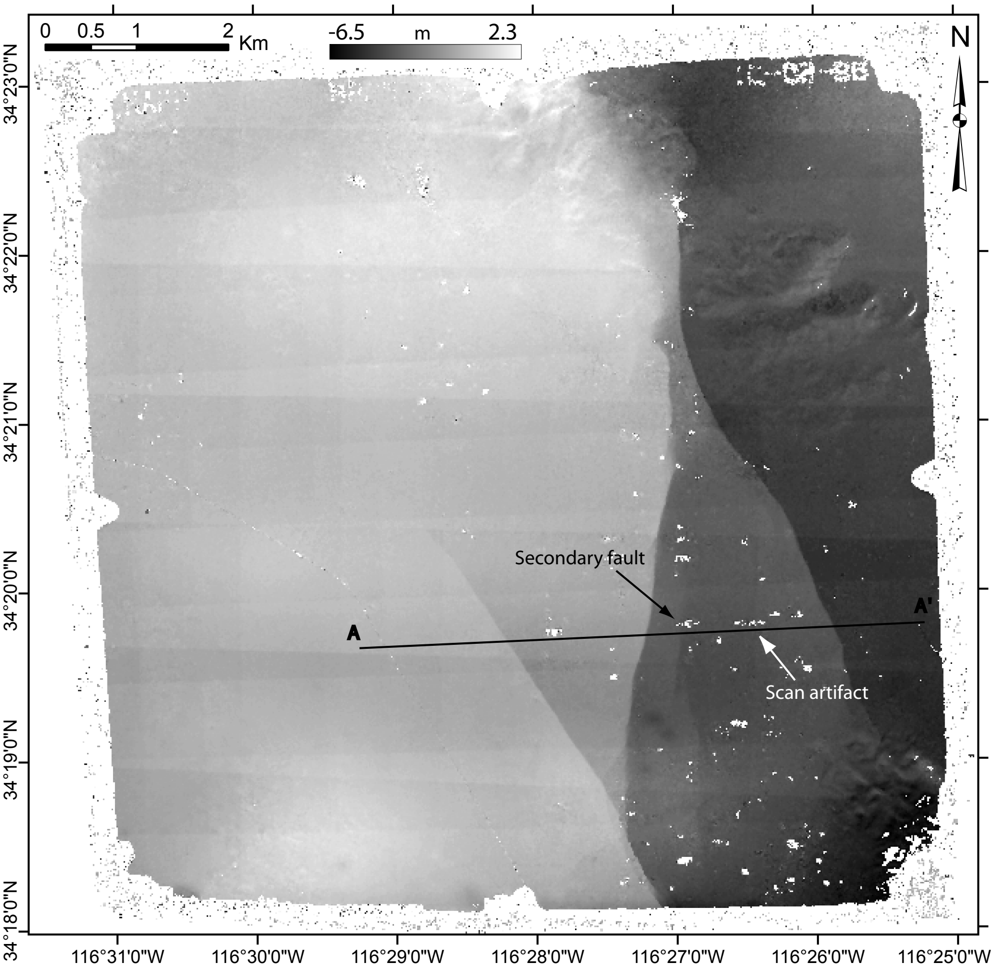

Figure 1.2: North/South displacement map of the Landers 1989/1995 correlation. Images were orthorectified on a 1 m grid and correlated using a 64 × 64 pixel window with a 16 pixel step. Positive displacement is toward the North. The main fault shows up as the main discontinuities, as well as a secondary fault trace with a slip estimated at 20 cm. Film distortion and scan artifacts, with amplitude up to 40 cm, are visible. Profile AA' is reported on Fig. 1.5.

To assess the potential bias and error of the measurements, an image of 2002 was co-registered to the 1995 orthorectified image with 13 GCPs. The GCP optimization, carried out with 256 × 256 pixel patches, converged after 4 iterations. The average residual mis-registration was evaluated to 2 mm and the standard deviation residual to 30 cm. Results of the correlation are presented in Figs. 1.6 and 1.7. No significant ground deformation is expected given that the only large earthquake in the area over that period of time is the 1999, Mw 7.1, Hector Mine, California, earthquake which occurred about 30 km away from the study area. Locally, the measurement spread is Gaussian with a standard deviation of 7 cm.

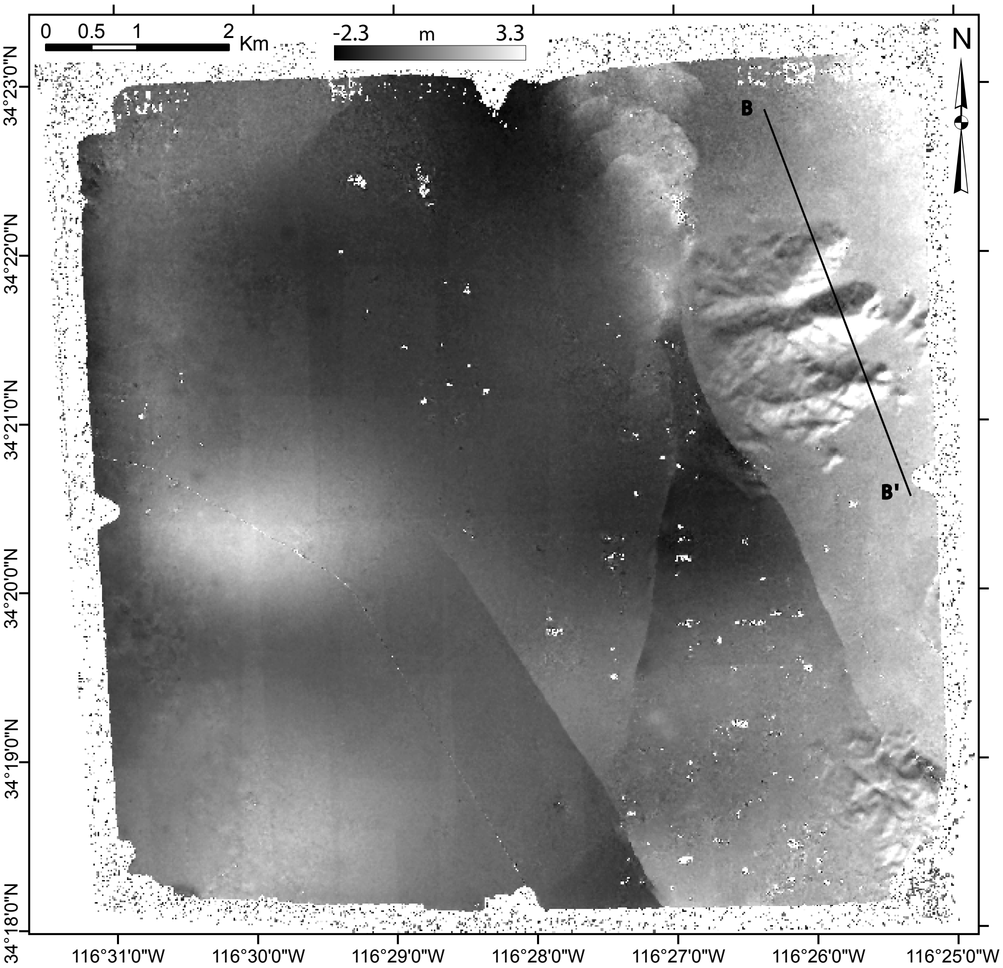

FIGURE 1.3: East/West displacement map of the Landers 1989/1995 correlation. Images were orthorectified on a 1 m grid and correlated using a 64 × 64 pixel window with a 16 pixel step. Positive displacement is toward the East. Topography and film artifacts are visible on the right and left side of the map respectively. Topographic artifacts are due to a parallax effect caused by the use of a unique DEM for the 1989 and 1995 images although the earthquake changed the topography. Profile BB' is reported on Fig. 1.10.

However, geometric artifacts mainly due to scan artifacts and film distortion cause the global measurement histogram to be not Gaussian with a spatially dependent distribution. The histogram is however centered at around zero, with a standard deviation of 25 cm and an amplitude maximum of up to 1 m.

As seen in the East/West displacement map (Fig. 1.7), deformation is everywhere negligible except along the 1992 fault trace event where some small amount of displacement are detected. This displacement corresponds to a right-lateral slip of about 10-15 cm. The possibility of a parallax effect due to a vertical up/down lift not accounted for in the DEM is discarded. Indeed, from Eq. 1.1, a 4 m

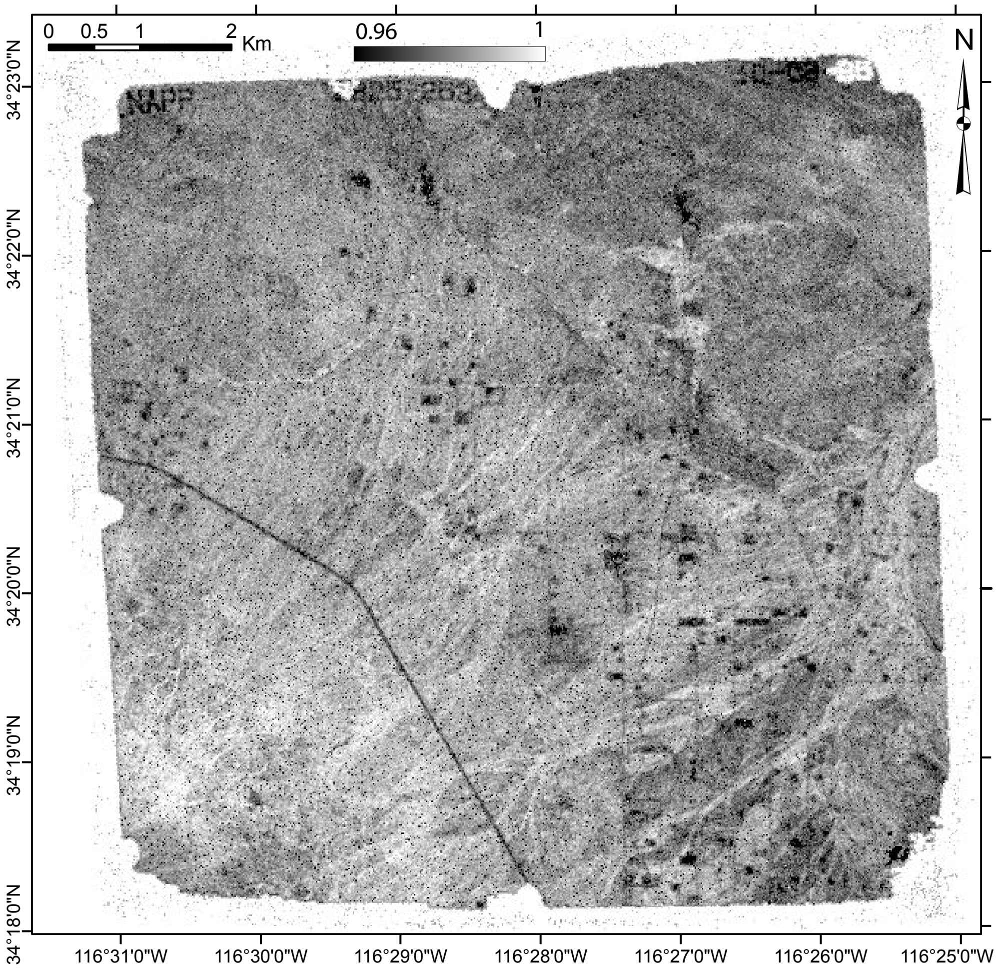

FIGURE 1.4: SNR map of the Landers 1989/1995 correlation. A higher SNR indicates a better correlation. Roads are visible and get a low SNR due to the poor correlation algorithm convergence on translation invariant features (Leprince et al., 2007). Other areas of decorrelation include man made changes. The total amount of decorrelation accounts for 0.3% of the measures.

up/down-lift would be necessary to cause a 15 cm horizontal parallax displacement. The displacement observed on the E-W component might be real and could correspond to aseismic slip triggered by the 1999, Hector Mine, earthquake, as reported on some other faults by Fialko et al. (2001) and discussed by Du et al. (2003). However, this deformation does not show up in the North/South displacement map, possibly because it is obscured by the particularly strong scan artifacts on this component (Fig. 1.6).

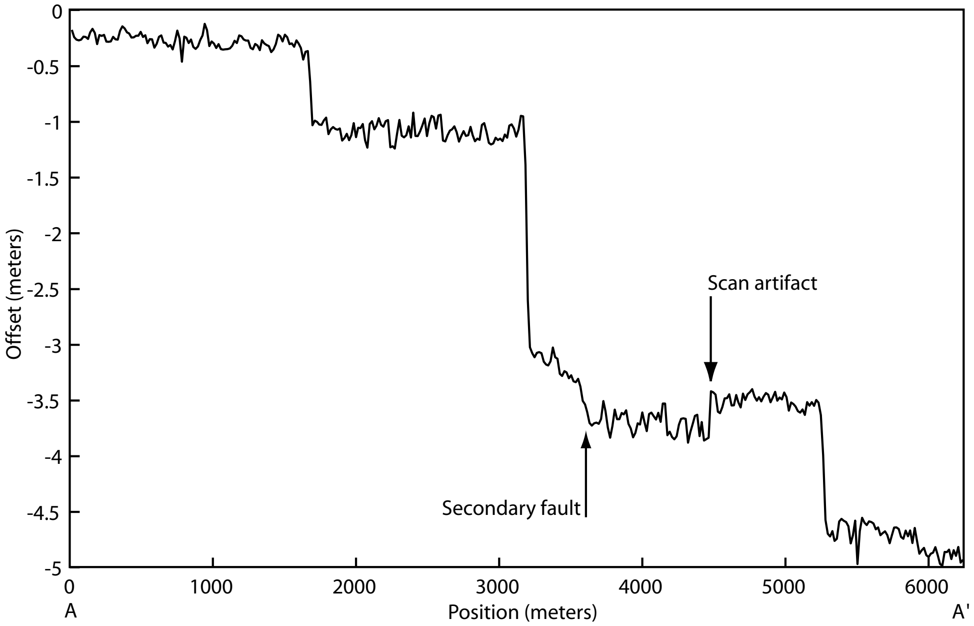

FIGURE 1.5: Profile AA' from Fig. 1.2. Secondary fault with slip amplitude as low as 20 cm is detected and its location is indicated by a black arrow on Fig. 1.2. At around the same amplitude a scan artifact is also detected and is indicated by a white arrow on Fig. 1.2. The standard deviation of the measurements is 7 cm.

1.3.2 Sensitivity to DEM artifacts

Topographic artifacts are seen on both 1989/1995 and 1995/2002 displacement maps, as suggested by the obvious correlation with the shaded topography (Figs. 1.1, 1.2, 1.3). The artifacts are most obvious on the 1989/1995 displacement map (Fig. 1.3) in the area of profile BB' where the relief is the roughest. A simple interpretation of this correlation is that the change of the topography due to co-seismic deformation cannot be ignored.

Assuming a perfect acquisition system and ignoring film distortions, scan errors, and correlation bias, the effect of the change of the topography (Fig. 1.8) can be accounted for by writing:

$$\begin{cases} DX = \underbrace{(h-h_1)\frac{x_1}{f_1}}_{a_x} + u - \underbrace{(h-h_1+dh)\frac{x_2}{f_2}}_{b_x} + \underbrace{\Delta DEM(u,v)\frac{x_2}{f_2}}_{c_x} \\ DY = (h-h_1)\frac{y_1}{f_1} + v - (h-h_1+dh)\frac{y_2}{f_2} + \Delta DEM(u,v)\frac{y_2}{f_2} \end{cases} \tag{1.1}$$

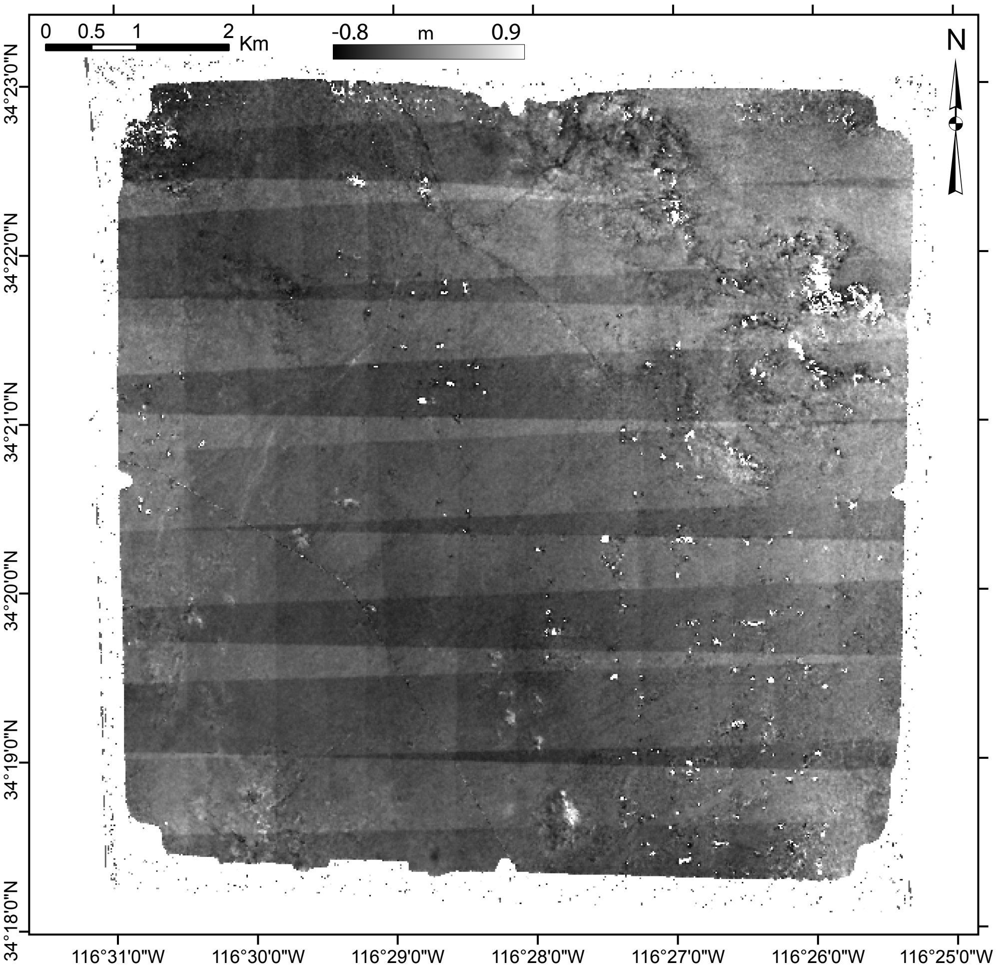

FIGURE 1.6: North/South displacement map of the Landers 1995/2002 correlation. Images were orthorectified on a 1 m grid and correlated using a 64 × 64 pixel window with a 16 pixel step. Strong scan artifacts are visible along the line and column directions. They have an amplitude up to 40 cm, which is above the 20 cm fault detected in Fig. 1.2, and can limit the technique depending on their amplitude and location. Notice that the fault displacement detected in Fig. 1.7 does not appear here, although it may be masked by the strong scan artifacts.

where DX and u refer respectively to the real and measured displacements in the East/West direction. DY and v apply to the North/South direction. Subscripts 1 and 2 refer to the master and slave images. h, h_1, and dh represent respectively, the real elevation of a ground point, the DEM elevation read at the ground point, and the vertical displacement of the ground point caused by the earthquake. f_1 and f_2 are the focal lengths of the master and slave cameras respectively, and x_1, y_1 and x_2, y_2 are the camera coordinates of the ground point image in the master and slave images respectively. Rearranging Eq. 1.1 and using standard trigonometric equalities we obtain:

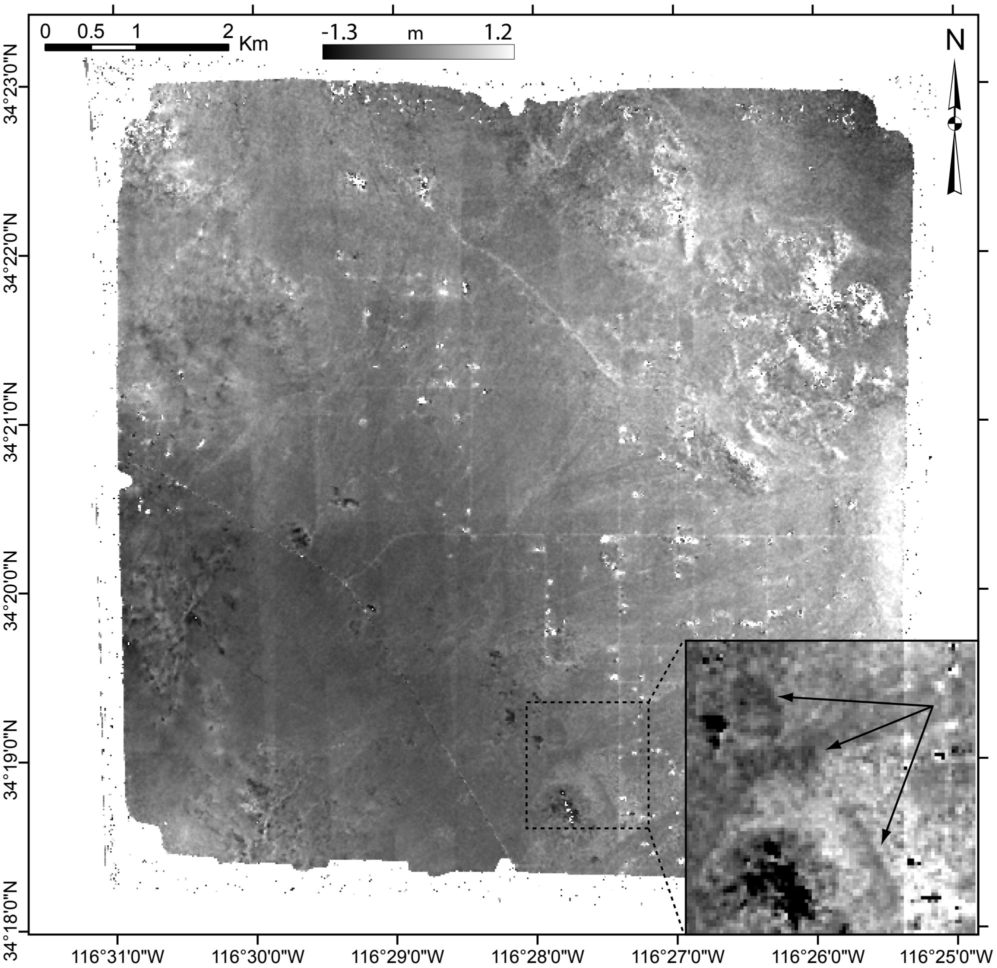

FIGURE 1.7: East/West displacement map of the Landers 1995/2002 correlation. Images were orthorectified on a 1 m grid and correlated using a 64 × 64 pixel window with a 16 pixel step. Inspection of decorrelation areas on topography revealed non negligible shadowing differences. Slight scan artifacts are visible in the column direction. Black arrows indicates fault displacements with an amplitude estimated at around 10-15 cm. No clear explanation has yet been found. A parallax effect due to a vertical uplift not accounted for in the DEM is discarded as 4 m of up/down lift would be necessary.

$$\begin{cases} DX = \underbrace{(h-h_1)\left[\frac{x_2}{f_2}\left(\frac{H_2-h-dh}{H_1-h}-1\right)-\frac{B_x+DX}{H_1-h}\right]}_{i} + \underbrace{\frac{x_2}{f_2}\Delta DEM(u,v)}_{ii} \\ \qquad\qquad -\underbrace{\frac{x_2}{f_2}dh}_{iii}+u \\ DY = (h-h_1)\left[\frac{y_2}{f_2}\left(\frac{H_2-h-dh}{H_1-h}-1\right)-\frac{B_y+DY}{H_1-h}\right] + \frac{y_2}{f_2}\Delta DEM(u,v) \\ \qquad\qquad -\frac{y_2}{f_2}dh+v \end{cases} \tag{1.2}$$

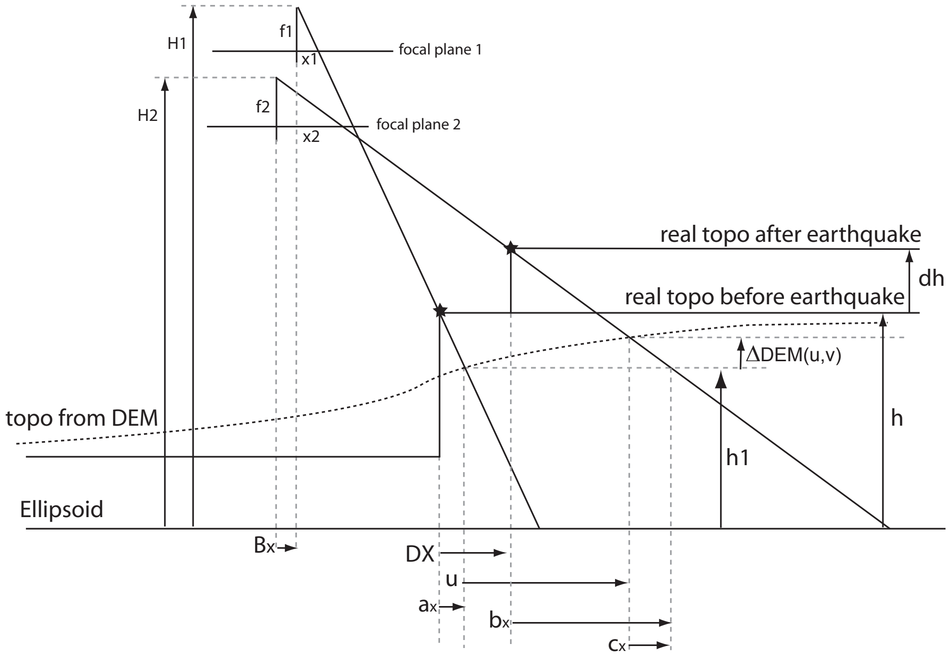

FIGURE 1.8: Geometry of the orthorectification and correlation measure in case of a unique DEM use (in one dimension) when other possible artifacts are considered null (film distortions, correlator bias,...). DX and u represent the real and measured horizontal displacement in the x direction.

where H_1 and H_2 are the optical center altitudes of the master and slave cameras respectively, and B_x, B_y are the optical center base in East/West and North/South direction respectively. i represents the displacement induced by the DEM elevation error, taking into account the difference of the exposure stations' location. It is the absolute DEM error $(h - h_1)$ weighted by the stereoscopic parallax coefficient at the ground point considered. This coefficient is composed of an acquisition altitudes ratio, and the base/height ratio. ii represents the term originating from the approximation of the topography by a single DEM. The corresponding artifacts are thus correlated to the topographic gradients and can then be easily identified. iii represents the horizontal offset resulting from a vertical displacement not accounted for when using a single DEM.

Field investigations by Sieh et al. (1993) have shown that vertical displacement in the Kickapoo area was small everywhere compared to the horizontal displacements. iii can therefore be neglected. Moreover, from the EOs of the 1989 and 1995 images, optical centers are close enough that stereoscopic parallax effects are also negligible. Considering that the co-seismic displacements are at most a few meters, we then have $(B_x + DX) \ll H_1$. In addition, we have $H_1 \approx H_2$, so that i can be neglected. i is indeed estimated to at most 6 cm, assuming a DEM error of 16 m, in the upper range of estimated errors on the SRTM DEM. The real displacements given by Eq. 1.2 are then estimated by correcting the displacements determined from the correlation maps according to:

$$\begin{cases} DX = \dfrac{x_2}{f_2}\Delta DEM(u,v) + u \\ DY = \dfrac{y_2}{f_2}\Delta DEM(u,v) + v \end{cases} \tag{1.3}$$

Using the apparent displacements estimated from the correlation maps (u, v), the DEM, and the slave image information, the corrected displacement field (DX, DY) can thus be retrieved. This correction is very effective in our case study: the topographic artifacts are no longer visible in Figs. 1.9, and 1.10. This simple procedure allows the correction of the correlation map for the DEM artifacts induced by the use of a single DEM. Note that in the case of a significant vertical displacement, the term *iii* in Eq. 1.1 cannot be neglected. In that case the measured offsets (u, v) are a linear combination of the horizontal and vertical displacements (DX, DY, dH). All three components of the displacement can be determined only if a second pair of images with a different viewing angle is available.

1.3.3 Sensitivity to Scan Characteristics

1.3.3.1 Scan Artifacts

In addition to topographic artifacts, scan artifacts are visible in both 1989/1995 and 1995/2002 displacement maps (Figs. 1.2, 1.3, 1.6, 1.7) in the North/South and East/West directions. The artifacts amplitude in the North/South (line) direction is the largest and accounts for up to 40 cm on the ground.

To assess the quality of USGS digitized images, additional 1989 and 1995 film scans at 7 and 14 μm were obtained from the USGS (Table 1.1). A Zeiss Precision Scanner using a PHODIS Photogrammetric Image Processing System and a Leica Geosystems DSW600 Digital Scanning Workstation were used for the digitization. Both instruments are attributed a positional accuracy of 1.5 μm (rmse) (USGS personal communication).

These scans were compared to the MD scans of Michel and Avouac (2006) as the MD offers a practical positional accuracy of 1 μm (rmse). 1989 and 1995 USGS

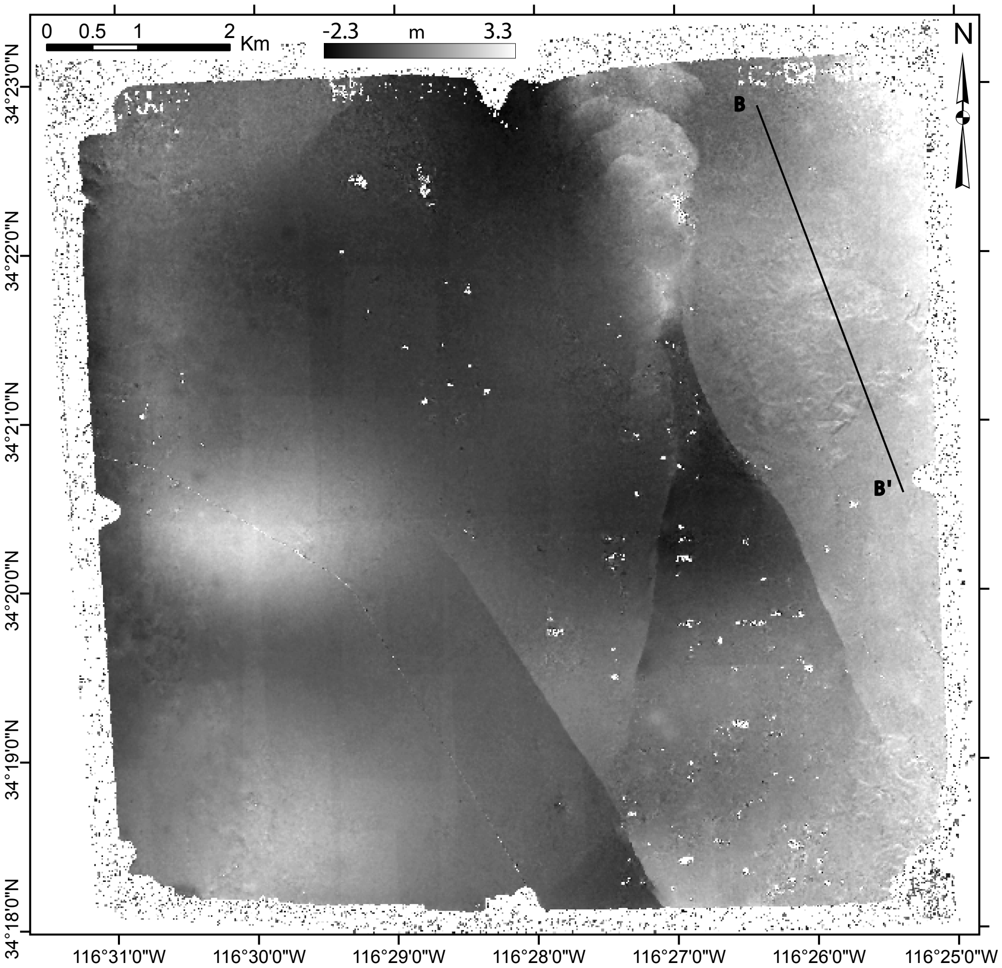

Figure 1.9: East/West displacement map of the Landers 1989/1995 correlation corrected for artifacts due to a single DEM use, according to Eq. 1.1. Profile BB' is reported on Fig. 1.10.

images were co-registered using manual tie points selection, wrapped (simple affine transformation), and correlated to the 1989 and 1995 MD images respectively. Note that, in this particular test, the images were not orthorectified, they were left in the camera geometry to avoid introducing other geometric artifacts. Apart from some long wavelength artifacts due to imprecision in co-registration and film distortions, scan artifact patterns are easily recognizable (Figs. 1.11, 1.12). The artifacts amplitude are presented in Table 1.2. Artifacts measured along the line and column directions are clearly visible, with larger amplitude found in the line direction. Scans at 7 and 14 μm provided different patterns but no better stability than scans at 21 μm. The artifacts are smaller on the B/W scans than on the color-infrared (CIR) scans. Surprisingly, the 21 μm B/W scans present the smallest artifacts.

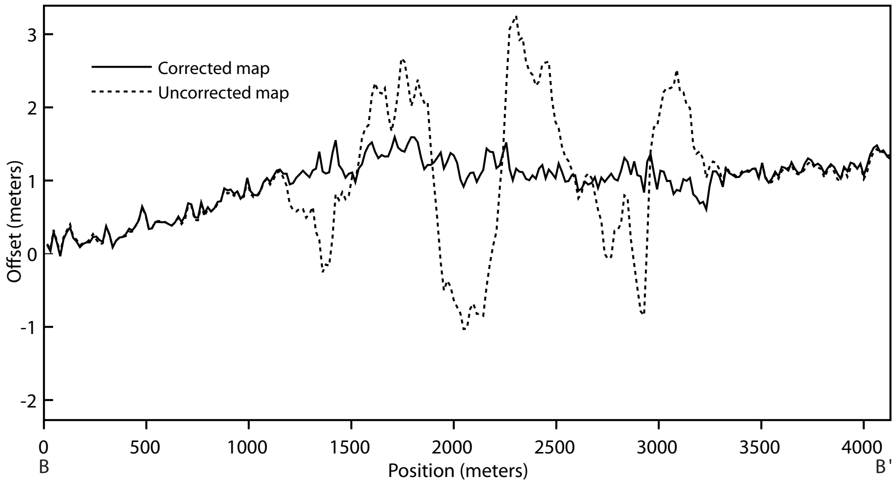

FIGURE 1.10: Profile BB' of the uncorrected (Fig. 1.3) and corrected (Fig. 1.9) East/West displacement map. Notice that artifacts are correlated to the topography (Fig. 1.10).

Year	Master Scan MD(μm)	Slave Scan USGS(μm)	Max Artifacts Row (μm)	Max Artifacts Column (μm)
1989	10	14	20	10
	10	21	8	4
1995	10	7	6	4
	10	14	6	4
	10	21	5	3

TABLE 1.2: USGS scan artifacts amplitude measured in row and column direction. Scans from the USGS are wrapped onto scans from an MD and correlated using a 64 × 64 pixel sliding window.

The observed scan artifacts, which are much stronger than what the nominal characteristic of the scanners would suggest, may put a severe limitation on the technique depending on their amplitude and orientation relative to the displacement to measure. However, scan artifacts produce patterns that are easily identified and relevant information (e.g. surface rupure map and fault slip) might be retrieved correctly from the correlation map using adequate care (Fig. 1.5).

1.3.3.2 Scan Resolution

The photographs of the USGS NAPP program have an estimated ground resolution of 1 m, although the film's nominal resolution is around 40 cm. Scans at 7, 10, 14, and 21 μm correspond to an average ground resolution of 20, 40, 56, and 84 cm

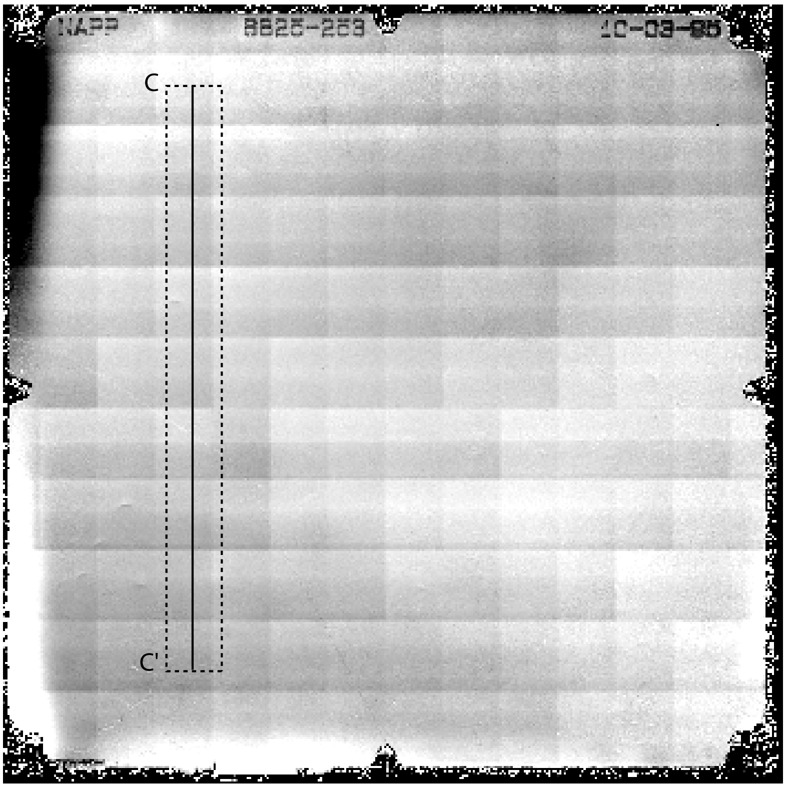

Figure 1.11: Displacement map along the line direction of the MD/USGS scans correlation. Scans of the 1995 film were obtained at 21 μm from the USGS and at 10 μm from a MD. MD scan was co-registered and wrapped onto the USGS scan using a sinc kernel for resampling. Correlation used a 64×64 pixel window with a 32 pixel step. Scan artifacts are also visible in the column direction but with smaller amplitude. Profile CC' is reported on Fig. 1.12. Other long wavelength deformation are due to film distortions and mis-registration.

respectively. Displacement maps obtained from scans at 7, 10, 14 and 21 μm did not present any improvement with increasing scan resolution. The quality of the measurement even degrades with the scan resolution due to the stronger scan artifacts as discussed above. For this particular study, a scan resolution close to the nominal image resolution is sufficient; higher scan resolution do not deliver additional information.

1.3.4 Sensitivity to GCPs

1.3.4.1 GCPs - Absolute Accuracy

To assess the sensitivity of the technique to the choice and accuracy of GCPs, the 1995 aerial photograph was orthorectified with 4 different GCP sets:

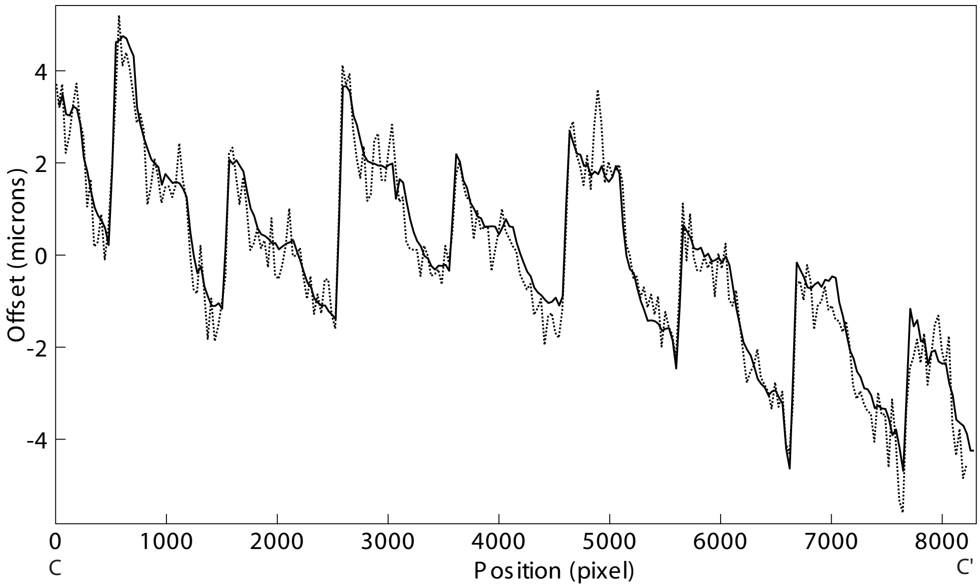

FIGURE 1.12: Profile CC' (Fig. 1.11) showing scan artifacts with amplitude up to 5 μm (around 20 cm on ground), above the scanner specifications announced at 1.5 μm rmse.

- case 1 - 10 GCPs obtained from a field survey using a differential Real Time Kinematics GPS, with an accuracy of a few centimeters.
- case 2 - 10 GCPs optimized with a 10 m ground resolution orthorectified SPOT image (which georeferencing was optimized with the shaded SRTM DEM).
- case 3 - 4 GCPs optimized with the shaded SRTM DEM.
- case 4 - 4 GCPs carefully selected manually but not optimized from the shaded SRTM DEM. This case simulates the situation where a poorly contrasted shaded DEM due to low relief prevents a good correlation during the optimization.

Orthorectified images from cases 2, 3, and 4 were correlated with the image from case 1, considered as the reference. The displacement maps show long wavelength distortions with some high frequency distortions correlated to the topography. Maximal mis-registrations are 10 m, 18 m, and 25 m for case 1/2, case 1/3, and case 1/4, respectively. Case 2 and case 3 are within the SRTM DEM absolute horizontal accuracy (20 m), whereas case 4 is outside. Although the SPOT image was also coregistered with the shaded SRTM DEM, case 2 absolute georeferencing is better than case 3. This is explained by the larger area and larger number of GCPs (~ 20) used to coregister the SPOT image to the shaded DEM.

To assess the consequence of these mis-registrations on the co-seismic displacement maps, the 1989 slave image was co-registered and correlated with the four-case 1995 orthorectified images. The results were found to be similar regarding the surface rupture mapping and fault slip vectors. However, long wavelength displacements were different.

1.3.4.2 GCPs - Tectonic signal distortions

The major source of distortion at long wavelength found in 1.3.4.1 comes from the assumption made during the slave image's GCP definitions. Indeed, tie points are selected between the slave and the orthorectified master to co-register the two images. These tie points are converted to GCPs using the orthorectified master georeferencing for horizontal coordinates and the DEM for the vertical coordinate (elevation). The possible ground displacement at each GCP location is then cancelled out by equating the slave ground coordinates with the master ground coordinates for each GCP. We illustrate this from NAPP aerial images of the 1999, Mw 7.1, Hector Mine, California, earthquake (Table 1.1). Pre- and post-earthquake images were processed using the methodology described in 1.2. Three tie points were selected between the slave and orthorectified master and the derived GCPs were optimized. The North/South displacement map is presented in Fig. 1.13. The 2D displacement is overlaid as vectors on the figure, together with the GCP locations. The fault rupture is clearly visible. Its geometry and horizontal slip are in accordance with the field measurements by Treiman et al. (2002). As expected, displacement falls to zero at GCP locations. The co-registration compensated the real ground displacements at the GCP locations and introduced long wavelength distortion in the displacement maps. Forcing the co-registration at GCP locations without accounting for the ground displacement introduces long wavelength distortion biasing ground displacements in the far-field.

This bias can be avoided if estimates of the ground displacements at the GCP locations are known and taken into account during the optimization. To demonstrate this point we used the Hector Mine earthquake displacement maps determined from the correlation of 10 m SPOT images (Leprince et al., 2007). The SPOT images were co-registered using GCPs far away from the fault zone where co-seismic displacement could be neglected. A subset of the North/South displacement map

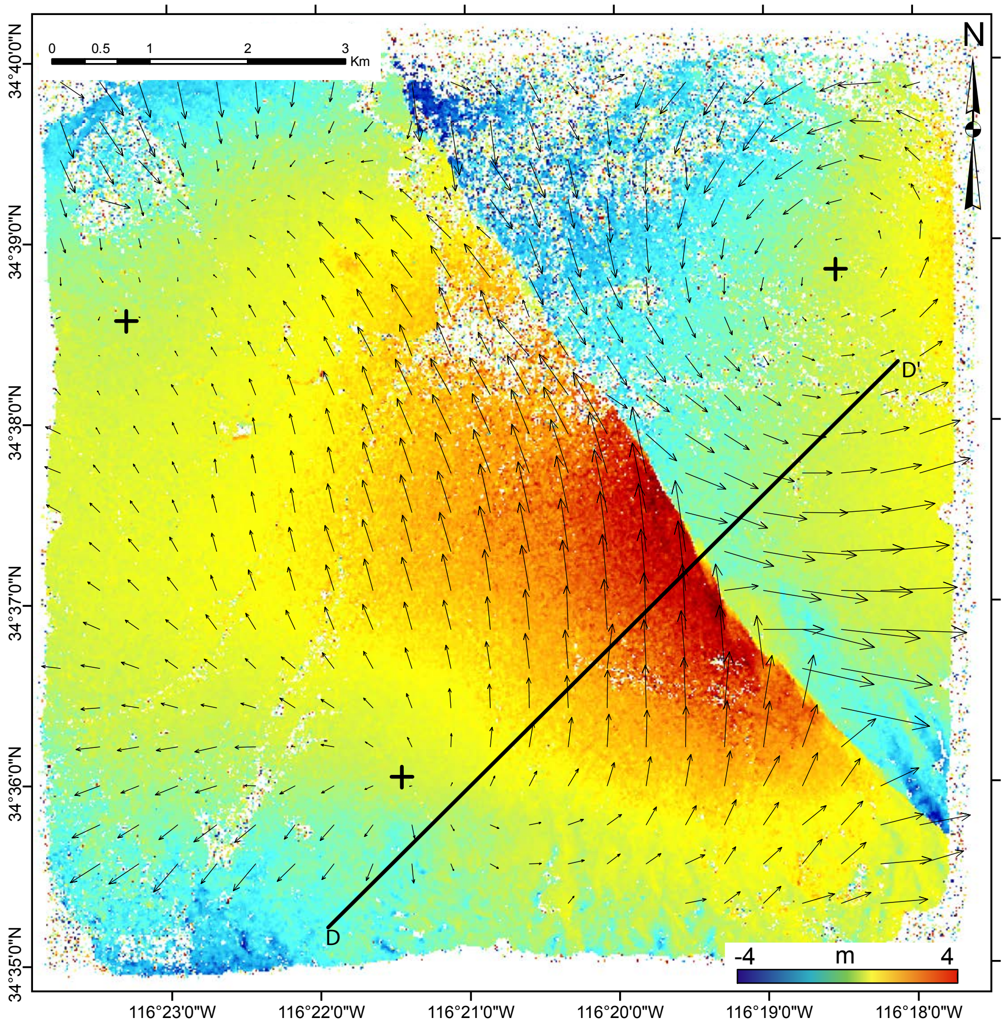

Figure 1.13: North/South displacement map of the 1989/2002 correlation of images bracketing the Hector Mine earthquake. Images were orthorectified on a 1 m grid and correlated using a 64×64 pixel window with a 16 pixel step. Three GCPs, indicated by the black crosses, were optimized to co-register the master and slave images without accounting for seismic ground displacement at their ground location. Overprinted vectors were generated from the North/South and East/West displacement maps, and represent the 2D ground displacement. Long wavelength distortions (vortices) are introduced to satisfy the master and slave co-registration. Profile DD' is reported on Fig. 1.16.

obtained from the SPOT images is shown in Fig. 1.14. The dashed square represents the aerial images footprint.

The GCPs of the aerial slave image were then re-optimized taking into account the displacements measured from SPOT at the three GCP locations (Fig. 1.14). The North/South component of the displacement obtained from this procedure is shown in Fig. 1.15. The fault geometry and fault slip value are identical to the ones from the first process. However, the long wavelength component of the

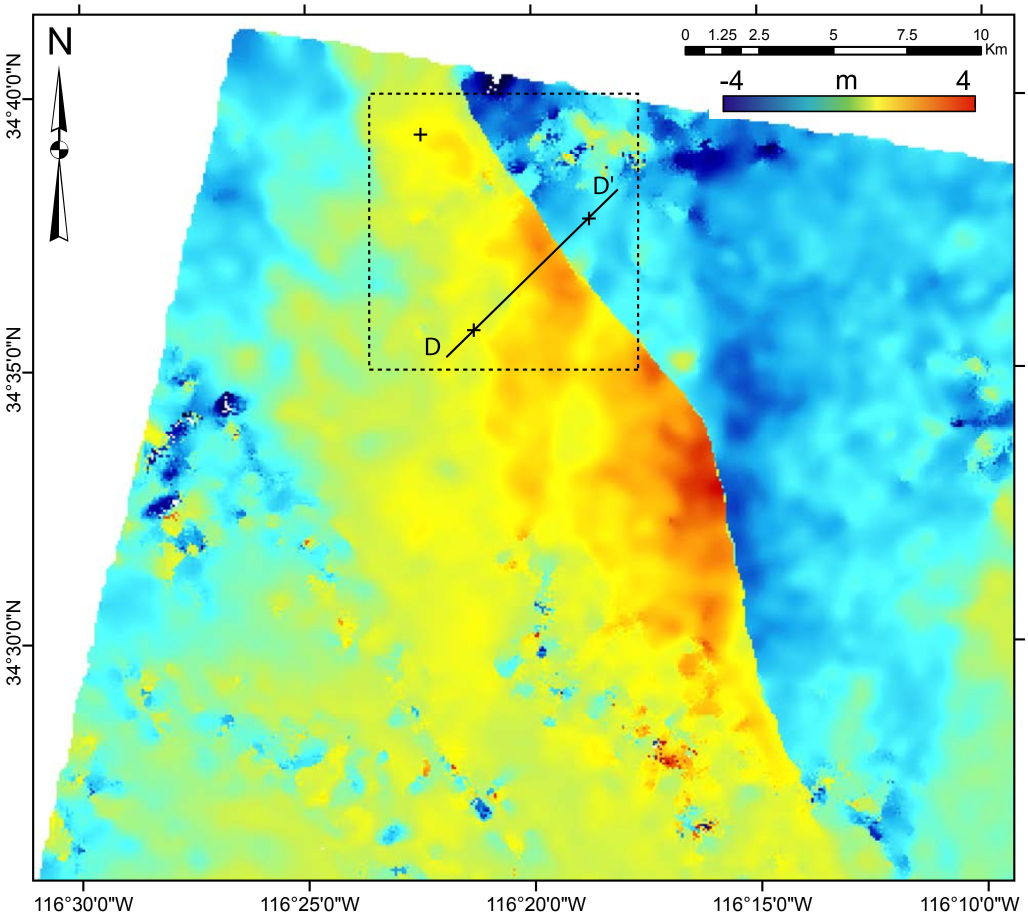

FIGURE 1.14: North/South displacement map of the denoised SPOT correlation of images bracketing the Hector Mine earthquake. Three GCPs located far enough away from the fault to assume a null ground displacement were optimized to co-register the master and the slave. Images were orthorectified on a 10 m resolution grid and correlated using a 32×32 pixel window with an 8 pixel step. Positive displacement is toward the North. The raw displacement maps were denoised by a technique preserving fault offset (personal communication, Leprince). The dotted square represents the aerial photograph footprint, and black crosses indicate the location of the aerial photograph GCPs. Profile DD' is reported on Fig. 1.16.

displacement map now matches the SPOT displacement map, and the distortion found on Fig. 1.13 was corrected. Nevertheless, far-field ground deformation must be considered carefully with film based imagery as film distortion, for example, manifests itself in the displacement map by deformation of similar frequency and amplitude (e.g., Fig. 1.3).

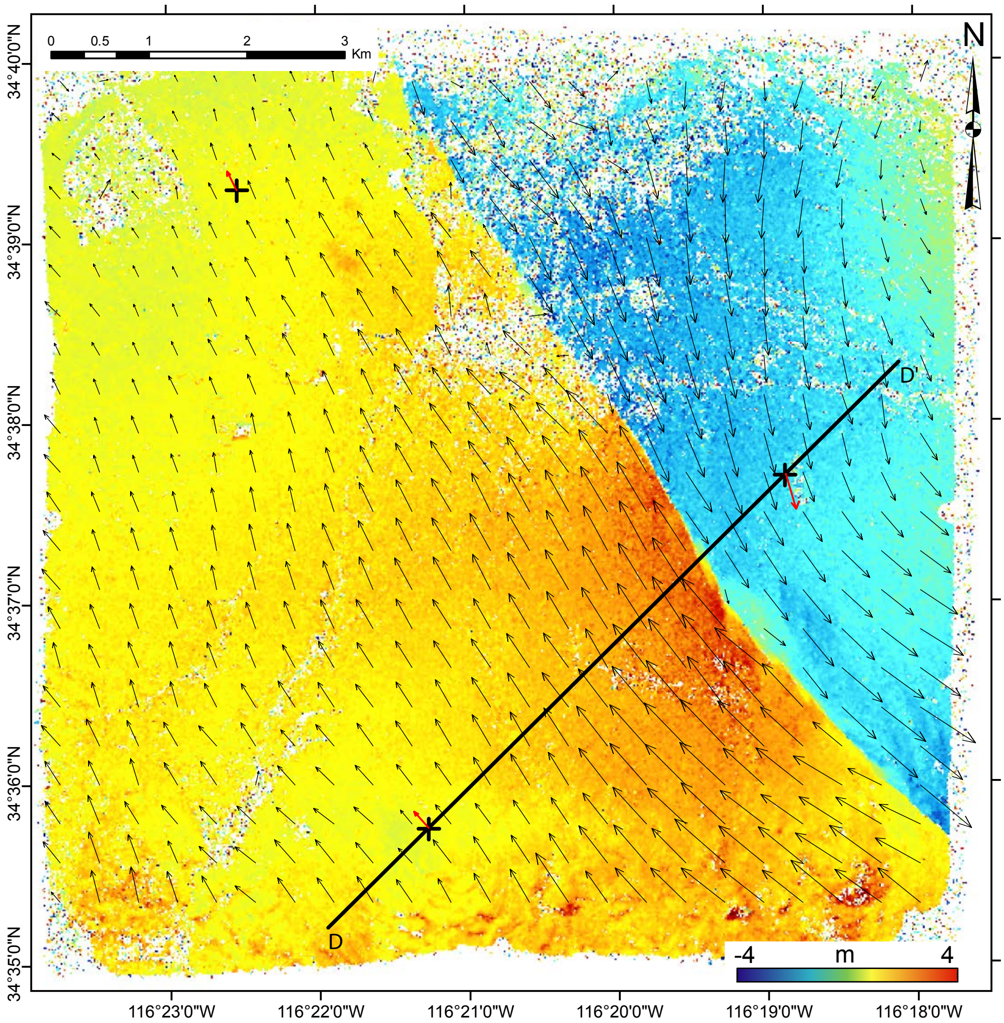

Figure 1.15: North/South displacement map of the 1989/2002 correlation map of images bracketing the Hector Mine earthquake. Images were orthorectified on a 1 m grid and correlated using a 64 × 64 pixel window with a 16 pixel step. Three GCPs, located by the black crosses, were optimized to co-register the master and the slave images while accounting for ground displacement at their ground location (red arrow) from SPOT measures (Fig. 1.14). Major long wavelength distortions seen in Fig. 1.13 were removed. Only the long wavelength distortions caused by the SPOT correlation error may remain, along with those introduced by film distortions. Profile DD' is reported on Fig. 1.16.

1.4 Conclusion

This study describes how the procedure originally developed to process optical satellite images can be adapted to aerial photographs, taking into account the specific characteristics of these types of images. Orthorectification and georeferencing can be achieved using the DEM only, without any other external data. In that case, the absolute georeferencing of the images is limited by the accuracy of

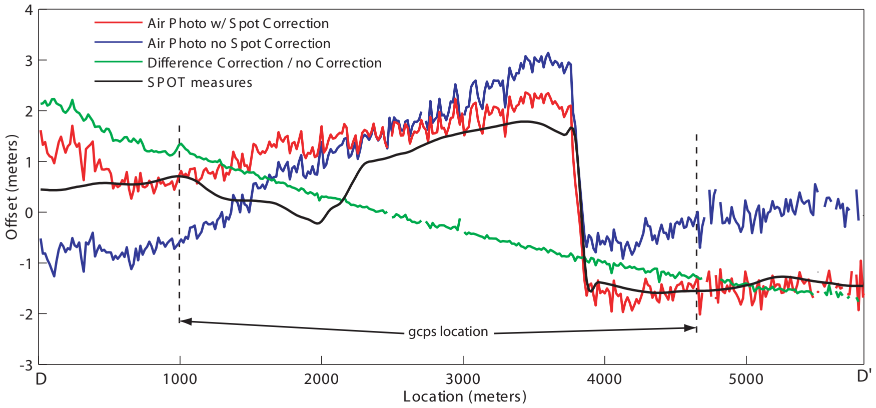

FIGURE 1.16: Profiles from Figs. 1.13, 1.14, 1.15. GCP correction brings a 2nd order polynomial correction in each North/South and East/west direction. High frequency signals such as the fault slip, are not affected however.

the DEM georeferencing. The correlation of two images taken before and after an earthquake yields offsets which primarily represent the ground horizontal displacements. Some artifacts are introduced when using a single DEM, but they can be corrected in postprocessing. In case of large stereoscopic parallax and significant ground up/down lift, the horizontal displacements measured also depend on the vertical displacement; however, Eq. 1.2 and Eq. 1.3 suggest that horizontal and vertical displacement can be retrieved if a third image is available, or, alternatively, if a pair of images from the adjacent flight strip overlaps the area of interest. The images co-registration is achieved with a sub-pixel accuracy of around 1/3 of a pixel. The limitation on the images' co-registration comes from film distortions, scan artifacts, DEM error, and the assumption of no ground displacements at the tie point locations. This latter assumption can be reduced if the ground displacements at the tie point locations can be estimated independently (from other measurements or an a priori model of co-seismic ground deformation). Better performance should be achievable in the future thanks to the rapid spread of digital aerial photography and to a better control on the geometry of the images thanks to Real-Time-Kinematic GPS and Inertial Navigation Unit. Finally, the technique is sensitive to temporal decorrelation such as those due to shadowing differences, man made changes, changes of the vegetation cover and clouds.

Despite these limitations, this study presented a powerful technique to precisely map the fault trace and measure fault slip and near-field ground deformation. With images at 1 m resolution, the technique applies to ruptures with a minimum length of a few kilometers and a minimum displacement of a few tens of centimeters. It should thus be applicable to earthquakes breaking the surface with a moment magnitude exceeding about 6.5. This opens the possibility to reassess a number of past earthquakes for which aerial photography archives would be available. Aerial photographs are less adapted to measuring ground deformation in the far-field which will be best measured with optical satellite imagery (e.g. SPOT, ASTER) or interferometric synthetic aperture radar. Aerial photographs and these latter techniques are complementary as they provide unprecedented accuracy in the near- and far-field measurements, respectively.

Seismotectonic applications have been the primary motivation for this study but the method described here is also applicable to measure ice flow, landslides or sand dune migration for example (Leprince et al., 2008a). The algorithms were implemented in the software package COSI-Corr (ENVI module) complementing the satellite image processing package. The software is available for download from the Tectonics Observatory (www.tectonics.caltech.edu).

Chapter 2

Deformation during the 1975–84 Krafla rifting crisis, NE Iceland, measured from historical optical imagery

James Hollingsworth, Sébastien Leprince, François Ayoub, Jean-Philippe Avouac

Foreword - This chapter presents a study relying heavily on the methodology presented in chapter 1, and is one of the most extensive in terms of dataset variety. My contribution was essentially focused on the aerial images and spy image integration and processing. Some improvements from the original framework had to be developed, in particular the adaptation of COSI-Corr to space-based frame imagery (spy imagery), and the epipolar/perpendicular-epipolar development to reduce topographic residual. J. Hollingsworth and S. Leprince provided the satellite image processing and geological analysis. In another study, not presented here, the horizontal and vertical Chi-Chi earthquake surface rupture was mapped in details with aerial imagery using the overlapping ground deformation from different view angles (Kuo et al., 2014). This work is referenced under Hollingsworth et al. (2012).

2.1 Introduction

With the obvious technical challenges in studying oceanic rift zones directly, our understanding of the processes that operate within rift zones and that influence their topographic and structural evolution remain relatively poor. The interplay between diking and faulting is a key factor controlling the structural development of spreading centers; differences in the amount of plate spreading accommodated by diking versus faulting ultimately lead to the very different topographic expressions of rift zones from around the world (Buck et al., 2006, De Chabalier and Avouac, 1994). Injection of dikes and slip on faults occur as instantaneous events in the geological record. Therefore, geodetic measurements which span a volcanic or tectonic event provide a method for measuring the displacement field associated with that event. Deformation associated with a single volcanic or seismic cycle can then be scaled up to see how it may produce the geological deformation we see preserved in the landscape. Obviously this can only be achieved where the coseismic and geologic ground displacements can be measured from remote sensing or geodesy.

The only other region where plate spreading occurs on land, and may therefore be imaged geodetically, is Iceland. Recent injection of a dike in an off-rift setting in southern Iceland resulted in the Eyjafjallajökull eruption, the ash clouds from which caused major disruption to European air traffic in spring 2010 (Sigmundsson et al., 2010). Although no inner-rift dike injections have occurred in Iceland in the period of GPS and InSAR observation (1990's and later), a major volcanic episode occurred between 1975–84, known as the Krafla rifting crisis, or 'Krafla Fires', during which around 20 dikes were injected into the crust within the Northern Volcanic Zone (NVZ) of NE Iceland (Fig. 2.1, see also Björnsson, 1985, Buck et al., 2006, Sigmundsson, 2006, Tryggvason, 1984). Geodetic measurements of surface extension from triangulation and EDM data were very limited in the early stages of the crisis, during which dikes were injected at depth with relatively little material erupted at the surface. Although surveying of the Krafla caldera, which lies at the southern end of the dike-affected region, increased during the latter stages of the crisis, our knowledge of the spatial extent of opening for the whole region, particularly in the north, remains poor.

In this paper, we use sub-pixel correlation of recent SPOT5 satellite data with declassified US spy images from the 1970's and historical aerial photos from the

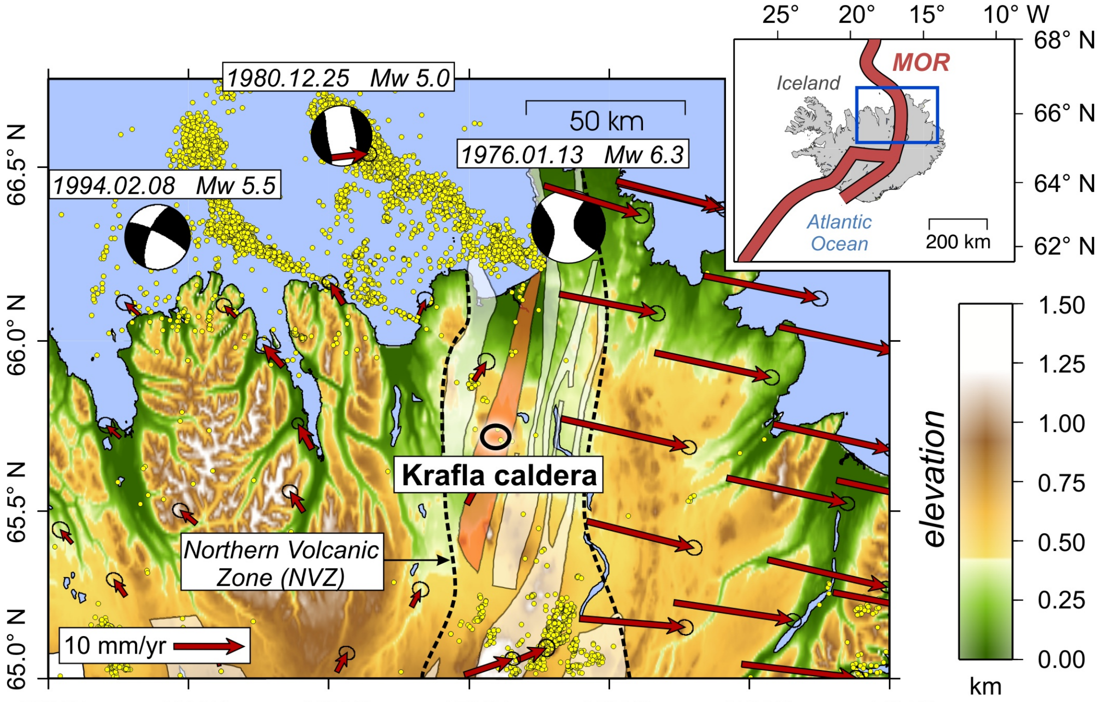

Figure 2.1: Topographic map of the northern central region of Iceland (inset figure shows the location within the wider mid-Atlantic plate spreading zone). Yellow circles show the location of micro-earthquakes ($M_w \geq 2.8$) between 1990–2010 from the SIL earthquake catalog of the Iceland Meteorological Office (http://hraun.vedur.is/ja/google/index.html). Red arrows show GPS velocities from Árnadóttir et al. (2009) relative to stable North America. Black earthquake focal mechanisms are earthquake centroid determinations from the Harvard CMT catalog. Heavy dashed black lines show the boundaries of the Northern Volcanic Zone (NVZ), across which all the plate spreading between Eurasia and North America is accommodated at this latitude. Transparent white areas highlight the various fissure swarms which lie within the NVZ, which accommodate this plate spreading through a combination of fault slip and magmatic injection. The red area highlights the Krafla fissure swarm, which was active through a number of dike injections between 1975–1984, an event known as the Krafla Fires. The heavy black circle shows the location of the Krafla caldera, which was the focus of much of the Krafla Fires activity.

1950's, 1960's, 1970's and 1990's to measure the horizontal displacement field produced during the 1975–84 Krafla rifting crisis. This allows us to significantly revise the location, magnitude, and evolution of opening, as well as investigate the interaction between magmatic (i.e. dike) and tectonic (i.e. fault) deformation in this rifting episode. We first outline the procedure for producing displacement maps from optical images, before discussing the results and the main implications for deformation during the Krafla Fires. We build on these observations in a second paper (Hollingsworth et al., 2013), which focuses on modeling of the optical displacement data to determine the best-fitting dike injection and surface faulting parameters throughout the Krafla Fires.

2.2 Overview of the 1975–84 Krafla rifting crisis

Deformation during the 1975–84 Krafla Fires was accommodated by diking at depth, and faulting/fissuring near the surface. Opening was confined to a 2–5 km wide zone characterized by clear NNE-SSW striking normal faults which offset post-glacial lavas throughout the NVZ (Fig. 2.2). Modeling dike propagation in the Krafla region, Buck et al. (2006) produced a similar pattern of dike injections away from a magma chamber as those measured during the Krafla Fires (Einarsson, 1991). However, the magnitude and distribution of opening were both significantly smaller and more uniform than was measured during the Krafla Fires. Furthermore, the first, and largest dike injection could not be modeled with the same parameters as the subsequent dikes. This suggests that either the modeling was too simplistic, which the authors acknowledge, or the measurements of total opening were incorrect, or both.

Although geodetic measurements of deformation from triangulation, EDM, tilt and leveling surveys were made throughout the Krafla Fires crisis (e.g. Tryggvason, 1984, 1994, Wendt et al., 1985), the spatial coverage of measurements is very sparse, and almost completely confined to the southern region around the caldera itself, thereby preventing a more detailed investigation of how plate spreading is accommodated by dike injection. Measurements from the northern and extreme southern ends of the fissure swarm are generally poorly constrained, although some individual dike injections from these regions have been studied in detail, providing some information on the geometry of diking and faulting (Rubin, 1992). Buck et al. (2006) provides a most comprehensive summary of events throughout the crisis; the onset of activity was signaled by intense seismicity in the Krafla region on the 20th December 1975, coupled with significant tilting and eruption of volcanic material within the caldera (Björnsson et al., 1977). Seismic activity remained high until January-February 1976, with much of the activity confined to the caldera itself. However, the largest earthquake of the entire crisis occurred on the 13th January (M_w6.3) at the northern end of the rift zone, some 60 km north of the caldera. This earthquake occurred offshore in the Axarfjördur region

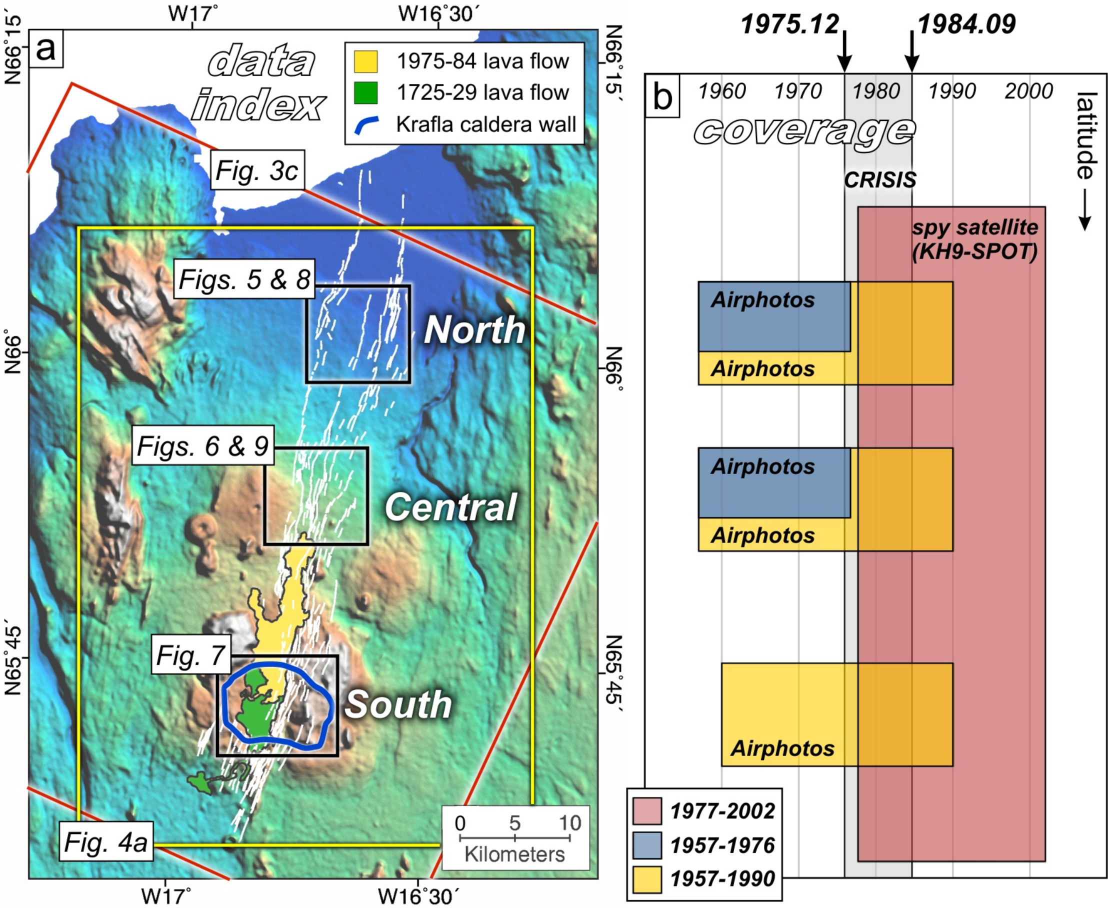

Figure 2.2: Topographic map of the Krafla region of NE Iceland. White lines show various faults and fissures active throughout the Late Quaternary. Blue circle shows the boundary of the Krafla caldera (from Björnsson et al., 1977), which is thought to have formed during the last interglacial (Eemian) period (114-130 kyr, Brandsdotttir et al., 1997). Yellow and green areas show the extent of lava flows during the 1975–84 and 1725–29 eruptions, respectively (Björnsson et al., 1977). Large red box shows the footprint of the SPOT5 satellite image correlated with a KH-9 hexagon spy satellite image from 1977 (the footprint of which covers an even larger area than shown in this figure). Black boxes show the location of aerial photo correlations throughout this study. (b) Plot showing the spatial and temporal coverage of the different datasets used to constrain opening during the 1977-84 Krafla rifting crisis. The gray zone shows the duration of the crisis.

(Fig. 2.1). The right-lateral focal mechanism suggested slip on a NW-SE transform fault, in response to NW-SE extension in the south resulting from dike injection.

Once the majority of extension had been relieved by dike injections at mid-to-shallow crustal levels, increasing amounts of magma were erupted throughout the crisis, mostly in the vicinity of the caldera. The crisis ended with its most extensive eruption, occurring between 4–18th September 1984, which covered the caldera-region and extended 10 km to the north (Fig. 2.3c).

Between 1975 and 1984 around 9 separate eruptions occurred and 20 dikes were injected into the crust, which resulted in 9–10 m of surface opening near the caldera (Árnadóttir et al., 1998, Buck et al., 2006, Tryggvason, 1984, Wendt et al., 1985). However, since the region of diking extended more than 50 km north and 10–20 km south of the caldera, our knowledge of the distribution of opening along the whole length of the fissure swarm remains poor. The aim of this paper is to revise current estimates of opening over the entire Krafla rift, using new measurements from correlation of optical satellite and aerial photo data.

2.3 Methods: optical correlation of spy satellite and aerial photos

Correlation of both satellite and aerial images have been successfully used to identify co-seismic ground ruptures and quantify fault offsets during large earthquakes (Avouac et al., 2006, Copley et al., 2011, Michel and Avouac, 2002, 2006, Wei et al., 2011), and the displacement field produced by injection of magmatic dikes (Barisin et al., 2009, Grandin et al., 2010a). While previous studies have focused on using modern satellite data such as SPOT and ASTER imagery, we discuss a new procedure for co-registering and correlating older KH-9 spy satellite and aerial photos for the purposes of measuring ground displacements. In the following section we discuss the key aspects of this new procedure which are relevant to the results and discussion sections of this study. However, further details on the methodology may be found in Appendix A.1.

2.3.1 Orthorectification and correlation of KH-9 and SPOT5 satellite images

We measure the displacement field associated with the 1975–84 Krafla rift crisis using the COSI-Corr software package[1], which compares two images of the Earth's surface that were acquired at different times, and measures any pixel shifts between them with an accuracy around 1/10 of the input image pixel size. Although this technique was developed primarily for use with modern pushbroom satellite

---

[1] freely available from www.tectonics.caltech.edu/slip_history/spot_coseis/index.html

systems, recent development has enabled its use for correlating aerial photos (Ayoub et al., 2009). Surazakov and Aizen (2010) recently showed that declassified KH-9 Hexagon US spy images could be treated as very high altitude aerial photos for the purposes of orthorectifying, which resamples the image to account for any topographic component in oblique view images — for more details on the orthorectifying procedure, see Appendix A.1.1. For these purposes, information about the camera system is required, such as focal length, optical distortions, and film size, and which currently remains classified for all declassified US spy images. After experimenting with different camera parameters, Surazakov and Aizen (2010) concluded that KH-9 images were acquired with a similar camera system as the NASA Large Format Camera (LFC, see Mollberg and Schardt, 1988). Therefore, we use the LFC focal length of 30.5 cm, and define the extents of the image using the 1×1 cm grid of reseau points which cover the image. KH-9 images were acquired globally between 1971 and 1980; each image measures 250×125 km, with a resolution of 6–9 m, and may be purchased from the USGS[2] for $30.

Fig. 2.3a and b shows a KH-9 Hexagon spy satellite image covering the NE Iceland region, acquired on the 15th September 1977. This image was correlated with a SPOT5 pushbroom satellite image of the Krafla region acquired on the 3rd October 2002 (Fig. 2.3c). The SPOT5 image is first orthorectified with COSI-Corr using georeferencing information contained within the accompanying header (or 'dim') file, and a 30 m ASTER Global DEM. The KH-9 Hexagon image is then co-registered to the SPOT5 orthorectified image using 3 tie points collected 20–30 km from the deforming region (Fig. 2.3b). Because we do not have a pre-crisis DEM, the KH-9 image is then orthorectified with the same post-crisis ASTER GDEM. The KH-9 and SPOT5 orthoimages are shown in Fig. 2.3b and c. The uniform black area which strikes northwards from the caldera in the post-event SPOT5 image corresponds to the 1981 and 1984 lava flows.

Correlation of the KH-9 and SPOT5 orthoimages is performed using COSI-Corr, which outputs E-W and N-S displacement maps showing how the pixels move between the two image acquisitions. A multiscale sliding correlation window of 64 to 32 pixels is used, with a measurement made every 8 pixels (64 m). This method matches groups of pixels based on their frequency content, and is typically more accurate than matching based on grayscale value. Displacements can be resolved

---

[2] earthexplorer.usgs.gov

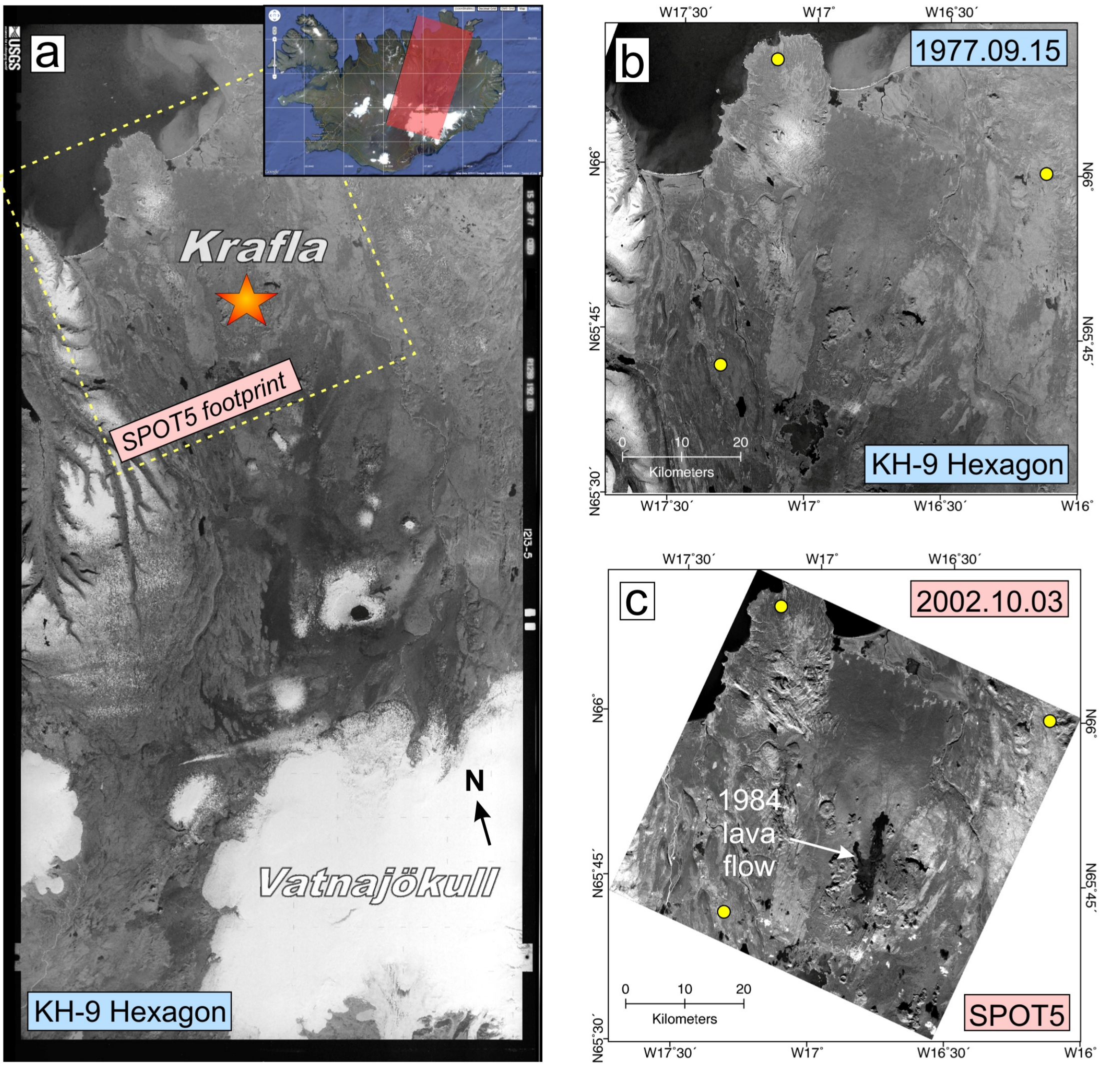

FIGURE 2.3: (a) KH-9 Hexagon satellite image of the Krafla region, NE Iceland, acquired on the 15th September 1977. Orange star shows the location of the Krafla caldera. Dashed yellow box shows the 60×60 km footprint of the post-crisis SPOT5 image. The white region in the SE of the image is the Vatnajökull ice cap. Inset shows the footprint of the KH-9 image relative to Iceland. Overlapping regions of the KH-9 and SPOT5 images are shown in (b) and (c), respectively. Yellow circles show the location of tie points used to co-register the KH-9 and SPOT5 images. Lavas erupted near the Krafla caldera in 1984 are only visible in the post-crisis SPOT5 image.

down to 1/10 of the input pixel size, i.e. ∼1 m for KH-9 images. For further details on the correlation method, see Leprince et al. (2007).

2.3.2 Removal of non-tectonic noise from KH-9 and SPOT5 correlation map

In contrast with pushbroom satellite images, film-based satellite images are subject to additional sources of error resulting from film-distortions, scanning of the film, and inadequate knowledge of the camera system used to acquire the images. These effects may produce signals which overprint the tectonic signal in displacement maps, albeit at wavelengths usually longer than the short-wavelength deformation produced by localized surface slip, i.e. across fault ruptures.

Topography unaccounted for by the DEM during the orthorectification process may result in an additional source of noise present in the correlation maps. Residual short-wavelength topographic signals may remain in the correlation map, and can significantly overprint the displacement field. This problem occurs if the two images are acquired with an oblique view component, and the DEM's used to correct them are of lower resolution than the input satellite images, e.g. ∼8 m KH-9 images orthrectified with a 30 m ASTER GDEM (Version 1). In these cases, there is a stereo effect between the two images, which records the surface topography, and which is not corrected by the coarser DEM — it is this principle which allows DEM's to be extracted from stereo imagery. Because the topographic signal between the two images is greatest in the direction of stereo overlap, known as the epipolar direction or plane of parallax, and negligible in the direction perpendicular to this, we can project our displacement maps into the epipolar-perpendicular direction to retrieve a displacement signal with minimal topographic residuals. For more details on the procedure for removing topographic residuals from displacement maps, see Appendix A.1.2. Topographic residuals may also occur if the topography moves significantly between image acquisitions, and the same DEM is used to orthorectify both images. This effect is particularly strong with large lateral ground displacements in hilly or mountainous terrain (Ayoub et al., 2009, Oskin et al., 2012).

Other factors may also affect the correlation of pre- and post-crisis images, such as quality of the film, changes in vegetation, differences in sun shading, presence of snow, deposition of sediment, erosion, anthropogenic effects, and various other processes which change the Earth's surface. These may combine in ways which act to hinder the correlation (e.g. it may be hard to correlate a snowy image with a non-snowy image), or may produce a directional bias in the correlation, thereby complicating the tectonic signal (e.g. different sun shading may bias the correlator in the direction of the shadows). Such effects vary between different images, and may be difficult to remove from the final displacement map, especially if their affects are very small, and non-uniform across the image. Nevertheless, even the qualitative recognition of these various factors may help in assessing the quality of a correlation.

2.3.3 Orthorectification and correlation of historical aerial photos

Unfortunately there are no KH-9 satellite images available which pre-date the rift crisis onset in 1975. To assess opening across the rift zone over the entire crisis (1975–1984), we correlate aerial photos acquired in 1957 and 1960, with photos from 1990, acquired after the crisis ended. Aerial photos were purchased from the National Land Survey of Iceland[3]. Because the ground footprint of these photos are relatively small (8 km), we cannot recover the long-wavelength deformation because the images do not extend into the non-deforming regions. Nevertheless, correlation of aerial photos can still provide accurate measurements of the short-wavelength displacement produced by faults (Ayoub et al., 2009). Furthermore, very precise measurements of the displacement field can be obtained with aerial photos due to their relatively high resolution compared with satellite imagery; Ayoub et al. (2009) is able to resolve fault displacements of only 20 cm for aerial photos correlations covering the 1992 Landers earthquake. Therefore, by correlating pre- and post-crisis aerial photos we are able to resolve the total surface opening produced during the crisis, where it is localized onto major faults and fissures (Section 2.4). We also correlate pre- and inter-crisis aerial photos to examine the displacement field resulting from the early stages of the crisis, which is less well understood.

The method for co-registering and correlating aerial photos is similar to KH-9 Hexagon spy images; both datasets must be orthorectified using the 'Aerial Imagery' module within COSI-Corr, see Appendix A.1.3 for more details. However, because aerial photos are often high resolution, typically ≤1 m, topographic residuals are correspondingly very large in the absence of a high-resolution DEM to

---

[3] www.lmi.is

orthorectify the photos. Therefore, we project all aerial photo correlations into the epipolar-perpendicular direction to minimize topographic residuals.

Furthermore, because a typical aerial photo is acquired at elevations of ∼5 km, the resulting image footprint covers an area of ∼10×10 km. Because the width of the Krafla rift zone is around 5 km wide, the camera incidence angle varies significantly over the deforming region — although KH-9 images are subject to similar variations in incidence angle, they are acquired at much higher elevations of ∼166 km, resulting in much larger footprints of 250×125 km; therefore the incidence angle varies only a small amount over the 5 km wide Krafla rift. As the incidence angle increases away from the center of an aerial photo, it gains a significant oblique component around the edges of the photo. Therefore, in the absence of a high resolution pre- and post-crisis DEM for orthorectification, some care is needed when interpreting an aerial photo correlation map, because vertical deformation around the edges of the image may produce an apparent horizontal displacement signal — this problem is discussed further in Appendix A.1.4. In the case of the Krafla rift, vertical displacement on the rift-bounding normal faults may slightly enhance, rather than cancel out, the values of horizontal extension at the margins of the correlations, which is where the incidence angles are greatest (i.e. the displacement will include both horizontal and vertical components). This is because the photos were acquired from a flight line which lies in the middle of the rift, and so the camera looks westward at the western rift boundary and eastward at the eastern boundary. Therefore, the fault displacements we measure from correlation of aerial photos are likely to be maximum values.

2.4 Measuring Krafla surface extension

The results of our optical image correlation analysis is presented in the following section. Figure 2.2 outlines the spatial and temporal coverage of data used in the analysis, and provides an index for the various figures in this section.

2.4.1 Estimates of mid-late crisis rift extension: 1977–2002

Figure 2.4 shows the surface extension across the Krafla fissure swarm between 1977 and 2002. Due to the proximity of the tie points to the rift zone (Fig. 2.3), partuclarly east of the rift, artifacts related to scanning, and the lower image quality of the KH-9 compared to the SPOT5 image, the long wavelength decay of the horizontal displacement signal and the quality of the co-registration may be slightly biased. Nevertheless, the relative displacements across discontinuities are well resolved (see also Ayoub et al., 2009).

The majority of extension is accommodated on rift bounding faults and fissures. The width of the rift increases from ∼1 km in the south, to ∼5 km in the north. Although the spatial and displacement resolution of the KH-9-SPOT correlation is too low to resolve details of inner rift extension, the relatively smooth displacement profile across the inner rift for the northern section of the swarm suggests little or no extension is accommodated by localized faulting or fissuring between the rift bounding faults. Virtually all of the extension is accommodated on the rift-bounding faults shown as black lines in Fig. 2.4a. Surface extension across the rift varies between 4–5 m, and is relatively uniform along the rift zone, with slightly elevated opening in the central section. The presence of the river delta at the northern end of the rift results in poor coherence, thus preventing the measurement of extension near the coastline. A kink in the strike of surface opening occurs in the middle of the rift (Fig. 2.4a), and corresponds to a similar kink in the migration of seismicity during the July 1978 earthquake swarm (Einarsson and Brandsdottir, 1980).

2.4.2 Estimates of total rift extension: 1957–1990

2.4.2.1 Northern rift-segment

Correlation of aerial photos from 1957 and 1990 for the northern section of the Krafla fissure swarm, near the Axarfjördur coastline, are shown in Fig. 2.5. Both image correlations are produced from overlapping 1957 and 1990 aerial photos taken along N-S flight lines. In each case, pre- and post-crisis images were co-registered using tie points collected from the eastern rift flank, which is assumed to be stable. Displacement values are given in the epipolar perpendicular directions, shown by the black arrows, which are free from topographic residuals and approximately perpendicular to the faults/fissures within the fissure swarm. It is necessary to look at displacement in the epipolar perpendicular direction because the aerial photos (0.5 m resolution) are orthorectified with the much coarser

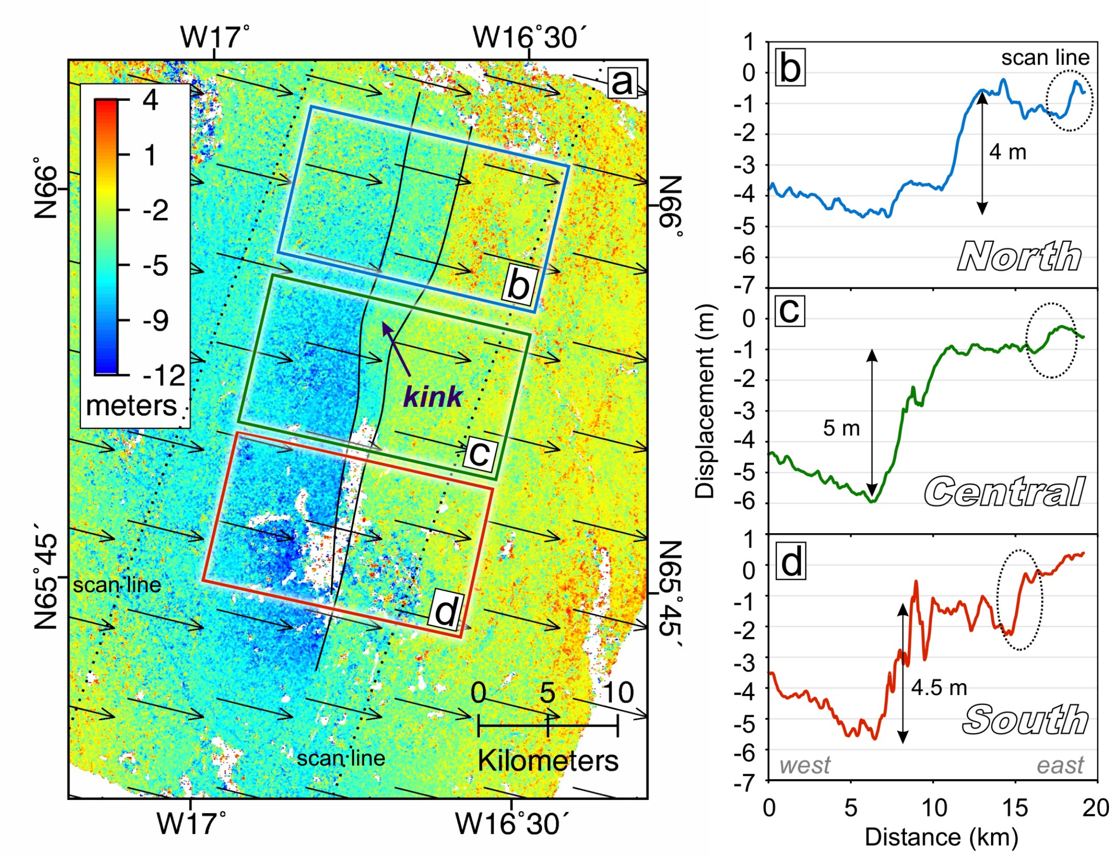

FIGURE 2.4: (a) Reprojection of the epipolar perpendicular displacement field into the 104° direction (i.e. perpendicular to the strike of the rift zone) — see Fig. 2.2 for location. Black lines show the simplified location of rift bounding faults which were activated between 1977–2002. Blue arrow shows a kink in the strike of the rift bounding faults. Dotted black lines show steps in the displacement field which result from film scanning artifacts. Stacked displacement profiles are shown across the north (b), central (c), and southern (d) parts of the rift zone. Displacement values are relative to the tie point locations (Fig.2.3b and c); because the tie points do not extend far enough from the rift zone, the values are not absolute, but relative. Dotted black circles show steps in the displacement field produced by scanning.

ASTER GDEM, and so the raw E-W and N-S displacement fields output by COSI-Corr are obscured by topographic residuals.

Figure 2.5b and d show swath profiles of displacement across the rift zone, taken approximately perpendicular to the fissure swarm and sub-parallel to the epipolar perpendicular direction. The positive signal within the middle of the rift zone is likely an artifact produced by subsidence in the left side of the image, which is viewed obliquely by the camera, and then orthorectified using the post-crisis DEM — see Appendix. A.1.4 for more details. The eastern rift flank is fixed between both images, yielding approximately zero horizontal displacement. Discontinuities in the displacement field indicate extension accommodated on faults/fissures. The northern-most correlation (Fig. 2.5a) only just spans the entire rift, which is widest (∼5 km) at this latitude. Approximately 2.0–2.5 m extension is accommodated across a 1.5 km-wide distributed zone of faults/fissures forming the eastern margin of the rift zone, while 1.0–1.5 m extension is accommodated on a fault/fissure forming the western margin of the rift. Decorrelated areas occur due to rapid temporal changes in the river delta. Vertical displacements do not contribute significantly to the horizontal displacement values from the center of the correlation, because the incidence angles from the pre- and post- images are close to nadir — see Appendix A.1.4. The incidence angle at the western edge of the image is 25–30°, and so a vertical displacement of 2.2–3.3 m could produce an apparent westward displacement of 1.0-2.5 m. Alternatively, the same signal could be produced by pure horizontal displacement, or some combination of horizontal or vertical motion; equal values of 0.8 m vertical and horizontal slip could constructively produce 1.2 m westward motion. Therefore, a horizontal displacement of 1.5 m is likely to represent a maximum value. The 4–5 km width of the rift is the same as seen on the KH-9-SPOT5 correlation in Fig. 2.4. The total extension accommodated at the surface is 3.5–3.7 m; less than the 5.5–7 m estimated by Tryggvason (1984). However, it should be noted that due to the small 6 km swath size of the aerial photos, we are less sensitive to long-wavelength distributed deformation, which could account for some of this difference.

Figure 2.5c shows a correlation immediately south of Fig. 2.5a. Only the central and eastern parts of the rift zone are covered by the correlation, and so the total extension cannot be resolved here. Nevertheless, extension on the eastern rift margin is well resolved at 2.1 m, consistent with the 2.0–2.5 m estimate from Fig. 2.5b. Deformation becomes more localized to the south. Because the epipolar perpendicular direction in Fig. 2.5a and c contains a large N-S component, slip on normal faults will produce subsidence and thus a northward signal in the rift zone for the southern part of the correlation (negative/blue epipolar perpendicular displacement), and a southward signal for the northern part of the correlation (positive/red displacement) — see Appendix A.1.4 for more details. For the west and east parts of the correlation, subsidence will produce eastward (positive) and westward (negative) motion respectively. This effect is the likely cause of the positive bulge in the middle of the rift zone in the Fig. 2.5b and d profiles. Nevertheless, the displacement values for the western rift flank in Fig. 2.5b begin to

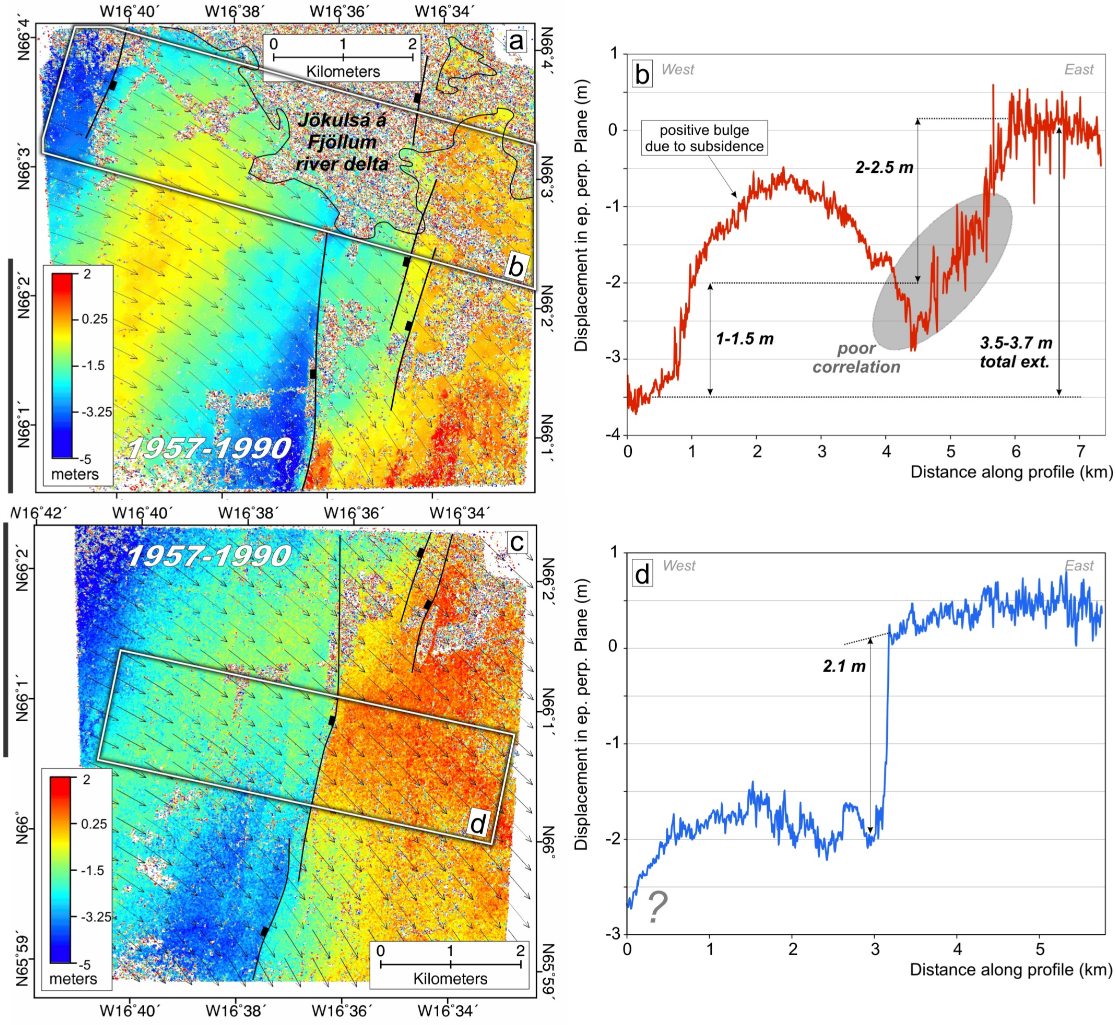

FIGURE 2.5: (a) Epipolar perpendicular displacement field for the northern end of the Krafla fissure swarm (see Fig. 2.2 for location) from 1957 and 1990 aerial photos. Decorrelated areas in the north of the image coincide with the Jökulsá á Fjöllum river delta. Black lines show normal faults which moved during the crisis. Tie points were collected from the eastern rift flank. (b) Swath profile of the deformation across the rift zone (shown by the white box in a). Although the swath crosses the river delta, it is the only profile to span the entire northern section of the rift. The relative displacements across faults are robust, while distributed deformation is hard to distinguish from displacement ramps introduced by mis-registration of the pre- and post-crisis images (see Appendix A.1.4). Gray area is poorly constrained due to low coherence. (c) Epipolar displacement map, and (d) displacement profile for the region immediately south of (a). The displacement maps in (a) and (c) overlap in the areas shown by the black bars at the side of the image.

flatten out, suggesting no more localized deformation is occurring outside the rift zone, consistent with the KH-9-SPOT5 correlations. If we assume the relative elevations of the east and west rift flanks have not changed significantly throughout the crisis, i.e. minimal relative subsidence/uplift between the rift flanks, which is also consistent with the long term geomorphology, then 3.5–3.7 m difference between the east and west flanks reflects the maximum total horizontal extension.

2.4.2.2 Central rift-segment

Figure 2.6a and b shows aerial photo correlations for the central section of the Krafla fissure swarm, immediately north of the lava flow which erupted at the end of the crisis in 1984. The eastern rift flank is fixed using tie points. Elevated values in the reference area of Fig. 2.6b are likely a result of fattening effects during the correlation; a defect by which the center of the pixel correlation window inherits the displacement of the more contrasted pixels within the window. However, the relative displacement between the east and west rift flanks is ∼6 m at the north of Fig. 2.6a, and ∼7 m in the south of Fig. 2.6a and north of Fig. 2.6b, which cover the same area (Fig. 2.6c and d). The correlations for this section of the rift zone are relatively noisy, which may partly be due to the presence of snow drifts west of the rift zone, which reduce the coherence between the pre- and post-crisis images.

2.4.2.3 Southern rift-segment

Figure 2.7a shows an aerial photo correlation (1960–1990) for the southern section of the Krafla rift zone, near the southern extent of the 1984 lava flow. The 1960 photo was correlated with the 1990 aerial photo using tie points collected either side of the rift zone; Ayoub et al. (2009) showed this approach allows displacements across faults and fissures to be well resolved, although may bias how the deformation signal decays at longer wavelengths. The obvious N-S discontinuity at the western edge of the image is a scanning artifact from the 1960 aerial photo. The rest of the correlation is relatively clean, with a typical noise level of 0.2–0.5 m. A complicated deformation pattern in the southeast corner of the correlation may result from vertical motion on normal faults. Fig. 2.7b shows a displacement profile across the north of the correlation, where patches of high ground remain clear of lava, thereby yielding displacement measurements across the rift. A total of 7.5–8.0 m extension is accommodated across a 1 km wide zone, which represents the peak extension value measured across the whole rift zone. These values decrease to 6–7 m in the south of this figure.

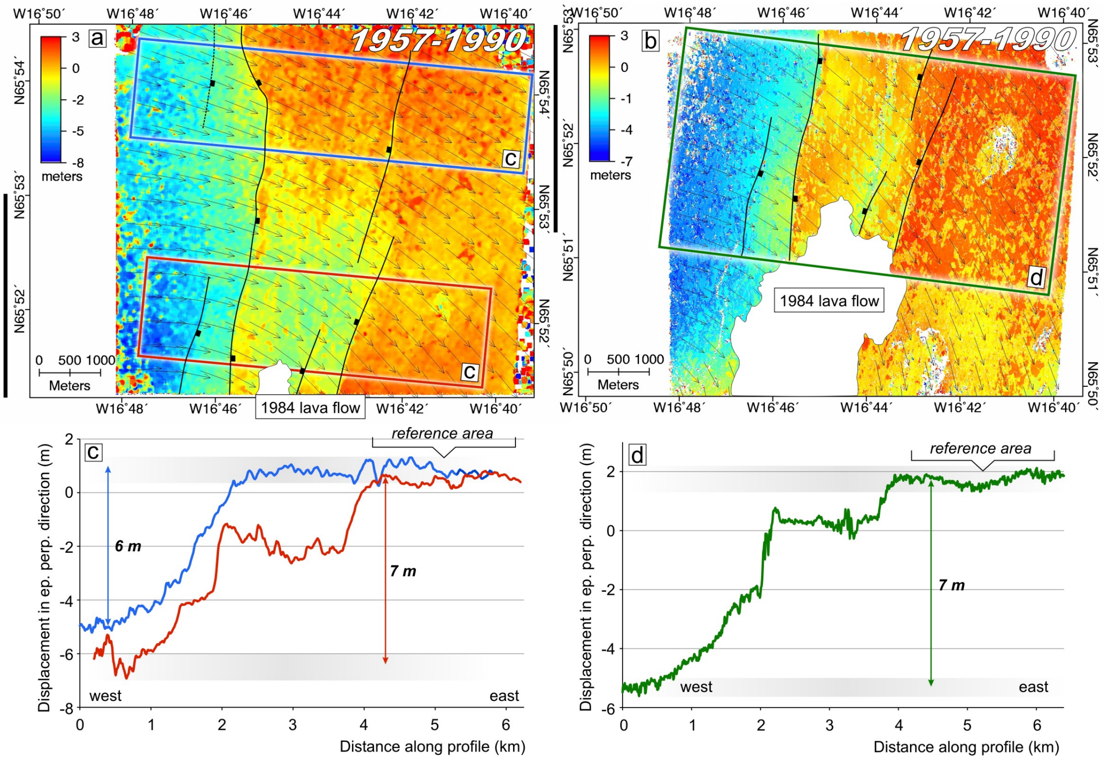

FIGURE 2.6: (a) and (b) Epipolar perpendicular displacement fields for the central section of the Krafla fissure swarm (see Fig. 2.2 for location) from correlation of 1957 and 1990 aerial photos. Decorrelated areas in the south of the images are due to lavas erupted in 1984. Black lines show normal faults which moved during the crisis. Displacement values of ∼2 m for the reference region in (b) result from problems co-registering the two images, due to fattening effects (see text for details). The two displacement maps overlap in the areas shown by the black side bar. (c) and (d) Swath profiles of the rift-perpendicular deformation, shown by the blue and red boxes in (a), and the green box in (b).

2.4.3 Estimates of early-crisis rift extension: 1957–1976

2.4.3.1 Northern rift-segment

Figure 2.8 shows the displacement field for the northern end of the fissure swarm for the early period of rifting, spanning 1957–1976 (same region as Fig. 2.5). Localized extension is clearly resolved at the northern edge of the correlation, close to where the Jökulsá á Fjöllum river delta cuts across the rocky lava flows which characterize the Krafla region; the river deposits do not correlate due to their rapid temporal evolution. Up to 2 m of opening is accommodated on faults/fissures within the delta, consistent with field reports from Tryggvason (1976). However, no obvious opening is present in the correlation maps to the south (Fig. 2.8a and

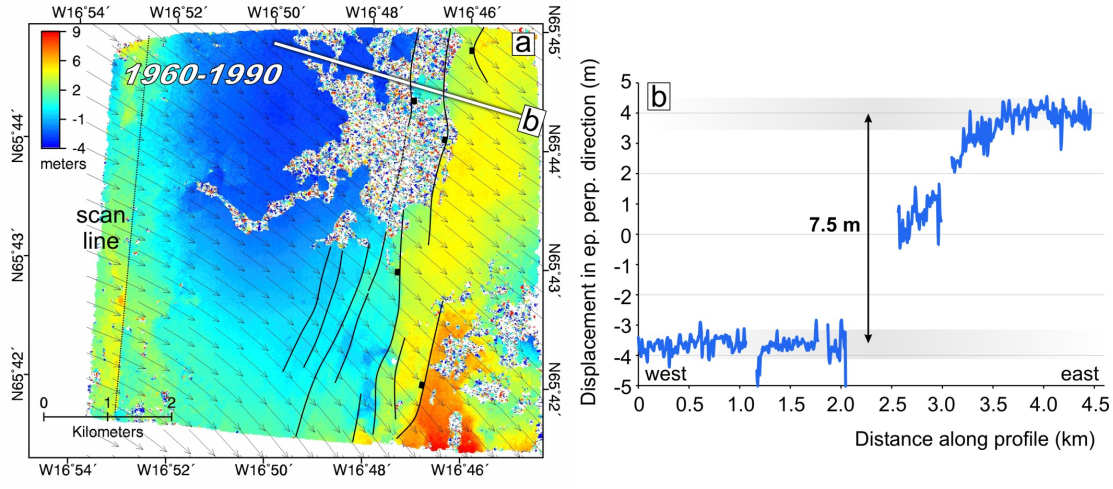

FIGURE 2.7: (a) Epipolar perpendicular displacement field for the southern section of the Krafla fissure swarm (see Fig. 2.2 for location) from correlation 1960 and 1990 aerial photos. Decorrelated areas in the north of the image corresponds with the southern limit of the 1984 erupted lavas. Black lines show normal faults which moved during the crisis. (b) Profile of the rift-perpendicular deformation (shown by the white line in a).

c), implying there was no extension on faults/fissures in this region. This pattern is confirmed by swath profiles across the northern (Fig. 2.8b) and southern (Fig. 2.8d) parts of these correlations. Around 0.6–1.1 m opening is accommodated across faults within the northern profile, although this value increases to >2 m further north within the river delta. Fault slip is less clearly resolved on the western rift boundary; the broad increase in westward motion of this rift flank may result from uplift associated with dike injection at depth but with no surface faulting, see Appendix A.1.4 for more details. Little or no localized extension is accommodated on the southern profile. Although image correlation is less sensitive to long-wavelength deformation, any distributed opening across the inner rift would still produce a short-wavelength ramp in the displacement profile, assuming it is accommodated over a few kilometers.

2.4.3.2 Central rift-segment

Figure 2.9a shows the 1957–1976 displacement field for the central section of the Krafla fissure swarm (same region as shown in Fig. 2.6), 10–15 km north of the caldera. A strong parallax effect between the two aerial photos, as well as snow drifts and low sun illumination in the 1957 photo result in a relatively noisy correlation, especially where a hill occurs in the center-right of the correlation. They may

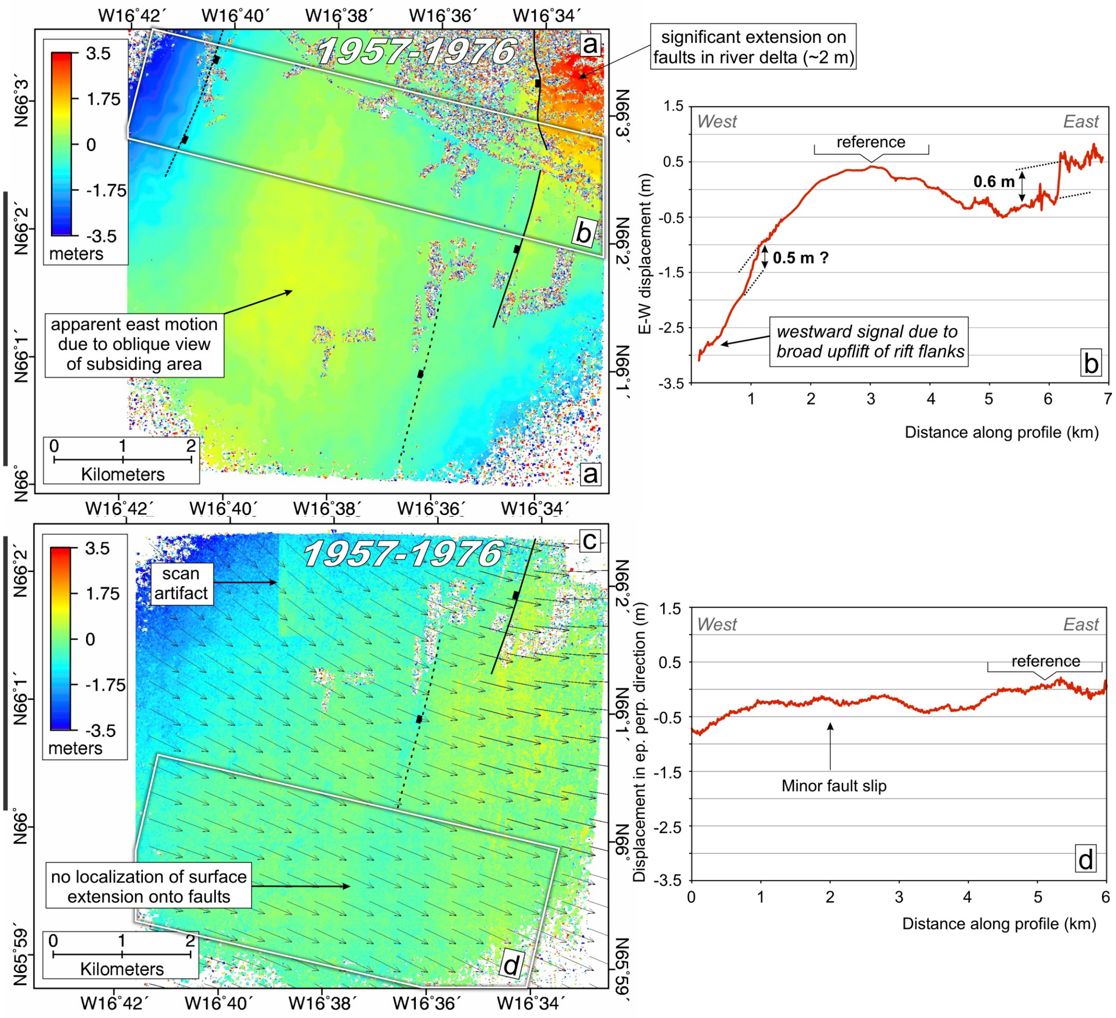

FIGURE 2.8: (a) East-west displacement field for the northern end of the Krafla fissure swarm (see Fig. 2.2 for location) from correlation of 1957 and 1976 aerial photos. Because the camera was in the same location for each photo acquisition, there is no parallax difference between the two images and both the E-W and N-S displacement fields are free from topographic residuals. Black lines show normal faults which moved during the early stages of the crisis. The 1976 photo was registered to the 1957 aerial photo using tie points from the middle of the image. (b) A swath profile of the deformation across the rift zone (shown by the white box in a). (c) Displacement map, and (d) displacement profile for the region immediately south of (a). Black side bars show the region of overlap between (a) and (c). Although the region shown in (c) does not span the entire rift zone, no obvious opening is observed across the eastern rift-bounding fault.

also account for the unexplained long-wavelength signals present across the rift zone, particularly around the edges of the correlation. Nevertheless, the amount of opening across the northern edge of the correlation is small — definitely less than 2 m, as seen at the northern end of the rift — with no obvious sign of localized opening. A possible opening of 1 m may occur at the southern edge of the correlation, along the western rift boundary, which may relate to dike injection beneath the caldera to the south. However, this opening signal also lies at the edge of the photo, where optical and film distortions are greatest, and coincides with the location of the greatest snow drift. Furthermore, long wavelength uplift of the rift flanks associated with dike injection at depth, but without fault slip at the surface, could result in a smooth westward displacement if the post-crisis DEM was used to orthorectifying both pre- and post-crisis aerial photos (see Appendix A.1.4).

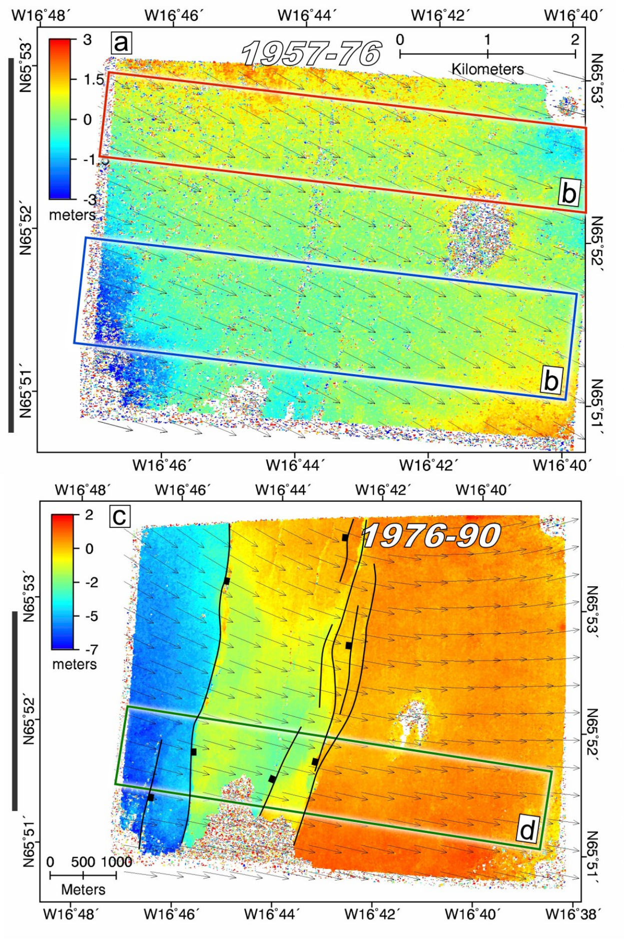

FIGURE 2.9: (a) Epipolar perpendicular displacement field for the central section of the Krafla fissure swarm (see Fig. 2.2 for location) from correlation of 1957 and 1976 aerial photos. The 1976 photo was registered to the 1957 aerial photo using tie points collected from the middle of the image, due to a lack of coverage of the rift flanks. (b) Swath profiles across the north and southern regions of the deformation map (shown by the white box in a). (c) Epipolar perpendicular displacement field for the period 1976–1990 and (d) displacement profile for the central section of the Krafla fissure swarm, which encompasses the area shown in (a). The displacement maps in (a) and (c) overlap in the areas shown by the black bars at the side of the image.

Figure 2.9c shows a correlation map for the central fissure swarm, but for the 1976–1990 period. The correlation is very clean, and the epipolar perpendicular direction is normal to the faults/fissures bounding the rift zone. A profile of displacement across the rift zone indicates 7 m of opening, with roughly equal opening accommodated on each rift boundary. Because this opening value is the same as that measured using aerial photos from 1957–1990 (Fig. 2.6a), it confirms that little or no localized surface opening occurred in the central section of the fissure swarm over a distance of ∼20 km between 1957 and 1976.

2.5 Discussion

2.5.1 Summary of opening during the Krafla rifting crisis (1975-84)

A summary of the results presented in Section 2.4 are shown in Fig. 2.10. The cumulative opening at various stages of the crisis is shown in Fig. 2.11. Our new displacement measurements from optical image correlation indicate a total of ∼8 m opening across the Krafla caldera, which is consistent with previous estimates of 9 m for this area (Buck et al., 2006, Tryggvason, 1984). However, our measurements fall short of previous estimates, by 1.5–2.5 m, for the northern part of the rift zone, where total localized extension was at most 3.7 m, based on our image correlation results.

During the period 1975–1984, E-W crustal extension was accommodated by dike injection and fault slip over a distance of ∼80 km. Surface extension is accommodated primarily on the rift-bounding normal faults above the dike, rather than by opening of fissures within the rift zone. Average surface opening along the entire 80 km zone of deformation was ∼2.5 m for the period 1977–1984, assuming extension decays linearly to zero at the northern limit of the rift zone, near the 1976 earthquake epicenter (Fig. 2.10b). The average surface opening spanning the entire rift crisis between 1975–1984 is ∼4.3 m along the 80 km length of the rift zone. Therefore, 40% of the total surface opening occurred during the first 20% of the crisis. This is similar to observations from the Afar region of East Africa, where a significant amount of the total opening, >75% at depths of 2–10 km, occurred during the first dike injection (Grandin et al., 2010b). Opening was not uniform along the Krafla rift zone, with maximum values of ∼8 m occurring at the southern end, near the caldera, and ∼4 m at the northern end, near the Axarfjördur coastline. This pattern is also similar to Afar, where ∼15 m opening occurred in the central section of the rift, and ∼5 m occurred at either end of the rift (at depths of 2–10 km, over a distance of 50–60 km, Grandin et al., 2010b). The distribution of opening along both the Krafla and Afar rift zones correlate with the regional topography, implying a first order link between topography and tectonics, as expected from mechanical analysis of diking (e.g. Behn et al., 2006, Fig. 2.10b and c). A more complete analysis of the deformation field, which uses elastic dislocation modeling to better constrain the geometry of surface faults and dikes injected throughout the Krafla rifting crisis, is given in Hollingsworth et al. (2013).

In the Axarfjördur coastal region, almost the entire opening during the 9 year crisis was accommodated in the first few months (between Dec 1975 and Sept 1976). Surprisingly, over the same time period, no localized opening is observed along a 20 km section of the fissure swarm between the Krafla caldera and the northern coast (Figs. 2.8 and 2.9). Although we do not present opening measurements for the southern caldera region during the early stages of the crisis (due to lack of data), significant seismic activity and localized volcanism in this area, coupled with field observations of fault movements within the caldera (Björnsson et al., 1977) suggest localized surface opening occurred at the southern end of the rift zone. Therefore, a bi-modal pattern of opening must have occurred along the fissure swarm during the early stages of the crisis, whereby surface extension was accommodated at the southern and northern ends of the rift, but not in the middle (Fig. 2.10c).

2.5.2 Implications for the kinematics of Krafla dike injections

If opening at the surface by faulting occurs in response to dike injection at depth, and over similar timescales to dike propagation (e.g. Hauksson, 1983, Rubin, 1992, Rubin and Pollard, 1988), we need to reconcile a bi-modal pattern of surface opening with a magma source which lies at the southern end of the rift zone, where modeling of regional tilt data indicates a magma chamber at 3 km depth beneath the Krafla caldera (Árnadóttir et al., 1998, Ewart et al., 1991), see also Fig. 2.10a. Buck et al. (2006) suggests this pattern could be produced by an increase in tensile stresses away from the magma chamber: a dike would first open near the magma source and propagate laterally, while the driving pressure equals

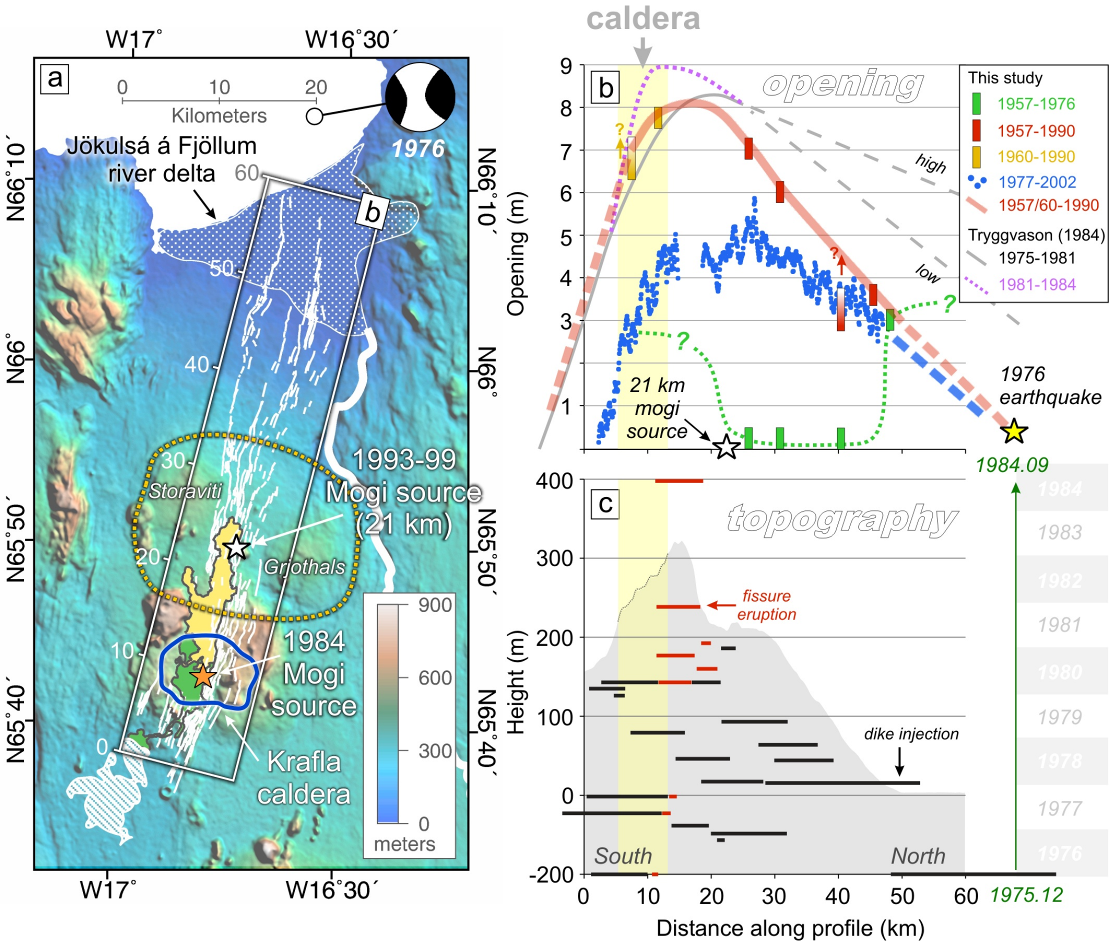

FIGURE 2.10: (a) Topographic map of the Krafla region. White lines show faults which have been active in the Quaternary (mapped from aerial photos). Heavy white line and stippled white region show the Jökulsá á Fjöllum river and delta. White dashed region is Myvatn lake. Blue circle shows the Krafla caldera. Orange star is the location of the magma chamber beneath the Krafla caldera from Árnadóttir et al. (1998). White star shows a deeper magma source at 21 km (de Zeeuw-van Dalfsen et al., 2004). Yellow dotted lines shows a broad zone of uplift comprising the Storaviti and Grjothals topographic highs. The Global CMT solution is shown for the 13th January 1976 earthquake. (b) Profiles of opening (y-axis) along the fissure swarm (x-axis) for the different time periods investigated in this study (see key for details). Grey and purple lines shows the previous best estimate of opening between 1975–1981 and 1981–1984 (Árnadóttir et al., 1998, Tryggvason, 1984). The location along the rift of the 1976 earthquake (yellow star) and 21 km deep mogi source (white star) are shown. (c) Summary of timing and distribution of dike injections and fissure eruptions during the Krafla crisis (adapted from Buck et al., 2006). Grey region shows a swath topographic profile (left y-axis) along the length (x-axis) of the Krafla fissure swarm (swath corresponds to white box in a). Horizontal black and red lines show the location of injected dikes and fissure eruptions (x-axis) and their timing throughout the crisis (right y-axis, time increases vertically from 1975 to 1984 along green arrow). Location of the Krafla caldera is shown by the vertical yellow line in (b) and (c).

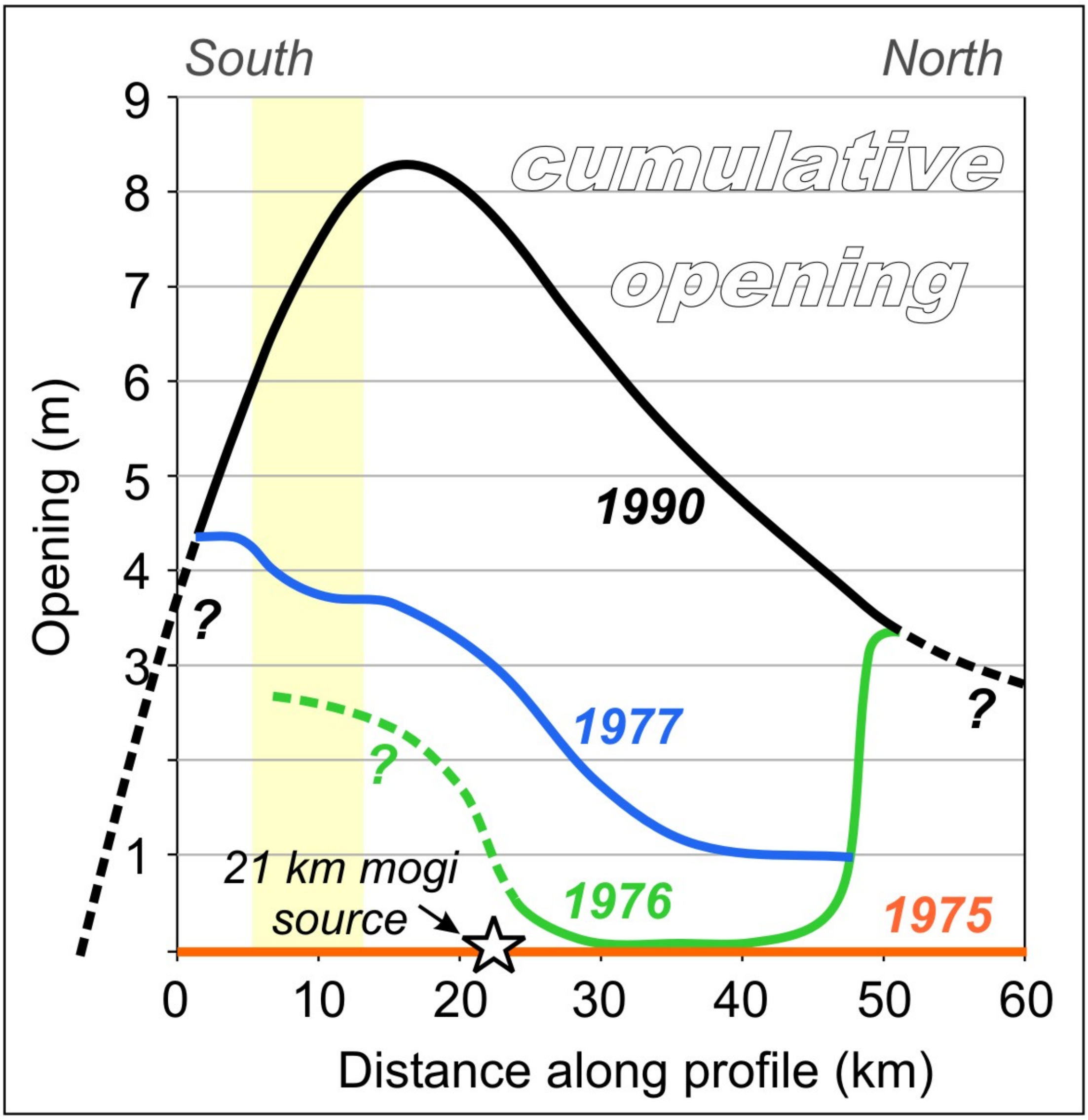

FIGURE 2.11: Cumulative opening along the length of the crisis (axes are the same as for Fig. 2.10b and c).

the breakout pressure, but then close up again as it propagated into more tensile regions away from the magma chamber.

One implication of this model is that for a dike to propagate along a crack, and then close up again as it moves along, it must not freeze. However, a dike may have to propagate at depths of >10 km to avoid freezing during propagation; at these depths the host rock temperature is greater than 600°C (Fialko and Rubin, 1998). Because the geothermal gradient likely decreases away from the caldera, the depth at which a dike must propagate to avoid freezing will correspondingly increase. This implies a significant increase in the depth of diking as it propagates away from the 3 km deep magma source near the Krafla caldera. Nevertheless, it should be noted if basaltic dikes inject a rhyolitic crust (rhyolitic volcanism is known from Krafla Jónasson, 1994), then the dikes could cause melt-back of the host rock, thereby allowing injection at shallower depths. Also, even a partially frozen dike may continue to flow, so long as the constituent crystals do not adhere to the dike walls.

If surface crustal extension is accommodated by normal faults which localize above the shallowest reaches of the dike, where there is a concentration of tensile stresses (Agnon and Lyakhovsky, 1995, Pinzuti et al., 2010), the width of the fault-bounded rift zone will reflect the depth to the top of the dike; a wide rift zone results from deep diking, while a narrow rift zone results from shallow diking (assuming a relatively constant fault dip). The Krafla rift zone increases from ∼1 km width near the caldera to ∼5 km near the coastline, and is consistent with an increase in dike depth as it propagates northward (Fig. 2.4 and Fig. 2.10). However, this observation does not explain the lack of surface faulting along the central section of the rift. Firstly, as the depth to the top of the dike increases northward, the amount of strain at the surface decreases, thereby inhibiting surface slip localization. Secondly, if a dike passes through the central section of the rift without freezing, and yet is wide enough to activate surface faulting north of this section, why does it not activate surface faulting across the central section? Although Buck et al. (2006) provides an explanation for dikes closing up at depth, based on a decrease in driving pressure, an additional model is required to explain how surface faults activated by a dike can slip back to their original positions.

An alternative explanation for the bi-modal distribution of surface opening during the early stages of the crisis may be that the strength of the host rock varies along the rift zone. As the driving pressure decreases northwards, and the depth to the dike top increases, the deformation is large enough to activate surface faults in the south, but not along the central section of the rift (Buck et al., 2006, Grandin et al., 2012). However, as the dike injects away from the magma chamber, the pressure in the dike tip cavity is initially maintained by magmatic volatiles. This produces a pore-pressure boundary layer in the dike tip, thus preserving low pressure in the host rock and increasing its strength (Ziv et al., 2000). The southern and central rift segments therefore remain elastic, and the change from surface faulting near the caldera to no surface faulting in the central section is a result of the decreasing driving pressure and increasing depth to the dike top. However, once the dike extends far enough from the magma chamber, the volatiles become fully exsolved from the magma, and the pressure in the dike tip cavity is then maintained by the ambient pore fluid pressure, with influx of fluids from the host rock into the dike tip. This results in a lower frictional resistance at the tip of the dike, causing weakening of the host rock (Ziv et al., 2000). This weakening may be enough to activate faults which extend to the surface along the northern section of the rift. This effect could be enhanced if the northern rift is in a greater state of tension. Nevertheless, if the dike propagates so fast that the length of the pore pressure boundary layer is less than the rock grain size, which could be the case near the magma chamber, then the frictional resistance ahead of the dike tip fed by magmatic volatiles may also be reduced.

Another explanation could be that the northern section opened at the surface in response to a deep dike injection sourced from the north, rather than the south; a relatively deep dike would be required to activate the normal faults bounding the 5 km wide rift. Dike injections sourced from different magma chambers along a rift zone was observed using satellite geodesy over the Afar rift in East Africa, which was activated during the 2005–2009 Afar rift crisis (Barisin et al., 2009, Grandin et al., 2009, Wright et al., 2006). In the early stages of the crisis, magma upwelling and dike injection in the Dabbahu-Gabho area at the northern end of the rift triggered further rifting and deep magma chamber discharge (10 km depth) in the Manda Hararo section of the rift 30 km to the south. Elastic dislocation modeling of geodetic data indicate significant variations in the magnitude of fault slip and dike opening along the rift zone, with a patch of low opening separating the Dabbahu-Gabho and Manda Hararo regions (Barisin et al., 2009, Grandin et al., 2009, Wright et al., 2006) — the 5 km width of this low slip section is nevertheless much smaller than the 20 km section at Krafla. Injection of a dike at depth beneath the northern Krafla rift early in the crisis may explain some aspects of the seismicity resulting the Krafla rift crisis. These are discussed below.

2.5.3 Seismicity of the early Krafla rifting crisis

On the 13th January 1975, the largest earthquake (M_w6.4) of the crisis occurred at the northern end of the rift, some 5 km north of the Axarfjördur coastline (Fig. 2.12). The earthquake centroid moment tensor (Global CMT) indicates significant strike-slip deformation during this event. Because the epicenter was located at the northern end of the rift zone, and the event occurred just a few weeks after the initial dike injection, Björnsson et al. (1977) interpreted it as resulting from right-lateral slip on a NW-SE transform fault, the Grimsey Lineament, which was thought to form a structural termination to the rift zone, in response to loading caused by the earlier dike injection. However, bathymetric data from the Axarfjördur region does not reveal any geomorphic features typical of prolonged right-lateral strike-slip activity. Major NNW-SSE trending scarps are clearly visible in the bathymetry, typical of normal faults, suggesting that the Krafla rift zone continues northward beyond the location of the 1976 earthquake epicenter. Rögnvaldsson et al. (1998) concluded right-lateral shear across the Grimsey Lineament is actually accommodated by block rotation between N-S faults which strike perpendicular to the transform fault, i.e. there is no single through-going transform fault in this region.

The relocated hypocenter for the 1976 event (Engdahl et al., 1998) is located directly above one of these normal faults, which strikes NNW for >30 km along the eastern margin of Axarfjördur bay (shown by yellow pointers in Fig. 2.12). The 1976 hypocenter also coincides with a patch of micro-earthquakes from the period 1981–1986 (Einarsson, 1991) and 2000–2010 (SIL catalog, see Fig. 2.12). The depth distribution for these events indicates brittle behavior throughout the entire crust, with 80% occurring between 3–15 km depth (see also Rögnvaldsson et al., 1998). This cluster of activity closely resembles another cluster of earthquakes to the south, associated with magmatic intrusion beneath the Krafla caldera between 1981–1986 (Fig. 2.12 inset). This similarity may indicate a similar response of the crust to the change in stresses associated with magma upwelling and dike injection.

The 1976 earthquake focal mechanism also contains a significant (30%) non-double couple component. Similar focal mechanisms have been reported in the Long Valley Caldera (Julian, 1983), which were originally interpreted as oblique strike-slip earthquakes, before being re-interpreted as CLVD mechanisms with a dilatational component associated with injection of fluids into the crust. CLVD mechanisms have also been reported for micro-earthquakes in the Krafla post-rifting period (Foulger et al., 1989). (On the 12th December 1980 a similar CLVD mechanism also occurred ∼60 km NW of the 1976 Krafla earthquake on the Grimsey Lineament, and may also be related to N-S injection of a dike at depth in 1980 — Fig. 2.1). Because the 1976 focal mechanism includes a significant dilatational component, the strike of a dike injected at depth would be approximately NNW-SSE, consistent with the strike of the normal faults at the surface (Fig. 2.12, see

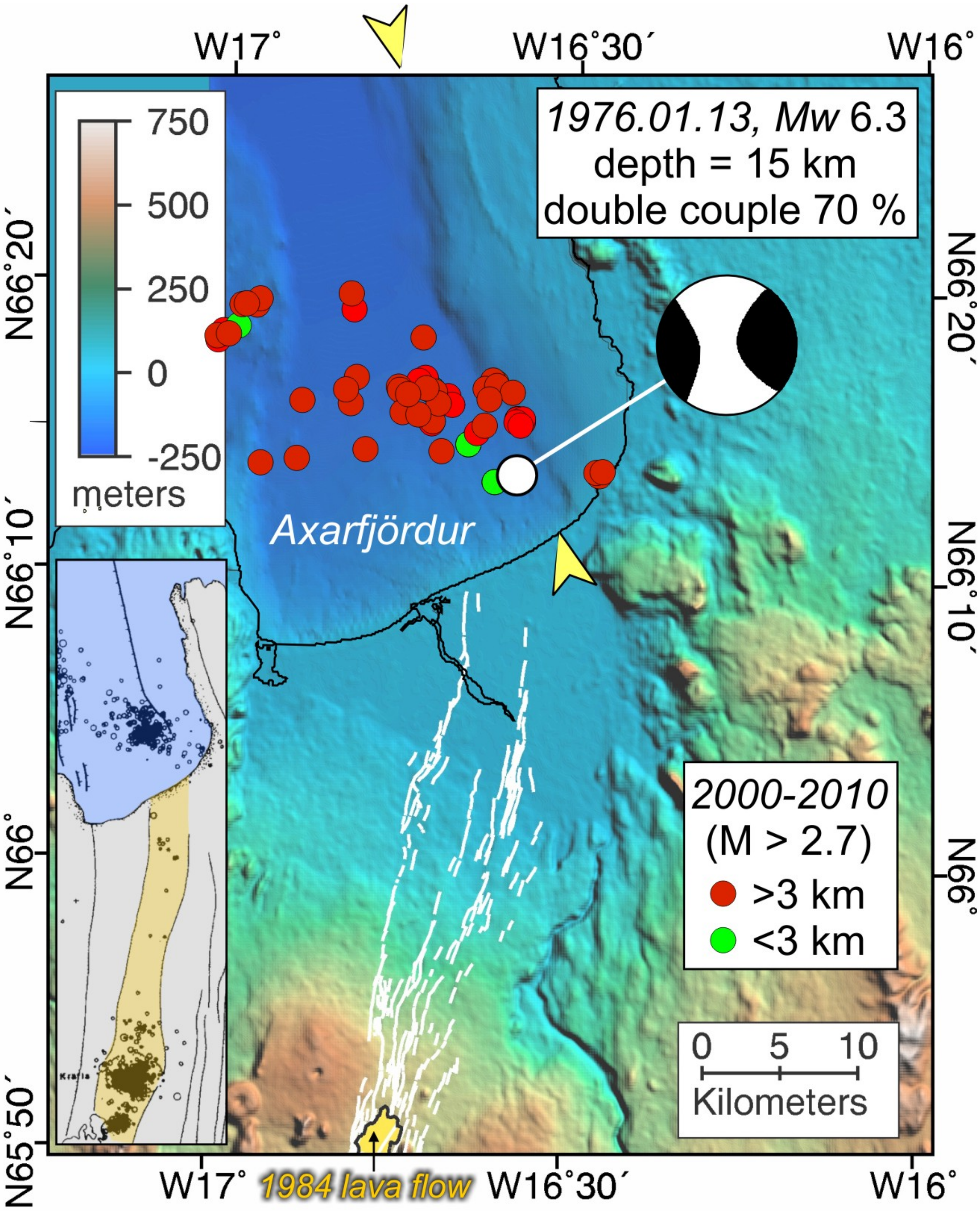

Figure 2.12: Bathymetry and topography of the northern Krafla fissure swarm. Faults are shown by white lines. The Engdahl catalog location for the 13th January 1976 earthquake is shown, along with the Harvard CMT solution. Red and green circles show microearthquakes at >3 km and <3 km depths, detected by the SIL network in the period 2000–2010. Inset figure shows microearthquakes recorded along the Krafla rift between 1981 and 1985 (adapted from Einarsson, 1991). A major NNW-SSE striking normal fault scarp in the Axarfördur bay is highlighted by yellow pointers (McMaster et al., 1977).

also McMaster et al., 1977). However, it should be noted that the non-double couple component could simply reflect a more complicated earthquake source, including multiple double-couple, or both dilatational and double-couple sub-events.

Although the various dike injections of the Krafla rifting crisis may have been sourced from various magma sources, lateral dike injection has clearly played an important role in accommodating along-strike opening of the Krafla fissure swarm (e.g. Einarsson and Brandsdottir, 1980). Therefore, perhaps the most likely scenario which explains both the seismicity, and pattern of surface opening is one in which a dike propagates from the caldera northward into a region of higher tension at the northern end of the rift (Buck et al., 2006). Surface faults are activated in the south as a result of wider opening on a shallower dike. Surface faulting in the north occurs above a thinner deeper dike because the host rock is weakened due to the transition from magmatic volatiles to ambient pore fluids feeding the dike tip cavity (Ziv et al., 2000). In this model, a relatively large and deep packet of magma would be delivered to the northern end of the Krafla rift, enough to activate normal faults at this location. Because the normal faults extend to greater depths in the crust, where they coincide with the dike top, they will have a bigger area than those closer to the caldera. Combined dike opening and normal slip on relatively large faults may therefore account for both the shear and dilatational components in the 1976 earthquake focal mechanism, as well as the epicentral location at the northern end of the rift Fig. 2.12. These conclusions are summarized on a crustal profile along the Krafla rift, shown in Fig. 2.13. It is also worth noting that Einarsson and Brandsdottir (1980) report a kink in the seismicity associated with the July 1978 dike injection, which propagated from the Krafla caldera to N66°3′ (Fig. 2.4, and thick black arrow in Fig. 2.13). This kink corresponds to the region of no surface faulting in the central rift at the start of the crisis, and may highlight a structural complexity at depth. The obliquity of the kink with respect to the strike of the wider Krafla rift raises the possibility that the January 1976 dike injection may have propagated through a self-generated crack analogous to 'wing-cracks' observed to form in the tips of pure mode-II fractures (Ziv et al., 2000). The generation of such a 'wing-crack' could occur at the transition of magmatic volatiles to ambient pore fluids feeding the dike tip cavity (Fig. 2.13).

2.5.4 Implications for magma migration throughout the Krafla crust

Although the shallow magma chamber beneath the Krafla caldera appears to have sourced material for the various dike injections throughout the crisis, de Zeeuw-van

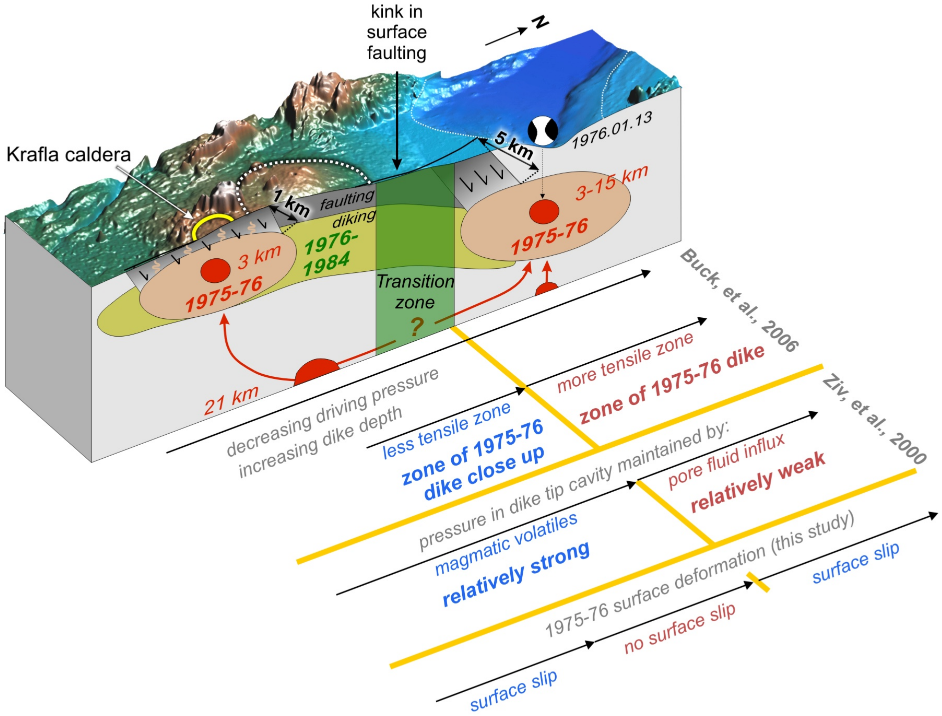

FIGURE 2.13: Schematic cross section along the Krafla rift zone summarizing the general sub-surface movements of magma throughout the 1975–84 rift crisis. Thick dotted white line shows the Storaviti and Grjothals topographic high; yellow line shows the Krafla caldera; thin white dotted line shows the coastline. Red areas show possible magma chambers at depth; pink areas show significant dike opening during the early stages of the crisis; yellow regions show significant dike opening in the mid-to-late stages of the crisis; dark gray region shows the region above the dike, which failed by faulting. Various aspects from the studies of Buck et al. (2006) and Ziv et al. (2000) relating to dike propagation and strength of the crust, and which may explain the bi-modal pattern of surface opening (this study) are summarized alongside the figure, see Section 2.5.2 for details. Green section of the crust indicates the transition from magmatic volatiles to influx of pore fluids in the dike tip cavity. See Section 2.5.2 for additional discussion.

Dalfsen et al. (2004) detected a much deeper accumulation of magma using InSAR observations over the period 1993–99, which may have also contributed to deformation during the crisis. The location of this deep accumulation, ∼15 km north of the Krafla caldera and at 21 km depth also coincides with the region of maximum opening during the 1975–84 crisis, as well as two topographic highs (Storaviti and Grjothals), which make up a broader long-wavelength high across the center of the rift zone, similar to the Mando Hararo section of the Afar rift. Therefore, it is possible that the shallow magma chamber beneath the caldera may have been sourced from a deeper, more centrally located magma chamber (Fig. 2.10a), which may also have sourced a magma chamber to the north (Fig 2.13). This idea is also consistent with geochemical data from the Krafla region (Gronvold, 2006, Maclennan et al., 2008, Nicholson et al., 1991), which shows significant variability in the depth of magma sources throughout the Krafla rift, particularly within and outside the caldera. However, it should be noted that the long-wavelength post-rifting signal over the Storaviti-Grjothals high may also be explained by visco-elastic relaxation models (e.g. de Zeeuw-van Dalfsen et al., 2004, DiCaprio, 2010), which also account for the co-location of the maximum post-rifting signal with the region of maximum co-rifting opening. de Zeeuw-van Dalfsen et al. (2004) rule out the visco-elastic relaxation hypothesis because the expected post-rifting deformation from Pollitz and Sacks (1996) is only 15% of the total broad deformation seen in their interferograms. However, DiCaprio (2010) showed that alternative post-rifting, viscoelastic models can exhibit much larger deformation rates. Nevertheless, a contraction of ∼0.5 m was measured across the Krafla caldera region between 1965–71 (Wendt et al., 1985), which could also be explained by deflation of the deep magma source of de Zeeuw-van Dalfsen et al. (2004), with melt migrating to shallower depths prior to the crisis. Similar migration of melt between 6–24th July 2007 from depths of 17.5 km to 13.5 km and at dip angles of 50° have recently been reported near Askja caldera, 80 km south of Krafla (White et al., 2011).

2.6 Conclusions

Correlation of a declassified KH-9 spy satellite image with a SPOT5 satellite image reveals the regional deformation pattern between 1977–2002 (2.5 m average opening), while correlation of aerial photos between 1957–1990 provide local measurements of the total extension close to the rift zone (average 4.3 m opening). These results were obtained using the COSI-Corr software package, which allows declassified spy satellite and aerial photos to be correlated with subpixel precision. Development of a new ‘Epipolar Map Projection’ tool within COSI-Corr also allows displacements to be measured in the epipolar perpendicular plane, which contains no topographic residuals. Therefore, high resolution optical imagery from different sources may now be successfully correlated without an equivalent resolution DEM. Our results provide new insights into the deformation accommodated at the northern end of the Krafla rift zone, where earlier geodetic measurements were relatively sparse. Correlation of aerial photos from 1957–1976 reveal the magnitude and extent of opening during the early stages of the crisis. This study provides new constraints on the displacement field resulting from the 1975–1984 Krafla rifting crisis, NE Iceland. Extension at the surface is accommodated primarily by normal faults which bound the rift zone, while extension is accommodated at depth by dike injection. A bi-modal pattern of opening along the rift during this period could be produced by two different magma sources, located at the northern and southern ends of the rift zone. This is similar to observations from the Afar rift zone in East Africa, where extensive and precise geodetic measurements allow the determination of dike opening and fault slip throughout the rift zone. Alternatively, the bi-modal pattern of opening may also result from a weakening of the host rock along the northern end of the rift, as magmatic volatiles transition to ambient pore fluids feeding the dike tip cavity. Variations in the magnitude of opening along the Krafla rift zone require that either different sections of the rift zone are subject to dike injection events at different times, or the remaining deformation is accommodated elsewhere in the region, such as the neighboring Theistareykir and Fremri-Námar fissure swarms. Our results are significant as they provide new information on how past dike injection events accommodate long-term plate spreading. Furthermore, this study highlights the potential of optical image correlation using inexpensive declassified spy satellite and aerial photography to measure deformation of the Earth's surface going back many decades. This latter point highlights the potential of image correlation for providing important contributions in other areas of Earth surface observation, and for periods where InSAR and GPS data are not available, such as glacial studies, landsliding, coastal erosion, volcano monitoring as well as earthquake studies.

Chapter 3

Influence of camera distortions on satellite image registration and change detection applications

François Ayoub[1], Sébastien Leprince[1], Renaud Binet[2], Kevin W. Lewis[1], Oded Aharonson[1], and Jean-Philippe Avouac[1]

[1]Division of Geological and Planetary Sciences, Caltech, California, U.S.A.

[2]LDG CEA, Arpajon, France (now at CNES, Toulouse, France)

Foreword - The next chapters we leave aerial imagery on Earth to move to satellite imagery on Mars. But before that, this chapter is a short investigation on the sources of bias in the displacement maps that are commonly found in pushbroom system. A set of active sensors are studied: SPOT, ASTER, Quickbird, and HiRISE which will be used in the next 2 chapters. The main sources of distortions are the CCD arrays geometry calibration residual, and the satellite jitter not recorded by the on-board devices which can account for few pixels mis-registration in the most severe cases. This study was presented at the IGARSS conference (Ayoub et al., 2008).

3.1 Introduction

Accurate geometrical modeling of optical imaging systems is of prime importance to finely monitor the Earth's surface. This is particularly relevant to digital elevation model (DEM) generation, measurement of surface displacement (ice-flow, landslide, coseismic deformation), and change detection applications. Recent methodological advances now allow for the co-registration of pushbroom satellite images with 1/50 pixel accuracy, which makes possible the measurement of ground displacement with accuracy better than 1/10 of the pixel size Leprince et al. (2007). This methodology was implemented in the Co-registration of Optically Sensed Images and Correlation (COSI-Corr) (Tectonics-Observatory, 2014) software package. As a drawback of such measurement accuracy, uncertainties on the imaging system are exacerbated, and unmodeled distortions may severely affect applications requiring high accuracy.

Here, we characterize the unmodeled distortions of several optical sensors currently in use, and we pinpoint the possible consequences for different applications. Multi-temporal images of the same area and from the same sensor are orthorectified, co-registered and correlated with COSI-Corr according to Leprince et al. (2007). The procedure applies a rigorous modeling using all available acquisition data (e.g. camera geometry, spacecraft attitudes, orbits). If the image's geometries were correctly modeled, the correlation map should be uniformly zero. However, tests ran on images from the SPOT, ASTER, Quickbird, and HiRISE satellites, revealed clear artifacts originating from focal plane distortions and from unmodeled platform attitudes (jitter).

3.2 SPOT 1,2,3 and 4

The SPOT (Satellite Pour l'Observation de la Terre) constellation comprises 5 satellites. The latest satellite, SPOT 5, has its panchromatic optical detector made of an unique CCD array, whereas the SPOT 1, 2, 3, and 4 detectors are composed of 4 CCD arrays combined together through an optical divider. The accurate knowledge of the CCD arrays alignment is essential for a geometrically correct image reconstruction. In Leprince et al. (2007), the ground deformation produced by the 1999, Mw 7.1, Hector Mine earthquake was retrieved through the correlation of a 10 m SPOT 2 and a 10 m SPOT 4 images bracketing the event. The standard deviation of the measurements was around 80 cm, and the coseismic ground deformation could be localized and measured. However, the measurements were polluted with along-track stripes from CCD misalignments whose amplitudes were up to 1.6 m.

The calibration of these CCD misalignments was studied in Leprince et al. (2008b) and applied to the SPOT 4 HRV1 sensor. The ground distortion induced by each CCD array was measured using subpixel correlation between the SPOT 4 HRV1 image and a SPOT 5 image that was assumed distortion-free. The images were precisely orthorectified and coregistered before correlation to account for the images' acquisition geometries and to remove any stereoscopic effect. Distortions found in the disparity map were then reprojected in the camera focal plane. CCD arrays misalignments were reduced by one order of magnitude (Fig. 3.1). As of now, the refinement of the SPOT 4 HRV1 and SPOT 2 HRV1 CCD arrays orientation were processed and implemented in the COSI-Corr package.

3.3 ASTER

ASTER (Advanced Spaceborne Thermal Emission and Reflection Radiometer) is an imaging instrument flying on Terra, a satellite launched in December 1999 as part of NASA's Earth Observing System (EOS). The ASTER Visible Near Infrared (VNIR) device is composed of an unique CCD array for each spectral band. In a context of tectonic investigation, an ASTER image acquired on May 10, 2000 was correlated with a SPOT 4 image acquired August 17, 1998, with the purpose of measuring the coseismic ground deformation sustained by the 1999, Mw 7.1, Hector Mine earthquake. Prior to correlation, the images were orthorectified and co-registered on a 10 m UTM grid using the methodology described in Leprince et al. (2007). The SPOT 4 CCD arrays alignments were refined as explained in 3.2.

On the East/West displacement map (Fig. 3.2), the fault discontinuity is readily identifiable. However, a strong, undulating pattern is corrupting the displacement map and impairs quantitative measurement of the coseismic displacement. This pattern has an amplitude of around 6-7 m and a frequency of 1.6 Hz. This artifact is attributed to the ASTER image only. Indeed, in Leprince et al. (2007), the same SPOT image was correlated with a non ASTER image, and no similar pattern was

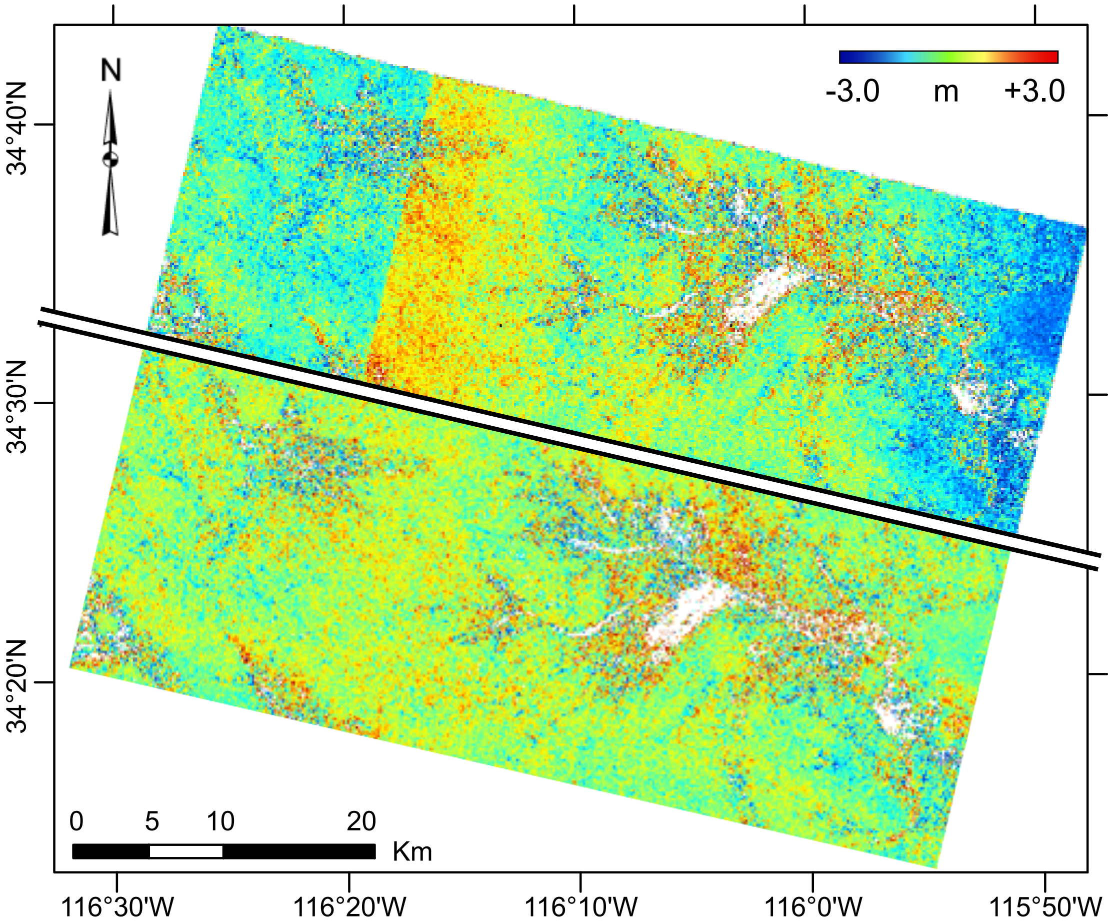

FIGURE 3.1: East-West component (eastward positive) of two disparity fields measured from subpixel correlation of a reference 5-m SPOT 5 image and a 10-m SPOT 4 image near Hector Mine (California). Top: the camera geometry provided by SPOT Image Corp. was accounted for. Linear artifacts from SPOT 4 CCD misalignments are identifiable with amplitude greater than 1 m. Bottom: the disparity field was generated using the same images but the SPOT 4 CCD arrays misalignments were calibrated according to Leprince et al. (2008b). Correlation analysis were performed on 32×32 pixel windows, sliding with a step of 8 pixels.

detected. This artifact is a consequence of unrecorded spacecraft jitter during the ASTER image acquisition.

The Terra on-board attitude recorders have a sensitivity of 1 arcsecond (around 3.4 m on ground for VNIR images) and a sampling rate of 0.97 Hz. The sampling rate is insufficient to record properly the spacecraft jitter observed on Fig. 3.2. The displacement generated from the jitter has an amplitude greater than the devices sensitivity, and should have been detected. The devices are either malfunctioning, or, possibly, the undersampled measurements provide an aliased jitter record. Similar artifacts in amplitude and frequency were also reported in Avouac et al.

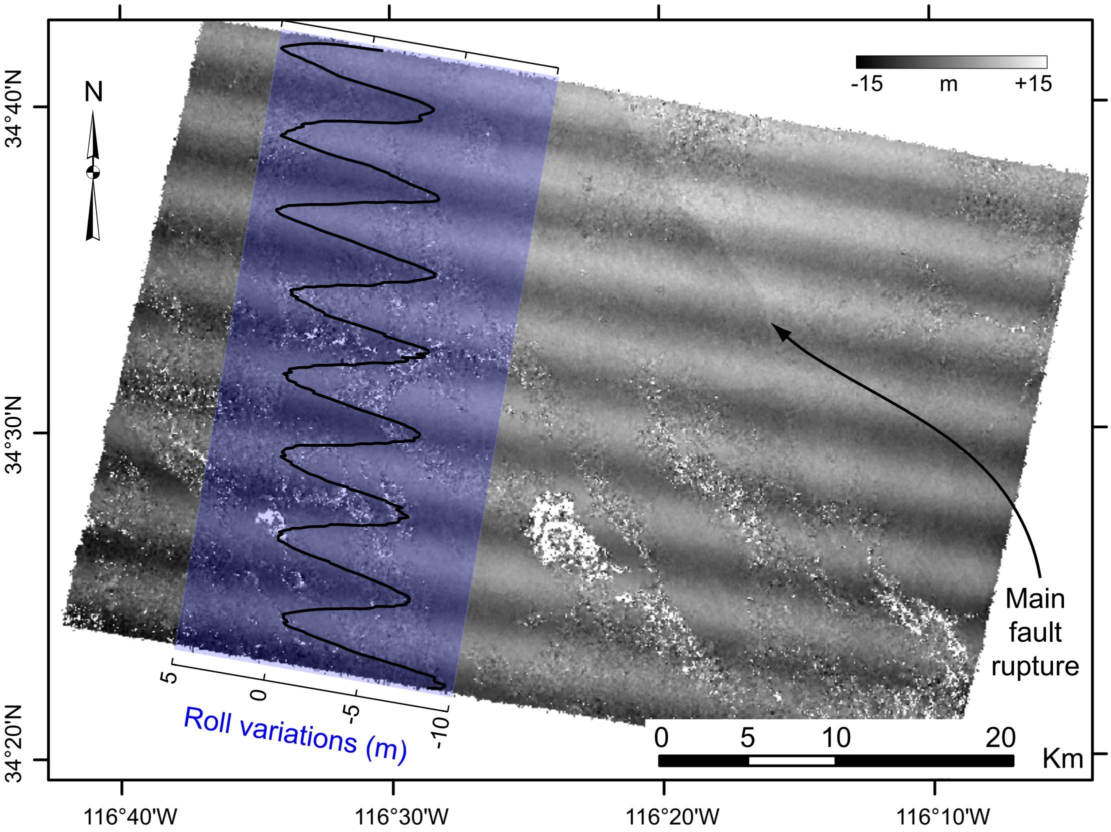

Figure 3.2: Disparity map in the East/West direction between a SPOT 4 and an ASTER images, acquired on May 10, 2000, and on August 17, 1998 over the Hector Mine area, California. Images were orthorectified on a 10 m resolution UTM projection, and subpixel correlation was performed on 32×32 pixels windows, sliding with a step of 8 pixels. The SPOT 4 image was corrected for CCD arrays misalignments as explained in 3.2. The goal of this study was to detect and measure the ground rupture produced during the 1999, Mw 7.1, Hector Mine earthquake. The fault rupture is identifiable but accurate measurements are difficult due to the oscillating bias induced by the unmodeled jitter of the ASTER spacecraft during the image acquisition.

(2006), Leprince et al. (2007), and Iwasaki and Fujisada (2003). The latter shows in addition that DEMs extracted from ASTER imagery are distorted with such artifacts.

3.4 Quickbird

Launched in 2001, the Quickbird satellite provides images with the highest resolution available to the general public. Its panchromatic detector is composed of six CCD arrays, alternatively placed aft and forth in the focal plane, and acquires images with a ground sampling of 60 cm. In Binet and Bollinger (2005), two

SPOT 5 - 2.5 m resolution images with similar viewing angles were correlated to reveal the location and to provide estimates of the surface offsets induced by the December 26, 2003, Mw 6.6 Bam earthquake in Iran. Building on this study, we applied a similar technique using Quickbird panchromatic imagery to refine the SPOT derived measurements. Unfortunately, the large viewing angle difference between the Quickbird images (14.3°) produced significant topography residuals in the correlation maps, that could not be corrected for using the 3-arcsec (90 m) SRTM DEM. We therefore resampled and co-registered both Quickbird images at 50 cm resolution in an epipolar geometry. Cross-correlation in this geometry leads to a displacement map with a component that supposedly only depends on the topography, while the other component is independent of the topography. This is this last component that we present in Fig. 3.3. We show that the fault rupture can indeed be recovered but that, unfortunately, residual distortions from the imaging system corrupt the measurements. A CCD discontinuity artifacts is indeed aligned with the fault rupture, mixing both signals. Unmodeled jitter produces distortion of around 5 pixels (2.5 m) which occurs mainly around 1 Hz. We also notice a jitter of 4.3 Hz of amplitude 0.2 pixel. Finally, we notice seam artifacts between CCD arrays that are produced during the image stitching process. Indeed, adjacent CCD arrays do slightly overlap and the necessary merging of overlapping areas involves a registering step subject to errors.

3.5 HiRISE

Since 2006, the High Resolution Imaging Science Experiment (HiRISE) on board of the Mars Reconnaissance Orbiter (MRO) images the Mars surface with unprecedented resolution (around 30 cm) McEwen et al. (2007). The monochromatic (red wavelength) optical detector is composed of 10 CCD arrays, alternatively placed aft and forth in the focal plane, and are slightly overlapping to insure a continuous ground imaging between CCD arrays. Two multi-temporal overlapping images, acquired over the Victoria crater in the Meridiani Planum, were retrieved in raw format (EDR) from the HiRISE website and reconstructed in the focal plane geometry. The reconstruction accounted for the acquisition parameters: radiometry, camera geometry, spacecraft attitudes and ephemerides (SPICE kernels). Topography was not accounted for, but the identical viewing angles between

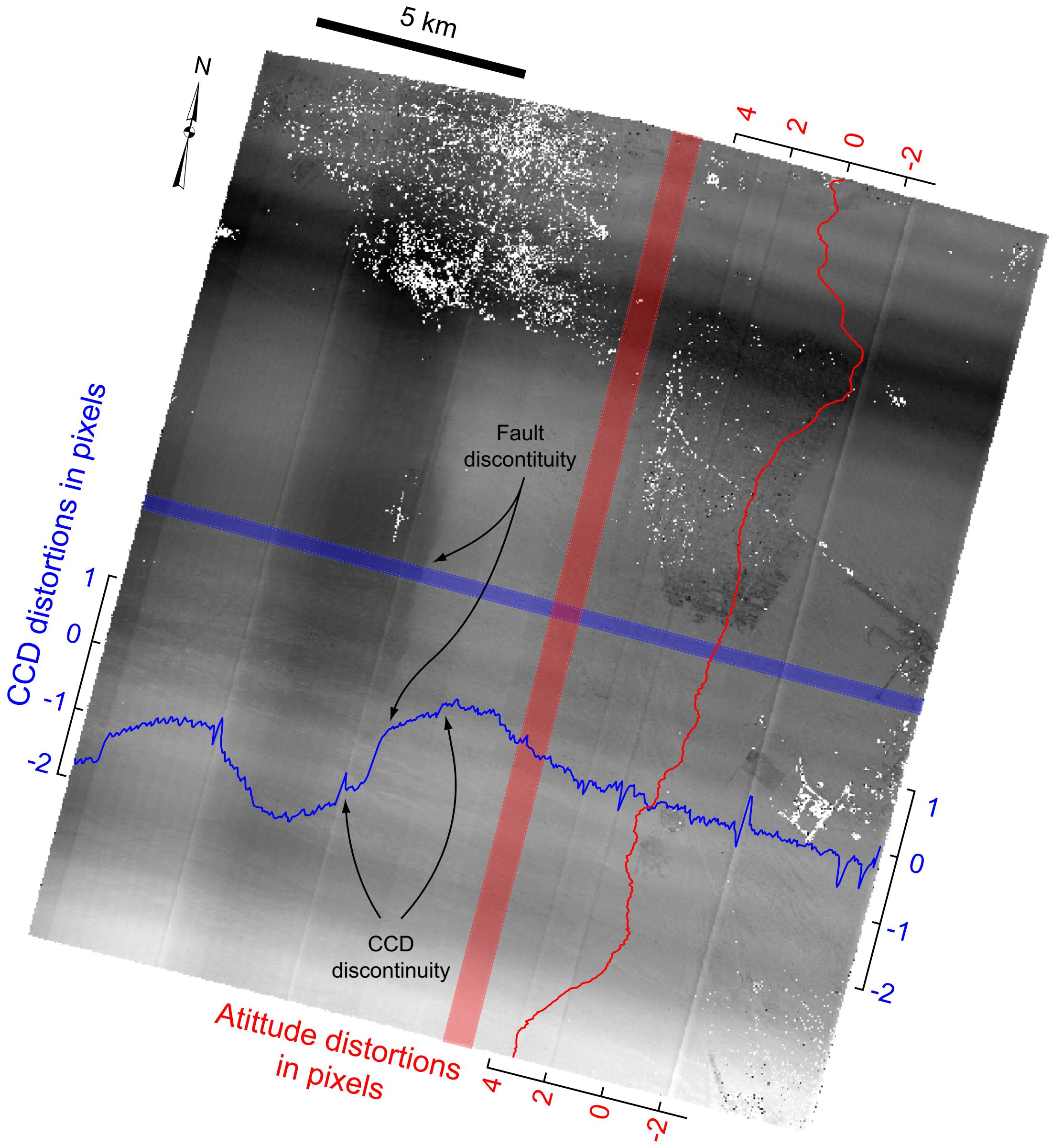

FIGURE 3.3: Disparity map in the direction orthogonal to the epipolar direction between two Quicbird images (03SEP30063637-P1BS-000000170456_01_P001 and 04JAN03064311-P1BS-000000170455_01_P001), acquired above the city of Bam, Iran, on September 30, 2003, and on January 03, 2004. Images were resampled at a 50 cm resolution and subpixel correlation was performed on 128×128 pixels windows, sliding with a step of 64 pixels. This disparity map should not show any particular pattern, and indeed, no topography signal is detected. The goal of this study was to detect and to measure the ground rupture produced during the Mw 6.6 Bam earthquake of December 26, 2003. In this geometry, the fault rupture is measured to be less than 2 pixels (less than 1 m), but accurate measurements are difficult due to the bias imposed by distortions from the imaging system such as CCD interconnection discontinuity and jitter artifacts. In particular, a CCD distortion seem to exactly coincide with the coseismic signal to be measured. White areas are decorrelation areas, mostly produced by the collapse of buildings during the earthquake.

the two images removes stereoscopic effects. The reconstructed images were then co-registered and correlated.

The along-track disparity map (Fig. 3.4) shows strong geometric distortions in column and line directions. The undulating pattern (red) reveals spacecraft jitter that was unmodeled during the images reconstruction. The vertical stripes (blue) originate, potentially, from two causes. The first cause would be the consequence of the unmodeled jitter on the staggered CCD arrays. Indeed, unmodeled jitter introduces a relative shift between images acquired by adjacent, staggered, CCD arrays. The amplitude of these shift depends on both the jitter characteristics (frequency and amplitude), and the time delay between adjacent CCD arrays to image a same ground location. The second cause would be a CCD arrays misalignment with respect to their nominal position. In the latter case, the absolute CCD array orientation in in the focal plane proposed by Leprince et al. (2008b) is limited here as no high resolution reference is available. However, a relative orientation between CCD arrays could be operated.

The amplitude of the jitter distortion is up to 3 pixels (around 1 m), whereas the amplitude of the CCD arrays induced distortion is around 4-5 pixels (1-1.5 m). The cross-track disparities map, not displayed here, presents the same artifacts with about the same amplitude. These artifacts can corrupt applications requiring precise photogrammetry. Indeed, we produced a DEM from HiRISE imagery using ISIS3 (USGS) and SOCET SET (BAE Systems) softwares and applying the procedure defined by the HiRISE team. CCD arrays artifacts, similar to the ones found in Fig. 3.4, were identified on the DEM as seen on Fig. 3.5, and generate an elevation error of around 1 m. In Kirk et al. (2007), DEM extraction with HiRISE imagery was confronted to similar CCD arrays and jitter artifact.

3.6 Conclusion

This study reveals that geometrical distortions of current pushbroom satellites are to be sought among two main causes: the modeling inaccuracy of the CCD sensor geometry, and the jitter of the instrument's platform during image acquisition. These two problems occur on most pushbroom systems, whether they orbit the Earth or Mars, and whether they deliver low- or high-resolution images. Artifacts induced in disparity maps hamper change detection applications as well as DEM

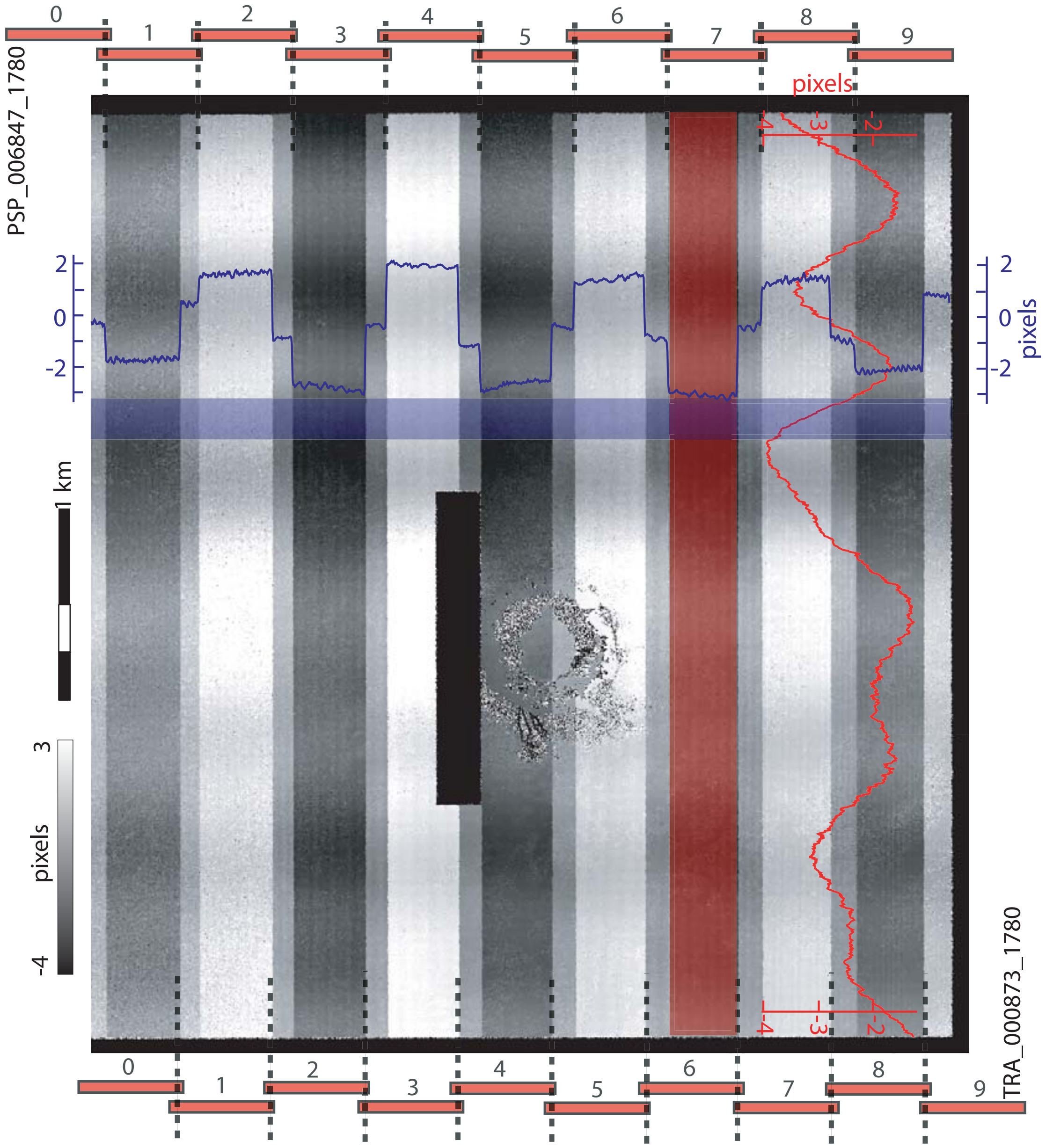

FIGURE 3.4: Along-track component (up positive) of the disparity field measured from subpixel correlation of two 25 cm HiRISE images (TRA_000873_1780 and PSP_006847_1780), acquired over the Victoria crater area in Meridiani Planum. The reconstruction accounted for the images radiometry, camera geometry, spacecraft attitudes and ephemerides. Topography was not accounted for, but the identical incidence angles removes any stereoscopic effect. They were correlated using a window size of 64×64 pixels and a sliding step of 16 pixels. The black stripe is due to missing data in the PSP_006847_1780 image, and the decorrelation area right of the black stripe is caused by large areas covered with fine material that appear featureless at the correlation window size. As expected, no topographic effect are noticed, but strong artifacts are found in the column and line directions. Cross-track artifacts (red profile averaged in line direction over the red box) reveal unmodeled spacecraft jitter, while along-track artifacts (blue profile averaged in column direction over the blue box) are produced by a probable combination of CCD arrays misalignment and unmodeled jitter on staggered CCD arrays. The CCD arrays' relative position of the two images are sketched above and below the disparity field.

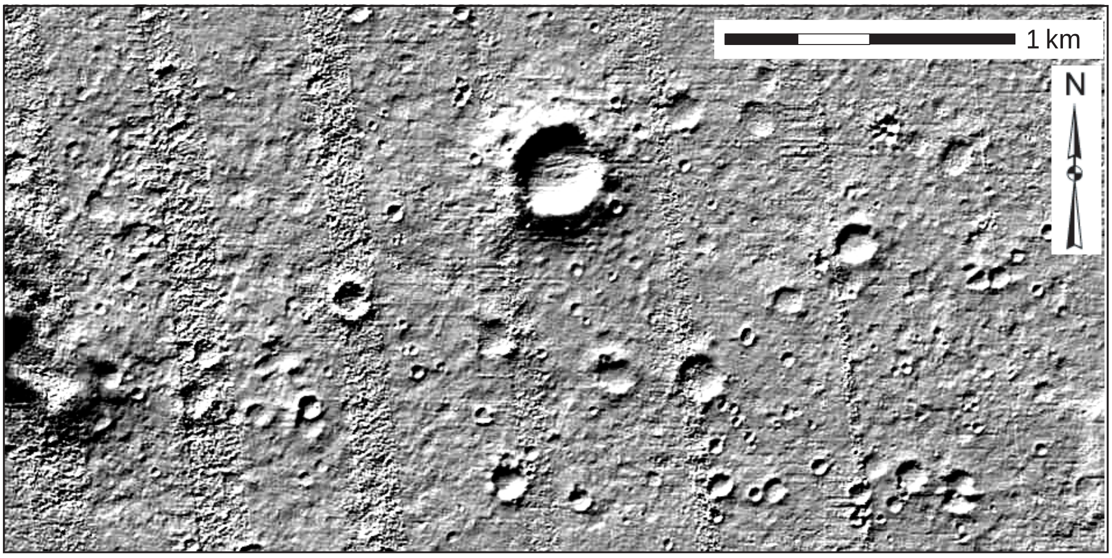

Figure 3.5: Shaded DEM generated from HiRISE imagery near Columbia Hills. Raw images were reconstructed using the USGS ISIS-3 software and the corresponding SPICE kernels, and DEM generation was operated using the SOCET-SET software. Although the camera geometry was recently refined, residual CCD misalignments generate artifacts in the DEM with an amplitude of around 1 m.

generation. Proper correction and modeling of these distorting causes is becoming an urgent need since these distortions may now be greater than the images resolution, limiting the potential of high-resolution systems. Solutions to correct for these distortions are appearing Leprince et al. (2008b), Teshima and Iwasaki (2008), Bamber et al. (2006), and precisely detecting and characterizing them is indeed a decisive step to this end.

Chapter 4

Earth-like sand fluxes on Mars

Nathan T. Bridges[1], François Ayoub[2], Jean-Philippe Avouac[2], Sébastien Leprince[2], Antoine Lucas[2], Sarah Mattson[3]

[1]Space Department, Johns Hopkins University Applied Physics Laboratory, Maryland, U.S.A.
[2]Division of Geological and Planetary Sciences, Caltech, California, U.S.A.
[3]Lunar and Planetary Laboratory, University of Arizona, Arizona, U.S.A.

Foreword - This study is the first application of COSI-Corr to extra-terrestrial imagery, targeted at the measurement of aeolian activity. My contribution focused on redesigning part of COSI-Corr (extra-terrestrial imager, non-Earth projection system, large size imagery), estimating the sand flux from the ripple migration measurements, and comparing it to Earth dune fields. N. Bridges provided the martian aeolian background and estimation of the erosive potential of the sand flux and was the main lead of the manuscript writing. This work is referenced as Bridges et al. (2012a).

4.1 Introduction

Strong and sustained winds on Mars have been considered rare, on the basis of surface meteorology measurements and global circulation models (Arvidson et al., 1983, Haberle et al., 2003), raising the question of whether the abundant dunes and evidence for wind erosion seen on the planet are a current process. Recent studies (Bridges et al., 2012b, Chojnacki et al., 2011, Hansen et al., 2011, Silvestro et al., 2010) showed sand activity, but could not determine whether entire dunes were moving—implying large sand fluxes—or whether more localized and surficial changes had occurred. Here we present measurements of the migration rate of sand ripples and dune lee fronts at the Nili Patera dune field. We show that the dunes are near steady state, with their entire volumes composed of mobile sand. The dunes have unexpectedly high sand fluxes, similar, for example, to those in Victoria Valley, Antarctica, implying that rates of landscape modification on Mars and Earth are similar.

The Martian surface displays abundant bedforms (ripples and dunes) (Malin and Edgett, 2001), and evidence for wind erosion ranging from centimetre-scale ventifact rock textures (Laity and Bridges, 2009) to kilometre-scale yardangs and exhumed mantles (Malin and Edgett, 2001). But whether these features are actively moving has been an open question, as sand-transporting winds have been considered rare in the low-density atmosphere of Mars (Arvidson et al., 1983, Haberle et al., 2003). Although many bedforms have been interpreted as static, relict features (Malin and Edgett, 2001), and dune formation times are predicted to be five orders of magnitude slower than on Earth (Claudin and Andreotti, 2006), recent high-resolution orbiter (Bridges et al., 2012b, Chojnacki et al., 2011, Hansen et al., 2011, Silvestro et al., 2010) and rover (Sullivan et al., 2008) images have provided evidence of sand movement. Whether these observations document surficial migration, or bedforms in equilibrium (the full volume undergoing movement) — and therefore large sand fluxes capable of actively eroding the surface — could not be determined using the traditional measurement techniques of the earlier studies. Resolution of this problem has implications for understanding past Martian climates, as it has been suggested that significant erosion on Mars may have required a higher-pressure atmosphere in the past (Armstrong and Leovy, 2005).

4.2 Measuring bedforms migration and sand flux

Recent advances in optical image correlation (Leprince et al., 2007) have allowed dune migration rates and associated sand fluxes in terrestrial dune fields to be estimated from satellite data (Vermeesch and Drake, 2008). We took advantage of the High Resolution Imaging Science Experiment (HiRISE) on the Mars Reconnaissance Orbiter, a push-broom imager with pixel sizes of $\sim 25\,\mathrm{cm}$ (McEwen et al., 2010), to track the displacement of sand ripples covering the dunes. We implemented the HiRISE geometry in the "Co-registration of Optically Sensed Images and Correlation" (COSI-Corr) tool suite, which provides quantitative surface dynamics measurements by automatic and precise orthorectification, co-registration, and sub-pixel correlation of images (Leprince et al., 2007). The resulting data rival those obtained using remotely sensed images of Earth dunes (Vermeesch and Drake, 2008).

The high spatial resolution of HiRISE combined with COSI-Corr allows us to quantify dune ripple migration rates and the derivation of sand flux across the entire image, a critical measurement that we perform for the first time on a planetary surface. To undertake this investigation,we chose the Nili Patera dune field, a location containing abundant barchan dunes with morphology typical of dunes elsewhere on Mars and on Earth, and for which localized ripple migration has been identified using visual comparison of images acquired at different times (Bridges et al., 2012b, Silvestro et al., 2010). Four HiRISE images centred on the Nili Patera dune field (8.8° N, 67.3° E) were used: two to quantify changes that occurred in the time interval (105 Earth days) between their acquisition (subsequently referred to as images T1 and T2); and another two to construct a stereo-derived Digital Elevation Model, on which the images were orthorectified and co-registered (images S1 and S2; Supplementary Table 1). The correlation of T1 and T2 provides dense measurements of ripple migration (Fig. 4.1a). We find that ripple migration occurs across the entire dune field, and increases with elevation along the stoss slopes. Measurable ripple motion is up to 4.5 m, confirming high sand activity. As dunes become more sheltered towards the southwest, ripple displacement generally decreases, consistent with active, northeasterly winds. The azimuthal distribution of displacement vectors (Fig. 4.1a, inset) is consistent with the southwesterly trend inferred from the orientation of the dune slip faces and barchan horns.

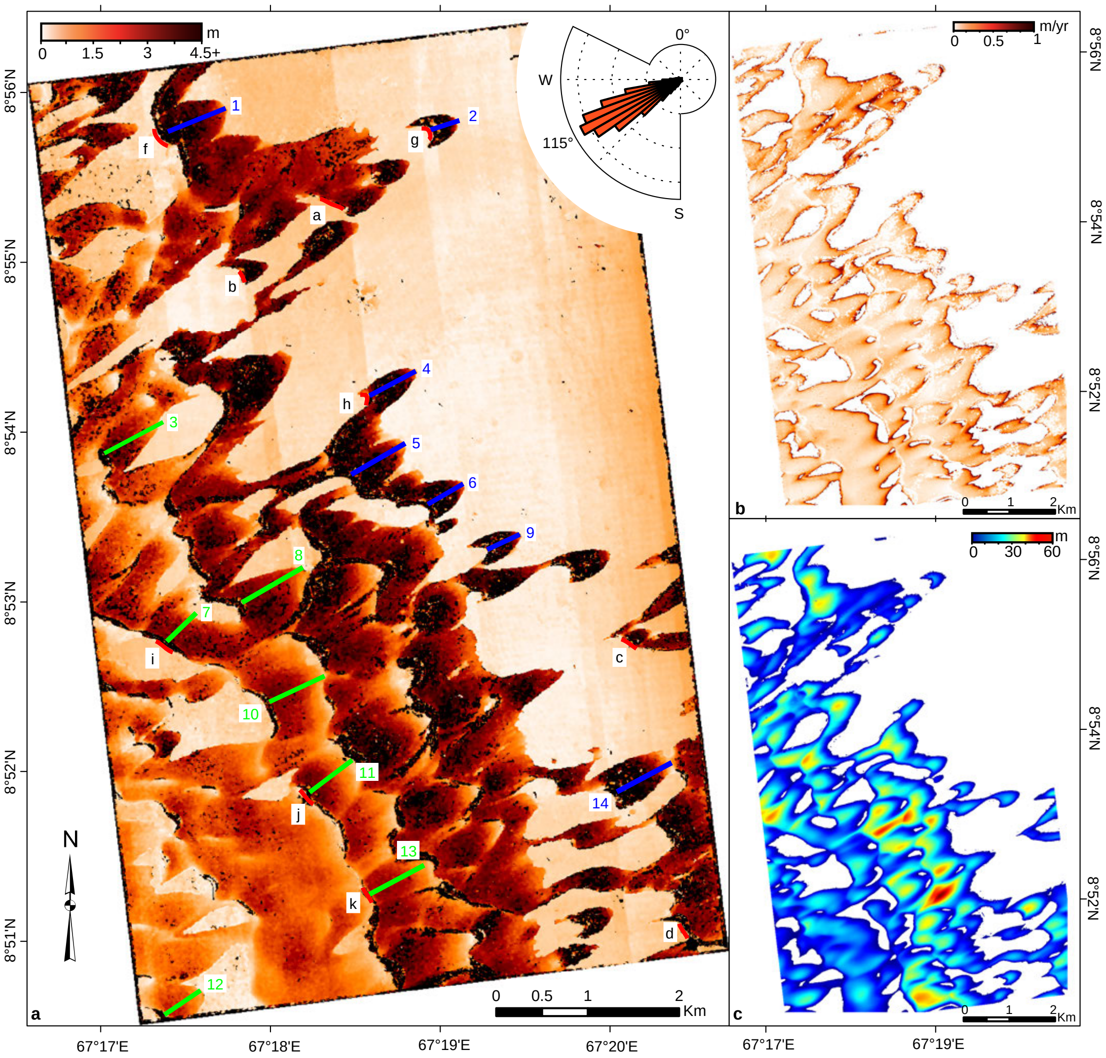

FIGURE 4.1: **Ripple migration, dune migration and dune elevation**. **a**, Ripple displacements in the Nili Patera dune field derived from correlating HiRISE images PSP_004339_1890 (30 June 2007) and PSP_005684_1890 (13 October 2007). Green and blue numbered lines show where profiles of ripple displacement were retrieved. Red lines with letters show where dune lee-front displacements were measured between images PSP_004339_1890 and ESP_017762_1890 (11 May 2010). Inset rose diagram shows distribution of ripple migration azimuth. **b**, Dune migration rate derived from the ripple migration rates and dune elevation. **c**, Dune elevation relative to bedrock base. Elevation and height maps are based on stereo images ESP_017762_1890 and ESP_018039_1890 (2 June 2010). See Supplementary Information for details of how dune height was estimated.

Ripple displacement (d_r) increases linearly with elevation on a given dune (h_D) (Fig. 4.2). The fastest ripples, those with the steepest slopes in Figure 4.2, moved so far that the correlation breaks down once the displacement exceeds a distance approximately equal to the ripple wavelength ($4.6 \pm 0.09\,\mathrm{m}$; see Supplementary

Information). This linear relationship is consistent with the behaviour of steady-state migrating dunes in which mass is conserved while shape and volume are maintained (Ould Ahmedou et al., 2007), and wind shear stress increases with dune elevation (Andreotti et al., 2006, Claudin and Andreotti, 2006) (see Supplementary Information).

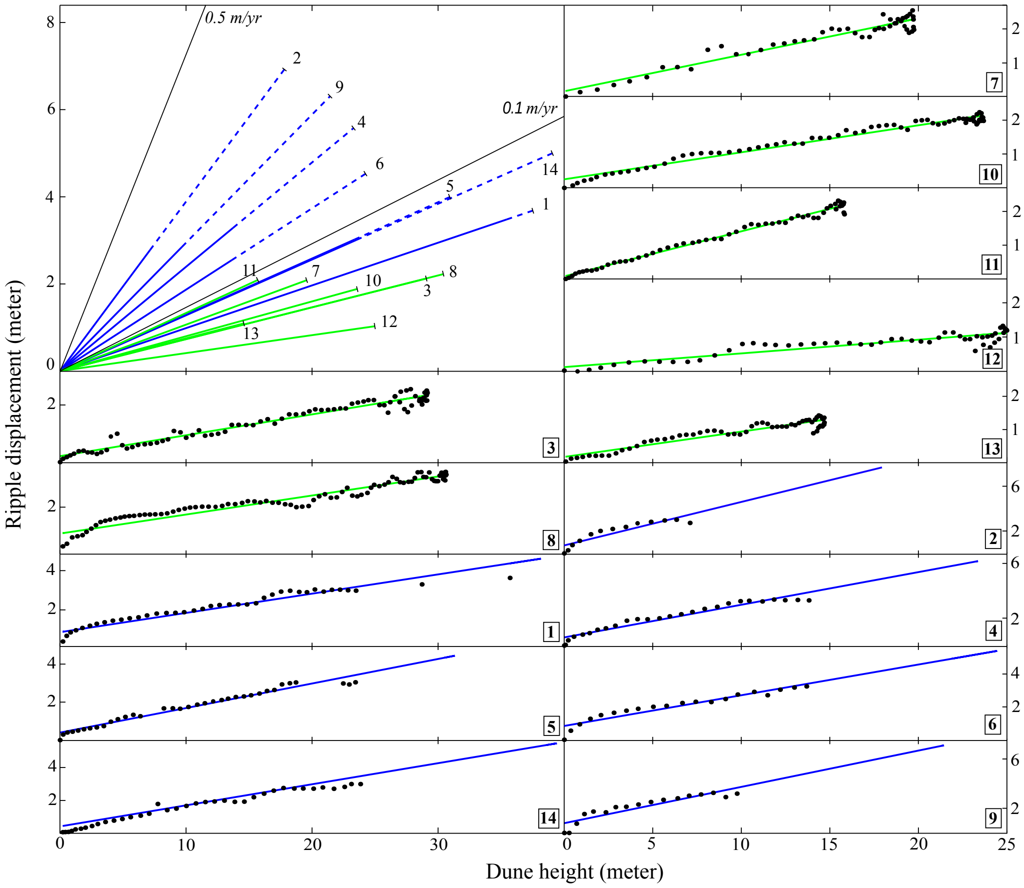

FIGURE 4.2: **Linear correlation between ripple migration and dune height**. Upper left frame: ripple displacement versus local dune elevation for profiles on upwind (blue) and downwind (green) dunes. Profile locations are shown in Figure 4.1a. ("Upwind" dunes are in the northeast part of the field, unsheltered from prevailing northeasterly winds; "downwind" dunes are in the southwest part of the field, partially sheltered by the dunes to the northeast.) Solid lines are best-fitting linear functions, shifted to go through the origin to facilitate slope comparisons. Dashed lines are extrapolations out to the dune crest for cases where displacements could not be estimated, owing to decorrelation of the ripple patterns. Black lines are isopleths of dune migration rates. The individual profiles and measured ripple displacements are shown in the other frames.

We also measured dune migration from the advancement of lee fronts between T2 and S1 (941 days), taking advantage of the accurate registration of the two images obtained with COSI-Corr. Fronts showed measurable advancement, but were negligible between T1 and T2 (105 days) except for a few isolated cases where avalanches occurred (Bridges et al., 2012b, Silvestro et al., 2010). These measurements were performed only where the lee advance was clear, and therefore may not represent the average migration of the whole dune field.

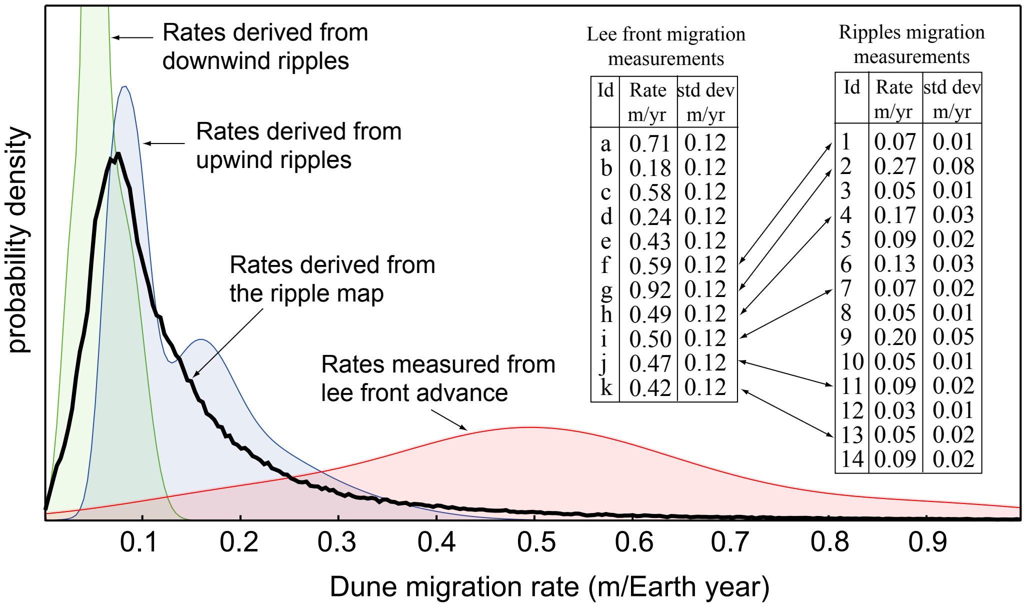

Lee front migration measurements

Id	Rate m/yr	std dev m/yr
a	0.71	0.12
b	0.18	0.12
c	0.58	0.12
d	0.24	0.12
e	0.43	0.12
f	0.59	0.12
g	0.92	0.12
h	0.49	0.12
i	0.50	0.12
j	0.47	0.12
k	0.42	0.12

Ripples migration measurements

Id	Rate m/yr	std dev m/yr
1	0.07	0.01
2	0.27	0.08
3	0.05	0.01
4	0.17	0.03
5	0.09	0.02
6	0.13	0.03
7	0.07	0.02
8	0.05	0.01
9	0.20	0.05
10	0.05	0.01
11	0.09	0.02
12	0.03	0.01
13	0.05	0.02
14	0.09	0.02

FIGURE 4.3: **Dune migration rates.** Normalized histogram (black) of dune migration rates over the 105-day T1–T2 time interval, derived from all measurements of Figure 4.1b where dune height (elevation above the bedrock base) exceeds 0.5 m. (All time intervals and rates in this paper refer to Earth days and years.) The right-side tail is mostly attributable to rates measured on the dunes' upwind and lateral edges, where the measured rates are probably erroneously large because the ripples there are not fully developed to the equilibrium height that is assumed in the calculations. (See Supplementary Information.) These large values appear as rims around the dunes in Figure 4.1b. The blue and green probability density functions show, respectively, the migration rates inferred for individual upwind and downwind dunes (Fig. 4.2). (See inset tables and Supplementary Table 2 for all migration rates and uncertainties.) The mean heights of the upwind and downwind dunes are 27 and 22 m, respectively. The red probability density function shows migration rates derived from lee-front advance over the 941-day T2–S1 interval. The location of these lee fronts is shown in Figure 4.1a (except for measurement e, which is located outside the area shown in the figure). Black arrows between the inset tables link dune migration rates obtained on the same dune from lee-front tracking (thus resulting from reptation and saltation) and from ripple migration (resulting from reptation only). Assumptions about ripple geometry result in uncertainty in the mean height of the ripples (see Supplementary Information), which propagates to a 20% uncertainty in dune migration rate.

Our measurements of ripples and dune migration are related, as they both reflect sand transport, and can be used to estimate sand flux. Sand transport results from saltation and reptation (Anderson, 1987, Andreotti, 2004). Saltation is the hopping motion of grains over long trajectories which, when they collide with a sand bed, results in a splash of shorter reptation trajectories. Reptation causes ripple migration,whereas both processes contribute to dune advancement. The reptation sand flux is estimated by multiplying the ripples' migration rate by their average height, h_r, estimated to be $20 \pm 6\,\mathrm{cm}$ (Supplementary Information). Assuming the reptation sand flux equals that of the whole dune, the dune migration rate is $d_r h_r/(h_D t)$ (Supplementary Information),where t is the time interval (105 days). The histogram of dune migration rates over the whole study area peaks at an average value of $\sim 0.1\,\mathrm{m/yr}$ (Earth year) (Fig. 4.3). This distribution is consistent with the dune speeds derived from linear fits to the selected ripple profiles of Figure 4.2, which range from 0.03 ± 0.01 to $0.27 \pm 0.08\,\mathrm{m/yr}$ (Fig. 4.3). The relative uncertainty in dune migration rate derived from these measurements is estimated to be less than 20% (Fig. 4.3, inset table); however, this is a minimum estimate because the saltation sand flux contribution is not yet considered. Extrapolating the dune migration rates derived from lee-front advancement to a year shows that the lee-derived rates are approximately five times larger than the ripple-derived rates (Fig. 4.3). The higher values reflect the contribution of the saltation sand flux, which is not considered in the ripple-derived rates.

4.3 Earth - Mars sand flux comparison

Comparison with terrestrial dunes (Fig. 4.4), shows that the Nili migration rates are about 1–2 orders of magnitude slower than for dunes of comparable height on Earth. Multiplying the dune migration rates by their maximum heights ($h_{D_{max}}$) gives sand fluxes at the dune crests: $Q_0 = d_D h_{D_{max}}/t$ where d_D is the dune displacement (Vermeesch and Drake, 2008). Mean fluxes for reptation and reptation plus saltation are 1.4 and $6.9\,m^3\,m^{-1}\,yr^{-1}$, respectively (Fig. 4.4). This is comparable to sand fluxes for dunes in Victoria Valley, Antarctica (Bourke et al., 2009). Terrestrial studies show that bulk and interdune sand fluxes are about one-third of the crest flux (Ould Ahmedou et al., 2007), so that typical fluxes in Nili should be $\sim 2.3\,m^3\,m^{-1}\,yr^{-1}$. The Nili dunes have $\sim 1,000$ times the volume of those in Victoria Valley, yet similar sand fluxes, indicating that the characteristic timescales of formation are $\sim 1,000$ times longer, showing that dunes on Mars evolve much more slowly than their counterparts on Earth. The timescale associated with the formation and evolution of the Nili Patera dune field, estimated by dividing the dunes' volume by the average sand flux times the length scale of the dune field, is $\sim 9,800\,\mathrm{yr}$. Similarly, turnover times needed for dunes to migrate over a distance equal to their length are very short,ranging from $\sim 170\,\mathrm{yr}$ for the fastest dune (Fig. 4.1a, dune c) to a few thousand years for the slower ones.

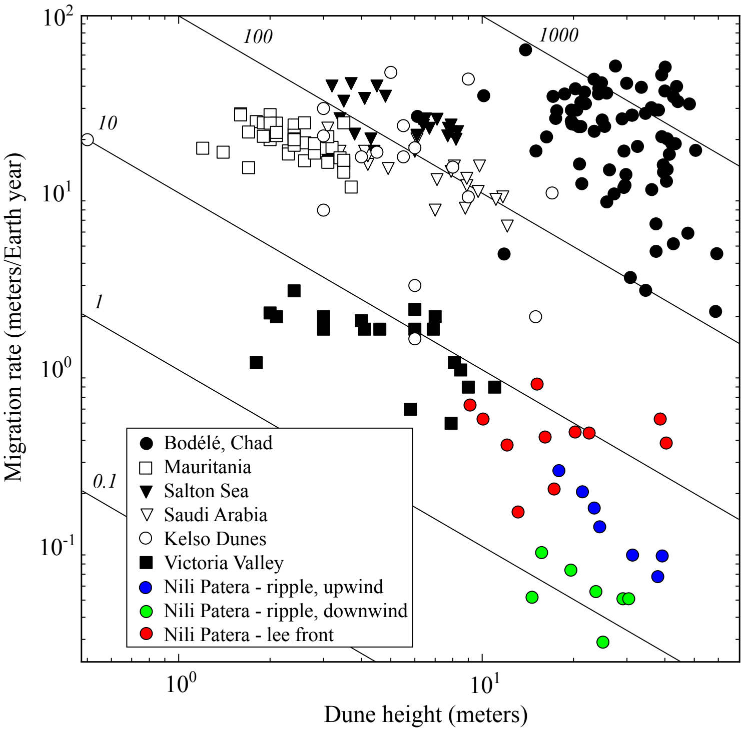

FIGURE 4.4: **Comparison of dune migration rates and sand flux on Mars and Earth.** Dune migration rates versus dune height for a number of sites on Earth (with reference numbers in parentheses); the 14 dunes selected in Figure 4.2; and dunes for which the lee-front advance was measured (locations in Fig. 4.1a). Black diagonal lines are isopleths of sand flux. Red and blue/green diagonal lines are mean sand fluxes derived from the lee-front advance and ripple migration measurements, respectively. Vertical error bars show 1σ (1 standard deviation) confidence intervals for the dune migration rates. The mean sand flux derived from the lee-front advance is 6.9 ± 0.52 (1σ) $m^3/m/yr$, and the mean sand flux derived from the ripple migration measurements is $1.4{\pm}0.08\,m^3/m/yr$. (See Supplementary Table 2 for individual measurements.) The factor of five between the two fluxes suggests that the saltation flux is about four times the reptation flux.

The observed correlation between ripple and dune displacement implies that the entire volume of the dunes is composed of mobile sand. The alternative, a mobile rippled skin over an indurated sand core, cannot be maintained for long time periods and is therefore improbable.The measured ripple reptation flux implies a rapid erosion rate of $\sim 0.01\,\mathrm{m/yr}$ (mean dune speed of $0.1\,\mathrm{m/yr}$, multiplied by the tangent of the average stoss slope (6°)). In the absence of a net influx from saltation to compensate for this erosion, the dunes would erode very rapidly. Because saltation drives reptation, the two processes scale (Anderson, 1987, Andreotti, 2004), so that saltation flux should increase up the stoss slope in proportion to the reptation flux. This implies dune erosion as great as $0.05\,\mathrm{m/yr}$. Such a rapid rate would quickly erode any mobile sand layer and expose the indurated core, effectively shutting off subsequent ripple migration. In this picture, the Nili ripple migration rates and patterns would represent a very short time window (maximum duration of the order of the turnover time — a few hundred to a few thousand years) following the formation of an immobile dune core. Finding the dunes in this rare state seems very improbable. More likely is that erosion of the stoss slope is compensated by deposition on the lee front, resulting in whole dune migration and complete recycling of the entire dune volume.

4.4 Some interpretations. . .

These results demonstrate that conditions in Nili Patera, and probably over much of Mars, are sufficient to move large dunes and transport fluxes of sand equivalent to those on Earth. This is in contrast to predictions from the Ames General Circulation Model (GCM) (Haberle et al., 2003) that threshold wind speeds sufficient to move sand at Nili Patera should not occur. The spatial resolution of GCMs is insufficient to resolve boundary-layer turbulence that may cause gusts above threshold (Fenton and Michaels, 2010). Even mesoscale simulations need a spatial resolution of kilometres to a few hundred metres to properly model the atmospheric turbulence that accounts for topography and thermal contrasts at the scales of individual dunes (Fenton et al., 2005, Spiga and Forget, 2009). The work exemplified in this study can be applied to other regions of Mars, thereby providing ground calibrations for GCMs and mesoscale models, and descriptions of small-scale atmospheric turbulence.

The occurrence of such large sand fluxes, despite the limited winds in Mars' low-density atmosphere (Arvidson et al., 1983, Haberle et al., 2003), is probably related to fundamental differences in how sand is mobilized by the wind on Mars compared to Earth. Although saltation due to aerodynamic shear at fluid threshold is required to initiate grain motion, once started, the sand ejection resulting from grain impact is the major contributor to the particle flux. On Earth, this results in the wind speed required to maintain saltation being about 80% that required for initiation (Bagnold, RA, 1954). But because of the higher and longer saltation trajectories on Mars, grains are accelerated to a greater fraction of the wind speed than on Earth,resulting in impact threshold speeds that are only about 10% of the fluid threshold, equivalent in magnitude to that on Earth (Kok, 2010). Thus, once saltation is initiated by low-frequency gusts, moderate wind speeds can maintain significant fluxes of sand.

4.5 Erosion potential

To assess the derived sand fluxes in regard to landscape modification, we consider the abrasion susceptibility, S_a, defined as the mass of sand required to erode a unit mass of rock. For basalt grains striking basaltic rocks at the impact threshold for Mars, $S_a = 2 \times 10^{-6}$ (Greeley et al., 1982). The average flux of $2.3\, m^3\, m^{-1}\, yr^{-1}$ implies that for the saltation trajectories of $0.1 - 0.5\, m$ that are likely on Mars (Kok, 2010), the abrasion rate would be $\sim$ 1–10 $\mu m\, yr^{-1}$ on flat ground, and $\sim$ 10–50 $\mu m\, yr^{-1}$ for a vertical rock face (see Supplementary Information), spanning field measurements of basalt abrasion rates in Victoria Valley of $\sim$ 30–50 $\mu m\, yr^{-1}$ (Malin, 1986).

4.6 Conclusion

One view of Mars has been that conditions since the end of the Hesperian period ($1.8 - 3.5\, Gyr$ ago) have been fairly static, with very low erosion rates (Golombek et al., 2006). This study shows that this is not the case at Nili Patera, and probably not at other areas of Mars where there are significant gusts of sand and wind. This may explain why vast areas of the Martian surface show evidence of erosion and removal, including of mantle materials for which the processes and agents of exhumation have been a mystery (Malin and Edgett, 2001), yet also contain fields of large dunes that migrate at relatively slow rates. Over long time periods, it may be that much or all of Mars has been subjected to large sand fluxes, with associated erosional modification of the landscape. The techniques reported here can be applied to many dunes and other slowly changing features on Mars and Earth, allowing sand flux and landscape modification to be assessed in a variety of terrains, latitudes, seasons and climates.

Chapter 5

Threshold for sand mobility on Mars calibrated from seasonal variations of sand flux

François Ayoub[1], Jean-Philippe Avouac[1], Claire E. Newman[2], Mark I. Richardson[2], Antoine Lucas[1], Sébastien Leprince[1], Nathan T. Bridges[3]

[1]Division of Geological and Planetary Sciences, Caltech, California, U.S.A.
[2]Ashima Research, California, U.S.A.
[3]Space Dept., Johns Hopkins Univ. Applied Physics Laboratory, Maryland, U.S.A.

Foreword - The results obtained in chapter 4 incited the HiRISE PI to scheduled a time-series acquistions over Nili Patera covering one Mars year. This new dataset allowed us to carry the study presented in this chapter in collaboration with Ashima Research. My contribution was centered on the seasonal flux measurement from the image time-series and the shear stress threshold estimation from the wind simulation. C. Newman and M. Richardson provided the simulated sand flux from a GCM. In addition to Nili Patera dune field, some other dune

fields have been since the target for monitoring with COSI-Corr. This work is referenced as Ayoub et al. (2014).

5.1 Introduction

Coupling between surface winds and saltation is a fundamental factor governing geological activity and climate on Mars. Saltation of sand is crucial for both erosion of the surface and dust lifting into the atmosphere. Wind tunnel experiments along with measurements from surface meteorology stations and modeling of wind speeds suggest that winds should only rarely move sand on Mars. However, evidence for currently active dune migration has recently accumulated. Crucially, the frequency of sand-moving events and the implied threshold wind stresses for saltation have remained unknown. Here, we present detailed measurements over Nili Patera dune field based on HiRISE images, demonstrating that sand motion occurs daily throughout much of the year and that the resulting sand flux is strongly seasonal. Analysis of the seasonal sand flux variation suggests an effective threshold for sand motion for application to large scale model wind fields (1-100 km scale) of $\tau = 0.01 \pm 0.0015\, N/m^2$.

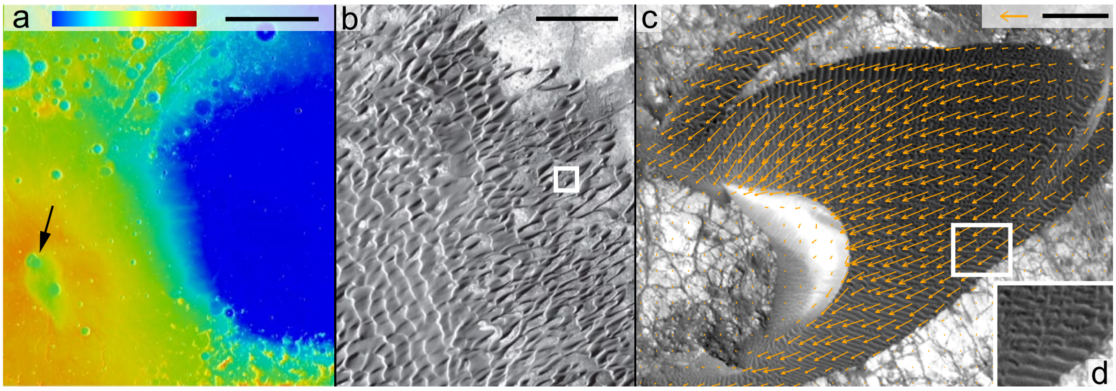

Figure 5.1: **Geographic setting and illustration of study area.** **(a)**, Location of the Nili Patera dune field ($8^\circ\, N$, $67^\circ\, W$) and surrounding topography (Elevation color scale $-4000\, m$ (blue) to $4000\, m$ (red), scale bar $400\, km$). The arrow points to the Nili Patera caldera that contains the Nili Patera dune field. Notice the large Isidis basin to the east (blue), and smooth topography between the basin rims and Nili Patera. **(b)**, CTX image of the Nili Patera dune front (scale bar $2\, km$). The white square indicates the location of panel c. **(c)**, HiRISE (ESP_018039_1890) close up view of a Nili Patera dune with vector field overlay of the ripple migration measured between two time-adjacent HiRISE images (arrow scale $50\, cm$, scale bar $50\, m$). **(d)**, Close-up view (black rectangle in (c)) of sand ripples.

Mars' current landscape and stratigraphic observations attest to the importance of aeolian processes in shaping the planet and building its sedimentary cover (Greeley, R and Iversen, JD, 1985, Grotzinger et al., 2005). Aeolian processes are known to dominate the current Martian climate through the modulation of atmospheric thermal forcing by suspended dust (Haberle et al., 1982, Moriyama, 1976, Strausberg et al., 2005, Wilson and Hamilton, 1996). However, the intensity of wind activity has been judged to be significantly lower than on Earth, such that recent evidence for currently active dune migration (Bridges et al., 2012b, Hansen et al., 2011, Silvestro et al., 2010) and measurements of Martian sand-fluxes comparable to terrestrial values (Bridges et al., 2012a) came as a surprise. Prevailing expectations based on wind tunnel experiments, theory for initiation of saltation, atmospheric modeling, and limited in situ wind measurements suggested that sand-moving winds should be very rare (Arvidson et al., 1983, Chojnacki et al., 2011, Haberle et al., 2003, Moore, 1985, Pollack et al., 1976, Sullivan et al., 2000). The apparent contradiction between rare implied saltation and reasonably common dust lifting (Newman et al., 2002, Szwast et al., 2006) remains unresolved but has variously been ascribed to the uncertainties in interparticle cohesion, the role of electrostatics, the role of gustiness, and the vertical wind shear and suction in dust devils (Kok and Renno, 2009, Newman et al., 2002). Indeed, a major dust storm occurred during the time period between the acquisitions of the two images analyzed in the Nili Patera HiRISE study (McCleese et al., 2010) allowing the possibility that anomalously high storm winds accounted for a significant fraction of the measured sand flux.

Quantitative interpretation of aeolian features and realistic dynamical modeling of the Martian dust cycle are impeded by the difficulty of transferring to Mars the semi-empirical laws of sand transport established for Earth and estimating the time-integrated effect of high speed winds based on dynamical simulations. An extra uncertainty for dust emission is the question of whether saltation of sand is the dominant mechanism for dust lifting. Saltation appears to be required, given that sand-sized particles ($\sim\ 100\,\mu m$) are significantly easier to mobilize than dust ($\sim 1\,\mu m$) under most reasonable assumptions regarding the interparticle cohesion of dust (particles larger than $100\,\mu m$ are also progressively harder to mobilize) (Greeley, R and Iversen, JD, 1985, Kok, 2010). The key parameter for sand motion is the effective stress threshold for saltation (Kok et al., 2012). When applied to wind stress output from an atmospheric model, the threshold determines the fraction of the year over which sand transport is active, the seasonal variation of sand fluxes and hence the annual erosive potential, and the seasonal evolution and magnitude of saltation-induced dust lifting. The latter factor yields a feedback loop in the Martian climate system as the mass of dust lofted modifies the atmospheric and surface thermal forcing (due to absorption/emission and shading, respectively), which in turn significantly modifies the strength of surface wind stresses. The identification of a stress threshold appropriate for use in mesoscale and general circulation models, which have computational grid scales of order 1 to 100 km (O[1-100 km]), is thus a crucial factor in simulating and thus better understanding the "steady-state" Martian dust cycle and the initiation and evolution of dust storms. The lack of viable constraints on the stress threshold in O[1-100 km] scale models creates a vast area of plausible domain space within which the dust cycle might be operating (Basu and Richardson, 2004, Kahre and Haberle, 2010), much of which ultimately will not be relevant to Mars.

We estimate an effective threshold from satellite-based observation of sand activity over an area of about 40 km^2. Sustained sand flux is observed throughout a Mars year, with strong seasonal variability. Wind simulations applied to a set of sand transport laws provide a predicted sand flux, which is compared to the measured sand flux. We determine the effective shear stress threshold that allows the predicted sand flux to best reproduce the measured sand flux variations. The threshold, estimated at around $\tau = 0.01 \pm 0.0015\, N/m^2$, is an effective threshold relevant for mesoscale and general circulation modeling in the O[1-100 km] scale range for which the turbulent characteristic of the wind is not resolved (though in such models the amount of turbulence, and its impact on surface exchange of momentum and mixing within the boundary layer, are typically parametrized in some manner).

5.2 Results

5.2.1 Seasonal sand flux measurement

In this study, we examine a time-series of HiRISE images (McEwen et al., 2010) of the Nili Patera dune field ($8.8°\, N$, $67.3°\, E$) over the course of a Mars year to determine the seasonal distribution of sand transport. The barchanoid dune field sits in Nili Patera, a 55 km diameter, $\sim$ 2 km deep caldera at the top of Syrtis Major, a 1000 $\times$ 1500 km wide shield volcano lying a maximum of $\sim$ 6 km above the neighboring Isidis Planitia basin (Isidis) to the east. The dune field covers an area of approximately 200 km^2 and is located 500 km west of Isidis (Fig 1). The HiRISE imager aboard the Mars Reconnaissance Orbiter acquired a time-series of nine optical images (see Supplementary Tab. 1) at 25 cm pixel scale during Mars Year (MY) 30 (2010-2011), which cover an area of $\sim 43\,\mathrm{km}^2$ at the eastern (upwind) edge of the dune field. The resolution of the imagery allows observation of ripples that cover the dune surfaces. The sand ripple migration is measured with a precision of a few centimeters from the precise registration and cross-correlation of pairs of successive images using the Co-registration of Optically Sensed Images and Correlation (COSI-Corr) methodology (Leprince et al., 2007). For each pair of images, a "difference" image is constructed that represents the magnitude of ripple migration during the analyzed time interval. We apply a principal component-based analysis which takes into account the uncertainties assigned to each local measurement, and which produces a time-series of ripple migration images with non-correlated noise filtered out (see Methods). We estimate the average sand flux over each time interval based on ripple migration (Moriyama, 1976). The total sand flux, q, scales with the ripple migration sand flux, q_r, as $q \sim q_r^{1.2}$ (Andreotti, 2004). Our results show a sustained sand flux throughout the year with a strong seasonal variation: during the southern summer period, which includes perihelion (time of closest approach to the Sun), the flux is about three times larger than during the northern summer (Fig. 2). The sand flux measured over a 3 month period in the northern winter of MY28 (2007) (Bridges et al., 2012a) is comparable, though about 30% lower, to the winter values obtained for MY30 in this study. We measure only the space- and time-averaged values within each period separating each data acquisition, although a glimpse of the stochasticity of sand-moving winds can be inferred, as follows. All the analyzed pairs show evidence of significant ripple migration, even two pairs of images taken only 17 or 16 days apart (corresponding to the periods with planetocentric solar longitude (Ls) $= 322 - 332°$ and Ls $332 - 340°$, respectively). Over these two consecutive periods the average flux is different by a factor of two, suggesting that while sand-moving wind events were probably numerous during both of these short time periods, the variability in frequency, duration, and/or strength of these winds must have been large. However, the south-westward direction of the flux, indicated by the migration direction of the sand ripples, is stable over the year (see Supplementary Tab. 1), indicating a fairly constant direction of sand-moving winds.

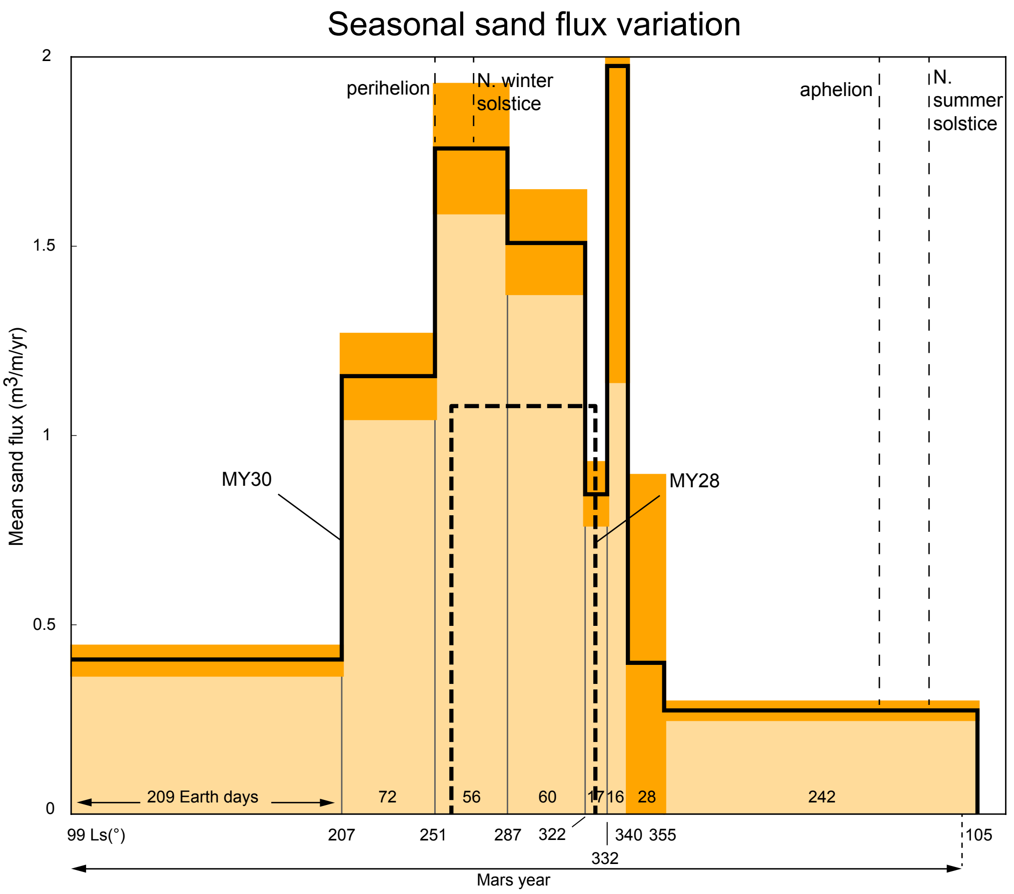

FIGURE 5.2: **Mean sand flux over Nili Patera as a function of solar longitude.** The sand flux is derived from measuring ripples migration from the correlation of HiRISE images in MY30 (2010-2011) using COSI-Corr (see Methods). We estimate a mean sand flux for each period separating the dates of acquisition of two successive images (acquisition date is given in solar longitude (Ls) along the x-axis). 1-σ errors of the flux due mainly to acquisition geometric artifact are displayed in dark orange. The sustained sand flux throughout the year, and the significant values obtained over periods of only 16-17 days, suggest that sand-moving winds probably occur daily. The flux is about three times larger in northern winter than in northern summer. The dashed histogram represents the mean sand flux, averaged over the same area, measured in MY28 (2007) (Bridges et al., 2012b). The flux in MY28 is smaller than in MY30, probably due to the effect of the large global dust storm which occurred this year between the two acquisition times. The increased atmosphere opacity would have reduced the effect of Isidis basin on slope flow, resulting in weaker diurnal winds at Nili Patera.

5.2.2 Climate situation at Nili Patera

Atmospheric models on various scales show that the circulation at Nili Patera is dominated by a combination of the tropical-mean overturning ("Hadley") circulation, thermal tides, and slope flows associated with the dichotomy boundary and the Isidis basin (Fenton and Richardson, 2001, Greeley et al., 1993, Rafkin et al., 2004, Toigo et al., 2012). Nili Patera is located roughly 9° North of the equator within the seasonally-reversing Hadley circulation. During northern summer, the intertropical convergence zone (the location of mean upwelling in the Hadley circulation) is displaced northward of Nili Patera. The cross-equatorial surface expression of this cell (the "monsoonal" circulation) curves due to planetary rotation yielding mean north-eastward winds at the latitude of Nili Patera. This flow reverses in southern summer, generating south-westward winds. A significant thermal tide (Wilson and Hamilton, 1996) is superposed on the monsoonal flow, yielding major daily variations of wind speed and direction, with the latter rotating over a full cycle during the day. Finally, the daily solar heating of the surface in the presence of the dichotomy boundary and the Isidis impact basin yields strong daytime winds that blow up the rim of the basin and then flow radially outward for hundreds of kilometers, contributing west-south-westward winds to the circulation at Nili Patera (Fig. 1). By contrast, nighttime flow down the Isidis rim does not significantly influence Nili Patera flows.

We observe that ripple migration occurs throughout the year, and remarkably keeps a south-westward direction, suggesting that sand-moving winds are most likely dominated by the daily flows running outward over the southern highlands from the Isidis basin rim. The peak speed of these winds varies over the year due to the variation of solar heating of the surface with season that is produced for Mars's current orbital configuration (specifically its obliquity and eccentricity). In southern summer the background winds of the Hadley circulation also blow toward the south-west, reinforcing the Isidis basin topographic forcing. The lower sand flux in MY28 compared to MY30 at the same time of year (Fig. 2) additionally suggests that the global dust storm of MY28 may have inhibited sand transport. Observations from the Martian surface during the 1977a and b dust storms show that increased atmospheric opacity during storms reduces the solar heating of the surface. The MY28 storm is thus likely to have damped buoyancy slope winds at Isidis in that year.

5.2.3 Wind shear stress threshold constrain

We use the observed seasonal evolution of the sand flux to estimate an effective wind stress threshold. To do so, we simulate the seasonal evolution of sand flux using a numerical atmospheric model, and adjust the stress threshold used in the sand flux equation such that the predicted seasonal flux variation matches the observed one. The physical validity of the model wind fields are tested to some degree via the demand that — for some choice of threshold — they fit the evolution of the sand flux throughout the year.

Our numerical modeling of the wind field uses the MarsWRF (Richardson et al., 2007, Toigo et al., 2012) system, a multiscale, nonhydrostatic Mars atmospheric model based on the NCAR Weather Research and Forecast (WRF) system (Skamarock and Klemp, 2008). The model was sampled in seasonal windows over the annual cycle, with near-surface winds, densities, and wind stresses output every Martian minute ($1/1440^{\text{th}}$ of a Martian day or sol; see also Methods) on a grid spacing scale of 120 km (O[120 km]). We also run a mesoscale model on a scale of O[1.5 km], not continuously through the year because of the massive computing time that would involve, but for periods of $\sim 5 - 10$ continuous days, every 30° Ls. We find that the two models yield similar output (see Supplementary Fig. 1), which suggests that the winds captured by the O[120 km] simulation dominate even in the presence of more local flows. We therefore infer that — whereas the seasonal variation of sand flux predicted by the model is very sensitive to the choice of wind stress threshold — the stress threshold for scales O[1-100 km] should be consistent with the one defined from the O[120 km] scale; we assume so for the rest of the study.

A variety of sand transport laws have been proposed which relate the sand flux to the wind stress, τ, in excess of some threshold wind stress, τ_s, which is the minimal threshold shear stress required to sustain transport, once initiated. Most agree that sand flux scales between the square and the cube of the frictional velocity ($u^* = \sqrt{\tau/\rho}$). To investigate the sensitivity of our analysis to the chosen law, we predict the sand flux, q, using six different equations (see Methods).

Figure 3 shows the seasonal evolution of sand flux predicted at O[120 km] for the 6 sand flux formulations, and for 5 of the 25 values of the stress threshold examined in this study. The most noticeable aspects of these results are the similarity of the predicted sediment fluxes between the four transport laws tested, and that a strong seasonal variation is predicted in all cases. However, the observed ratio of the summer to winter sand flux is globally reproduced in the predictions for only a limited range of threshold stresses. If the threshold is larger than $0.015\,N/m^2$, the predicted summer flux drops to nearly zero and the predicted ratio of winter to summer sand flux is significantly too large. Conversely, if the stress threshold is smaller than 0.05 N/m^2, the predicted ratio of winter to summer sand flux is too small, less than half the ratio observed. The correlation is generally good, with the exception of the two shortest periods (Ls $322 - 355°$ and Ls $355 - 105°$), possibly due to uncertainties in the measurements or to the stochastic nature of the sand-moving winds as discussed above. The shear stress threshold for sand motion is thus estimated to be for simulation at a grid scale of O[1-100 km] (Fig.4).

5.3 Discussions

We note that the effective threshold value is in between the impact thresholds determined from simulations, 0.003 N/m^2 (Kok, 2010) and 0.02 N/m^2 (Almeida et al., 2008), and much below the fluid threshold estimated at about 0.008 N/m^2 (Iversen and White, 1982). However, the significance of this similarity is unclear as the impact thresholds are defined from high resolution turbulence resolving models, whereas the effective threshold in this study is defined from non-resolving turbulence large scale simulations. The value of stress threshold inferred should be interpreted as the effective threshold, that is a unique threshold for initiation and sustenance of sand flux, for the instantaneous mean wind over scales from kilometers to a few degrees. This threshold is much lower than would be expected for turbulence-resolving models, wind tunnel experiments, or lander-based local in situ observations (Greeley, R and Iversen, JD, 1985, McCleese et al., 2010). Large scale models do not resolve boundary layer turbulence (on scales O[1-1000 m]) and hence do not simulate gust distributions superposed upon the area-mean winds. However, the estimation of the area average of the unresolved eddy wind stresses (the coherent net effect of "gustiness") is a critical component of the surface layer parameterization included within global and mesoscale models, as realistic surface sources and sinks of angular momentum are needed to generate the observed large-scale circulation. Since turbulent gusts represent a distribution about the mean wind speed, there is a monotonic relationship between the area mean wind stress threshold and the local instantaneous value. Further, the consistency over the Nili dune field over an area O[100 km^2] and the barchanoid nature of the dunes suggest that the dunes form under strong mean winds and that the dune field is not dominated by the structure of the O[1-1000 m] wind field. As such, the stress threshold estimated from the Nili observations is inherently the O[1-100 km] threshold that would result in a distribution of wind stresses such that some fraction of this distribution is above the local stress threshold for grain motion. This study does not address the nature of the mapping from O[1-100 km] scales to the local scale (O[1-1000 m]), and it should be noted that this mapping may vary spatially with factors such as the interparticle cohesion, grain size or surface roughness. However, the estimation of the O[1-100 km] threshold stresses estimated here is relevant to estimate dust lifting, sand motion, dune formation, and aeolian erosion based global and mesoscale models.

5.4 Methods

5.4.1 Image processing

All images were provided by the USGS in a radiometrically calibrated format ("balance cube"). Each image came in the form of 10 stripes corresponding to each of the CCD array in the broadband "red" channel. The stripes were processed using the USGS recommended procedure with ISIS. The process stitches back the CCD stripes while accounting for any geometric distortions in order to provide a reconstructed, distortion-free, full image. Camera and orbital geometries were extracted from the SPICE kernels and imported into COSI-Corr along with the images. In addition to the nine images, a stereoscopic pair was acquired at the beginning of the time series to extract a 1m post-spacing Digital Elevation Model (DEM) of the dune field. The second image of the stereoscopic pair is the first image of the time series. The topography was extracted using BAE SOCET SET® software. Using COSI-Corr, all the images were registered to the first image of the time series, which warrants a perfect registration of the first image to the DEM by construction. Approximately 25 tie-points were selected between the first image and each image of the time series. The tie-points were the same for all images, except where footprint differences prevented it, in which case the tie points were relocated inside the overlap of the two images. All the tie-points were located on the bedrock, away from the dunes. The tie-points accuracy was optimized with COSI-Corr using a 256 × 256 pixels window size. The average misregistration at the tie-point locations of the resulting registered pair of images are on the order of few millimeters, with a standard deviation of around 25 cm (see Supplementary Tab. 1). Most of the registration residual comes from unrecorded jitter of MRO during image acquisition, and residual in the CCD arrays relative orientations. Images were then orthorectified with COSI-Corr on the same 25 cm resolution grid, using the optimized set of tie-points, the DEM, and the ancillary data. Pairs of time-adjacent images were correlated with COSI-Corr using a sliding window of 70 × 70 pixels (17.5 × 17.5 m) and a step of 16 pixels (4 m).

5.4.2 Bias in ripple migration maps due to DEM error

DEM extraction using a stereoscopic pair of images relies on feature tracking and measurement of feature shift due to the parallax. An underlying assumption to reconstruct a DEM is the stability of the scene between the images' acquisitions. Indeed, to recover an accurate topography model, parallax is ideally due to topography only, and not to the topography augmented with a physical shift of the terrain. In this study, the DEM extraction on dunes tracks the ripples features to estimate the dune height. Ripples migration between the acquisitions, if any, will therefore bias the overall dune height. To estimate the bias on the ultimate ripple migration maps due to a potentially biased DEM, we estimated the error in elevation assuming a ripple migration based on the first measurement map. Using this estimated DEM error, we estimated its contribution on all the migration maps by taking into account the stereoscopic angle between each image pairs of the time series. Ripple migration linearly scales with the elevation of the dune(Bridges et al., 2012a), such that the error in elevation will linearly scale with the dune elevation. We estimate the maximum, average, and standard deviation of the dune elevation error to be respectively 77, 26, and 14 cm. The DEM error contribution to the subsequent ripple migration maps is listed in C.1, but overall the error is small, about few centimeters, with a maximum of around 20 cm in the worst case (pair 21652–22364 with a stereoscopic angle of 17°.

5.4.3 Bias in ripple migration maps due to the use of a unique DEM

The DEM was generated at the beginning of the time series. The first image is actually part of the stereo pair that was used to extract the topography. The last image of the time series was acquired 700 days after. In the meantime, dunes migrate, such that using a unique DEM may cause a misalignment of dunes with the images. In Bridges et al. (2012a), dune migration speed was estimated to around 1 m/yr for the fastest dunes. According to the DEM, the slopes of the dunes' stoss slopes in the "axial" direction are 4–8°. Assuming a dune displacement of 2 m (in 700 days) and a static morphology and height over this time scale, an error of around 28 cm in elevation would be introduced, which would contribute to a maximum of around 8 cm in ripple migration estimation in the worst case (pair 21652–22364 with a stereoscopic angle of 17°).

Overall, geometric errors due to 1) stability of the ripple between the stereopair acquisition, and 2) stability of the dunes during the time-series timespan, can be neglected in view of the measured ripple displacements (∼meters).

5.4.4 Jitter and CCD induced mis-registration

Unrecorded spacecraft jitter during image acquisition causes distortions in the imagery that are not corrected during the orthorectification. These geometric distortions are recovered in the subsequent correlation maps as erroneous "displacements". As seen in Figures C.2 and C.3, geometric distortions (most visible on the bedrock area) can be observed in the cross and along-track directions. The cross-track undulations are a direct effect of the jitter and the along-track stripes are caused by the effect of the jitter on the staggered CCD arrays. Collectively, these jitter and CCD artifact (jitter/CCD artifacts) account for up to 1–2 pixels (25–50 cm), and are the largest source of error in the ripple migration estimation. This source of error is accounted for in the weighted linear regression between predicted and measured fluxes (See Methods 5.4.9).

5.4.5 Principal Component Analysis

A principal component analysis (PCA) was applied to the time-series in order to filter out measurement noise and to extract the main signal from the data. In practice, we used a weighted low rank approximation of the covariance matrix to account for the missing values (decorrelated pixels), and different noise amplitude between the maps. Noise amplitude between maps can vary due to the irregular time sampling of the acquisitions which leads to different shadowing effects and temporal changes. We used an adapted version of PCAIM (Kositsky and Avouac, 2010), giving each map a weight inversely proportional to the number of decorrelated points in the dataset. The assumption is that a map containing a large number of decorrelated points is a noisier measurement map. Prior to computing the PCA, all displacement maps were time normalized, to account for the unequal time span between pairs. The chi-square measurement indicates that the first two components of the PCA accounts for 84% and 82% of the time-series variance, of the East/West and North/South displacement maps respectively.

5.4.6 Estimates of ripple height

The DEM cannot distinguish ripple topography, so we had to assume a standard ripple height. We used the ripple height of 40 cm defined in Bridges et al. (2012a). Visual observation of the ripple shape shows a stable ripple wavelength in time and space (except at the very base of the dune where ripples nucleate and grow to stable state). This wavelength stability suggests a stable ripple height over time and space as well. Therefore, because ripple height is not time dependent, and because we are interested in the relative variation of the flux only, the ripple height actual value does not play a role during the linear regression between predicted and measured sand flux. Ripple height would play a definite role if we were to estimate the absolute sand flux quantity however.

5.4.7 Sand flux estimation

The ripple displacement maps were reconstructed (see Supplementary Fig. 4-11) using the first two components of the PCA (see Supplementary Fig.2,3). The migration azimuth of the ripple is quite stable throughout the year (see Supplementary Tab. 1), and is around 115° from North counter-clockwise. This azimuth corresponds also to the azimuth found in Bridges et al. (2012a). The scattered azimuth distribution for pair 23564-23920 is due to strong un-modeled satellite jitter. To limit the jitter bias in the estimation of the sand flux, the ripple displacements are projected onto the main migration direction, and the average sand flux was estimated for each map using the method described in Bridges et al. (2012a). Because the displacement maps are co-registered, and because we used the reconstructed maps, the exact same pixels, in location and amount, were used to compute the average reptation sand flux of each displacement map of the time-series. Note that the sand flux estimated on every point on the dune scales linearly with the height of the dune (Bridges et al., 2012a), that is, for a given dune, sand flux will vary from approximately no sand flux (base) to a maximum (crest). The average flux computed in this study differs from the traditional ways of quantifying sand flux, e.g., at the crest, area based, but is relevant for the temporal evolution analysis.

5.4.8 GCM and mesoscale simulations

The MarsWRF model (Richardson et al., 2007, Toigo et al., 2012) was run at 2° global grid spacing, with four levels of interactive nests used to increase the resolution over the Nili Patera region. Each embedded domain contained 120×120 grid points, and had a factor of three refinement of the grid (i.e., produced a three-fold increase in resolution), resulting in a grid spacing of ~ 1.5 km in the innermost nest, centered on the Nili Patera caldera.

MarsWRF, as run for this study, used surface boundary conditions from the 1/64th degree MOLA topographic map, $\frac{1}{2}$ degree MOLA roughness map, and MGS TES-derived albedo and thermal inertia maps (Toigo et al., 2012). The simulation used the 2-stream "KDM" radiative transfer model, treating CO_2 and dust radiative heating (Mischna et al., 2012) and the MRFPBL boundary layer scheme. The dust distribution was defined using the Mars Climate Database "MGS" dust scenario. The model includes a full carbon dioxide cycle that produces a roughly 30% variation of atmospheric mass over a Mars year. The cycle is calibrated with respect to the multi-year Viking lander pressure datasets (Toigo et al., 2012).

The GCM 2° output used in this study was taken from the last year of a multiyear run. The output (drag velocity, air density and vector winds near the surface) was sampled every Martian minute ($1/1440^{\text{th}}$ of a Mars day or Sol) over the whole year. Mesoscale simulations were not run for the whole year, but were sampled every minute for ~ 10 Sols over intervals starting at Ls=0° and every 30° of Ls thereafter. Each mesoscale simulation was initialized using output at the required Ls from the global 2° run, and the first 3 sols were discarded to avoid "spin-up" effects (see Supplementary Fig. 1).

5.4.9 Shear stress threshold estimation

The objective is to adjust the sand shear stress threshold used with the prediction of atmospheric simulations and a transport law, such that the predicted sand flux matches the observed sand flux (from the imagery). Using the GCM prediction of the wind shear, we tested a total of six transport laws to estimate the shear stress threshold for sustained transport, once initiated. Because we are matching the seasonal variation of flux (i.e., the relative flux, rather than the absolute magnitude of flux at a given time) the constants at the start of the equations are factored out:

$$\begin{aligned}
&q \propto \rho u^{*2}(u^* - u_t^*) && \text{(Lettau, K and Lettau, HH, 1978)}\\
&q \propto \rho(u^{*2} - u_t^{*2})^{1.2} && \text{(Werner, 1990)}\\
&q \propto \rho u_t^*(u^{*2} - u_t^{*2} && \text{(Duran et al., 2011)}\\
&q \propto \rho(u^{*3} - u_t^{*2}/u^*)(\alpha + \gamma u_t^*/u^* + \beta u_t^{*2}/u^{*2}) && \text{(Sorensen, 2004)}\\
&q \propto \rho u_t^*(u^* - u_t^*)^2 && \text{(Almeida et al., 2008)}\\
&q \propto \rho(u^* - u_t^*)(u^* + u_t^*)^2 && \text{(White, 1979)}
\end{aligned} \tag{5.1}$$

where u_t^* is the threshold velocity calculated from the atmospheric density, ρ, and stress threshold $\tau_s = \rho(u_t^*)^2$. Note that while the threshold is often stated in terms of the frictional velocity, as the latter is easier to measure, it is the shear stress that is of primary physical importance for the initiation of grain motion. We estimated the optimal shear stress threshold from the chi square analysis of the best fit (linear regression) between predicted and measured fluxes for a range of threshold values. Two main elements taken into account in the weighted linear regression are detailed below:

The measured sand flux represents only the reptation sand flux. However, the predicted sand flux from the simulations represents the total sand flux, which is composed of the reptation and saltation sand fluxes. (Andreotti, 2004) proposed that the reptation flux scales with u^{*2}, and that the total flux scales with $(u^{*2}–u_t^{*2})^{1.2}$, which is a relation also proposed by (Werner, 1990). We therefore assume the repton flux q_r to scale with the total flux q as $q \propto q_r^{1.2}$ for u^* above the threshold. This relation was accounted for during the estimation of the shear threshold, as the predicted sand flux from the simulations represents the total sand flux.

The larger source of flux measurement error is the jitter/CCD artifact (Methods - Jitter and CCD induced mis-registration), which we accounted for in the linear regression as follows. For each pair, the error from the jitter/CCD artifact on the estimated sand flux is quantified: the East/West and North/South displacement maps of the bedrock only (that is, no dunes) are projected on the main migration direction (115°). The average and variance of the "equivalent" sand flux is computed. In an artifact free setup, the average and variance of the resulting "equivalent" sand flux should be null. As expected, the average is close to zero as the satellite ancillary parameters are optimized such that the overall coregistration of the 25 tie points located on the bedrock is optimal. The variance however is not null (see Supplementary Tab. 1). Although the CCD/Jitter error is not uniformly distributed on the field area, the bedrock and dunes are sufficiently interlaced to consider the sand flux error estimated from the bedrock to correctly represent the sand flux error on the dunes. This error variance was used as a confidence weight on the measurement during the linear regression. Note, the jitter/CCD artifact does not depend on the time span between acquisitions. However, the resulting 'equivalent' sand flux does, and the larger the time span, the smaller the error on the measured sand flux.

The reduced Chi square curves have a minimum around 10, which indicates that some error sources, whether they originate from the measurement, the simulation or the transport law, are not properly accounted for. One source of error is the stochastic nature of wind events which cannot be captured in the simulations, but which are observed in the measurements with low time-span. To account for the error sources that are not captured, we increased the error on the measurement such that the resultant reduced Chi square falls to unity. The resulting probability density function gives us a conservative confidence level on the shear stress and are represented on Fig 4.

5.4.10 List of software used

SOCET-Set[1]: Commercial software provided by BAE Systems used for the DEM generation from stereogrammetry. We followed the procedure recommended by the

---

[1] www.baesystems.com

USGS (http://webgis.wr.usgs.gov/pigwad/tutorials). Along with the DEM, the two orthorectified images from the stereopairs were generated, and one of them was used as the reference to register the time-series to the topography.

ISIS[2]: Free, open source image processing software developed and provided by the USGS. This software was used to pre-process the raw HiRISE imagery into a format that can be handled by COSI-Corr. The ISIS processing also extract the metadata of the images (telemetry, camera geometry, satellite jitter) from the NASA SPICE kernels, and store them into an ascii file that can be read by COSI-Corr.

COSI-Corr[3]: Free, not open source software provided by Caltech and used to orthorectify, register, and correlate the image time-series. The output of COSI-Corr is the ripple displacement maps. The methodology used to process and generate these images is the one described in the User Guide. The HiRISE capability of COSI-Corr, developed by the authors of this study, will be part of the next COSI-Corr release.

PCAIM[4]: Free and open source software provided by Caltech. This software was used to compute the PCA on the HiRISE time series.

MarsWRF[5]: Free and open source atmospheric simulation software, developed and provided by Ashima Research (http://ashimaresearch.com/). The GCM and mesoscale simulations of the wind regime at Nili Patera were computed using MarsWRF with the parameters that are described in Methods - GCM and mesoscale simulations.

---

[2] http://isis.astrogeology.usgs.gov/

[3] http://tectonics.caltech.edu/slip_history/spot_coseis/

[4] http://tectonics.caltech.edu/resources/pcaim/

[5] http://planetwrf.com/

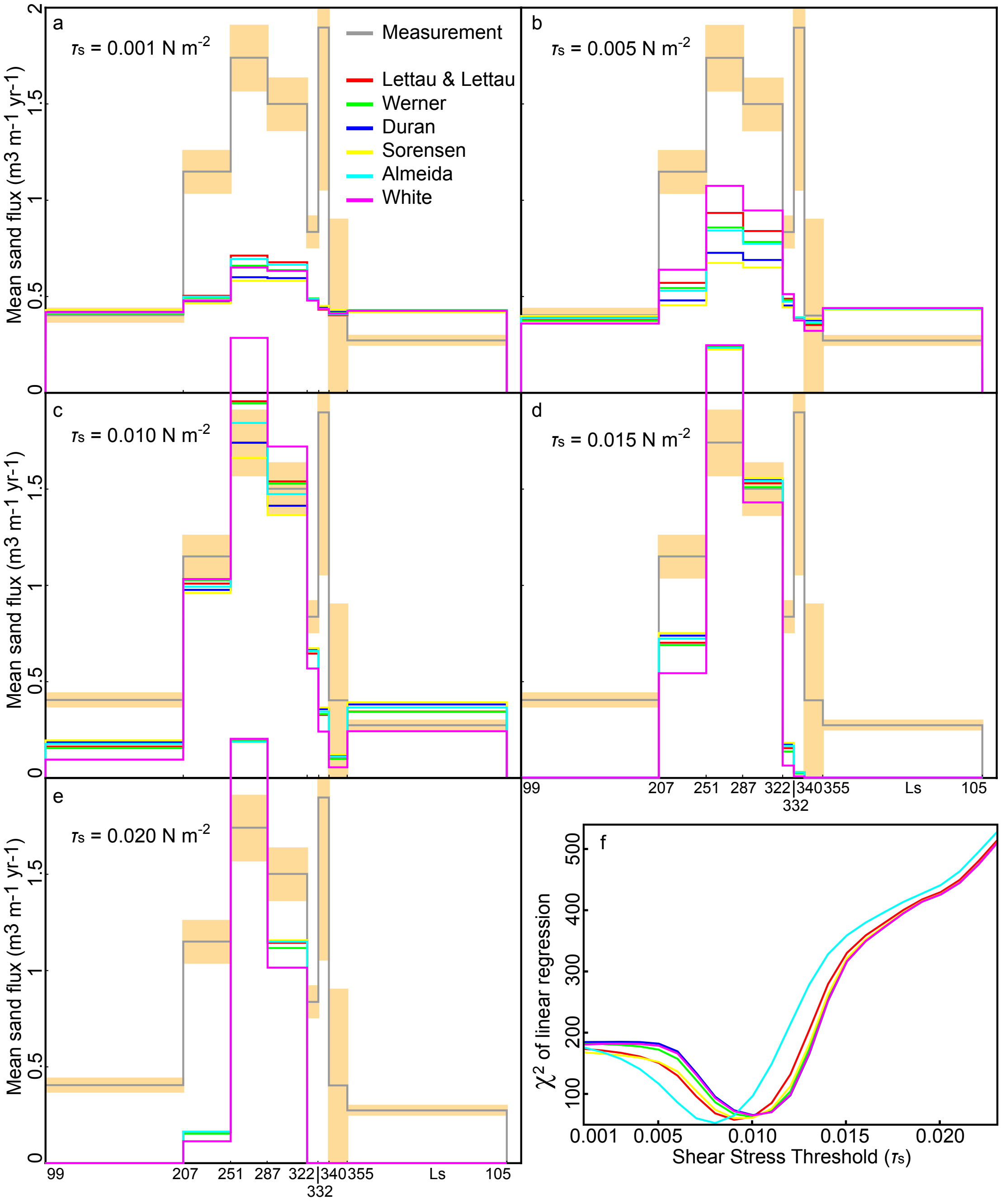

FIGURE 5.3: **Comparison of measured and predicted sand fluxes computed for different shear stress threshold.** Shear stress thresholds (τ_s) from 0.001 N/m^2 to 0.024 N/m^2 with a step of 0.001 N/m^2 were tested. Only five of these tests are represented here (a-e). The gray histogram and orange bars represent respectively the measured sand flux and its 1-σ error; the colored histograms represent the predicted sand fluxes computed from GCM wind output and four transport laws: equation 1 (red); equation 2 (green); equation 3 (blue); equation 4 (yellow, using $\alpha = 0$, $\beta = 3.0$, $\gamma = 2.1$ as proposed for a grain size of 170 μm (Kok et al., 2012)); equation 5 (cyan); equation 6 (magenta). Equation 4 has been also tested for grain size of 125, 242, and 320 μm, with threshold within 0.00005 N/m^2 of the threshold for grain size 170 μm. The colored plots are linearly scaled according to the linear regression between the predicted and measured fluxes. (f) displays the chi square of the linear regression for the set of threshold and transport laws tested. The best linear correlation minimum is obtained for a shear stress threshold between 0.008 and 0.01 N/m^2 depending on the transport law considered, indicating a weak sensitivity of the stress threshold to the transport law considered.

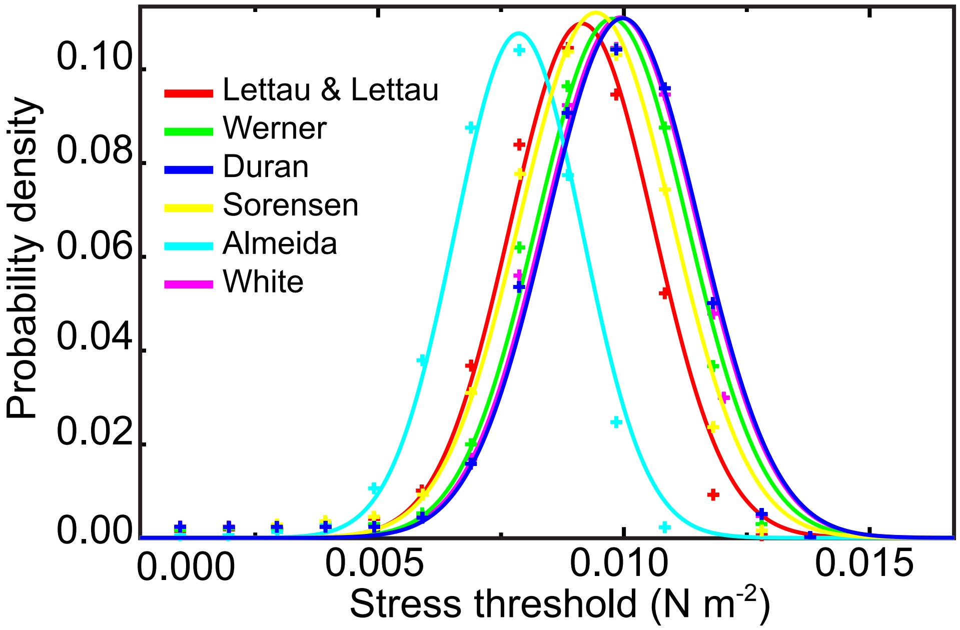

Figure 5.4: **Probability density function of the shear stress threshold for various transport laws.** The crosses are the Probability Density Function (PDF) at each of the threshold values tested; the continuous curves show best fitting Gaussian curves. The optimal threshold values and confidence level (at the 1-σ confidence level) are $0.009 \pm 0.00149\, N/m^2$, $0.0091 \pm 0.00146\, N/m^2$, $0.0098 \pm 0.00152\, N/m^2$, $0.01 \pm 0.00155\, N/m^2$, $0.0094 \pm 0.00155\, N/m^2$, $0.0079 \pm 0.00129\, N/m^2$ for equation 1 (red), equation 2 (green), equation 3 (blue), equation 4 (yellow), equation 5 (cyan), equation 6 (magenta), respectively. To account for all the un-modeled sources of error from the measurement, transport law, and atmospheric simulations, the sand flux measurements errors were scaled such that the reduced chi square of the linear regression falls to unity.

Conclusion

In this thesis we explored archive aerial images for Earth surface displacement measurement, and the monitoring of aeolian activity on Mars from satellite images. Although closely related in the remote sensing field as a whole, the objectives were sufficiently different to divide the conclusion in distinct sections.

5.5 Contributions to the aerial (frame) imagery

5.5.1 Methodological contributions

The work presented in chapter 1 proposes a framework, based on the proven satellite framework developed in COSI-Corr, to the processing of aerial (film-based frame) imagery for the measurement of surface displacement. Using traditional photogrammetry recommendations, specificities of aerial imagery were evaluated and accounted for. The extension of COSI-Corr framework to aerial imagery makes it possible to combine aerial and satellite imagery whether for cross-registration or cross-correlation. Processing of declassified space imagery was also developed. Only the frame system was considered[6]. In terms of processing it is similar to a very high aerial image, but necessitated some algorithmic adjustments to account for the Earth curvature. The main algorithms and post-processing tools such as the epipolar and perpendicular-epipolar projection used in Chapter 2 have been implemented into COSI-Corr.

The methodology has been successfully applied to the 1992, M_w 7.3 Landers, and 1999, M_w 7.1 earthquakes. The main surface rupture was mapped accurately, and the fault slip could be measured with limited uncertainty. Secondary and small

---

[6] Depending on the spy satellite mission, either frame or pushbroom-equivalent on a cylindrical focal plane systems were used.

surface ruptures of amplitude about 20 cm (1/5th of the native resolution), missed during the field reconnaissance (Sieh et al., 1993), were identified. The Hector Mine earthquake study demonstrated the possibilities and advantages of the simultaneous use of satellite and aerial imagery in situation of large, distributed surface displacement. The Krafla rift study is one of the most elaborate project using archive imagery that we worked on. Four datasets, two aerial imagery campaigns, one declassified spy imagery and one modern satellite imagery, all acquired at different periods ranging from 1957 to 2002, were processed to quantify the rift crisis opening while providing information on the event temporal sequences. This study demonstrates the benefits of archive imagery to document events which happened at a time when the ubiquitous satellites (GPS, optical, radar,. . .) were not available.

Overall, aerial imagery is a good complement to satellite imagery. First it augments the chance to find the necessary imagery to study a given process. This is particularly true for the revisit of past events or to extend time-series back in time. Aerial imagery can also be used jointly with satellite imagery. In case of spatially large process, the coarser resolution and larger footprint of satellite imagery can be used to monitor the full spatial extent of the process at a medium resolution, and capture the long wavelength of the surface displacement. The higher resolution and smaller footprint of aerial imagery can be used to “zoom” in an area of interest for finer details. Last, aerial imagery can be the only option for event that occurred before the satellite era or for surface displacements that are too small to be recovered by satellite imagery. The spatial resolution between satellite and aerial imagery has only been comparable since very recently. In the Krafla study presented in Chapter 2, the aerial imagery of 1957 was at a resolution of 60 cm/pix. This is to be put in perspective to the 80 m/pix that became available 15 years later in 1972, followed by 10 m/pix in 1986, to 1 m/pix in 2000 with satellite imagery.

5.5.2 Limitations

The use of archive aerial imagery for a surface process is still somewhat opportunistic. Not so much because of the processing technique but mostly because of the data itself.

Aerial imagery can be decades old. Films are subject to aging and storage conditions, which irremediably deteriorate the image quality. Whether geometric (film distortion), or radiometric (graininess, chemical instability, lost of radiometry), these defects reduce the overall measurement quality. Systematic digitization of aerial films, although a titanic endeavor, should be done as soon as possible with high qulity photogrammetric scanners. The USGS started systematic digitalization of their archives only few years ago, and is still an ongoing process. In addition to aging, film imagery lacks the radiometry depth that is offered with digital imagery, leading to occasional saturated acquisition campaigns.

High spatial resolution is both a blessing and a curse. High resolution captures small displacement and details out of reach with coarser resolution imagery. But at the same time, high resolution images are more subject to parallax effect, and require high resolution DEM to limit topographic residual in the displacement maps.If too strong, topographic residual can overcast the surface displacement signal[7].

The higher the resolution, the faster are the temporal changes. Aerial imagery is therefore sensitive to the time-span between the images to correlate. It also depends on the scene: remote, poorly vegetated, and unhabited areas are more stable in time than highly populated areas. The older are the acquisitions, the more likely they are "temporally" isolated, with higher chances to be too distant in time from the other dataset to compare with.

Limitations of the image footprint: Aerial image covers a footprint area much smaller than satellite image - usually about a few kilometers per side[8]. For large natural scenes such as earthquake, glacier, dune field, the size of the footprint can be a limitation. Either because the entire process is not covered by the imagery available, or because it would entails the processing of a large number of images with all the mosaicking artefacts that it would cause. The technique also relies on the presence of stable areas in the image footprint to co-register the images prior comparison; a small footprint may prevent that depending on the surface process at stake, as seen in Chapters 1 and 2.

The last but not least of the limitations is to know that the data exists and how to find it. Satellite imagery is highly centralized compared to aerial imagery. In

---

[7] Extraction of a high resolution DEM from the along-track and side aerial images can remedy the problem.

[8] This is not the case for the declassified imagery which have very large footprint.

a handful websites browsing, one can access the entire satellite imagery database. Aerial imagery is different. There are hundreds of acquisitions companies, which do not publicize their database content. The USGS, a federal agency, is digitizing their film-based imagery and makes them available, but there are other federal, state, and local agencies which have acquired (and still are) aerial imagery, but don't have a policy to publish their database content. Let alone that archive imagery has not been necessarily digitized and are still on films, in a storeroom, somewhere to be found, hopefully correctly stored and indexed, with the calibration report of the camera somewhere nearby. Depending on the area and country, it can become very challenging to obtain the data. Picture yourself trying to get the digitized films along with the camera calibration reports of an aerial photo campaign carried somewhere in Asia in 1967 by a mapping company that does not exist anymore! Definitively an arduous task than browsing a few online satellite database.

5.5.3 Looking forward

In this thesis we purposefully considered only archive, film-based imagery. As mentioned earlier, all the method proposed here are readily applicable to digital imagery. The only change would concern the Interior Orientation that would be slightly different (no film distortion, no fiducial points). Speaking about perspectives of aerial imagery, however, we need to look forward and consider modern, digital imagery. Some of the limitations mentioned in the previous paragraph still, somehow, hold for digital imagery. The aging of digital imagery is not a concern anymore, but the reduced footprint, high resolution parallax residual, and accessibility of the data are still a hinder.

Images resolution is getting higher and higher. High resolution, whether from satellite or aerial imagery, allows theoretically the monitoring of process of smaller amplitude. However, the limitation due to an under-resolved DEM becomes increases, such that it becomes unlikely that an approach consisting of comparing two multi-temporal images that have been orthorectified with an external DEM would work. Unless access to a very high resolution DEM is possible, which is rarely the case. An alternate approach would consist in the simultaneous solving of the topography and the surface displacement. The process would move from the comparison of multi-temporal acquisitions to the comparison of multi-temporal, *stereo* acquisitions, with two benefits: 1) mitigation of the DEM resolution limitation, and 2) measurement of the 3D surface displacement, as opposed to just the 2D-horizontal displacement. This approach is currently investigated in our group, emboldened by preliminary results obtained on a multi-temporal stereo imagery study on the Franz Joseph glacier in New Zealand (Leprince, 2013). The drawback of this approach is the stronger constrain on the data. Images have to be available in stereo. It is a limitation for satellite as stereo acquisitions are mostly on-demand only (default acquisition is monoscopic), but not so much for aerial imagery which is always acquired in multi-stereo with the along-track and side track overlap. Despite this constrain, it seems to be the only way to best use the very high resolution available today.

Regarding instrument and hardware, Unmanned Aerial Vehicles (UAVs) have been rapidly developing in the last years. A wide range of UAVs are available for imagery acquisition. The low costs of UAVs (few k$) and ease of use, bring the concept of “personal remote sensing” for a research group or even for a single researcher, concept unimaginable a decade ago. Imagery can be acquired at the desired spatial and temporal resolutions, with as much overlapping as desired. UAVs come with their share of limitations, the main ones being the smaller footprint that they can image, the low grade camera, and the need to be physically at the areas of interest to acquire the imagess. However, we shall see in the very close future the emergence of studies using UAVs.

In the context of measuring surface displacement, laser technology (aerial LIDAR) has been popularized over the last ten years. Oskin et al. (2012) used multi-temporal liDAR acquistion to map the 2010, M_w 7.2 El Mayor-Cucapah earthquake ground deformation. LIDAR acquistions are still airborne only, with no program of global coverage. The database is very sparse compared to optical imagery (satellite and aerial), but is being enriched at specific locations. Radar (SAR, InSAR) continues to be a well developed and popular technology for surface displacement measurement.

To wrap up about modern digital imagery in the context of measuring surface displacement such as earthquake ground deformation, glacier flux, landslides, sand dunes migration: Aerial imagery advantages and monopole have reduced thanks to the increase of satellite image resolution, the active development of airborne LiDAR acquisitions, and the development of affordable UAVs. One commonality between all these sources is the very high image resolution which necessitates the simultaneous surface displacement measurement and topography extraction.

5.6 Contributions to Martian eolian processes

The work on the Martian sand dunes presented in this thesis was the first COSI-Corr technique application on extra-terrestrial data, and the longer — in number of epochs — time-series that we have worked on so far. This type of study has not been done on Earth, and ironically, cannot be done on Earth easily. The sand activity monitoring was made possible thanks to the very high resolution of HiRISE imagery and the large size of the sand ripples laying on top of the dunes. On Earth, the size of the ripples are much smaller and migrate much faster which would require centrimetric resolution imagery and a temporal resolution of a couple of minutes! To cover an area similar to the area imaged on Mars, that would require an army of hovering UAVs taking pictures every few minutes. This is not an easy and cheap field experiment to set up. The tracking of the Mars beforms is therefore a new measurement type that opened up several research avenues.

5.6.1 Methodological and scientific contributions

Overall the methodological approach used in the processing of the HiRISE images is similar to the one used for Earth satellite imagery and described in (Leprince et al., 2007). The main technical contributions concern the implementation of the planetary imagery to COSI-Corr and development of methods to post-process this long time-series.

The processing of HiRISE imagery into COSI-Corr needed first the implementation of the camera geometry, that is, modelling of the camera geometry and accounting for the satellite telemetry. Second, initially developed for Earth, the software had to be re-engineered to accept other planetary bodies. As of now, Mars and the Moon have been implemented. Third, COSI-Corr was modified to ingest and process the large size of HiRISE images, which was not possible with the version at the beginning of the project. All of these updates have been fully implemented in COSI-Corr and are available the academic community.

Roughly at the time of the project start, and despite regular observed dust storms, a debate on the current Mars weather conditions was opposing proponents of a static, fossilized, landscape to proponents of active landscape dynamics. The advent of HiRISE and its very high resolution was a good opportunity to look at the dynamics of the aeolian bedforms - wind being the main erosion agent on the planet today. Following the work of (Silvestro et al., 2010) who identified few migrating ripples from 2 images acquired 3 months apart in 2007, we used COSI-Corr and the same images to measure the sand ripple migration. We observe that the entire dune field is subject to ripple migration, and show that the ripple migration speed along the stoss slope increases linearly with dune height as predicted by the theory, but measured here for the first time. We also observe using images taken three years apart dunes migration (not ripples), which confirms that the dune field is active and not fossilized. After determining the ripple height, we could estimate a sand flux from the ripples migration. To our surprise the sand flux is quite high, comparable to some of the dune field on Earth.

Once the methodology to measure the sand flux from HiRISE and COSI-Corr was established, we extended our study to a time-series of ∼10 images covering one Mars year. From the time-series of ripples migration maps, the objective was to compute a time-series of sand flux. However, the geometric distortion of HiRISE identified in Chapter 3, polluted the measurement. The distortion amplitude was not negligible with respect to the ripple migration of some maps. Consequently we proposed a method to denoise the images based on a Principal Component Analysis. This allowed us to minimize the geometric distortion before computing the sand flux. We observed a very clear seasonal variation of the sand flux throughout the year, which can be easily explained from the topographic situation around Nili Patera and the Mars orbital eccentricity.

With a quantified seasonal sand flux variation at Nili Patera, we investigated the benefit this measurement could bring to the atmospheric community. We collaborated with Claire Newman and Mark Richardson from Ashima Research which develop and maintain marsWRF, an adaptation to Mars of the Weather and Forecasting Model (WRF) developed by NCAR (National Center for Atmospheric Research, USA). The measurement of the sand flux and its variability, over an area of several square km is of great interest for climate simulation. As a direct result of the wind, we used the sand flux to bring a constraint on the sand shear stress threshold that is to be used with climate simulation. We asked the question:

Which threshold would allow marsWRF simulation to reproduce the variability of the sand flux observed? Constraining this threshold is critical for global modeling of the Mars weather as moving sand is the main driver to dust lofting in the atmosphere, which in turn strongly influence the weather through atmosphere opacity and surface thermal change. The output of this study is the proposition of an effective stress threshold relevant for use with GCM and mesoscale simulations.

5.6.2 Limitations

Despite the good results obtained on the sand flux study using HiRISE, the approach has strict constraints and does not leave a lot of freedom in the data requirements.

HiRISE images resolution is high, and subject to the DEM resolution limitation, as mentioned in the previous section. On Mars, there is no choice regarding the availability of a DEM of sufficient resolution: the only source is a DEM generated with HiRISE stereo-pair. In practice that means that anyone who want to do a change detection and/or surface displacement measurement need to ask the HiRISE team to specifically acquires a HiRISE stereo-pair. In addition to the stereo-pair a third image (minimum) needs to be acquired for the temporal coverage, and also need usually to be tasked specifically. Hence, a change detection study on Mars using HiRISE will require the tasking of all the images necessary, along with a stereo-pair.

The HiRISE coverage of Mars is very sparse. In 2008 after the primary phase (2 years), only 0.5% of the Mars surface had been imaged. The official objective of the HiRISE mission is to cover 3% of the planet (McEwen et al., 2010). The archive limitation that was mentioned for aerial imagery is even more critical with HiRISE.

A limitation that can be serious depending on the change or surface displacement that is looked for is the CCD striping and jitter distortions. These distortions can account for up to a few pixels and if the displacement is small it can be overcast by the geometric distortion. To reduce the distortion, a better calibration of the CCD misalignement is needed. One way to calibrate the CCD misalignment, that we are currently investigating, is to take profit of the large time-series of HiRISE used in this study. In the study of the sand flux, we removed and discarded the distortion from the sand activity signal. Here we propose to do the opposite and remove the sand activity signal from the CCD/jitter distortion. Using the time-series of distortions we hope to invert for the precise CCD misalignement. The resulting calibration of the CCD could be systematically applied to further HiRISE processing. The jitter attitude would be still be uncorrected however.

5.6.3 Looking forward

The study on the sand ripples migration opened up new research possibilities in aeolian bedforms and atmospheric/climate sciences. Much more work can be done with some suggestions listed here.

The shear stress threshold estimate is just an estimate derived from one location, using one atmospheric model, and one GCM grid resolution. It would be interesting to confront this threshold with the ones that would be found: 1) Using a different atmospheric model, such as Mars Regional Atmospheric Modeling System (MRAMS, 2014) or LMD Mars Global Climate Model (LMD, 2014), 2) From a complete mesoscale simulation using a high resolution grid, 3) at a different dune fields locations (which would requires another time-series acquisition).

The time-series covering Nili Patera is extending. Motivated by the results of the first analysis, HiRISE images are still acquired over Nili Patera. In a few months an additional Mars year will be available which will allows us to look at the annual variation of the sand flux.

Numerous evidences of morphological processes of glacier-type flux and landslides have been identified and could benefit from the high resolution of HiRISE and the change detection capability of COSI-Corr.

Appendix A

Appendix Chapter 2

A.1 Optical Image Correlation Methodology

Here we provide further details on the methodology used to correlate SPOT5 and KH-9 satellite images, and aerial photos. All processing was done using the COSI-Corr software package, which is a plugin for ENVI Exelis.

A.1.1 Orthorectification and correlation of SPOT5 and KH-9 satellite images

During the orthorectification process, both the SPOT5 and KH-9 images are resampled to correct for the effect of topography, which occurs because of the stereoscopic effect produced when images are acquired with an oblique view of the Earth's surface (i.e. off-nadir incidence angles). Orthorectification gives both images a common viewing geometry, equivalent to the satellite looking exactly normal to Earth's surface everywhere across the image, after which they can be correlated to measure horizontal tectonic displacements. If the two images are not corrected for topography, the offset or disparity map will include a tectonic displacement overprinted by a much larger topographic signal which results from the parallax difference between the two images (Fig. A.1). To precisely orthorectify SPOT5 and KH-9 images, a digital elevation model of a similar resolution to the image acquisitions, and ideally from the same time period is needed. Unfortunately, the limited availability of suitable topographic data precludes such a precise orthorectification. Therefore, we use the 30 m global ASTER GDEM, which is produced by stereo extraction and stacking of multiple ASTER DEM's. We filter the ASTER GDEM with a 3×3 low pass and 3×3 median filter to reduce high frequency noise.

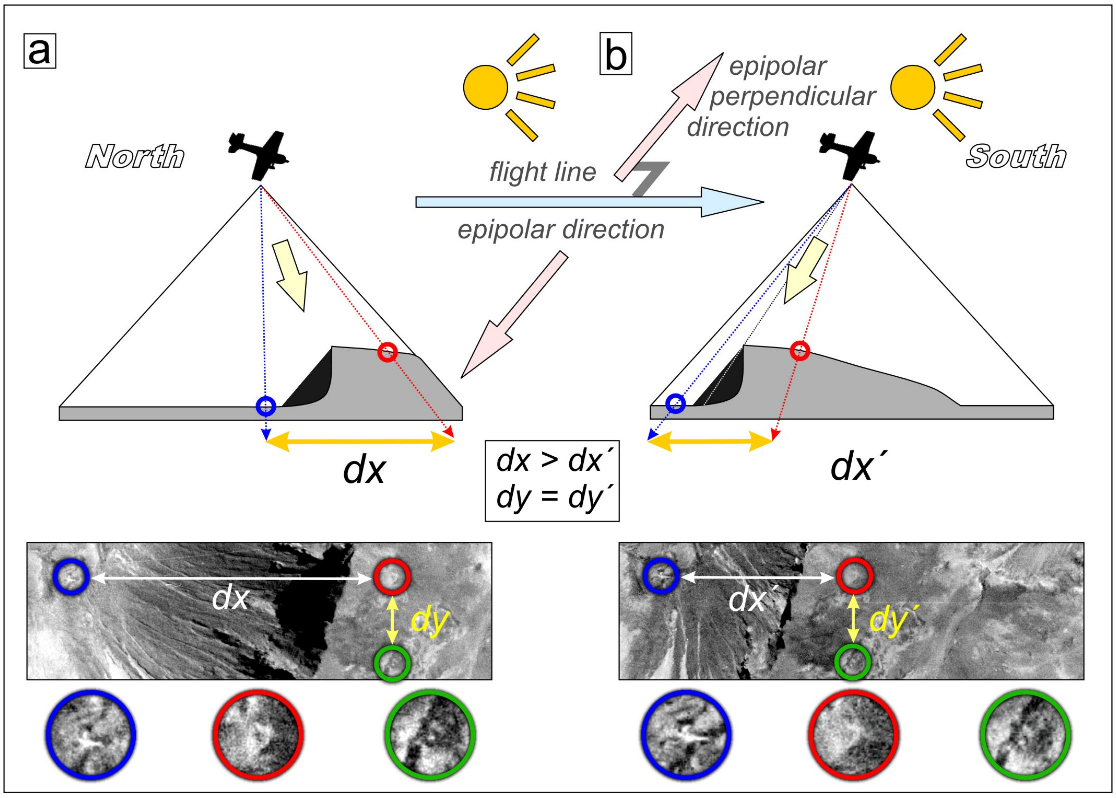

FIGURE A.1: As an airplane flies over the ground (i.e. from point a to b) acquiring aerial photos, the incidence angle changes across the image. The result is that the ground is viewed at different oblique angles around the edges of the image, which result in visual differences of the same feature in the landscape (due to a change in parallax). The number of pixels (dx) between the red and blue features in (a), is much greater than the number of pixels (dx') between the same features in (b), because the cliff which separates them is being viewed at different angles. However, the number of pixels between the red and green features is the same in both images. This is because the viewing angle is the same for both the red and green features in the y-direction. Therefore, the parallax difference between the images is greatest in one direction, known as the epipolar direction, and in this example corresponds to the flight direction of the airplane. Topographic information can be extracted from aerial photos reprojected into the epipolar plane. Conversely, there is no topographic information recorded in the epipolar perpendicular direction.

A.1.2 Post Processing: Removal of topographic residuals

Due to the much lower resolution of the ASTER GDEM (30 m) compared with the KH-9 (∼8 m) and SPOT5 (2.5 m) images, we cannot account for all of the topographic signal during orthorectification. This results in a displacement signal which correlates with high-frequency topographic noise in our correlation maps (Fig. A.2), thus slightly obscuring the tectonic signal. Because the parallax difference between the two images, i.e. the topographic signal, is at a maximum in the plane of parallax (also called the epipolar plane, see Fig. A.1), the topographic noise can be isolated by looking only at the epipolar plane displacement field. Conversely, the displacement perpendicular to the epipolar plane contains no topographic information (Renaud Binet, personal communication, 2010). We project our E-W and N-S displacement field into the epipolar and epipolar perpendicular displacement fields using the ‘Epipolar Map Projection’ tool in COSI-Corr (Fig. A.3). This allows us to measure the opening accommodated across the rift between September 1977 and October 2002 (Fig. 2.4). For the KH-9-SPOT5 image pair (Fig. 2.3), the epipolar perpendicular direction is approximately parallel to the maximum opening direction (i.e. WNW-ESE, see Fig. A.3) — the variation in this direction across the wider Krafla region results from differences between the radial incidence angle of the KH-9 image and the constant near-vertical incidence angle (0.78° east looking) angle of the SPOT5 image. However, the variation in epipolar direction across a 10 km wide zone over the Krafla fissure swarm is small (Fig. A.3a).

A.1.3 Orthorectification and correlation of historical aerial photos

Although KH-9 and traditional aerial photos may both be orthorectified using the ‘Aerial Imagery’ module within COSI-Corr, a few important differences exist between KH-9 and aerial photos which may result in different correlation results. Firstly, because camera calibration reports were supplied with the 1957 and 1990 aerial photos, we are able to generate more robust interior orientation models for the aerial camera systems used; this is not the case for the KH-9 images, for which the calibration reports remain classified. Therefore, using the aerial camera calibration information, we are able to account for optical distortions produced by the lens. Furthermore, a very precise and accurate determination of the focal

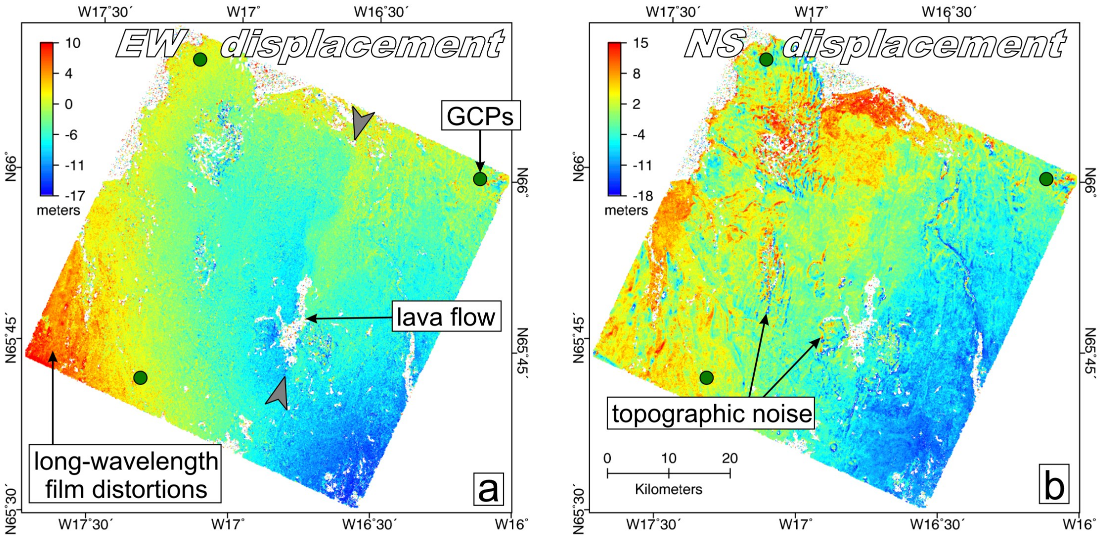

FIGURE A.2: (a) East-west and (b) north-south displacement fields produced from correlation of the 1977 KH-9 and 2002 SPOT5 satellite images. The area covered by these images corresponds to that shown in Fig. 2.3b and c. Positive values indicate eastward/northward movement of pixels between the two images. Opening of the Krafla rift zone occured between the gray pointers in (a), see Buck et al. (2006). Eruption of lavas in 1984 results in a decorrelated patch around the caldera in both displacement maps. Green circles show the locations of tie points used to co-register the KH-9 image to the SPOT5 image.

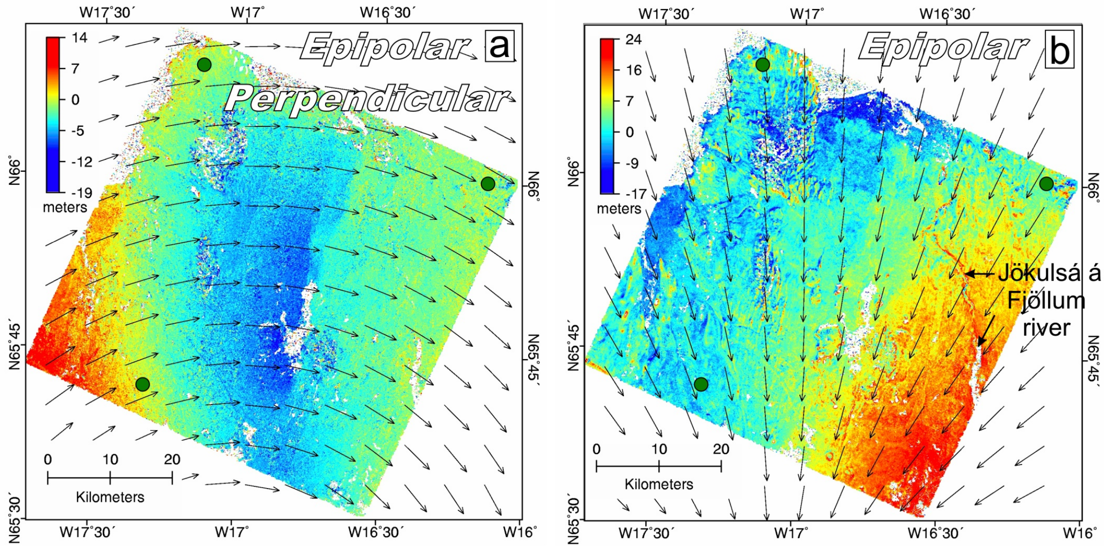

FIGURE A.3: Reprojection of the KH-9-SPOT5 displacement maps into the epipolar perpendicular (a), and epipolar planes (b). Region corresponds to that shown in Fig. 2.3b and c. Black arrows show the direction of these planes across the image, which vary due to combining a pushbroom satellite with a frame camera satellite system from different altitudes. Topographic noise, such as the Jökulsá á Fjöllum river valley, is visible in the epipolar direction, but not the epipolar perpendicular direction.

length helps to reduce topographic residuals throughout the image, as well as enabling the photo to be successfully orthorectified.

The high resolution of aerial photos (typically <1 m) means we need similarly high resolution digital elevation models to accurately orthorectify them. Unfortunately, the best available DEM we have for the Iceland region is the Global ASTER GDEM Version 1 (30 m). Orthorectifying aerial photos with such a coarse DEM means there are many topographic residuals remaining in the photos, which produce large displacement values during correlation, thus obscuring the real signal. Using high resolution stereo DEMs extracted from the aerial photos themselves does not account for all the topographic residuals, and may even add additional topographic noise if the two DEMs are not perfectly co-registered. We did not use pre- and post-crisis DEMs due to the significant challenges co-registering them precisely. We therefore orthorectify all aerial photos with the same ASTER GDEM, thereby providing consistency in processing between all datasets. We then reproject the displacement field into the epipolar and epipolar perpendicular geometry. Because the latter is free from stereoscopic effects, we analyze only epipolar perpendicular displacement fields for aerial photo correlations. It is therefore important to choose aerial photo pairs where the epipolar perpendicular directions are close to direction with the greatest displacement, i.e. rift-perpendicular for Krafla.

A.1.4 Interpreting vertical deformations from correlation of aerial photos and satellite images

When the incidence angle for satellite images and aerial photos deviate from nadir, and the images become oblique to the Earth's surface, the images become increasingly sensitive to vertical deformation. This effect is particularly strong in aerial photos, where the incidence angle increases radially outwards from the center of the image, and therefore the sensitivity to topography increases around the edge of the photos. When we do not have adequate pre- and post-event DEMs, we must use the same DEM to orthorectify both the pre- and post-event aerial photos. However, any vertical displacement which occurs around the edges of the images will produce an apparent horizontal signal, because the same DEM was used for the pre- and post-event images (Fig. A.4 and Copley et al., 2011).

For the case where a camera is looking obliquely west at the ground, and there is subsidence between images, (Fig. A.4a) the subsidence will produce a positive eastward signal unless suitable pre- and post- DEM's are used to orthorectify the images. In the western parts of the image (Fig. A.4a), the camera is looking obliquely west. Therefore, if the green point in the post-crisis image has subsided from its original location, the blue circle in the pre-crisis image, which is orthorectified using the post-crisis DEM, will be projected to the location shown by the yellow circle. When correlating the pre- and post-crisis images, the yellow circle will appear to move eastwards, thereby giving an apparent positive eastward displacement. If a camera is looking obliquely north (Fig. A.4b), a subsidence signal will produce an apparent southward displacement. In the northern part of an aerial photo, the camera looks obliquely north. Therefore, the green circle, which lies in the middle of the rift in the post-crisis, has subsided from its original position (blue circle), which then gets projected to the location of the yellow circle. Thus, the pre-crisis yellow circle appears to be displaced southward to the green circle location in the post-crisis image. If the incidence angle looks obliquely south or east, subsidence will produce a north or westward motion, respectively (Fig. A.4c). The resulting E-W displacement profile for a rift-zone oriented N-S is shown in Fig. A.4d,e,f. The eastern rift-flank is the stable reference area between the two images, and so the western-rift flank moves west, relative to the eastern rift-flank, thereby accommodating E-W extension. Subsidence and E-W extension are accommodated on N-S rift-bounding normal faults (A.1a). Subsidence occurs on the west side of the correlation/displacement map, and is therefore being imaged obliquely, looking west (Fig. A.4d and e). A profile of displacement taken across the rift is shown in Fig. A.4f. The eastern rift-flank is flat/stable, and both the inner rift and western rift-flank move to the west. However, the obliquity increases westward across the inner rift, which results in an increasing eastward component as one moves westward along the profile. If the heights of the east and western rift-flanks do not change considerably throughout the period of deformation, the E-W displacement of the western rift-flank will represent the total horizontal extension across the rift.

Figure A.5a shows how using the same post-crisis DEM can explain the positive eastward increase in displacement seen across the Northern Krafla inner rift (Fig. 2.5). The pre-crisis topography is shown in green, and the post-crisis topography in gray; the black arrows show the camera incidence angles, which increase westward across the image. At the eastern rift boundary, shown by the heavy

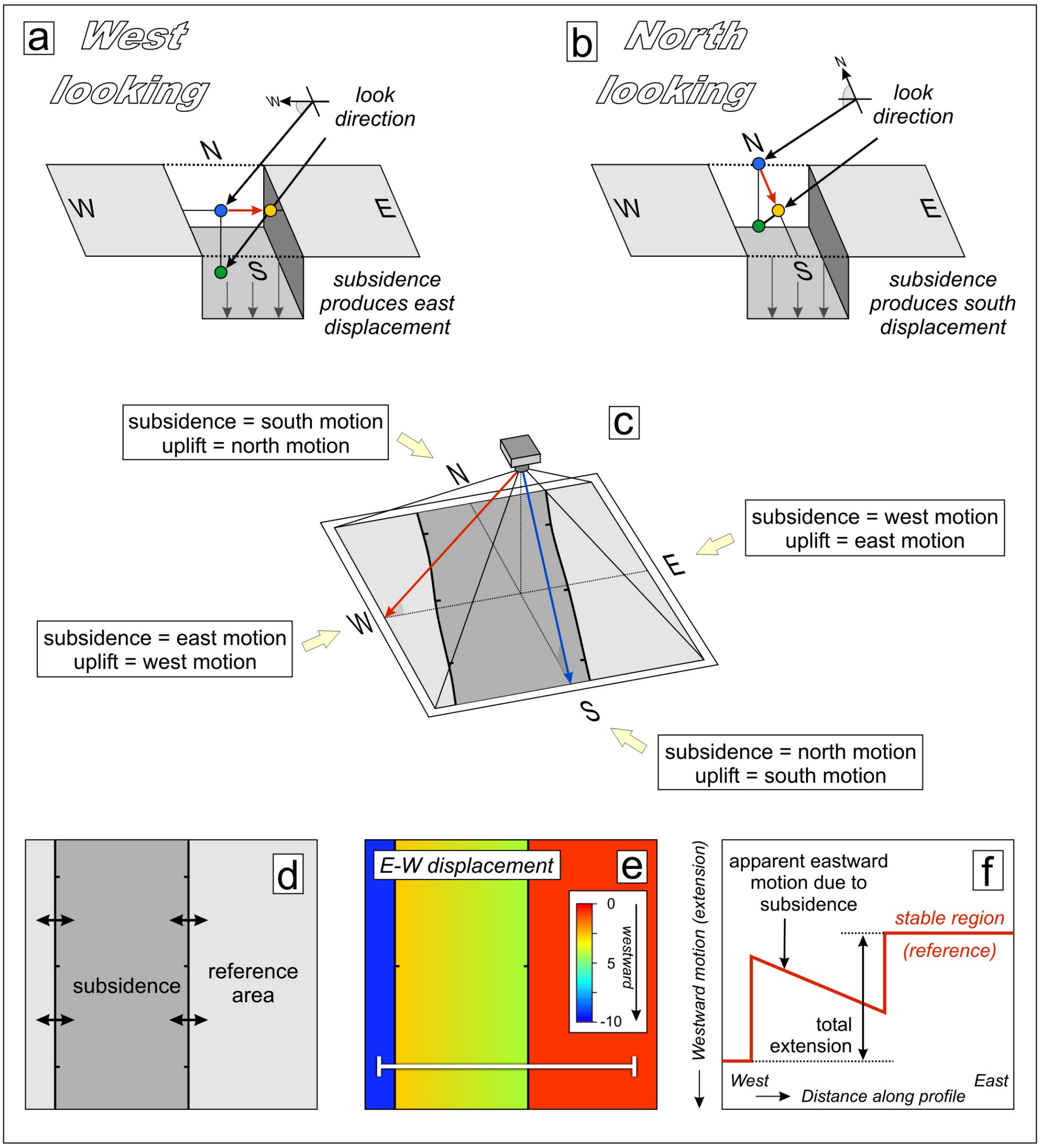

FIGURE A.4: Cartoon showing the effect of using the same DEM for orthorectifying the pre- and post-crisis images, and changes in the camera viewing geometry on a displacement field involving vertical motions. If a camera is looking obliquely west (a) or obliquely north (b), a subsidence signal will produce an apparent eastward and southward displacement, respectively (see text for details). (c) Summary diagram showing how vertical motions produce apparent horizontal displacements across different parts of an aerial photo. (d) Cartoon showing two rift bounding faults located at the western edge of an aerial photo correlation. Tie points are collected from the eastern rift flank; displacements are relative to this reference area. The E-W displacement field resulting from normal slip on the two faults is shown in (e), and a profile of displacement is shown in (f). Apparent eastward motion due to subsidence in the western part of the image produces a ramp in the inner rift displacement.

black line with fault arrows on the right of the image, the camera looks straight down. The blue circle represents a pixel in the post-crisis aerial photo, which moved from its original location in the pre-crisis topography, shown by the orange cricle. When the pre-crisis aerial photo is orthorectified using the post-crisis DEM, the orange pixel is projected to the location shown by the red box. Image correlation measures the horizontal shift between the red and blue boxes. If there has been more normal slip on the eastern rift boundary than the western, consistent with our results, then the westward displacement measured by COSI-Corr will decrease westward. The thick black arrows along the bottom of the figure show the decrease in westward displacement across the image, which varies as a function of the camera incidence angle and elevation change. The percentage values are shown relative to the true westward displacement, δx, which is 100% and is constant everwhere west of the eastern rift boundary. Figure A.5b shows the resulting E-W displacement profile (positive eastward motion increases upwards). E-W extension is accommodated only on the eastern rift bounding fault, while both east and west bounding faults accommodate vertical motion, which produces the change in elevation between the two images. The resulting increase, or bulge in eastward displacement across the inner rift resembles the displacement profiles measured in the Northern Krafla Rift.

In Figure A.5a, the western rift flank has not changed elevation between the pre- and post-crisis images. However, levelling profiles across the northern Krafla rift which span the 1978 dike injection revealed significant rift flank uplift (Sigurdsson, 1980). Figure A.5c shows how rift flank uplift will effect the western Krafla rift boundary if a pre-crisis DEM is not used. Blue pixels in the post-crisis image move back to their original locations, orange circles, which are then projected back onto the post-crisis topography, red square locations. COSI-Corr will then measure the horizontal displacement between the blue circles and red squares, and will overestimate the real horizontal displacement where the pre-crisis topography was lower than the post-crisis topography. Figure A.5d shows the resulting displacement profile, which increases exponentially towards the rift flanks. This effect may explain similar features seen at the edges of many of our correlations. For example, the large increase in westward motion seen in Fig. 2.8 could occur if the 1976 dike injection did not activate the western boundary fault at this location. The resulting broad zone of uplift over the western rift flank would then produce an increase in the westward horizontal displacement value. This is a more likely explanation, because we do not see any distributed deformation outside of the rift zone in the KH-9-SPOT5 correlation (Fig. 2.4).

Finally, because all our aerial photos were acquired from flights paths oriented along the Krafla inner rift, the images always look westward at the western rift boundary and eastward at the eastern rift boundary. Because uplift occurs in the rift flanks, and subsidence in the inner rift, any vertical motion will produce an additional horizontal signal, rather than cancelling out the real displacement (consistent with Fig. A.5c). Our estimates of extension are therefore likely to represent maximum values. Furthermore, this effect is specific to the geometry of the aerial photo survey and tectonic displacements at Krafla. Therefore, care must be taken when interpreting aerial photo displacement maps from other regions in which large vertical displacements have occured.

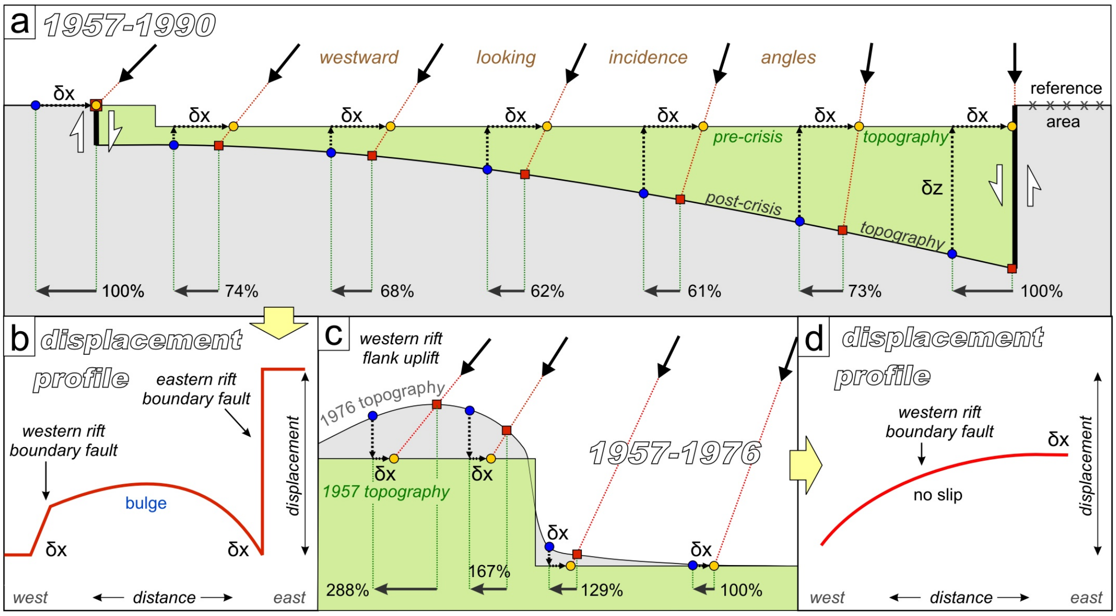

Figure A.5: (a) Cartoon showing a profile across the Northern Krafla rift corresponding to the area imaged in the 1957–1990 aerial photo correlations (Fig. 2.5). If the post-crisis DEM is used to orthorectify the pre-crisis aerial photos, post-crisis pixels (blue) are projected back to the locations shown by the red squares, which leads to an underestimation of the true westward displacement (δx) — see text for details. (b) Displacement profile across the rift shown in (a). Positive eastward displacement increases upwards. (c) Cartoon showing a profile across the western boundary of the Northern Krafla rift, corresponding to the area imaged in the 1957–1976 aerial photo correlations (Fig. 2.8). If the 1976 topography is used to orthorectify the 1957 aerial photos, blue pixels in the 1976 image are projected back to the red squares, leading to an overestimation of the true westward displacement (δx) — see text for details. (d) Displacement profile across the rift shown in (c).

Appendix B

Appendix Chapter 4

B.1 Methods

B.1.1 Background

Recent advances in image modeling and processing (Leprince et al., 2007) permit the measurement of relative displacements between images to the sub-pixel level. Methodological improvements in this field have been implemented in the software package Co-registration of Optically Sensed Images and Correlation (COSI-Corr) (Tectonics-Observatory, 2014). Correlation requires unambiguous discrimination features. This technique has been successfully employed to measure displacements on Earth, including fault offsets, ice flows, landslides, and sand dune migration (Avouac et al., 2006, Leprince et al., 2007, Necsoiu et al., 2009, Vermeesch and Drake, 2008).

B.1.2 Data set

A total of four HiRISE images were used to measure ripple migration rates (Table B.1). Two images were used to extract the topography (S1 and S2), and the others used to measure ripple migration (T1 and T2). Images T2 and S1 were also used to assess overall dune displacement.

Image ID	ID	Roll angle (°)	Ls (°)	Acquisition date	ΔTime (days)
PSP_004339_1890	T1	-0.353	268	06/30/07	0
PSP_005684_1890	T2	-4.001	330	10/13/07	105
ESP_017762_1890	S1	25.269	89	05/11/10	1046
ESP_018039_1890	S2	-4.98	99	6/02/10	1068

TABLE B.1: ID = Abbreviated identification used in the text; roll angle is the off-nadir pointing of the spacecraft (which is equivalent to the HiRISE boresight), with positive values toward the West and negative toward the East; Ls is the areocentric longitude of Mars's orbit around the Sun, with Ls = 0^{circ} corresponding to the beginning of northern spring and southern autumn. All images have a resampled pixel scale of 25 cm.

B.1.3 Digital Elevation Model extraction

Images S1 and S2 were specifically acquired for stereo-photogrammetry. They were taken 22 days apart in 2010 with a viewing angle difference of 32.9°. The Digital Elevation Model (DEM) extraction was carried out at the HiRISE Operations Center at University of Arizona using the United States Geological Survey (USGS) recommended procedure (USGS, 2014a) that incorporates the Integrated Software for Imagers and Spectrometers (ISIS) image processing package (USGS, 2014b) and SOCET SET stereo software (USGS, 2014a). The extracted DEM had a post-spacing of 1 m and was manually edited in some places. At these locations the DEM extraction failed mainly because of textureless areas, especially on the dunes' lee side. The two images were subsequently orthorectified on a ∼25 cm resolution grid.

HiRISE imagery is subject to jitter that, if not corrected, may introduce distortions in the DEM (Kirk et al., 2007). The University of Arizona developed a procedure to remove jitter distortions from HiRISE images prior to further processing (Mattson et al., 2009). However, corrections are only applied if jitter amplitude is larger than 1–2 pixels, which was not the case with the S1 and S2 images. Notice that we neglect possible topographic changes between these two images. This assumption is discussed and justified below.

B.1.4 Dune height extraction

The first step for determining dune height based on the DEM was to define regions of bedrock. This was done by setting an amplitude threshold on the ripple displacement map (Fig. 4.1a). The bedrock area was then adjusted from visual inspection of the images (the sand being darker than the bedrock) in areas close to the dunes, and in areas for which bedrock mis-registration was above the threshold. The bedrock topography beneath the dune field was then extrapolated using a thin plate spline interpolation (Bookstein, 1989). In practice, the bedrock contained too many points for the thin plate spline algorithm to ingest. Therefore, around 5000 points, evenly spread, were extracted from the bedrock areas. Additional points were extracted around the dune footprints. The interpolated bedrock topography beneath the dunes was then replaced in the main DEM. The resulting bedrock topography model was then subtracted from the DEM to yield the dune height map shown in Figure 4.1c.

B.1.5 Image processing

Images T1 and T2 were used to evaluate ripple migration. These were acquired 105 days apart in 2007, with a difference in viewing angle of 4.0°. Both images have a resampled ground resolution of 25 cm. Before correlation, the images went through a two step process using ISIS and COSI-Corr.

Both images were supplied by the USGS in a radiometrically and geometrically calibrated format ("balanced cubes") in the form of 10 stripes corresponding to the 10 CCD arrays in the broadband "red" channel (Kirk et al., 2007, McEwen et al., 2007, 2010). Camera jitter was estimated by the University of Arizona using standard procedures (Mattson et al., 2009). The stripes were then processed using ISIS and the USGS procedure (hijit4socet script). This process stitched the stripes together, while correcting for the jitter estimate and accounting for the camera geometry, outputting an image as if it was acquired by an ideal, distortion-free camera. The images were then formatted into a SOCET SET® readable format with the ancillary data (e.g., ephemeris, camera geometry) extracted from the SPICE (ancillary data) kernels (NASA, 2014).

The images and the extracted ancillary data were plugged into COSI-Corr (Leprince et al., 2007) rather than into SOCET SET to take advantage of the optimized co-registration feature in order to finely register images before correlation. Fifty tie-points were selected between image T1 and orthorectified image S1. The tie-points were evenly spread over the images and were located in bedrock areas away from the dunes. The tie-points were optimized using COSI-Corr using a window size of 256 × 256 pixels. The resulting average mis-registration between the two images at the tie-point locations was less than $1/100^{\text{th}}$ of a pixel with a standard deviation of 0.46 pixel (11.5 cm) in the East/West direction and 0.58 pixel (14.5 cm) in the North/South direction. Image T1 was then orthorectified with COSI-Corr on a 25 cm grid, using the ancillary data, the optimized set of tie-points, and the DEM previously extracted. Image T2 was then co-registered to orthorectified image T1. The same procedure as above was applied with similar co-registration accuracy.

Orthorectified images T1 and T2 were correlated with COSI-Corr using a sliding correlation window of 70 × 70 pixels (17.5 × 17.5 m) and a step of 16 pixels (4 m). The displacement maps obtained are presented in Figure B.2 and B.3 and represent respectively the East/West (positive eastward) and North/South (positive northward) components of the displacement field. Figure B.4 presents the histogram of the entire bedrock mis-registration. The average ripple displacement is about 2.5 m, with measureable peaks at 4 m. In the North/South displacement map, CCD artifacts can be seen that are residuals of the camera geometry model. Their amplitude varies from negligible up to ∼0.35 m. Theses artifacts are also found in the East/West direction but are overprinted by ripple displacements. The amplitude displacement map (Fig. 4.1a) represents the norm of the displacement from the East/West and North/South components.

B.1.6 Elevation error ambiguity

As observed in Figure 4.1), the displacements are highly correlated to dune topography, such that topographic error could be considered a factor. We show that this is not the case because:

1. Given the baseline and height ratio of the two images, an error of 30 m in elevation would be necessary to produce 2.5 m of displacement. This is highly unlikely as the vertical DTM accuracy is a few tens of centimeters for a SOCET SET matching accuracy of one pixel. The dunes themselves have a height ranging from a few meters to around 50 m.

2. Displacements visually estimated in previous work (Silvestro et al., 2010) from images T1 and T2 compare well with our results.

3. The displacement maps, which are in East/West and North/South directions, were projected onto the epipolar and perpendicular-epipolar directions that are defined from the image acquisition geometries. All parallax related displacements are therefore projected onto the epipolar direction, in particular the topographic residuals. If the ripple displacements measurements were only due to topographic error, they would be entirely in the epipolar direction. However, the perpendicular epipolar direction displays ripple displacements, invalidating the hypothesis possibility of parallax error.

B.1.7 Error due to topographic changes between S1 and S2

This study assumes that the dunes and ripples remain static in the 22 days between S1 and S2, such that an accurate DEM is derived. This was verified as follows:

1. **Stereoscopic error induced by ripple migration** — SOCET SET matches textured surfaces for topographic extraction. The ripple pattern is used during the matching to infer the dune heights. We determined the error made on the DEM if the ripples moved during the 22 day span between S1 and S2.

   Taking the average and maximum displacements of 2.5 and 4 m in the 105 days between T1 and T2 implies that motion in 22 days would be 0.52 m and 0.83 m, inducing an error on the dune topography of 0.8 m and 1.29 m respectively. This elevation error would in turn causes a displacement map bias of about 6 and 11 cm, respectively. This value (a few centimeters) is small enough relative to the measured displacements (a few meters) to be negligible. In addition, no ripple displacement could be detected visually between the stereo images, suggesting an even smaller topographic error.

2. **Error due to the assumption of static dune topography** — With an average of 2.5 m ripple displacement in 105 days, the dunes themselves may well have moved in the three year period between the acquisition of the images for correlation (T1 and T2) and the ones for DEM extraction (S1

and S2), making the assumption of static dune topography incorrect. Dune fronts were visually checked between the 941 day time separation between T2 and S1. Obviously the images could not be correlated as the ripples pattern changed entirely in three years. However, taking advantage of the good images registration between T2 and S1, up to 2–3 m of dune migration was manually measured in some cases, whereas other dunes were static. According to the DEM, the slope of the dunes' stoss sides in the "axial" direction is in the range 4–8°. Assuming a dune displacement of 3 m, a stoss slope of 6°, and a static morphology and height over this time scale, an error of around 30 cm in elevation would be introduced. As discussed above, an elevation error of 1 m induces a ∼10 cm bias in the displacement maps. Consequently, a 30 cm error in elevation would introduce a displacement bias at the centimeter scale, which can be neglected in view of the measured ripple displacements.

B.1.8 Estimate of the mean ripple height

The ripple pattern is clearly seen in the HiRISE images as they form alternating thin bright bands between thick dark bands, implying asymmetric slopes analogous to ripples on Earth (Ashley, 1990, Zimbelman, 2010). The DEM has insufficient resolution to resolve the ripple topography. The mean height of the crest of the ripples (measured with respect to the elevation of the trough between the ripples) can nonetheless be estimated to 40 cm, based on the following two approaches.

We measured 5 ripple trains consisting of 9–13 ripples each. These had average wavelengths ranging from 3.6 m to 5.3 m. The mean value is estimated to 4.6±0.09m . Assuming that the Nili ripples have height to wavelength ratios like those of many terrestrial aeolian ripples (Ashley, 1990, Zimbelman, 2010) and "transverse aeolian ridges" elsewhere on Mars (Zimbelman, 2010), values are ∼1:10. Therefore, assuming a typical wavelength on the order of 4.5 m, implies that the ripples are ∼45±9 cm high. The uncertainty on the height to wavelength ratio is difficult to assess and not taken into account in this estimate.

In some areas the shape of ripples that are in contact with the bedrock at the dune base can be clearly delineated against the bedrock. Using the local slope of the dune and the profiles of the ripple projections on the bedrock, an estimate of the ripple height was obtained. On average, from 7 measurements at 2 different sites the height was estimated at 35±3 cm. Based on these two approaches, we estimate the ripple height at the crest, as 40±9 cm.

The mean height, h_r, of the ripples, which is the quantity that determines the reptation sand flux, depends on the crest height but also on the ripple geometry. If the ripples are assumed sinusoidal or triangular (Simons et al., 1965) makes no difference as in both cases the mean height is actually half the crest height. The ripple geometry need only be considered if there is a significant dissymmetry of concavity between the convex and concave portions of the ripple profile. In absence of constraints on ripple geometry we assume that this factor might result in an additional 10% source of relative uncertainty. Altogether we estimate the relative uncertainly on the mean ripple height as on the order of 30%, so $h_r =$ 20±6 cm.

B.1.9 Relation between dune celerity and sand flux in steady-state

A migrating dune that maintains its shape and volume is considered at steady-state. Conservation of mass for such a dune writes in 1-D as

$$\rho_s \partial_{h_D} / \partial_t = -c \rho_s \partial_{h_D} / \partial x = -\nabla q \tag{B.1}$$

where ρ_s is the sand density, h_D is local dune height, t is the time, c is the dune migration rate, x is the transport direction, and $q(x, t)$ is the mass sand flux (Ould Ahmedou et al., 2007). The dune slope from the upwind edge to the crest should be nearly constant. Integrating the above equation therefore gives

$$c \rho_s h_D = q \tag{B.2}$$

Therefore, the flux increases with increasing elevation on a dune surface. The total flux is the combined saltation (q_s) and reptation (q_r) fluxes. The ratio, α between the two fluxes depends on the local conditions (Anderson, 1987, Andreotti, 2004); we can write:

$$c \rho_s h_D = (1 + \alpha) q_r \tag{B.3}$$

Considering the ripple migration-induced sand flux equal to the reptation sand flux. Hence,

$$q_r = h_r d_r \rho_s / t \tag{B.4}$$

with h_r the mean ripple height, d_r the ripple displacement, and t the time interval. Hence,

$$c = (1 + \alpha) h_r d_r / h_D t \tag{B.5}$$

For a constant mean ripple height h_r, a dune at steady state requires that d_r / h_D be constant. This linear relationship between d_r and h_D is observed in the measurements (Fig. 4.2), and we found no evidence for systematic spatial variation of ripple size (h_r is therefore assumed constant).

Because dune migration rate and flux derived from ripple displacement are proportional to the ripple height, deviation from the assumed constant h_r of 20 cm is the greatest contributor to the uncertainty. With the height measurement techniques varying by ±6 cm (see above), the reptation flux and the dune migration rates derived from ripple migration rates have an uncertainty of ∼30%.

B.1.10 Resolution of technique

The minimum derived dune migration contributed by reptation flux depends on the minimum ripple displacement that can be measured, or $c \sim d_r h_r / h_D t$. In practice, with HiRISE images, the COSI-Corr correlator has a displacement detection capability of around 3 cm, give or take a few centimeters depending on the scene texture. The detection threshold is usually assessed by looking at the standard deviation of the measured displacements over a patch of supposedly uniform displacement. In Nili Patera this estimation is hard to make on the dunes themselves, as ripple displacements increase or decrease along the dune slope and are not uniform on any given patch. We therefore estimated the measurement resolution on the bedrock, which is around 4 cm (Fig. B.4). Although the resolution could be different on the bedrock and on the dunes, the texture on both surfaces contain enough high frequencies to expect a similar measurement resolution. The smallest displacements are around 20 cm, so all measurements are well above this limit. Notice, however, the difference between the resolution and the absolute accuracy of the measurements which may be biased by local mis-registration. The ripple-derived dune migration rate is $c \sim d_r h_r / h_D t$. With a 20 cm mean ripple height, the minimum detectable dune migration rate over 105 days is therefore $8\,10^{-3}/h_D$ m. Dune heights range from the maximum brink value of 61.5 m to the minimum 0.5 m used in the calculation, translating into a threshold over 105 days of $1.3\,10^{-4}$ to $1.6\,10^{-2}$ m, or, over an Earth year, $4.5\,10^{-4}$ to $5.5\,10^{-2}$ m, respectively. Therefore, there is a range of thresholds, depending on the local dune height. However, the dropping of the histogram in Figure 4.3 at values < 0.1 m is not because of this limitation, since, as just described, all displacements were above the resolution limit. In other words, Figure 4.3 represents all ripple-derived dune migration rates.

B.1.11 Calibration of the abrasion rate

Abrasion susceptibility (S_a) is defined as the ratio of the mass lost from a rock surface to that of the impacting sand and has been measured for a range of conditions and compositions in the laboratory (Greeley et al., 1982). At fluid threshold, S_a for basalt grains hitting basalt rocks at $20\,m\,s^{-1}$ is $\sim 2\,10^{-4}$. However, as discussed in the main text, sand fluxes on Mars are sustained at impact threshold conditions with wind and particle impact speeds about 10% that at fluid threshold, equivalent to typical terrestrial values (Kok, 2010). Abrasion susceptibility is proportional to grain kinetic energy (Greeley et al., 1982), such that S_a should be $\sim 2\,10^{-6}$ at impact threshold. Because the density of both materials are the same, the abrasion susceptibility is also the ratio of rock volume loss to the volume of impacting sand. The flux of sand that we calculate is that passing through a vertical cross section and this must be converted to the flux hitting a surface ranging in slope (θ) from flat ground to a vertical face. We can therefore consider the abrasion rate equal to $(S_a Q_i / z)(\alpha \cos\theta + \sin\theta)$, where Q_i is the interdune sand flux and α is the ratio of saltation height to descending path length. The mean trajectory height (z) on Mars, considering both reptating and saltating grains, has been calculated as $\sim$10 to a few 10s of centimeters, with the exact value depending on grain size and shear velocity (Kok, 2010). The mean height to length ratio of typical saltation trajectories on Mars is 1:10 (Kok, 2010). Saltation trajectories are generally asymmetrical such that the descending portion of the path (that which contains sand that hits the ground) occupies the greatest portion (Bridges et al., 2005, Greeley, R and Iversen, JD, 1985, White and Schultz, 1977). This should especially be the case for Mars where path lengths are longer than on Earth. Therefore, α should range from 0.1 to 0.2, with most trajectories toward lower values. Taking the average interdune sand flux (Q_i) of 2.3 m^3/m/yr (Earth year), values of z of 0.1 – 0.5 m, and α ranging from 0.1–0.15 gives abrasion rates of 0.9–9 μm/yr for a flat ground surface. For vertical rocks, the range is 9–46 μm/yr. The field measurements in Victoria Valley, Antarctica (Malin, 1986) used samples elevated above the ground and sticking outward from an aluminum framework (Malin, 1984) and therefore closely represent that for vertical rock faces.

Dune label	Height (m)	Migration rate (m/yr)	Migration rate std. dev.	Sand flux (m^3/m/yr)	Sand flux std. dev.
1	38	0.07	0.01	2.66	0.38
2	15	0.27	0.08	4.05	1.2
3	29	0.05	0.01	1.45	0.29
4	22	0.17	0.03	3.74	0.66
5	31	0.09	0.02	2.79	0.62
6	24	0.13	0.03	3.12	0.72
7	20	0.07	0.02	1.40	0.40
8	30	0.05	0.01	1.50	0.30
9	21	0.20	0.05	4.20	1.05
10	24	0.05	0.01	1.20	0.24
11	16	0.09	0.02	1.44	0.32
12	25	0.03	0.01	0.75	0.25
13	12	0.05	0.02	0.60	0.24
14	39	0.09	0.02	3.51	0.78
a	9	0.71	0.12	6.39	1.08
b	13	0.18	0.12	2.34	0.28
c	10	0.58	0.12	5.8	1.2
d	17	0.24	0.12	4.08	2.04
e	40	0.43	0.12	17.2	4.8
f	38	0.59	0.12	22.42	4.56
g	15	0.92	0.12	13.8	1.8
h	22	0.49	0.12	10.78	2.64
i	20	0.50	0.12	10	0.24
j	16	0.47	0.12	7.52	1.92
k	12	0.42	0.12	5.04	1.44

TABLE B.2: Dune migration speed and sand flux.

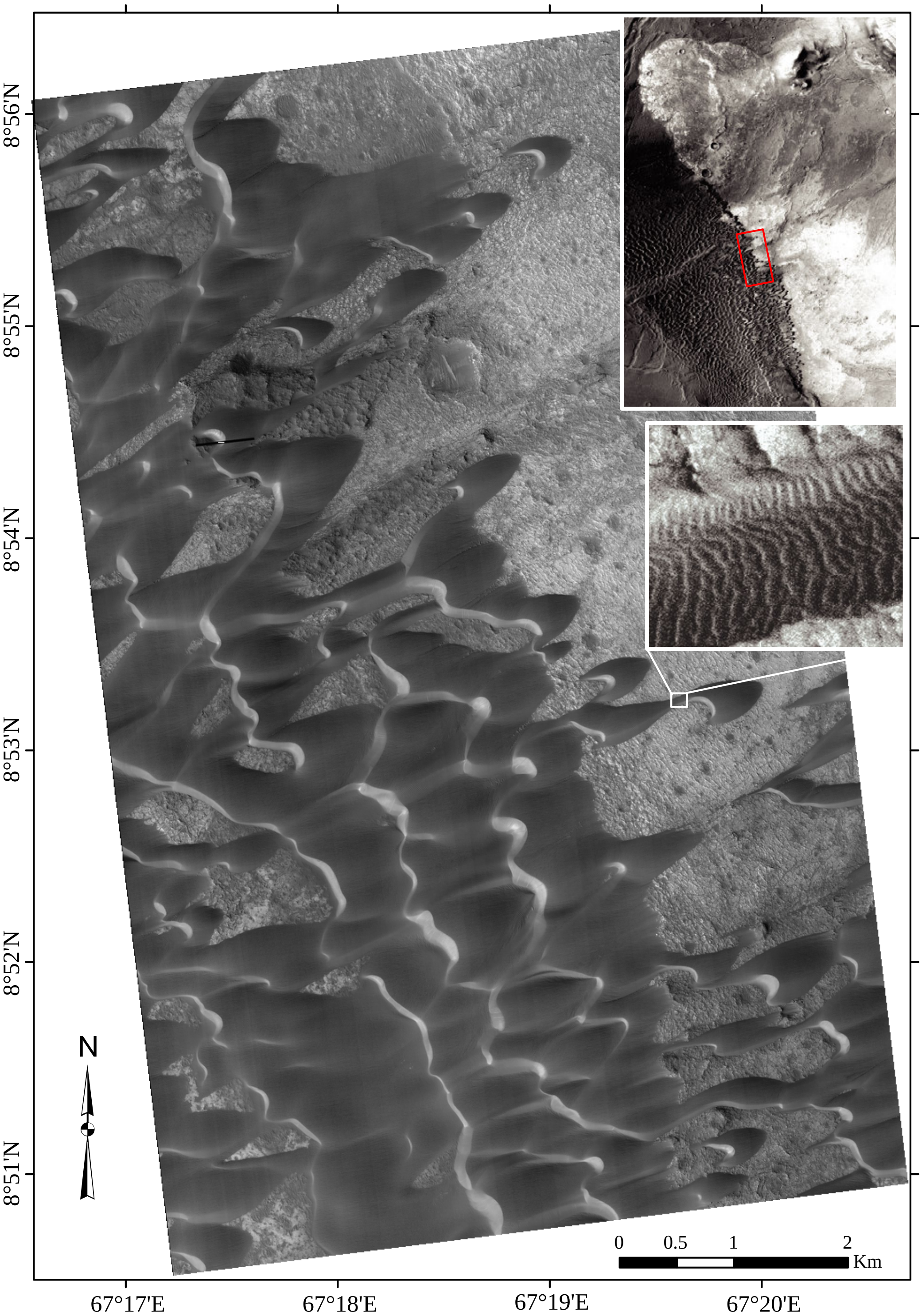

Figure B.1: **HiRISE image PSP_004339_1890 showing the Nili Patera dune field study area where images T1 and T2 overlap**. Upper inset of this area (red box) with respect to the entire dune shows location field in CTX image P04_002427_1888_XI_08N292W. Lower inset is a close-up view of one of the dunes, showing the rippled surface.

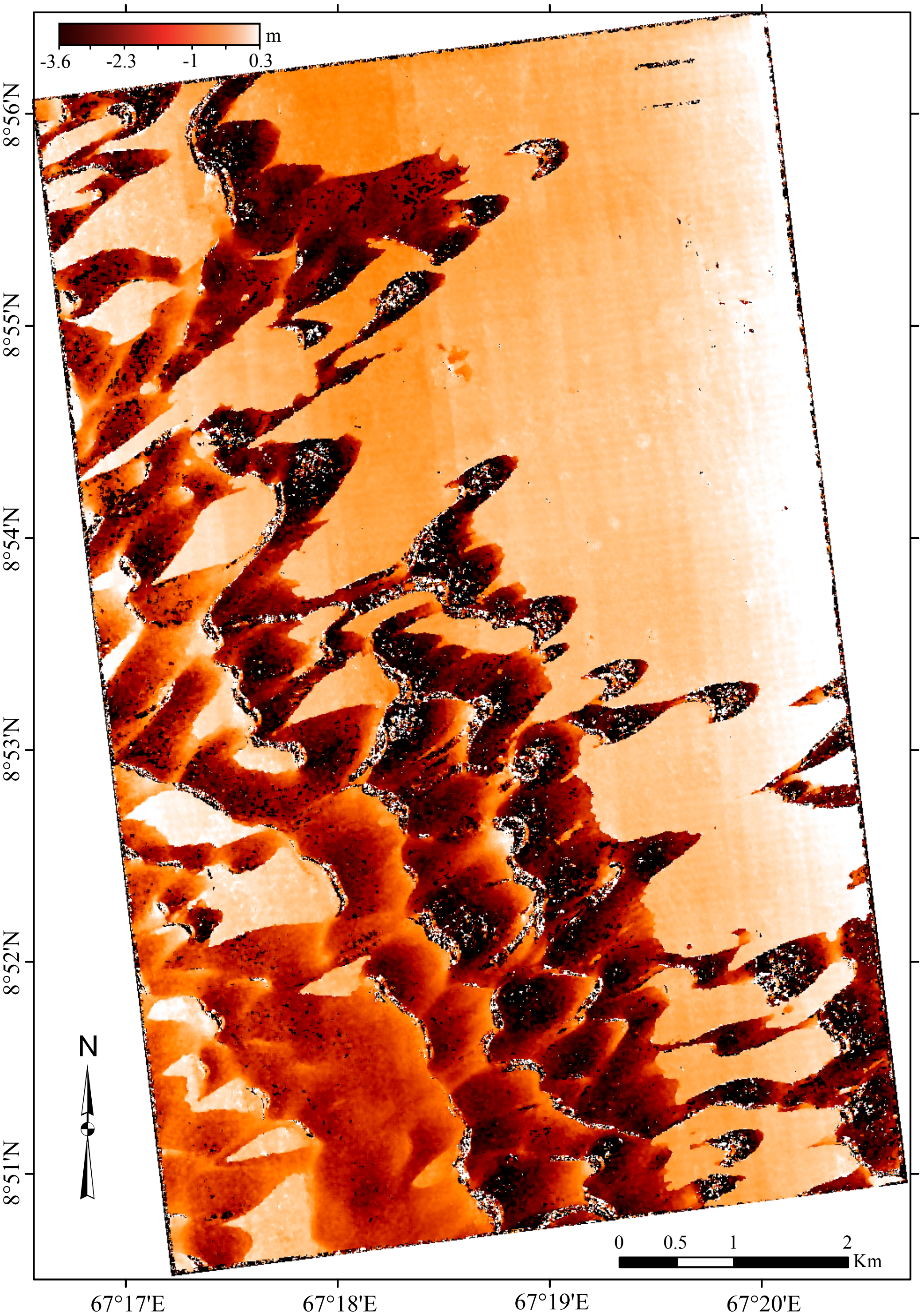

FIGURE B.2: **East/West component of the T1/T2 correlation**. Displacements are positive toward the East. Ripple displacements are measured up to around 3.6 m. Above this value, the correlation mostly fails as the ripple pattern changes too much between T1 and T2 (shown as white pixels).

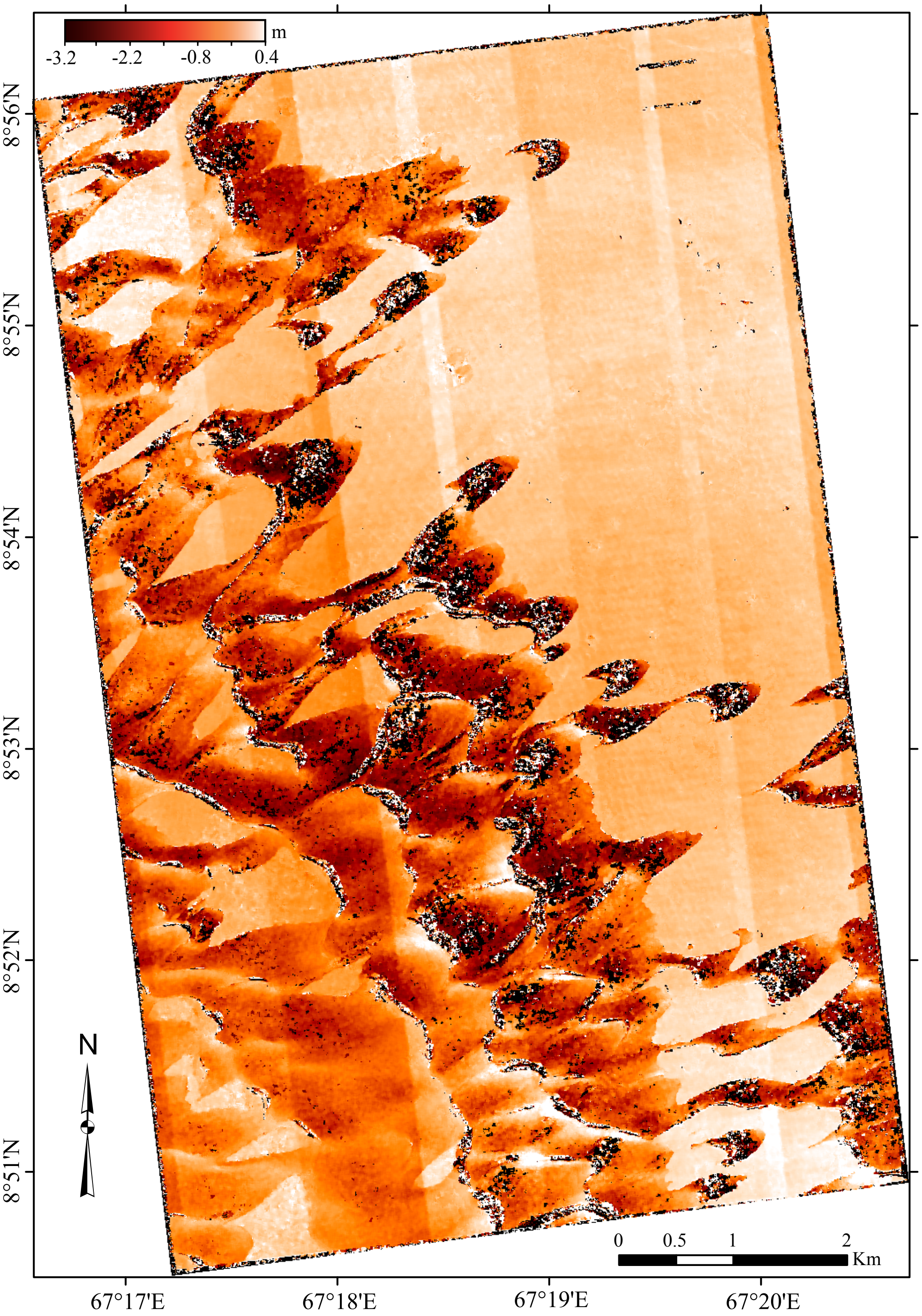

FIGURE B.3: **North/South component of the T1/T2 correlation**. Displacements are positive toward the North. Toward the south, values up to around 3.2 m are measured. Above this value, the correlation mostly fails as the ripple pattern changes too much between T1 and T2 (shown as white pixels). Along-track stripes are due to CCD array misalignment residual, with an amplitude of more than 1 pixel for the most misaligned CCD.

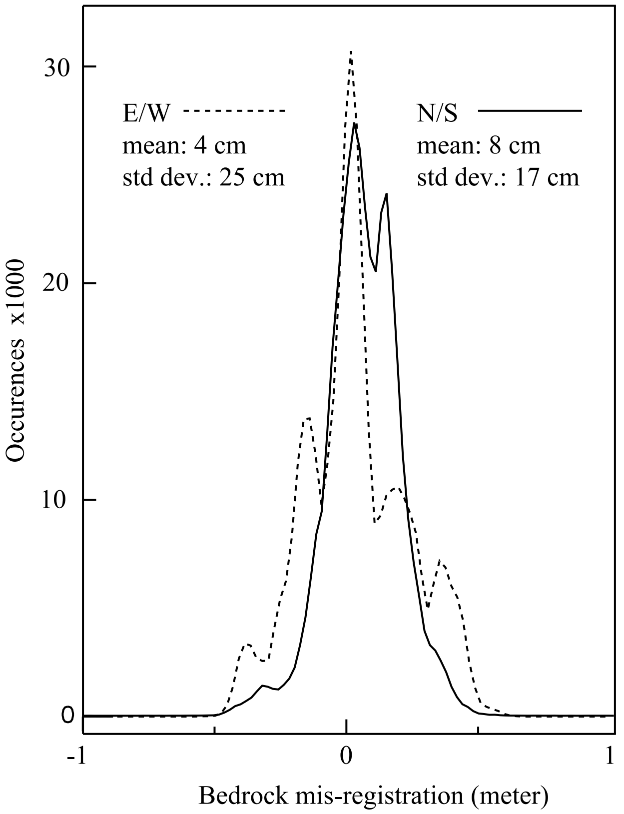

FIGURE B.4: **Histograms of displacement (in East/West and North/-South directions) measured on the bedrock only**. These measurements give an indication on the T1 and T2 registration quality and the minimum displacement that can potentially be measured.

Appendix C

Appendix Chapter 5

A	B	C	D	E	F	G	H	I
18039	98.8	06/02/10	-	-	-	-	-	-
20729	206.9	12/28/10	209	8	2.5-23.7	0.42–0.037	0.03-0.02-0.1	120-25.2
21652	251.8	03/10/11	72	5	0.0-28.5	1.16-0.111	0.02-0.01-0.06	110-25.2
22364	286.6	05/05/11	56	17	0.1-21.0	1.77-0.170	0.08-0.04-0.24	110-25.8
23142	322.4	07/04/11	60	4.5	0.0-21.5	1.52-0.136	0.02-0.01-0.06	110-24.8
23353	331.6	07/21/11	17	1	0.1-31.0	0.94-0.083	0.004-0.001-0.01	115-26.7
23564	340.4	08/06/11	16	13.4	0.2-33.2	1.98-0.846	0.06-0.03-0.18	120-43.3
23920	354.85	09/03/11	28	8.5	0.0-33.5	0.73-0.500	0.04-0.02-0.11	145-62.05
27032	105.0	05/02/12	242	5	0.0-18.2	0.29-0.025	0.02-0.1-0.06	110-25.9

TABLE C.1: **Parameters of HiRISE images composing the time-series**. A) Image IDs of the form ESP_0XXXXX_1890 with individual id listed in the column A. B) Solar Longitude (Ls) (degree). C) Acquisition date (mm/dd/yy). D) Number of Earth days between previous and current image. E) Parallax angle between previous and current image (degree). F) Registration residual (average and standard deviation) at the tie-points between the images and the reference image (ESP_018039_1890). G) Reptation sand flux ($m^3/m/yr$) (mean and error (1-σ)). H) Bias on the ripple displacement (m) due to the use of one unique DEM which does not capture the migration of the dune over time. This error is determined from the difference in emission angle between the two images, the average dune displacement between the DEM acquisition and the image, and the amplitude of the ripple migration, I) Ripple migration orientation (degree from North, positive counter-clockwise) (mode and standard deviation).

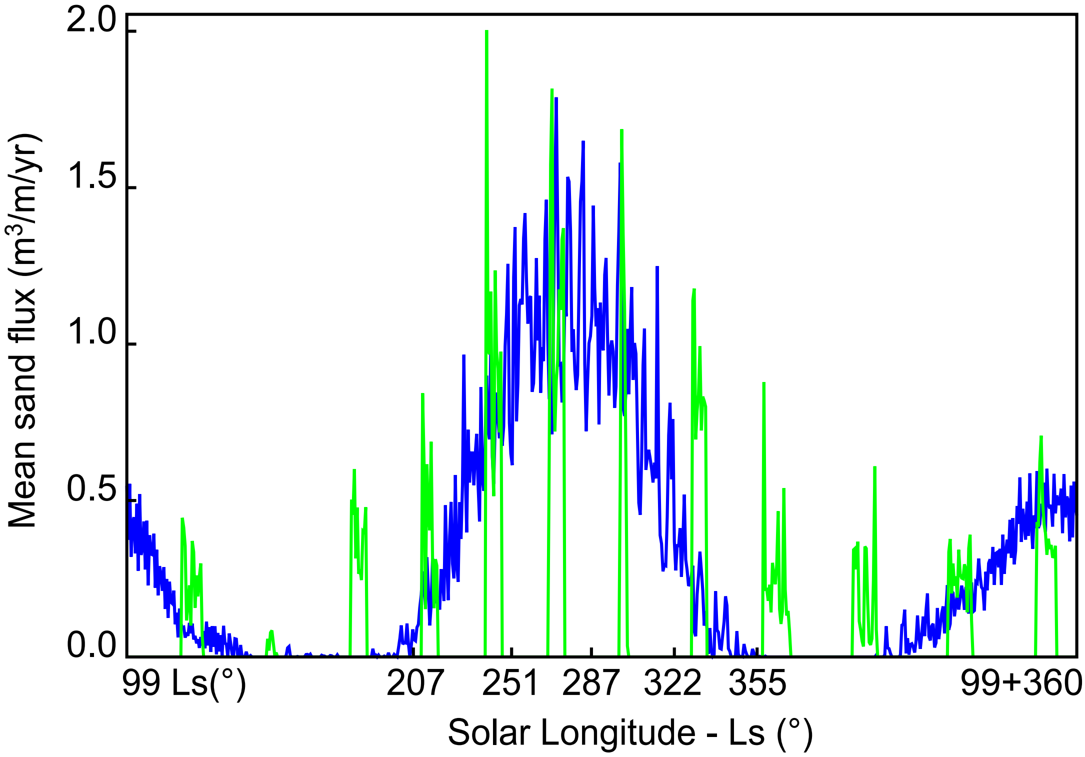

Figure C.1: Comparison between GCM and mesoscale sand fluxes predictions (using the Lettau & Lettau (Lettau, K and Lettau, HH, 1978) transport law, and a stress threshold of 0.01 N/m^2). GCM flux prediction (blue) was simulated every minute for a continuous Mars year, on a 2° resolution grid. Mesoscale flux prediction (green) was simulated every minute for 5–10 continuous days every 30° Ls, on a 1.5 km resolution grid. Both predictions display similar seasonal variation amplitude, suggesting 1) that most of the wind drivers are captured in the GCM in Nili Patera area, and 2) that the stress threshold estimated from the GCM would be in the same range as the stress threshold determined from the mesoscale. Note that on this graph, the mesoscale prediction has been linearly scaled (preserving the relative temporal variation) to allow comparison with the GCM prediction.

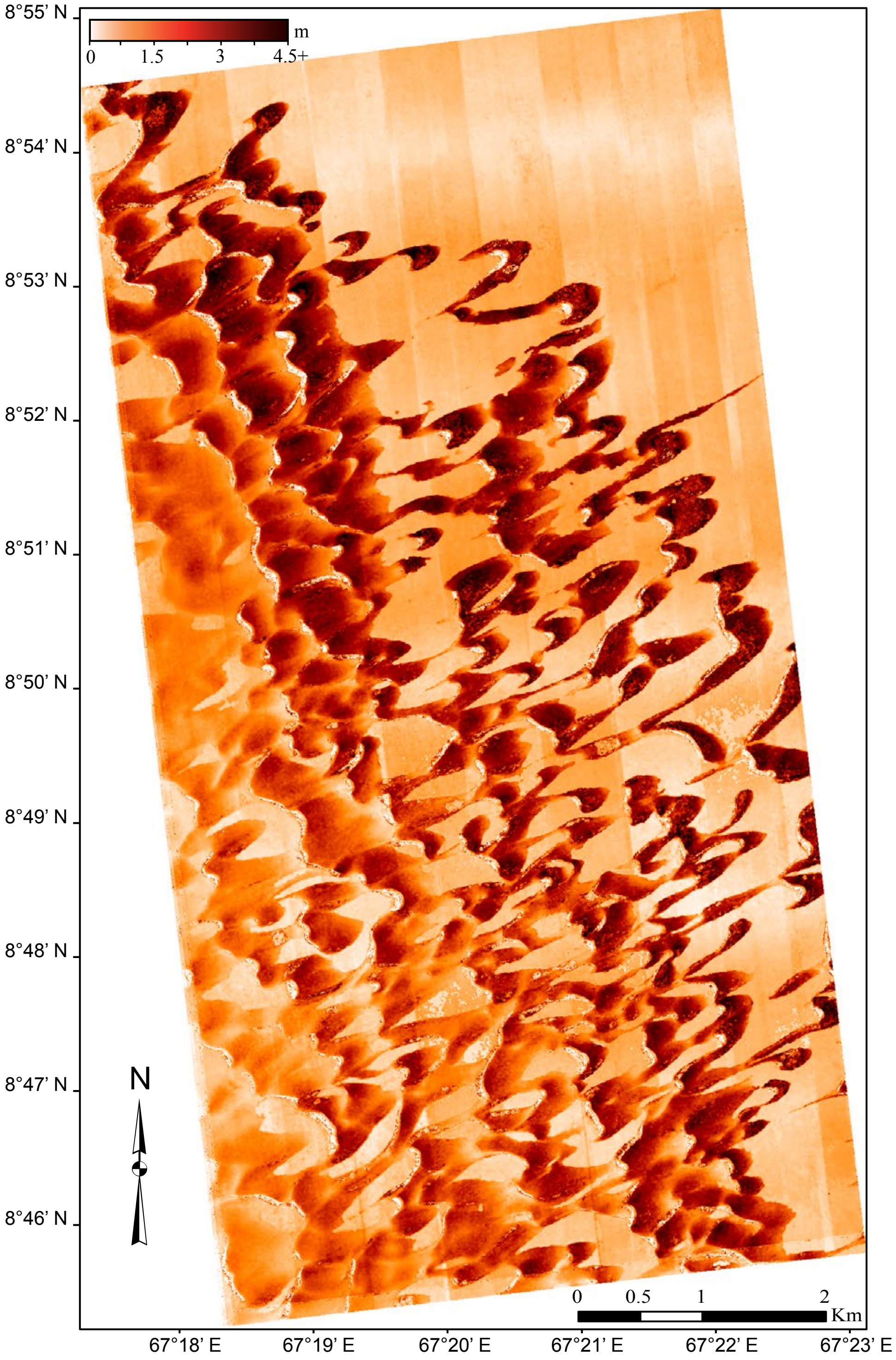

FIGURE C.2: First component of the PCA applied to the displacement maps time-series.

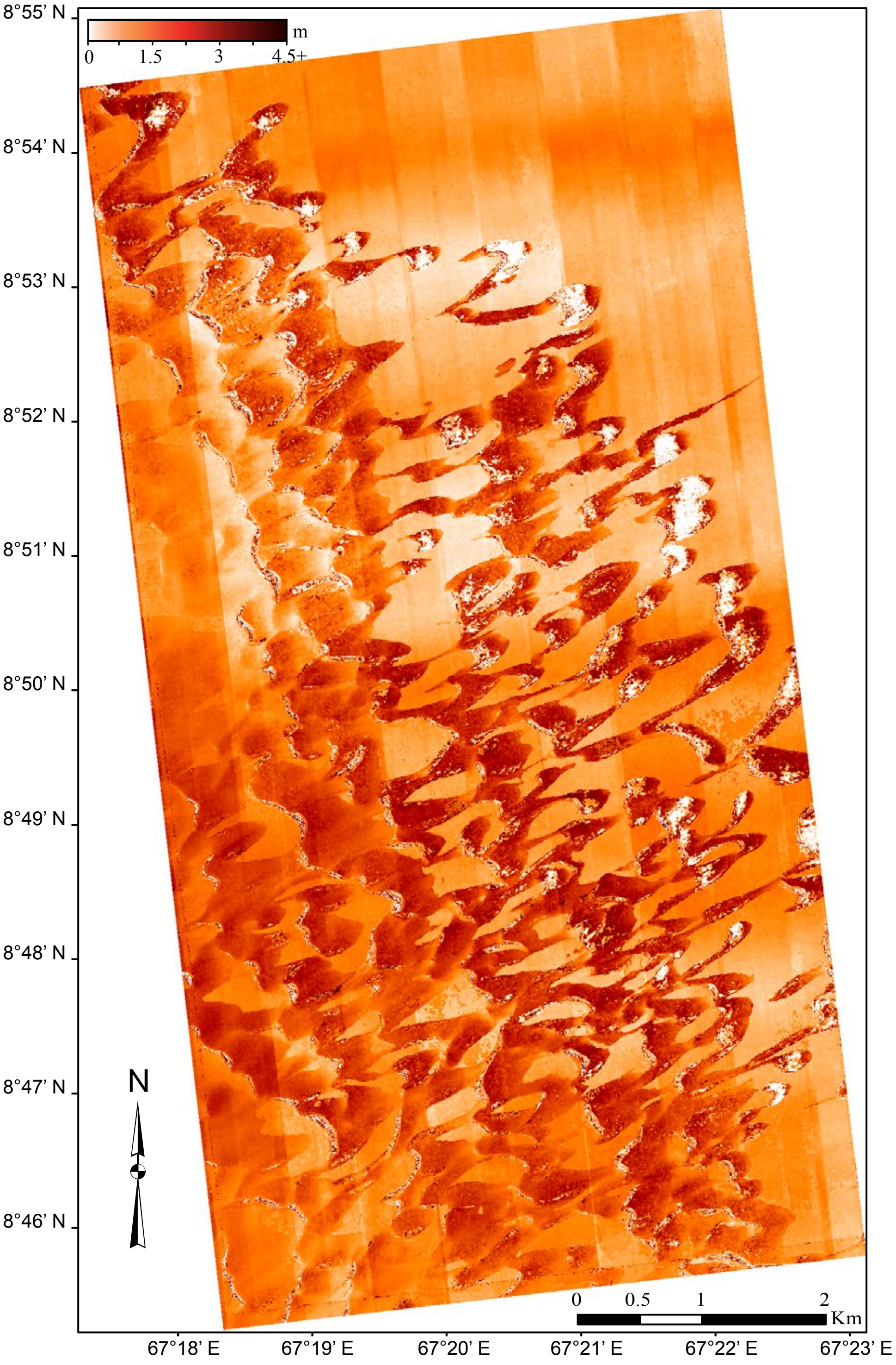

FIGURE C.3: second component of the PCA applied to the displacement maps time-series.

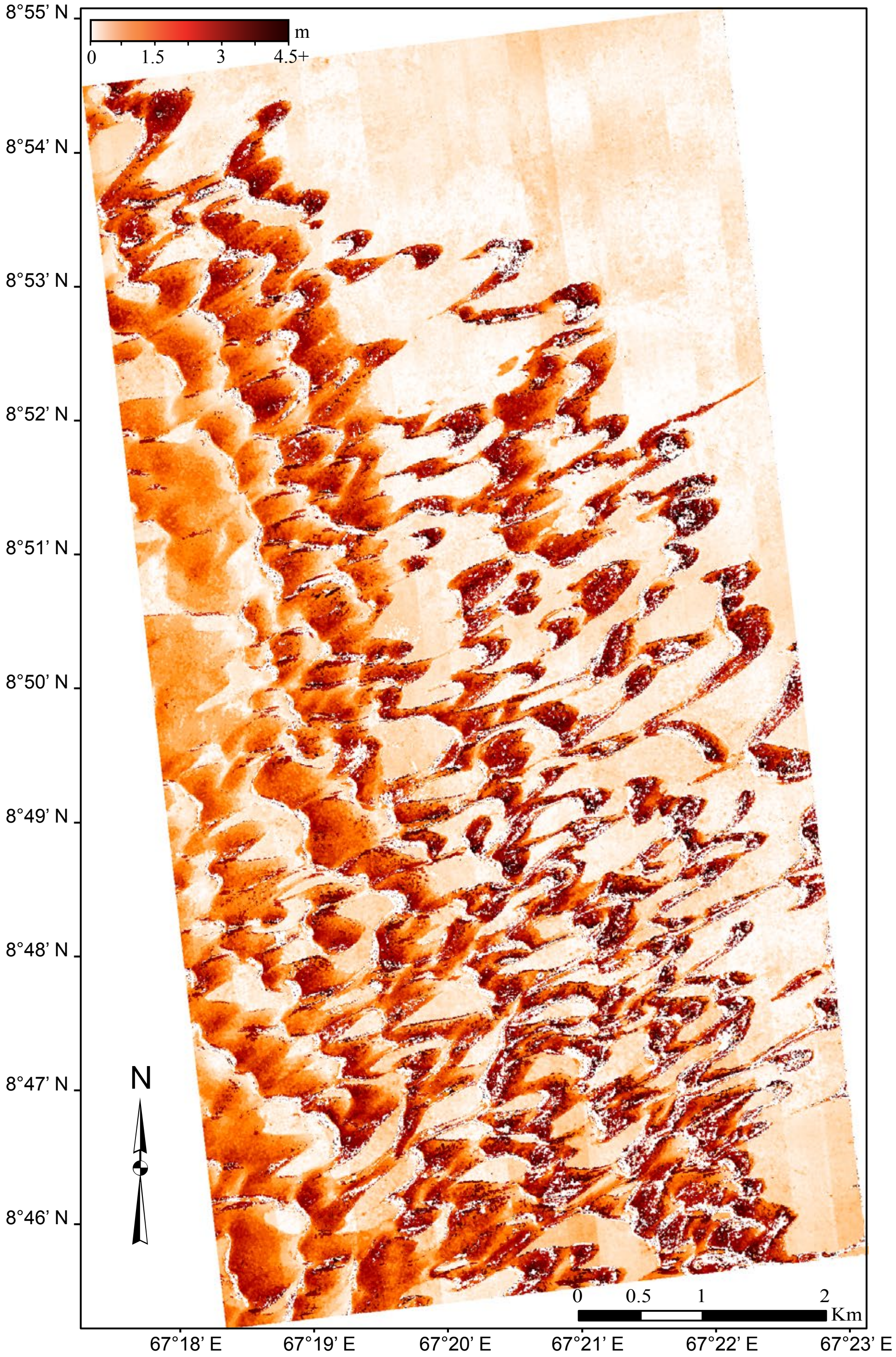

FIGURE C.4: Amplitude of the sand ripple displacements in the Nili Patera dune field derived from correlating HiRISE images 18039 and 20729 acquired 209 Earth days apart. The displacement map represented is the composition of the 2 first components (Figs. C.2, C.3) of the Principal Component Analysis (PCA) applied to the time-series. Azimuth of the ripples is given in Table C.1.

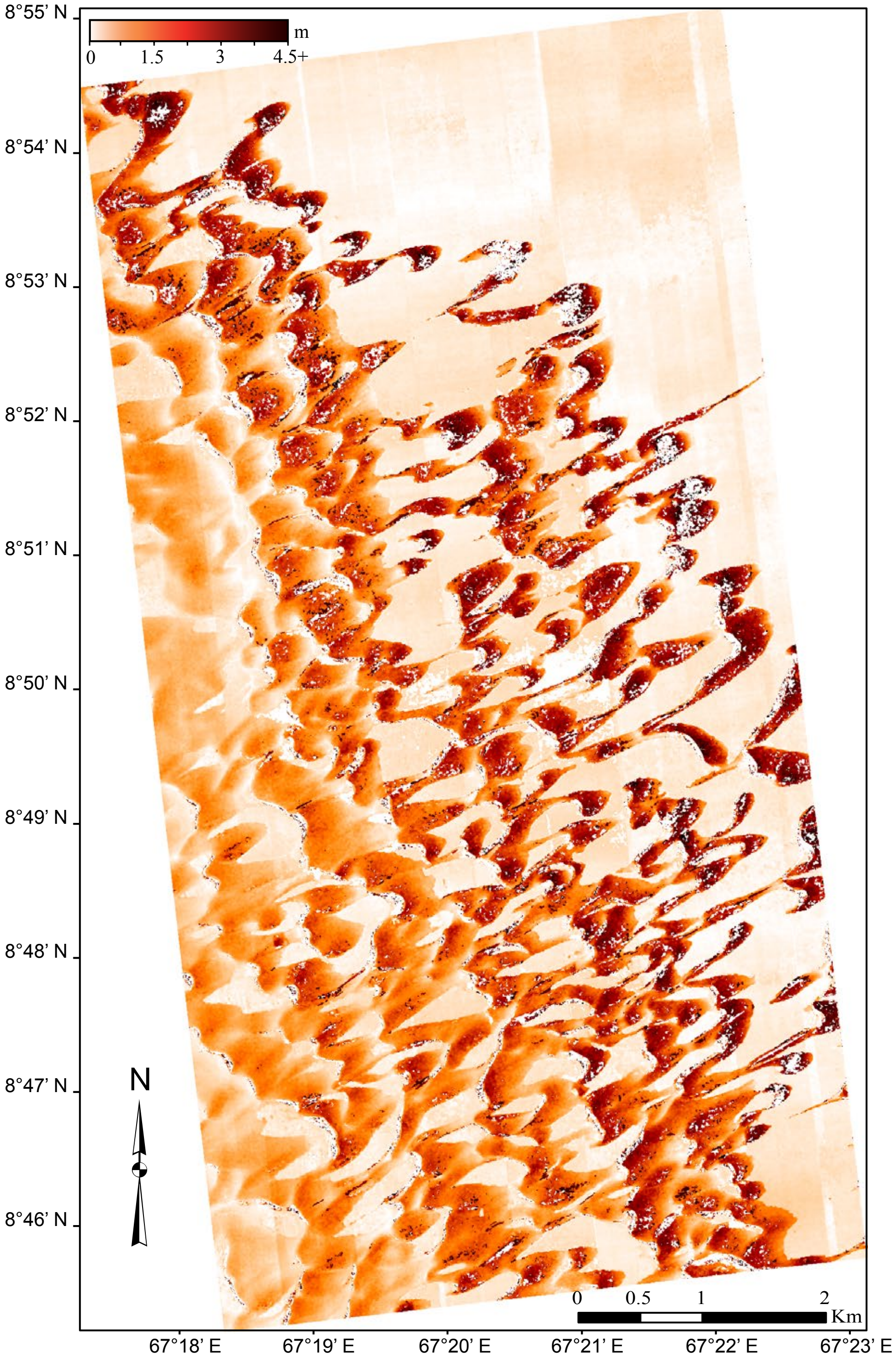

FIGURE C.5: Amplitude of the sand ripple displacements in the Nili Patera dune field derived from correlating HiRISE images 20729 and 21625 acquired 72 Earth days apart. The displacement map represented is the composition of the 2 first components (Figs. C.2, C.3) of the Principal Component Analysis (PCA) applied to the time-series. Azimuth of the ripples is given in Table C.1.

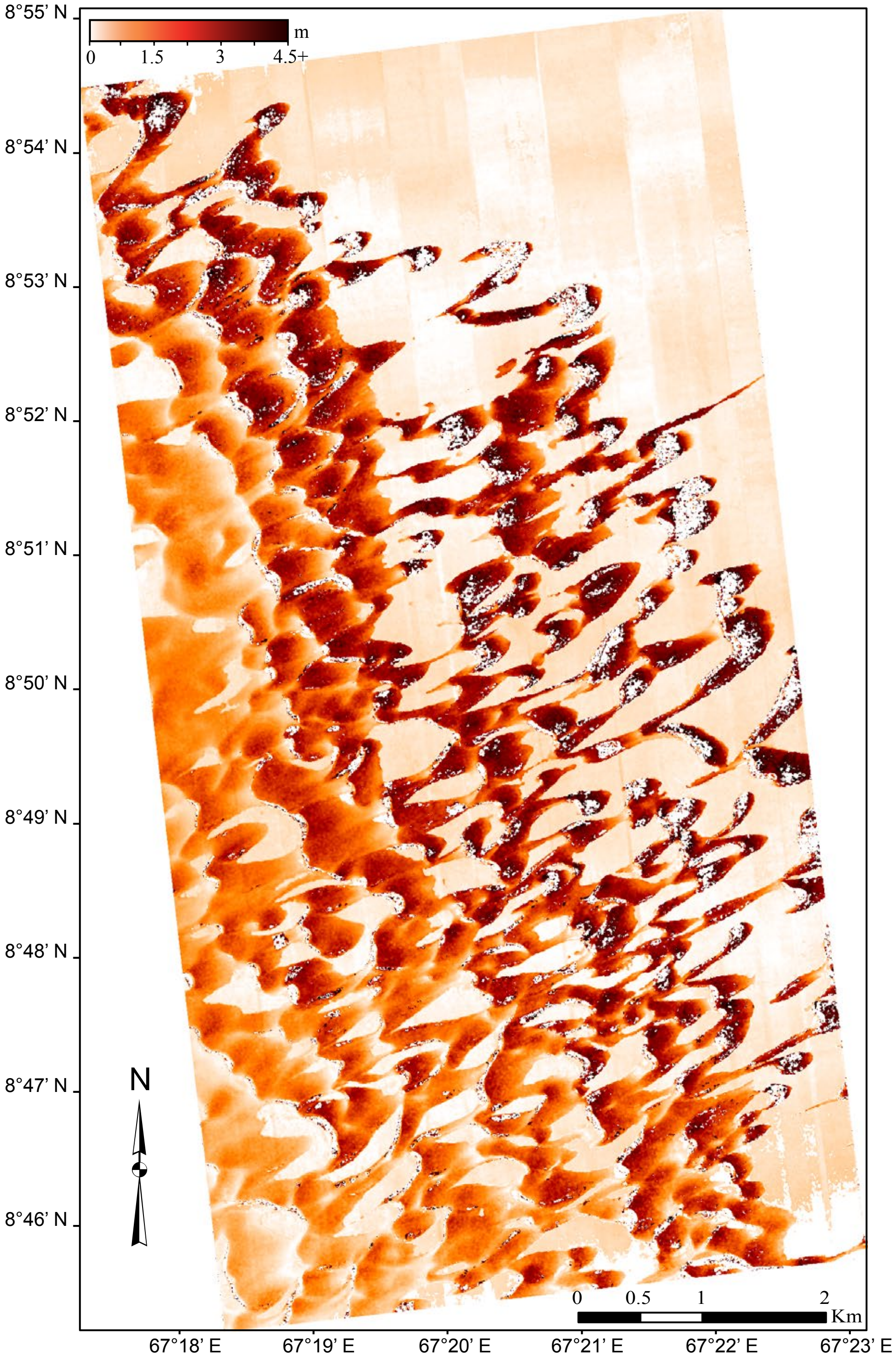

Figure C.6: Amplitude of the sand ripple displacements in the Nili Patera dune field derived from correlating HiRISE images 21625 and 22364 acquired 56 Earth days apart. The displacement map represented is the composition of the 2 first components (Figs. C.2, C.3) of the Principal Component Analysis (PCA) applied to the time-series. Azimuth of the ripples is given in Table C.1.

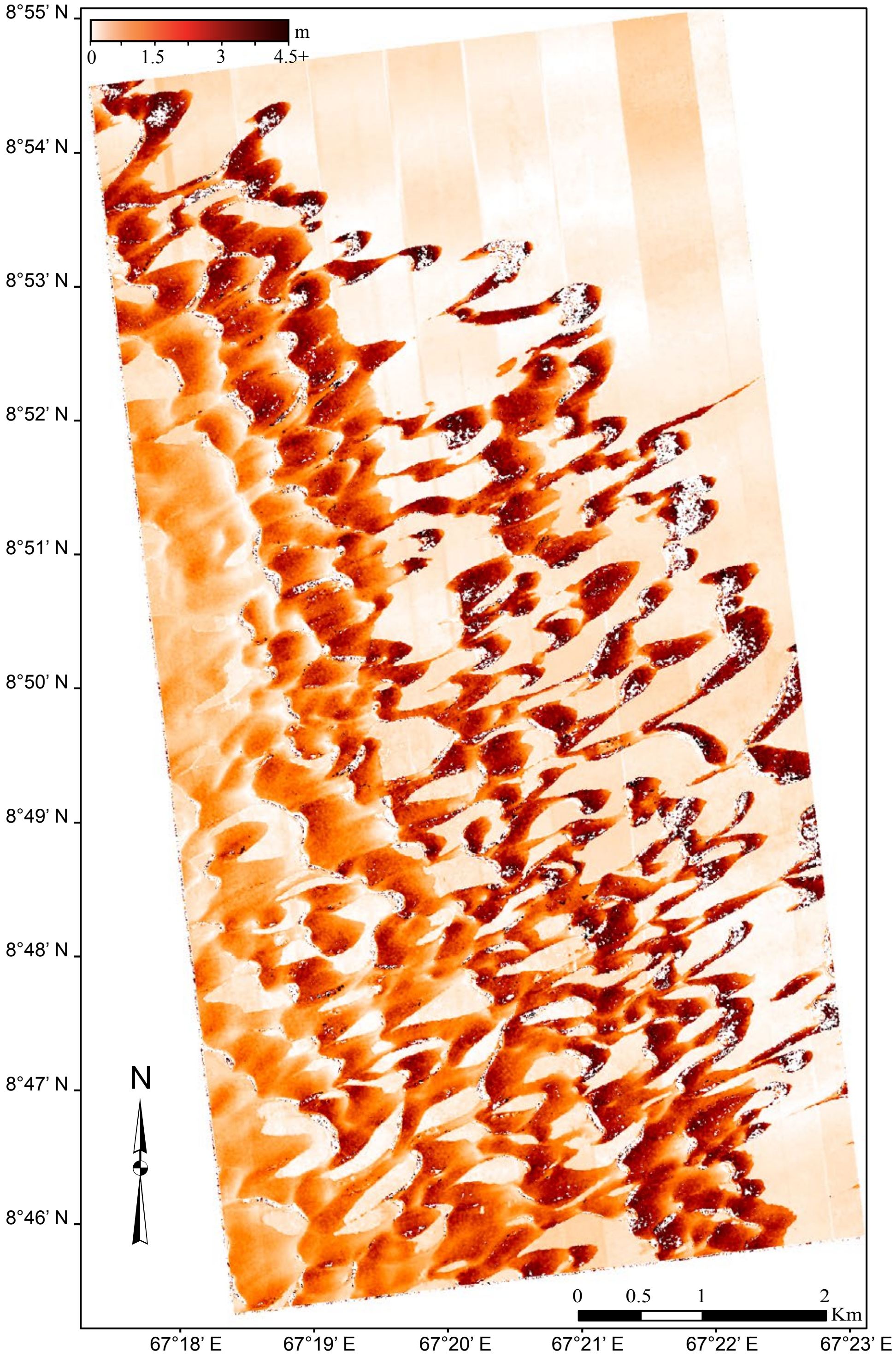

FIGURE C.7: Amplitude of the sand ripple displacements in the Nili Patera dune field derived from correlating HiRISE images 22364 and 23142 acquired 60 Earth days apart. The displacement map represented is the composition of the 2 first components (Figs. C.2, C.3) of the Principal Component Analysis (PCA) applied to the time-series. Azimuth of the ripples is given in Table C.1.

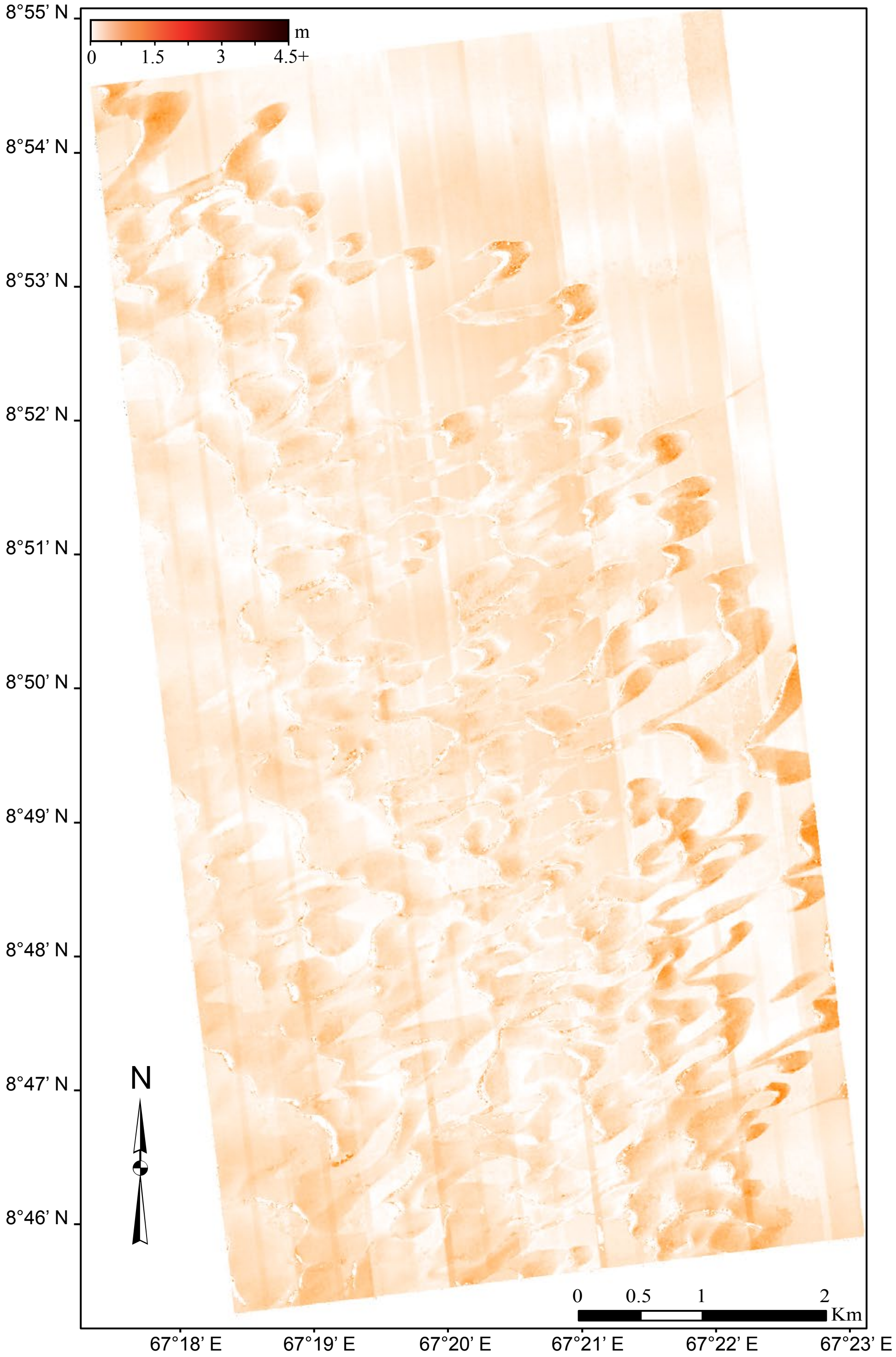

FIGURE C.8: Amplitude of the sand ripple displacements in the Nili Patera dune field derived from correlating HiRISE images 23142 and 23353 acquired 17 Earth days apart. The displacement map represented is the composition of the 2 first components (Figs. C.2, C.3) of the Principal Component Analysis (PCA) applied to the time-series. Azimuth of the ripples is given in Table C.1.

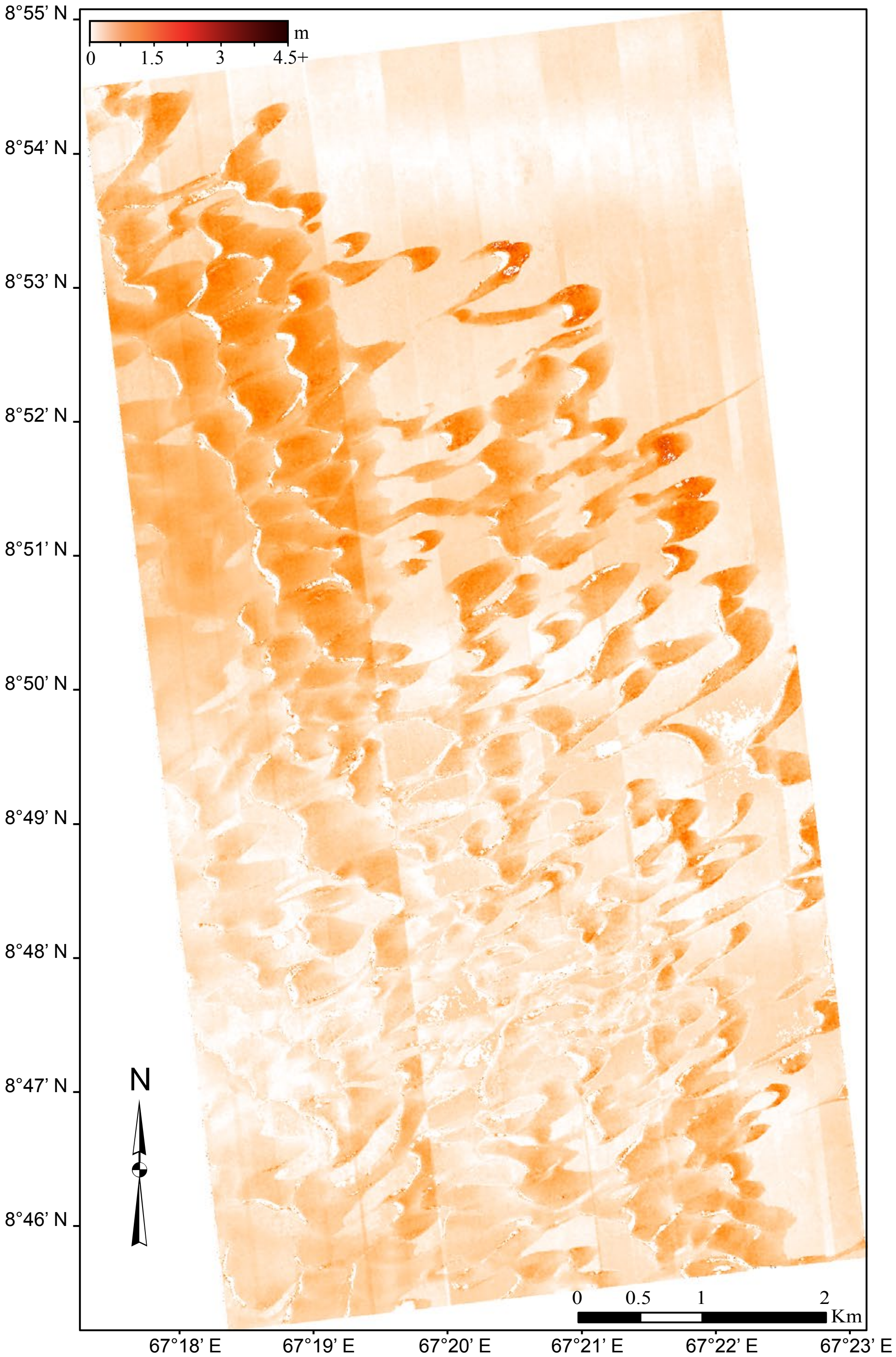

FIGURE C.9: Amplitude of the sand ripple displacements in the Nili Patera dune field derived from correlating HiRISE images 23353 and 23564 acquired 16 Earth days apart. The displacement map represented is the composition of the 2 first components (Figs. C.2, C.3) of the Principal Component Analysis (PCA) applied to the time-series. Azimuth of the ripples is given in Table C.1.

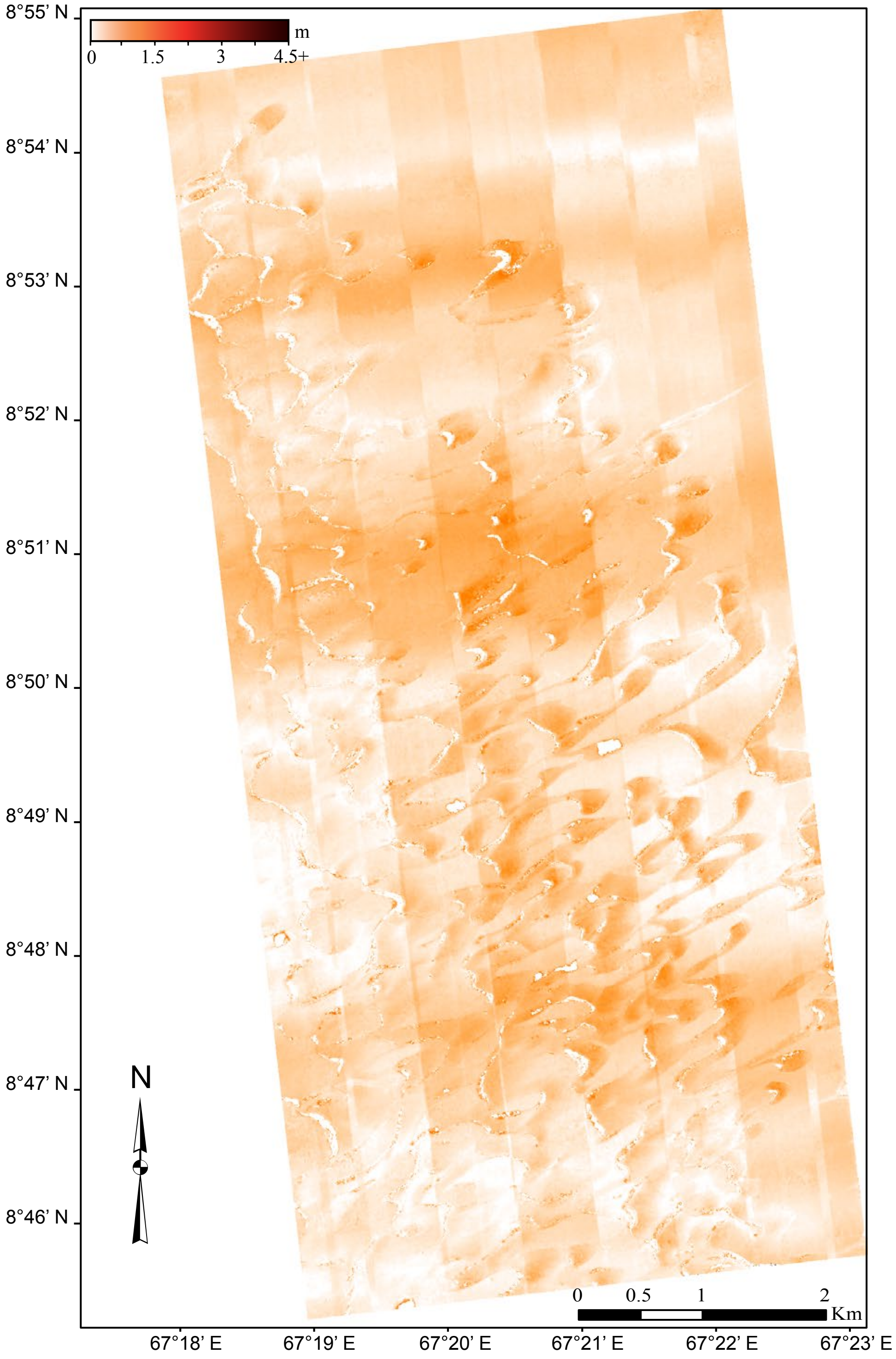

FIGURE C.10: Amplitude of the sand ripple displacements in the Nili Patera dune field derived from correlating HiRISE images 23564 and 23920 acquired 28 Earth days apart. The displacement map represented is the composition of the 2 first components (Figs. C.2, C.3) of the Principal Component Analysis (PCA) applied to the time-series. Azimuth of the ripples is given in Table C.1.

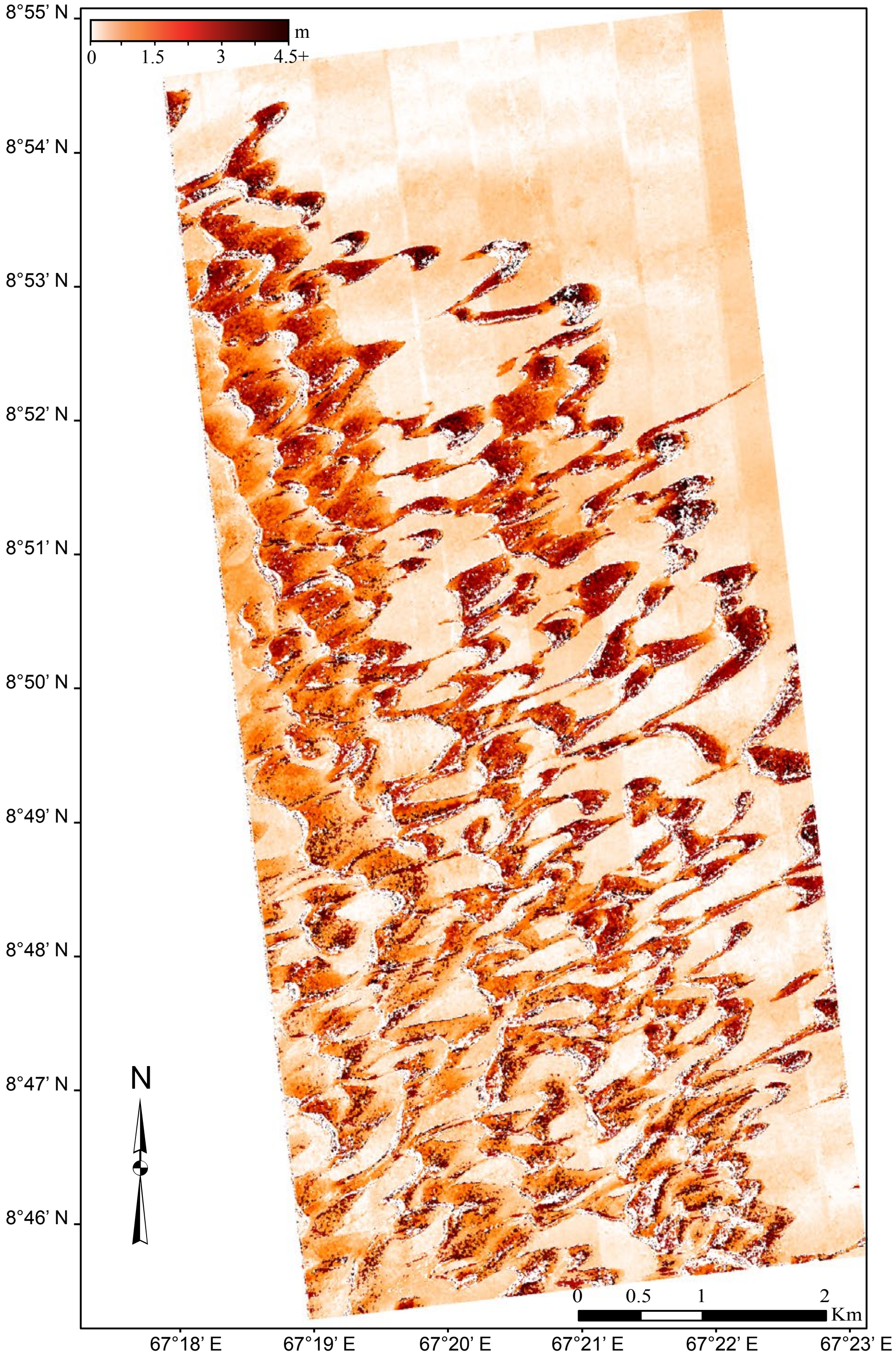

FIGURE C.11: Amplitude of the sand ripple displacements in the Nili Patera dune field derived from correlating HiRISE images 23920 and 27032 acquired 242 Earth days apart. The displacement map represented is the composition of the 2 first components (Figs. C.2, C.3) of the Principal Component Analysis (PCA) applied to the time-series. Azimuth of the ripples is given in Table C.1.

Bibliography

A. Agnon and V. Lyakhovsky. Damage Distribution and Localization During Dyke Intrusion. In Heimann Baer, editor, *Physics and Chemistry of Dykes*, pages 65–78. Balkema, Rotterdam, 1995.

MP Almeida, EJR Parteli, JrJS Andrade, and HJ Herrmann. Giant saltation on Mars. *Proceedings of the National Academy of Sciences fo the USA*, 105(17): 6222–6226, APR 29 2008. ISSN 0027-8424. doi: {10.1073/pnas.0800202105}.

RS Anderson. A theoretical model for aeolian impact ripples. *Sedimentology*, 34(5):943–956, OCT 1987. ISSN 0037-0746. doi: {10.1111/j.1365-3091.1987.tb00814.x}.

B Andreotti. A two-species model of aeolian sand transport. *Journal of Fluid Mechanics*, 510:47–70, JUL 10 2004. ISSN 0022-1120. doi: {10.1017/S0022112004009073}.

B Andreotti, P Claudin, and O Pouliquen. Aeolian sand ripples: Experimental study of fully developed states. *Physical Review Letters*, 96(2), JAN 20 2006. ISSN 0031-9007. doi: {10.1103/PhysRevLett.96.028001}.

JC Armstrong and CB Leovy. Long term wind erosion on Mars. *Icarus*, 176(1): 57–74, JUL 2005. ISSN 0019-1035. doi: {10.1016/j.icarus.2005.01.005}.

T Árnadóttir, F Sigmundsson, and P Delaney. Sources of crustal deformation associated with the Krafla, Iceland, eruption of September 1984. *Geophysical Research Letters*, 25(7):1043–1046, 1998.

T Árnadóttir, B Lund, W Jiang, H Geirsson, H Björnsson, P Einarsson, and T Sigurdsson. Glacial rebound and plate spreading: results from the first countrywide GPS observations in Iceland. *Geophysical Journal International*, 177:691–716, 2009.

RE Arvidson, EA Guinness, HJ Moore, J Tillman, and SD Wall. 3 Mars years - Viking-Lander-1 imaging observations. *Science*, 222(4623):463–468, 1983. ISSN 0036-8075. doi: {10.1126/science.222.4623.463}.

GM Ashley. Classification of large-scale subaqueous bedforms - A new look at an old problem - SEPM bedforms and bedding structures. *Journal of Sedimentary Petrology*, 60(1):160–172, JAN 1990. ISSN 0022-4472.

ASPRS. *Manual of Photogrammetry - Fifth Edition.* McGlone, 5th edition, 2004.

JP Avouac, F Ayoub, S Leprince, O Konca, and DV Helmberger. The 2005, M-w 7.6 Kashmir earthquake: Sub-pixel correlation of ASTER images and seismic waveforms analysis. *Earth and Planetary Science Letters*, 249(3-4):514–528, SEP 30 2006. ISSN 0012-821X. doi: {10.1016/j.epsl.2006.06.025}.

F Ayoub, S Leprince, R Binet, K Lewis, O Aharonson, and JP Avouac. Influence of camera distortions on satellite image registration and change detection applications. In *Proceedings IGARSS*, Boston, MA, 2008.

F Ayoub, S Leprince, and JP Avouac. Co-registration and correlation of aerial photographs for ground deformation measurements. *ISPRS Journal of Photogrammetry and Remote Sensing*, 64(6):551–560, NOV 2009. ISSN 0924-2716. doi: {10.1016/j.isprsjprs.2009.03.005}.

F Ayoub, J-P Avouac, CE Newman, MI Richardson, A Lucas, S Leprince, and NT Bridges. Threshold for sand mobility on Mars calibrated from seasonal variations of sand flux. *Nature Communications*, 5, SEP 2014. ISSN 2041-1723. doi: {10.1038/ncomms6096}.

Bagnold, RA. *The Physics of Blown Sand and Desert Dunes.* Dover Publications, 1954.

DC Bamber, P Palmer, and S Mackin. High performance attitude determination through analysis of geometric distortions within earth observational satellite imagery. In *20th Annual AIAA/USU Conference on small satellites*, Utah, 2006.

I Barisin, S Leprince, B Parsons, and T Wright. Surface displacements in the September 2005 Afar rifting event from satellite image matching: Asymmetric uplift and faulting. *Geophysical Research Letters*, 36:L07301, 2009. doi: 10.1029/2008GL036431.

S Basu and MI Richardson. Simulation of the Martian dust cycle with the GFDL mars GCME. *Journal of Geophysical Research - Planets*, 109(E11), NOV 24 2004. ISSN 0148-0227. doi: {10.1029/2004JE002243}.

MD Behn, WR Buck, and IS Sacks. Topographic controls on dike injection in volcanic rift zones. *Earth and Planetary Science Letters*, 246(3–4):188–196, 2006. doi: 10.1016/j.epsl.2006.04.005.

E Berthier, H Vadon, D Baratoux, Y Arnaud, C Vincent, KL Feigl, F Remy, and B Legresy. Surface motion of mountain glaciers derived from satellite optical imagery. *Remote Sensing of Environment*, 95(1):14–28, MAR 15 2005. ISSN 0034-4257. doi: {10.1016/j.rse.2004.11.005}.

R Binet and L Bollinger. Horizontal coseismic deformation of the 2003 Bam (Iran) earthquake measured from SPOT-5 THR satellite imagery. *Geophysical Research Letters*, 32(2), JAN 28 2005. ISSN 0094-8276. doi: {10.1029/2004GL021897}.

A Björnsson. Dynamics of Crustal Rifting in NE Iceland. *Journal of Geophsical Research*, 90(B12):10151–10162, 1985.

A Björnsson, K Saemundsson, P Einarsson, E Tryggvason, and K Gronvold. Current rifting episode in North Iceland. *Nature*, 266:318–323, 1977.

FL Bookstein. Principal warps - thin-plate splines and the decomposition of deformations. *IEEE Transactions on Pattern Analysis and Machine Intelligence*, 11(6):567–585, JUN 1989. ISSN 0162-8828. doi: {10.1109/34.24792}.

MC Bourke, RC Ewing, D Finnegan, and HA McGowan. Sand dune movement in the Victoria Valley, Antarctica. *Geomorphology*, 109(3-4):148–160, AUG 15 2009. ISSN 0169-555X. doi: {10.1016/j.geomorph.2009.02.028}.

B Brandsdotttir, W Menke, P Einarsson, RS White, and RK Staples. Faroe-Iceland ridge experiment 2. Crustal structure of Krafia central volcano. *Journal of Geophysical Research*, 102:7867–7886, 1997.

NT Bridges, J Phoreman, BR White, R Greeley, EE Eddlemon, GR Wilson, and CJ Meyer. Trajectories and energy transfer of saltating particles onto rock surfaces: Application to abrasion and ventifact formation on Earth and Mars. *Journal of Geophysical Research - Planets*, 110(E12), DEC 7 2005. ISSN 0148-0227. doi: {10.1029/2004JE002388}.

NT Bridges, F Ayoub, JP Avouac, S Leprince, A Lucas, and S Mattson. Earth-like sand fluxes on Mars. *Nature*, 485(7398):339–342, MAY 17 2012a. ISSN 0028-0836. doi: {10.1038/nature11022}.

NT Bridges, MC Bourke, PE Geissler, ME Banks, C Colon, S Diniega, MP Golombek, CJ Hansen, S Mattson, AS McEwen, MT Mellon, N Stantzos, and BJ Thomson. Planet-wide sand motion on Mars. *Geology*, 40(1):31–34, JAN 2012b. ISSN 0091-7613. doi: {10.1130/G32373.1}.

W.R. Buck, P. Einarsson, and B. Brandsdóttir. Tectonic stress and magma chamber size as controls on dike propagation: constraints from the 1975-1984 Krafla rifting episode. *Journal of Geophsical Research*, 111:B12404, 2006. doi: 10.1029/2005JB003879.

M Chojnacki, DM Burr, JE Moersch, and TI Michaels. Orbital observations of contemporary dune activity in Endeavor crater, Meridiani Planum, Mars. *Journal of Geophysical Research - Planets*, 116, APR 7 2011. ISSN 2169-9097. doi: {10.1029/2010JE003675}.

P Claudin and B Andreotti. A scaling law for aeolian dunes on Mars, Venus, Earth, and for subaqueous ripples. *Earth and Planetary Science Letters*, 252 (1-2):30–44, NOV 30 2006. ISSN 0012-821X. doi: {10.1016/j.epsl.2006.09.004}.

A Copley, JP Avouac, J Hollingsworth, and S Leprince. The 2001 Mw 7.6 Bhuj earthquake, low fault friction, and the crustal support of plate driving forces in India. *Journal of Geophysical Research*, 116:B08405, 2011. doi: 10.1029/2010JB008137.

RE Crippen. Measurement of subresolution terrain displacements using SPOT panchromatic imagery. *Episodes*, 15(1):56–61, MAR 1992. ISSN 0705-3797.

J.B. De Chabalier and J.P. Avouac. Kinematics of the Asal rift (Djibouti) determined from the deformation of Fieale volcano. *Science*, 265:1677–1681, 1994.

M de Michele and P Briole. Deformation between 1989 and 1997 at Piton de la Fournaise volcano retrieved from correlation of panchromatic airborne images. *Geophysical Journal International*, 169(1):357–364, APR 2007. ISSN 0956-540X. doi: {10.1111/j.1365-246X.2006.03307.x}.

M De Michele, D Raucoules, H Aochi, N Baghdadi, and C Carnec. Measuring coseismic deformation on the northern segment of the bam-baravat escarpment associated with the 2003 bam (iran) earthquake, by correlation of very-high-resolution satellite imagery. *Geophysical Journal International*, 173(2):459–464, 2008. doi: 10.1111/j.1365-246X.2008.03743.x.

E de Zeeuw-van Dalfsen, R Pedersen, F Sigmundsson, and C Pagli. Satellite radar interferometry 1993-1999 suggests deep accumulation of magma near the crust-mantle boundary at the Krafla volcanic system, Iceland. *Geophysical Research Letters*, 31:L13611, 2004.

C Delacourt, P Allemand, B Casson, and H Vadon. Velocity field of the "La Clapiere" landslide measured by the correlation of aerial and QuickBird satellite images. *Geophysical Research Letters*, 31(15), AUG 14 2004. ISSN 0094-8276. doi: {10.1029/2004GL020193}.

CJ DiCaprio. *Measuring and modeling viscoelastic relaxation of the lithosphere with application to the northern volcanic zone, Iceland*. PhD thesis, California Institute of Technology, 2010. URL `http://thesis.library.caltech.edu/5538/`.

S Dominguez, JP Avouac, and R Michel. Horizontal coseismic deformation of the 1999 Chi-Chi earthquake measured from SPOT satellite images: Implications for the seismic cycle along the western foothills of central Taiwan. *Journal of Geophysical Research - Solid Earth*, 108(B2), FEB 7 2003. ISSN 0148-0227. doi: {10.1029/2001JB000951}.

WX Du, LR Sykes, BE Shaw, and CH Scholz. Triggered aseismic fault slip from nearby earthquakes, static or dynamic effect? *Journal of Geophysical Research - Solid Earth*, 108(B2), FEB 28 2003. ISSN 0148-0227. doi: {10.1029/2002JB002008}.

O Duran, P Claudin, and B Andreotti. On aeolian transport: Grain-scale interactions, dynamical mechanisms and scaling laws. *Aeolian Research*, 3(3):243–270, DEC 2011. ISSN 1875-9637. doi: {10.1016/j.aeolia.2011.07.006}.

P Einarsson. Earthquakes and present-day tectonism in Iceland. *Tectonophysics*, 189:261–279, 1991.

P Einarsson and B Brandsdottir. Seismological Evidence for lateral Magma Intrusion during the July 1978 deflation of the Krafla volcano in NE-Iceland. *Journal of Geophysics*, 47:160–165, 1980.

ER Engdahl, R van der Hilst, and R Buland. Global teleseismic earthquake relocation with improved travel times and procedures for depth determination. *Bulletin of the Seismological Society of America*, 88(3):722–743, June 1998.

JA Ewart, B Voight, and A Björnsson. Elastic deformation models of Krafla Volcano, Iceland, for the decade 1975 through 1985. *Bulletin of Volcanology*, 53: 436–459, 1991.

KL Feigl, F Sarti, H Vadon, S McClusky, S Ergintav, P Durand, R Burgmann, A Rigo, D Massonnet, and R Reilinger. Estimating slip distribution for the Izmit mainshock from coseismic GPS, ERS-1, RADARSAT, and SPOT measurements. *Bulletin of the Seismological Society of America*, 92(1):138–160, FEB 2002. ISSN 0037-1106. doi: {10.1785/0120000830}.

LK Fenton and TJ Michaels. Characterizing the sensitivity of daytime turbulent activity on Mars with MRAMS LES: early results. *Mars*, 5:159–171, 2010.

LK Fenton and MI Richardson. Martian surface winds: Insensitivity to orbital changes and implications for aeolian processes. *Journal of Geophysical Research - Planets*, 106(E12):32885–32902, DEC 25 2001. ISSN 0148-0227. doi: {10.1029/2000JE001407}.

LK Fenton, AD Toigo, and MI Richardson. Aeolian processes in Proctor Crater on Mars: Mesoscale modeling of dune-forming winds. *Journal of Geophysical Research - Planets*, 110(E6), JUN 16 2005. ISSN 0148-0227. doi: {10.1029/2004JE002309}.

Y Fialko, M Simons, and D Agnew. The complete (3-D) surface displacement field in the epicentral area of the 1999 M(w)7.1 Hector Mine earthquake, California, from space geodetic observations. *Geophysical Research Letters*, 28(16):3063–3066, AUG 15 2001. ISSN 0094-8276. doi: {10.1029/2001GL013174}.

YA Fialko and AM Rubin. Thermodynamics of lateral dike propagation: Implications for crustal accretion at slow spreading midocean ridges. *Journal of Geophsical Research*, 103:2501–2514, 1998.

GR Foulger, RE Long, P Einarsson, and A Bjornsson. Implosive earthquakes at the active accretionary plate boundary in northern Iceland. *Nature*, 337: 640–642, 1989.

MP Golombek, JA Grant, LS Crumpler, R Greeley, RE Arvidson, JF Bell, CM Weitz, R Sullivan, PR Christensen, LA Soderblom, and SW Squyres. Erosion rates at the Mars Exploration Rover landing sites and long-term climate change on Mars. *Journal of Geophysical Research - Planets*, 111(E12), DEC 8 2006. ISSN 2169-9097. doi: {10.1029/2006JE002754}.

R Grandin, A Socquet, R Binet, Y Klinger, E Jacques, JB de Chabalier, GCP King, C Lasserre, S Tait, P Tapponnier, A Delorme, and P Pinzuti. September 2005 Manda Hararo-Dabbahu rifting event, Afar (Ethiopia): Constraints provided by geodetic data. *Journal of Geophsical Research*, 114:B08404, 2009. doi: 10.1029/2008JB005843.

R Grandin, A Socquet, MP Doin, E Jacques, JB de Chabalier, and GCP King. Transient rift opening in response to multiple dike injections in the Manda Hararo rift (Afar, Ethiopia) imaged by time-dependent elastic inversion of interferometric synthetic aperture radar data. *Journal of Geophsical Research*, 115:B09403, 2010a. doi: 10.1029/2009JB006883.

R Grandin, A Socquet, E Jacques, N Mazzoni, JB de Chabalier, and GCP King. Sequence of rifting in Afar, Manda-Hararo rift, Ethiopia, 2005-2009: Time-space evolution and interactions between dikes from interferometric synthetic aperture radar and static stress change modeling. *Journal of Geophsical Research*, 115: B10413, 2010b. doi: 10.1029/2009JB000815.

R Grandin, A Socquet, C Doubre, E Jacques, and GCP King. Elastic thickness control of lateral dyke intrusion at mid-ocean ridges. *Earth and Planetary Science Letters*, 319–320:83–95, 2012.

R Greeley, RN Leach, SH Williams, BR White, JB Pollack, DH Krinsley, and JR Marshall. Rate of wind abrasion on Mars. *Journal of Geophysical Research*, 87(NB12):9–24, 1982. ISSN 0148-0227. doi: {10.1029/JB087iB12p10009}.

R Greeley, A Skypeck, and JB Pollack. Martian aeolian features and deposits - Comparisons with General Circulation Model results. *Journal of Geophysical Research - Planets*, 98(E2):3183–3196, FEB 25 1993. ISSN 0148-0227. doi: {10.1029/92JE02580}. Workshop on the Martian surface and atmosphere through time, Boulde, CO, SEP 23-25, 1991.

Greeley, R and Iversen, JD. *Winds as a geological process*. Cambridge University Press, 1985.

K Gronvold. Composition of Krafla Lavas 1975-84. *American Geophysical Union, Fall Meeting*, pages T33E–08, 2006.

JP Grotzinger, RE Arvidson, JF Bell, W Calvin, BC Clark, DA Fike, M Golombek, R Greeley, A Haldemann, KE Herkenhoff, BL Jolliff, AH Knoll, M Malin, SM McLennan, T Parker, L Soderblom, JN Sohl-Dickstein, SW Squyres, NJ Tosca, and WA Watters. Stratigraphy and sedimentology of a dry to wet eolian depositional system, Burns formation, Meridiani Planum, Mars. *Earth and Planetary Science Letters*, 240(1):11–72, NOV 30 2005. ISSN 0012-821X. doi: {10.1016/j.epsl.2005.09.039}.

RA Haberle, JR Murphy, and J Schaeffer. Orbital change experiments with a Mars general circulation model. *Icarus*, 161(1):66–89, JAN 2003. ISSN 0019-1035. doi: {10.1016/S0019-1035(02)00017-9}.

RM Haberle, CB Leovy, and JB Pollack. Some effects of global dust storms on the atmospheric circulation of Mars. *Icarus*, 50(2-3):322–367, 1982. ISSN 0019-1035. doi: {10.1016/0019-1035(82)90129-4}.

CJ Hansen, M Bourke, NT Bridges, S Byrne, C Colon, S Diniega, C Dundas, K Herkenhoff, A McEwen, M Mellon, G Portyankina, and N Thomas. Seasonal Erosion and Restoration of Mars' Northern Polar Dunes. *Science*, 331(6017): 575–578, FEB 4 2011. ISSN 0036-8075. doi: {10.1126/science.1197636}.

E Hauksson. Episodic rifting and volcanism at Krafla in North Iceland: growth of large ground fissures along the plate boundary. *Journal of Geophsical Research*, 88:626–636, 1983.

J Hollingsworth, S Leprince, F Ayoub, and JP Avouac. Deformation during the 1975-1984 Krafla rifting crisis, NE Iceland, measured from historical optical imagery. *Journal of Geophysical Reserach - Solid Earth*, 117, NOV 14 2012. ISSN 2169-9313. doi: {10.1029/2012JB009140}.

J Hollingsworth, S Leprince, F Ayoub, and JP Avouac. New constraints on dike injection and fault slip during the 1975-1984 Krafla rift crisis, NE Iceland. *Journal of Geophysical Reserach - Solid Earth*, 118(7):3707–3727, JUL 2013. ISSN 2169-9313. doi: {10.1002/jgrb.50223}.

KW Hudnut, Y Bock, M Cline, P Fang, Y Feng, J Freymueller, X Ge, WK Gross, D Jackson, M Kim, NE King, J Langbein, SC Larsen, M Lisowski, ZK Shen, J Svarc, and J Zhang. Coseismic displacements of the 1992 Landers earthquake sequence. *Bulletin of the Seismological Society of America*, 84(3):625–645, JUN 1994. ISSN 0037-1106.

JD Iversen and BR White. Saltation Threshold on Earth, Mars and Venus. *Sedimentology*, 29(1):111–119, 1982. ISSN 0037-0746. doi: {10.1111/j.1365-3091.1982.tb01713.x}.

A Iwasaki and H Fujisada. Image correlation tool for ASTER geometric validation. In Fujisada, H and Lurie, JB and Aten, ML and Weber, K, editor, *Sensors, Systems and Next-generation Satellites VI*, volume 4881 of *Proceedings of the Society of Photo-Optical Instrumentation Enginners (SPIE)*, pages 111–120. SPIE, 2003. ISBN 0-8194-4663-7. doi: {10.1117/12.462616}. Conference on Sensors, Systems and Next-Generation Satellites VI, AGIA PELAGIA, GREECE, SEP 23-26, 2002.

K Jónasson. Rhyolite volcanism in the Krafla central volcano, north-east Iceland. *Bulletin of Volcanology*, 56(6–7):516–528, 1994.

JPL-NASA. Shuttle Radar Topography Mission, 2000. URL http://www2.jpl.nasa.gov/srtm/statistics.html.

BR Julian. Evidence for dyke intrusion earthquake mechanisms near Long Valley caldera, California. *Nature*, 303:323–325, 1983.

MA Kahre and RM Haberle. Mars CO2 cycle: Effects of airborne dust and polar cap ice emissivity. *Icarus*, 207(2):648–653, JUN 2010. ISSN 0019-1035. doi: {10.1016/j.icarus.2009.12.016}.

RL Kirk, E Howington-Krauss, MR Rosiek, D Cook, J Anderson, K Becker, Archinal BA, L Keszthelyi, R King, and AS McEwen. Ultrahigh resolution topographic mapping of mars with hirise stereo images: Methods and first results. In *7th International Conference on Mars*, Pasadena, California, USA, July 2007.

Y Klinger, XW Xu, P Tapponnier, J Van der Woerd, C Lasserre, and G King. High-resolution satellite imagery mapping of the surface rupture and slip distribution of the M-W similar to 7.8, 14 November 2001 Kokoxili Earthquake, Kunlun Fault, northern Tibet, China. *Bulletin of the Seismological Society of America*, 95(5):1970–1987, OCT 2005. ISSN 0037-1106. doi: {10.1785/0120040233}.

Y Klinger, R Michel, and GCP King. Evidence for an earthquake barrier model from Mw similar to 7.8 Kokoxili (Tibet) earthquake slip-distribution. *Earth and Planetary Science Letters*, 242(3-4):354–364, FEB 28 2006. ISSN 0012-821X. doi: {10.1016/j.epsl.2005.12.003}.

JF Kok. Difference in the Wind Speeds Required for Initiation versus Continuation of Sand Transport on Mars: Implications for Dunes and Dust Storms. *Physical Review Letters*, 104(7), FEB 19 2010. ISSN 0031-9007. doi: {10.1103/PhysRevLett.104.074502}.

JF Kok and NO Renno. Electrification of wind-blown sand on Mars and its implications for atmospheric chemistry. *Geophysical Research Letters*, 36, MAR 11 2009. ISSN 0094-8276. doi: {10.1029/2008GL036691}.

JF Kok, EJR Parteli, TI Michaels, and DB Karam. The physics of wind-blown sand and dust. *Reports on Progress in Physics*, 75(10), OCT 2012. ISSN 0034-4885. doi: {10.1088/0034-4885/75/10/106901}.

AP Kositsky and JP Avouac. Inverting geodetic time series with a principal component analysis-based inversion method. *Journal of Geophysical Research - Solid Earth*, 115, MAR 3 2010. ISSN 2169-9313. doi: {10.1029/2009JB006535}.

YT Kuo, F Ayoub, S Leprince, YG Chen, JP Avouac, JBH Shyu, KY Lai, and YJ Kuo. Coseismic thrusting and folding in the 1999 mw 7.6 chi-chi earthquake: A high-resolution approach by aerial photos taken from tsaotun, central taiwan. *Journal of Geophysical Research: Solid Earth*, pages n/a–n/a, 2014. ISSN 2169-9356. doi: 10.1002/2013JB010308. URL `http://dx.doi.org/10.1002/2013JB010308`.

JE Laity and NT Bridges. Ventifacts on Earth and Mars: Analytical, field, and laboratory studies supporting sand abrasion and windward feature development. *Geomorphology*, 105(3-4):202–217, APR 15 2009. ISSN 0169-555X. doi: {10.1016/j.geomorph.2008.09.014}.

S Leprince. 3d high resolution tracking of ice flow using mutli-temporal stereo satellite imagery, franz josef glacier, new zealand. In *AGU Fall meeting*, 2013.

S Leprince, S Barbot, F Ayoub, and JP Avouac. Automatic and precise orthorectification, coregistration, and subpixel correlation of satellite images, application to ground deformation measurements. *IEEE Transactions on Geoscience* *and Remote Sensing*, 45(6, 1):1529–1558, JUN 2007. ISSN 0196-2892. doi: {10.1109/TGRS.2006.888937}.

S Leprince, E Berthier, F Ayoub, C Delacourt, and JP Avouac. Monitoring earth surface dynamics with optical imagery. *Eos, Transactions, AGU*, 89(1):1–2, 2008a.

S Leprince, P Muse, and JP Avouac. In-flight CCD distortion calibration for pushbroom satellites based on subpixel correlation. *IEEE Transactions on Geoscience and Remonte Sensing*, 46(9):2675–2683, SEP 2008b. ISSN 0196-2892. doi: {10.1109/TGRS.2008.918649}.

Lettau, K and Lettau, HH. *Exploring the world's driest climate*, volume 101. Institute for Environmental Studies, 1978.

LMD. Mars climate database, January 2014. http://www-mars.lmd.jussieu.fr/.

J Maclennan, E Passmore, G Fitton, T Thordarson, and B Winpenny. Concurrent mixing and cooling of melts under Iceland. *Journal of Petrology*, 49:1931–1953, 2008.

MC Malin. Preliminary abrasion rate observations in Victoria Valley, Antarctica. *Antartic Journal fo the United States*, 18(5):25–26, 1984.

MC Malin. Rate of geomorphic modification in ice-free areas southern Victoria Land, Antarctica. *Antartic Journal of the United States*, 20(5):18–21, 1986.

MC Malin and KS Edgett. Mars Global Surveyor Mars Orbiter Camera: Interplanetary cruise through primary mission. *Journal of Geophysical Research - Planets*, 106(E10):23429–23570, OCT 25 2001. ISSN 2169-9097. doi: {10.1029/2000JE001455}.

D Massonnet, M Rossi, C Carmona, F Adragna, G Peltzer, K Feigl, and T Rabaute. The Displacement Field of the Landers Earthquake Mapped by Radar Interferometry. *Nature*, 364(6433):138–141, 1993.

S Mattson, A Boyd, RL Kirk, DA Cook, and E Howington-Kraus. Hijack:correcting spacecraft jitter in hirise images of mars. In *European Planetary Science Congress*, Potsdam, Germany, September 2009.

DJ McCleese, NG Heavens, JT Schofield, WA Abdou, JL Bandfield, SB Calcutt, PGJ Irwin, DM Kass, A Kleinbohl, SR Lewis, DA Paige, PL Read, MI Richardson, JH Shirley, FW Taylor, N Teanby, and RW Zurek. Structure and dynamics of the Martian lower and middle atmosphere as observed by the Mars Climate Sounder: Seasonal variations in zonal mean temperature, dust, and water ice aerosols. *Journal of Geophysical Research - Planets*, 115, DEC 28 2010. ISSN 2169-9097. doi: {10.1029/2010JE003677}.

AS McEwen, EM Eliason, JW Bergstrom, NT Bridges, CJ Hansen, WA Delamere, JA Grant, VC Gulick, KE Herkenhoff, L Keszthelyi, RL Kirk, MT Mellon, SW Squyres, N Thomas, and CM Weitz. Mars Reconnaissance Orbiter's High Resolution Imaging Science Experiment (HiRISE). *Journal of Geophysical Research - Planets*, 112(E5), MAY 17 2007. ISSN 2169-9097. doi: {10.1029/2005JE002605}.

AS McEwen, ME Banks, N Baugh, K Becker, A Boyd, JW Bergstrom, RA Beyer, E Bortolini, NT Bridges, S Byrne, B Castalia, FC Chuang, LS Crumpler, I Daubar, AK Davatzes, DG Deardorff, A DeJong, WA Delamere, EN Dobrea, CM Dundas, EM Eliason, Y Espinoza, A Fennema, KE Fishbaugh, T Forrester, PE Geissler, JA Grant, JL Griffes, JP Grotzinger, VC Gulick, CJ Hansen, KE Herkenhoff, R Heyd, WL Jaeger, D Jones, B Kanefsky, L Keszthelyi, R King, RL Kirk, KJ Kolb, J Lasco, A Lefort, R Leis, KW Lewis, S Martinez-Alonso, S Mattson, G McArthur, MT Mellon, JM Metz, MP Milazzo, RE Milliken, T Motazedian, CH Okubo, A Ortiz, AJ Philippoff, J Plassmann, A Polit, PS Russell, C Schaller, ML Searls, T Spriggs, SW Squyres, S Tarr, N Thomas, BJ Thomson, LL Tornabene, C Van Houten, C Verba, CM Weitz, and JJ Wray. The High Resolution Imaging Science Experiment (HiRISE) during MRO's Primary Science Phase (PSP). *Icarus*, 205(1, SI):2–37, JAN 2010. ISSN 0019-1035. doi: {10.1016/j.icarus.2009.04.023}.

RL McMaster, JGE Schilling, and PR Pinet. Plate boundary within Tjörnes Fracture Zone on northern Iceland's insular margin. *Nature*, 269:663–668, 1977.

R Michel and JP Avouac. Deformation due to the 17 August 1999 Izmit, Turkey, earthquake measured from SPOT images. *Journal of Geophysical Research - Solid-Earth*, 107(B4), APR 10 2002. ISSN 0148-0227. doi: {10.1029/2000JB000102}.

R Michel and JP Avouac. Coseismic surface deformation from air photos: The Kickapoo step over in the 1992 Landers rupture. *Journal of Geophysical Research - Solid-Earth*, 111(B3), MAR 21 2006. ISSN 0148-0227. doi: {10.1029/2005JB003776}.

MA Mischna, C Lee, and M Richardson. Development of a fast, accurate radiative transfer model for the Martian atmosphere, past and present. *Journal of Geophysical Research - Planets*, 117, OCT 19 2012. ISSN 0148-0227. doi: {10.1029/2012JE004110}.

BH Mollberg and BB Schardt. Mission Report on the Orbiter Camera Payload System (OCPS) Large Format Camera (LFC) and Attitude Reference System (ARS). Technical report, Johnson Space Center (JSC-23184), 1988.

HJ Moore. The Martian dust storm of Sol-1742. *Journal of Geophysical Research - Solid Earth and Planets*, 90(S):D163–D174, NOV 15 1985. ISSN 0148-0227.

S Moriyama. Effects of dust on radiation transfer in the Martian atmosphere III: Numerical experiments of radiative-convective equilibrium of the Martian atmosphere including the radiative effects due to dust. *Journal of Meteorological Society of Japan*, 54:52–57, 1976.

MRAMS. Mars regional atmospheric modeling system, January 2014. http://www.boulder.swri.edu/ rafkin/.

NASA. Naif nasa, January 2014. http://naif.jpl.nasa.gov/naif/.

M Necsoiu, Sebastien Leprince, Donald M. Hooper, Cynthia L. Dinwiddie, Ronald N. McGinnis, and Gary R. Walter. Monitoring migration rates of an active subarctic dune field using optical imagery. *Remote Sensing of Environment*, 113(11):2441–2447, NOV 16 2009. ISSN 0034-4257. doi: {10.1016/j.rse.2009.07.004}.

CE Newman, SR Lewis, PL Read, and F Forget. Modeling the Martian dust cycle - 1. Representations of dust transport processes. *Journal of Geophysical Research - Planets*, 107(E12), DEC 10 2002. ISSN 0148-0227. doi: {10.1029/2002JE001910}.

H Nicholson, M Condomines, JG Fitton, AE Fallick, K Gronvold, and G Rogers. Geochemical and isotopic evidence for crustal assimilation beneath Krafla, Iceland. *Journal of Petrology*, 32:1005–1020, 1991.

ME Oskin, JR Arrowsmith, AH Corona, AJ Elliott, JM Fletcher, EJ Fielding, JJG Gold, PO and. Garcia, KW Hudnut, J Liu-Zeng, and OJ Teran. Near-Field Deformation from the El Mayor-Cucapah Earthquake Revealed by Differential LIDAR. *Science*, 335:702–705, 2012.

D Ould Ahmedou, A Ould Mahfoudh, P Dupont, AO El Moctar, A Valance, and KR Rasmussen. Barchan dune mobility in Mauritania related to dune and interdune sand fluxes. *Journal of Geophysical Research - Earth Surface*, 112 (F2), MAY 17 2007. ISSN 0148-0227.

G Peltzer, P Tapponnier, and R Armijo. Magnitude of Late Quaternary Left-Lateral Displacements Along the North Edge of Tibet. *Science*, 246:1285–1289, 1989.

P Pinzuti, A Mignan, and GCP King. Surface morphology of active normal faults in hard rock: Implications for the mechanics of the Asal Rift, Djibouti. *Earth and Planetary Science Letters*, 299:169–179, 2010.

JB Pollack, R Haberle, R Greeley, and J Iversen. Estimates of wind speeds required for particle motion on Mars. *Icarus*, 29(3):395–417, 1976. ISSN 0019-1035. doi: {10.1016/0019-1035(76)90141-X}.

FF Pollitz and IS Sacks. Viscosity structure beneath northeast Iceland. *Journal of Geophysical Reasearch*, 101(B8):17,771–17,793, 1996.

SCR Rafkin, TI Michaels, and RM Haberle. Meteorological predictions for the Beagle 2 mission to Mars. *Geophysical Research Letters*, 31(1), JAN 15 2004. ISSN 0094-8276. doi: {10.1029/2003GL018966}.

D Raucoules, B Ristori, M de Michele, and P Brioles. Surface displacement of the Mw 7 Machaze earthquake (Mozambique): Complimentary use of multiband InSAR and radar amplitude image correlation with elastic modelling. *Remote Sensing of Environment*, 114(10):221–2218, 2010.

MI Richardson, AD Toigo, and CE Newman. PlanetWRF: A general purpose, local to global numerical model for planetary atmospheric and climate dynamics. *Journal of Geophysical Research - Planets*, 112(E9), SEP 14 2007. ISSN 2169-9097. doi: {10.1029/2006JE002825}.

S Rögnvaldsson, A Gudmundsson, and R Slunga. Seismotectonic analysis of the Tjörnes Fracture Zone, an active transform fault in north Iceland. *Journal of Geophysical Reasearch*, 103(B12):30,117–30,129, 1998.

AM Rubin. Dike-induced faulting and graben subsidence in volcanic rift zones. *Journal of Geophsical Research*, 97(B2):1839–1858, 1992.

AM Rubin and DD Pollard. Dike-induced faulting in rift zones of Iceland and Afar. *Geology*, 16:413–417, 1988.

TA Scambos, MJ Dutkiewicz, JC Wilson, and RA Bindshalder. Application of images cross-correlation to the measurement of glacier velocity using satellite image data. *Remote Sensing of Environment*, 42(3):177–186, DEC 1992. ISSN 0034-4257. doi: {10.1016/0034-4257(92)90101-O}.

D Scherler, S Leprince, and MR Strecker. Glacier-surface velocities in alpine terrain from optical satellite imagery - Accuracy improvement and quality assessment. *Remote sensing of environment*, 112(10):3806–3819, OCT 15 2008. ISSN 0034-4257. doi: {10.1016/j.rse.2008.05.018}.

KP Schwarz, MA Chapman, MW Cannon, and P Gong. An integrated INS/GPS approach to the georeferencing of remotely-sensed data. *Photogrammetric Engineering and Remote Sensing*, 59(11):1667–1674, NOV 1993. ISSN 0099-1112.

K Sieh, L Jones, E Hauksson, K Hudnut, D Eberhartphillips, T Heaton, S Hough, K Hutton, H Kanamori, A Lilje, S Lindvall, SF McGill, J Mori, C Rubin, JA Spotila, J Stock, HK Thio, J Treiman, B Wernicke, and J Zachariasen. Near-field investigations of the Landers earthquake sequence, April to July 1992. *Science*, 260(5105):171–176, APR 9 1993. ISSN 0036-8075. doi: {10.1126/science.260.5105.171}.

F Sigmundsson. *Iceland Geodynamics: Crustal Deformation and Divergent Plate Tectonics*. Springer Praxis Books, 2006.

F. Sigmundsson, S. Hreinsdóttir, A. Hooper, T. Árnadóttir, R. Pedersen, M.J. Roberts, N. Óskarsson, A. Auriac, J. Decriem, P. Einarsson, H. Geirsson, M. Hensch, B. Ófeigsson, H. Sveinbjörnsson, and K. Feigl. Intrusion triggering of the 2010 Eyjafjallajökull explosive eruption. *Nature*, 468:423–430, 2010. doi: 10.1038/nature09558.

O Sigurdsson. Surface deformation of the Krafla fissure swarm in two rifting events. *Journal of Geophysics*, 47:154–159, 1980.

S. Silvestro, L. K. Fenton, D. A. Vaz, N. T. Bridges, and G. G. Ori. Ripple migration and dune activity on Mars: Evidence for dynamic wind processes. *Geophysical Research Letters*, 37, OCT 27 2010. ISSN 0094-8276. doi: {10.1029/2010GL044743}.

DB Simons, EV Richardson, and CF Nordin. Bedload equation for ripples and dunes. USGS Numbered Series Professional Paper, 1965. Series Number: 462-H.

WC Skamarock and JB Klemp. A time-split nonhydrostatic atmospheric model for weather research and forecasting applications. *Journal of Computational Physics*, 227(7):3465–3485, MAR 20 2008. ISSN 0021-9991. doi: {10.1016/j.jcp.2007.01.037}.

M Sorensen. On the rate of aeolian sand transport. *Geomorphology*, 59(1-4): 53–62, APR 2 2004. ISSN 0169-555X. doi: {10.1016/j.geomorph.2003.09.005}. Joint Meeting of the 5th International Conference on Aeolian Research/Global Change and Terrestrial Ecosystems-Soil Erosion Network, Texas Tech Univ, LUBBOCK, TX, JUL 22-25, 2002.

A Spiga and F Forget. A new model to simulate the Martian mesoscale and microscale atmospheric circulation: Validation and first results. *Journal of Geophysical Research - Planets*, 114, FEB 25 2009. ISSN 0148-0227. doi: {10.1029/2008JE003242}.

JA Spotila and K Sieh. Measurement of subresolution terrain displacements using SPOT panchromatic imagery. *Journal of Geophysical Research*, 100(B1):543–559, Jan 1995.

MJ Strausberg, HQ Wang, MI Richardson, SP Ewald, and AD Toigo. Observations of the initiation and evolution of the 2001 Mars global dust storm. *Journal of Geophysical Research - Planets*, 110(E2), FEB 26 2005. ISSN 0148-0227. doi: {10.1029/2004JE002361}.

R Sullivan, R Greeley, M Kraft, G Wilson, M Golombek, K Herkenhoff, J Murphy, and P Smith. Results of the imager for Mars Pathfinder windsock experiment. *Journal of Geophysical Research - Planets*, 105(E10):24547–24562, OCT 25 2000. ISSN 0148-0227. doi: {10.1029/1999JE001234}.

R Sullivan, R Arvidson, JF Bell, R Gellert, M Golombek, R Greeley, K Herkenhoff, J Johnson, S Thompson, P Whelley, and J Wray. Wind-driven particle mobility on mars: Insights from Mars Exploration Rover observations at "El Dorado" and surroundings at Gusev Crater. *Journal of Geophysical Research - Planets*, 113(E6), JUN 19 2008. ISSN 2169-9097. doi: {10.1029/2008JE003101}.

AB Surazakov and VB Aizen. Positional accuracy evaluation of declassified Hexagon KH-9 mapping camera imagery. *Photogrammetric Engineering & Remote Sensing*, 76:603–608, 2010.

MA Szwast, MI Richardson, and AR Vasavada. Surface dust redistribution on Mars as observed by the Mars Global Surveyor and Viking orbiters. *Journal of Geophysical Research - Planets*, 111(E11), NOV 22 2006. ISSN 2169-9097. doi: {10.1029/2005JE002485}.

P Tapponnier and P Molnar. Active faulting and tectonics in China. *Journal of Geophysical Research*, 82:2905–2930, 1977.

TO Tectonics-Observatory. Cosi-corr, January 2014. http://www.tectonics.caltech.edu/sliphistory/spotcoseis/index.html.

Y Teshima and A Iwasaki. Correction of attitude fluctuation of terra spacecraft using ASTER/SWIR imagery with parallax observation. *IEEE Transactions on Geoscience and Remote Sensing*, 46(1):222–227, JAN 2008. ISSN 0196-2892. doi: {10.1109/TGRS.2007.907424}.

AD Toigo, C Lee, CE Newman, and MI Richardson. The impact of resolution on the dynamics of the martian global atmosphere: Varying resolution studies with the MarsWRF GCM. *Icarus*, 221(1):276–288, SEP-OCT 2012. ISSN 0019-1035. doi: {10.1016/j.icarus.2012.07.020}.

JA Treiman, KJ Kendrick, WA Bryant, TK Rockwell, and SF McGill. Primary surface rupture associated with the M-w 7.1 16 October 1999 Hector Mine earthquake, San Bernardino County, California. *Bulletin of the Seismological Society of America*, 92(4):1171–1191, MAY 2002. ISSN 0037-1106. doi: {10.1785/0120000923}.

E Tryggvason. Ground movement in North Iceland during the earthquake swarm of 1975-1976 (in Icelandic, with English summary). *Náttúrufraedingurinn.*, 46: 124–128, 1976.

E. Tryggvason. Widening of the Krafla fissure swarm during the 1975–1981 Volcano-tectonic Episode. *Bulletin of Volcanology*, 47(1):47–69, 1984.

E Tryggvason. Surface deformation at the Krafla volcano, North Iceland, 1982–1992. *Bulletin of Volcanology*, 2:98–107, 1994. doi: 10.1007/BF00304105.

USGS. Socet set for hirise tutorial, January 2014a. http://webgis.wr.usgs.gov/pigwad/tutorials/socetset/SocetSet4HiRISE.htm.

USGS. Isis software, January 2014b. http://isis.astrogeology.usgs.gov.

USGS. Usgs landsat, January 2014c. http://http://landsat.usgs.gov/.

USGS-NAPP. National Aerial Photography Program, 1987. URL `http://www.usgs.gov/science/cite-view.php?cite=553`.

N Van Puymbroeck, R Michel, R Binet, JP Avouac, and J Taboury. Measuring earthquakes from optical satellite images. *Applied Optics*, 39(20):3486–3494, JUL 10 2000. ISSN 1559-128X. doi: {10.1364/AO.39.003486}.

P Vermeesch and N Drake. Remotely sensed dune celerity and sand flux measurements of the world's fastest barchans (Bodele, Chad). *Geophysical Research Letters*, 35(24), DEC 17 2008. ISSN 0094-8276. doi: {10.1029/2008GL035921}.

S Wei, E Fielding, S Leprince, A Sladen, JP Avouac, D Helmberger, E Hauksson, R Chu, M Simons, K Hudnut, T Herring, and R Briggs. Superficial simplicity of the 2010 El Mayor-Cucapah earthquake of Baja California in Mexico. *Nature Geoscience*, 4:615–618, 2011. doi: 10.1038/ngeo1213.

K Wendt, D Möller, and B Ritter. Geodetic measurements of surface deformations during the present rifting episode in NE Iceland. *Journal of Geophsical Research*, 90(B12):10163–10172, 1985. doi: 10.1029/jb090ib12p10163.

BT Werner. A steady-state model of wind-blown sand transport. *Journal of Geology*, 98(1):1–17, JAN 1990. ISSN 0022-1376.

BR White. Soil transport by winds on Mars. *Journal of Geophysical Research*, 84 (NB9):4643–4651, 1979. ISSN 0148-0227. doi: {10.1029/JB084iB09p04643}.

BR White and JC Schultz. Magnus effect in saltation. *Journal of Fluid Mechanics*, 81(JUL13):497–512, 1977. ISSN 0022-1120. doi: {10.1017/S0022112077002183}.

RS White, J Drew, HR Martens, J Key, H Soosalu, and SS Jakobsdottir. Dynamics of dyke intrusion in the mid-crust of Iceland. *Earth and Planetary Science Letters*, 304(3–4):300–312, 2011.

Wikipedia. Wikipedia remote sensing, 2014. URL `http://en.wikipedia.org/wiki/Remote_sensing`.

RJ Wilson and K Hamilton. Comprehensive model simulation of thermal tides in the Martian atmosphere. *Journal of the atmospheric sciences*, 53(9):1290–1326, MAY 1 1996. ISSN 0022-4928.

Wolf, P and Dewitt, B. *Elements of Photogrammetry with Applications in GIS.* McGraw Hill, 3rd edition, 2000.

TJ Wright, C Ebinger, J Biggs, A Ayele, G Yirgu, D Keir, and A Stork. Magma-maintained rift segmentation at continental rupture in the 2005 Afar dyking episode. *Nature*, 442:291–294, 2006.

JR. Zimbelman. Transverse Aeolian Ridges on Mars: First results from HiRISE images. *Geomorphology*, 121(1-2, SI):22–29, SEP 1 2010. ISSN 0169-555X. doi: {10.1016/j.geomorph.2009.05.012}.

A Ziv, A Rubin, and A Amotz. Stability of dike intrusion along preexisting fractures. *Journal of Geophsical Research*, 105):5947–5961, 2000.

AUTHOR: François AYOUB
TITLE: Monitoring morphologic surface changes from aerial and satellite imagery, on Earth and Mars
THESIS ADVISORS: Jean-Philippe AVOUAC and Alexis RIGO
DEFENSE LOCATION AND DATE: OMP, July 1, 2014

The analysis of satellites imagery acquired at different dates allows the measurement of Earth surface displacement (earthquake ground deformation, glacier advance and retreat, sand dunes migration, slow-moving landslide,. . .) that occured between the images acquisitions. In this thesis we investigate 1) the extension of the processing techniques established for satellite imagery to aerial imagery, and 2) the applicability of Earth-based technique to monitor eolian surface processes on Mars.

Aerial imagery, whose first acquisition dates back decades before the satellite era, and whose ground resolution is higher than satellite one, can be relevant to monitor Earth surface displacement. We present a methodological extension of the satellite technique to aerial imagery. Potential and limitations are investigated. Application to the Krafla rift opening in Iceland (1975-1984), using aerial imagery, declassied spy imagery, and modern satellite imagery is presented.

Next, we applied the method to Mars imagery taking advantage of the high resolution HiRISE instrument. A pair of HiRISE images is processed to monitor the activitys of a dune field. We measured sand ripple migration and inferred a sand flux comparable to some the Earth dune fields sand flux. We then expand our processing to a time-series of 10 HiRISE images, and characterized the seasonal variability of the sand flux throughout the year. This seasonal sand flux variability is used jointly with a sand flux prediction from atmospheric simulations to constrain the sand mobility threshold.

KEYWORDS: Remote sensing; Aerial imagery; Surface deformation; Earthquake; HiRISE; Mars; Dunes; Flux

AUTEUR: François AYOUB
TITRE: Suivi de changements morphologiques de surface à partir d'images aériennes et satellitaires, sur terre et mars
DIRECTEURS DE THESE: Jean-Philippe AVOUAC et Alexis RIGO
LIEU ET DATE DE SOUTENANCE: OMP, le 1$^{\text{er}}$ juillet 2014

L'analyse d'images satellitaires acquises à différentes dates permet la mesure des déplacements de la surface terrestre (déformation co-sismique du sol, avancée ou le recul de glacier, migration de dunes, glissements de terrain...) survenus entre les dates d'acquisition. Au cours de cette thèse nous étudions 1) l'extension des méthodes de traitement d'images satellitaires aux images aériennes et 2) l'applicabilitée des méthodes satellitaires terrestres pour l'étude des processus éoliens sur mars.

L'imagerie aérienne, par sa longue archive et haute résolution spatiale peut être utile pour le suivi des processus de surface terrestre. Nous proposons une méthode de traitement d'images aériennes, basée sur les méthodes satellitaires et prenant en compte les spécificités des images aériennes d'archive. Le potentiel et limites de ce type d'imagerie sont caractérisés. La méthode est appliquée à la mesure de l'ouverture du rift de Krafla en Icelande (1975-1984) à partir d'images aériennes, d'une image espion déclassifiée et d'une image satellitaire.

En seconde partie, nous appliquons ces techniques sur mars pour le suivi d'activité d'un champ de dunes. Après adaptation des méthodes terrestres au capteur HiRISE, nous mesurons la migration des rides de sable couvrant les dunes et estimons un flux de sable associé, qui s'avère être comparable au flux du champ de dunes d'antarctique. L'analyse d'une série temporelle de 10 images HiRISE permet de caractériser la variation saisonnière du flux au cours d'une année martienne et de calibrer la contrainte en cisaillement du sable sur mars via une prédiction de flux issue de simulation atmosphérique.

MOTS CLES: Télédétection; Imagerie aérienne; Déformation; Séisme; HiRISE; Mars; Dunes; Flux

DISCIPLINE: Sciences de la terre et des planètes solides

IRAP Observatoire Midi-Pyrénées, 14 avenue Edouard Belin, 31400 Toulouse